INVESTIGATION OF THIN MIDLEVEL ICE CLOUDS IN THE ARCTIC USING CALIPSO DATA AND RADIATIVE TRANSFER MODELING

By

Vinay Kumar Kayetha

RECOMMENDED:

Dr. Uma Bhatt

Dr. Anupma Prakash

Dr. Franz Meyer

Dr. Richard Collins
Advisory Committee Chair

Dr. Uma Bhatt
Chair, Department of Atmospheric Sciences

APPROVED:

Dr. Paul Layer
Dean, College of Natural Science and Mathematics

Dr. John Eichelberger
Dean of the Graduate School

11 August 2015
Date

INVESTIGATION OF THIN MIDLEVEL ICE CLOUDS IN THE ARCTIC USING CALIPSO DATA AND RADIATIVE TRANSFER MODELING

A

DISSERTATION

Presented to the Faculty

of the University of Alaska Fairbanks

in Partial Fulfillment of the Requirements

for the Degree of

DOCTOR OF PHILOSOPHY

By

Vinay Kumar Kayetha, M.S., M.TECH., B.TECH.

Fairbanks, Alaska

August 2015

Abstract

In this research we investigate the global occurrence and properties of optically thin midlevel ice clouds. These clouds are difficult to detect with passive radiometric techniques and are under-represented in current studies. We use the Cloud Aerosol Lidar and Infrared Pathfinder Satellite Observation (CALIPSO) data set to identify thin midlevel ice clouds and determine their global occurrence and distribution. For the first time, we find that the global mean occurrence of these clouds is at least 4.5%, being at least 7.3% of all the tropospheric clouds detected at a horizontal scale of 10 km. Seasonally, these clouds are found most commonly in the polar regions. These clouds occur most commonly in the Arctic in winter and least commonly in the summer. In winter these clouds can occur up to 19% of the time. The occurrence of these clouds decreases with increasing spatial scale and are most commonly found at spatial scales of 25 km or less. We found five large distinct clouds over the Arctic and investigated them for their meteorological conditions and radiative effects. These thin midlevel ice clouds are formed along the frontal zones in weakly ascending air masses. Our model simulations show that thin midlevel ice clouds have a net warming effect on the surface of $23 - 48$ W/m^2. We conclude that these clouds have a significant impact on the radiation budget in Arctic winters. Our study highlights the importance of active satellite-based remote sensing in globally detecting and characterizing optically thin clouds. Our estimates of occurrence and fraction of clouds represents a lower bound, as these clouds can be obscured by optically thicker clouds. The volume of measurements provided by the satellite allowed us to identify a small but consistent set of large clouds with which we could conduct a contemporary radiative analysis. These findings can be used to improve the representation of clouds and their impacts in regional and global climate models.

Table of Contents

List of Figures

Page

List of Tables

Page

Acknowledgements

Firstly, I would like to thank Professor Richard Collins for giving me an opportunity to work with him, for the several hours spent providing comments/suggestions and improving the work. I am also greatly indebted to my committee members Dr. Uma Bhatt, Dr. Anupma Prakash and Dr. Franz Meyer for helping me in this journey towards my goal and want to extend my heartfelt thanks to all of them.

I would like to thank my research group members Colin Triplett and Jintai Li for their help whenever I needed it. I would like to thank Peter Bieniek for his support and encouragement. Thanks also to the entire team of faculty and fellow students associated with the Department of Atmospheric Sciences for their enthusiasm and particularly Barbara Day for assistance with all deadlines and paper work.

I would like to also thank the staff at the Arctic Research Supercomputing Center (ARSC). Without access to the ARSC facilities I would not have been able to study this large satellite data set. Thanks also to the AFARS, CALIPSO and libRadtran staff for making the lidar data and radiative transfer model available.

Thanks to the Dean Paul Layer of the College of Natural Sciences and Mathematics, and the Dean John Eichelberger of the Graduate School for the financial support during my stay at the University.

Finally, I would like to thank my parents for their support and patience, which never let me down. Thanks to all of my friends here in Fairbanks who has been my surrogate family and made my life peaceful.

Chapter 1
Introduction

1.1 Clouds and climate

Fundamental questions of the climate system remain unsolved because of our limited understanding of how clouds, atmospheric circulation, and climate interact (*Bony et al.*, 2015). From a climate perspective it is important to understand the cloud processes and their radiative effects. Clouds interact with both solar (shortwave) and terrestrial thermal (longwave) radiation and thus regulate the amount of energy reaching the Earth's surface and leaving the Earth's atmosphere. The interaction of clouds with radiation acts to both warm and cool the Earth's surface [e.g., *Trenberth et al.* (2009)]. Clouds cool the Earth's surface by reflecting incoming solar shortwave radiation back to space ('albedo effect'). Clouds warm the Earth's surface by absorbing outgoing terrestrial longwave radiation and re-radiating it back to the ground ('greenhouse effect'). The net radiative effect of clouds is determined by the competition between the cloud albedo and greenhouse effects. The radiative effect of clouds depends on their macrophysical (altitude, temperature, geometrical thickness) and microphysical (particle sizes, concentration, and phase) properties (*Minnis et al.*, 1990; *Hartmann et al.*, 1991, 1992). Any systematic change in the properties of clouds or their geographical and seasonal occurrence can have profound effects on the climate.

Our limited understanding of the cloud's radiative effects has been highlighted by Intergovernmental Panel for Climate Change (IPCC) as one of the major uncertainties in assessing the present and projected climate (*Solomon et al.*, 2007). For example, because both water droplets and ice crystals nucleate on small aerosol particles, changes in concentration and properties of aerosols can alter the cloud albedo by changing the cloud particle concentration and sizes. This aerosol cloud albedo effect is one of the major components of radiative forcing in current climate models (*Solomon et al.*, 2007). However, as shown in Figure 1.1, the uncertainty in this forcing is the largest unknown in our current understanding of the climate. In the global average, this aerosol cloud albedo effect may have a cooling effect as large as the warming due to carbon dioxide (~1.5 W/m^2) or alternatively be have only a fraction of that effect (0.5 W/m^2). At a regional level, as clouds embedded in storm tracks shift, there are systematic changes in the radiation budget and temperature gradients that give rise to the storms in the first place. There is an increased understanding

on moist processes and radiative effects that influence storm development and the structure of the storm tracks (*Miyamoto et al.*, 2013; *Grise and Polvani*, 2014).

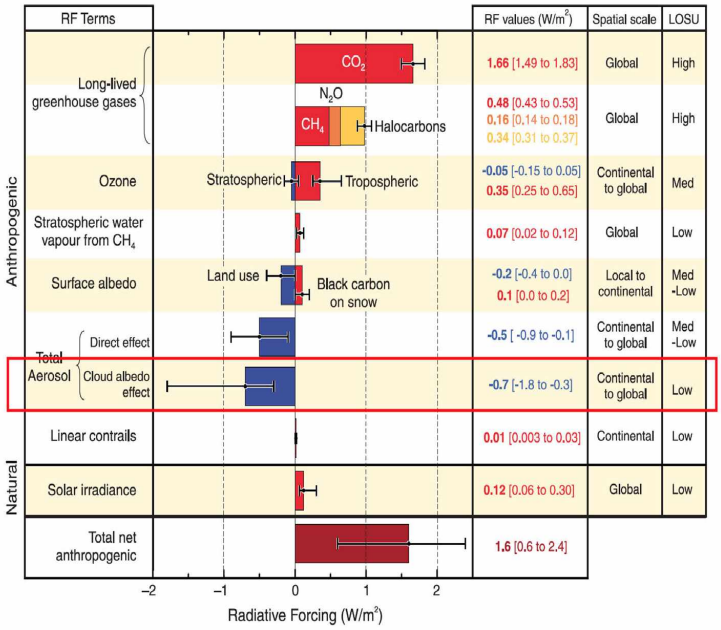

Figure 1.1: The contributions to radiative forcing from some of the factors influenced by human activities (*Solomon et al.*, 2007).

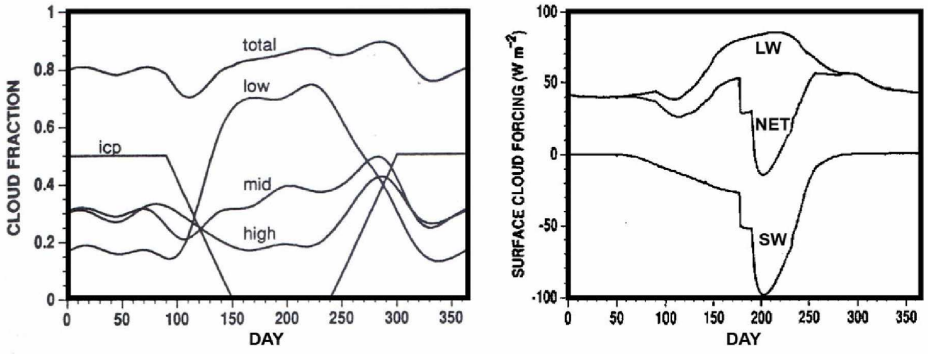

Figure 1.2: Annual cycle of arctic clouds and their radiative forcing at the surface (*Curry and Ebert*, 1992).

In the polar regions, day-night variations in cloud radiative forcing become seasonal cycles. Studies that show the annual cycle of radiative fluxes over the Arctic illustrates this effect (*Curry and Ebert*, 1992). In winter darkness the cloud forcing is positive, as the 'green-

house effect' of the clouds yield a surface forcing of ~40 W/m^2 (Figure 1.2). However, in summer sunshine the 'albedo effect' counteracts the 'greenhouse effect' to yield a surface forcing of ~–10 W/m^2. Recent interest in clouds in the Arctic has focused on the relationship between cloud cover and sea ice (*Eastman and Warren*, 2010). These authors report increased cloudiness in low sea-ice years. Given that long-term observations suggest increasing cloudiness in the Arctic, this may promote decreased sea-ice due to longwave radiative forcing.

New satellites with active remote sensing capabilities that directly resolve vertical structure in the atmosphere have removed ambiguities that are inherent in the passive remote sensing the atmosphere. One of the most important of these new satellites is the Cloud Aerosol Lidar Infrared Pathfinder Satellite Observations (CALIPSO) (*Winker et al.*, 2009). The Cloud-Aerosol Lidar with Orthogonal Polarization (CALIOP) aboard CALIPSO has enabled a view of how clouds of different depths couple to their large-scale environment. Furthermore, these lidar (or laser radar) measurements provide a global view of clouds and can detect even thin clouds that are not readily detected by passive satellites. This is particularly important in the Arctic winter, when first there is no sunlight to allow satellites with visible sensors to see the clouds and when second the ground temperatures are similar to the cloud temperatures and so confuse the satellites with infrared sensors. This dissertation focuses on midlevel thin ice clouds in the Arctic as measured by CALIOP on board CALIPSO. While we focus on the Arctic, the global nature of the data set allows us put these clouds in a global context in terms of geographic distribution, seasonal variation, and occurrence of other cloud types.

1.2 Midlevel clouds

According to the World Meteorological Organization (WMO), midlevel clouds are those that typically form with their base altitudes between 2 km and 7 km (*WMO*, 1987, 1988). There are commonly two types of midlevel clouds according to the WMO 'genera' of cloud classification (*WMO*, 1987): altostratus and altocumulus. In general, altostratus clouds are ice-dominated and altocumulus clouds are water dominated. This difference in the cloud composition contributes to their distinct visual appearances and radiative effects. Altostratus clouds are observed to form as thick and dark layers, that obscure the disk of Sun or Moon for surface observers. In general these clouds are the product of slow ascent or uplift of air mass over large areas or along frontal zones. Typical altostratus clouds

often resemble cirrostratus clouds in appearance and usually form in a gradual thickening process at upper levels that yields large ice particles. These ice particles then subside to midlevels (*Sassen*, 2002). Altocumulus clouds form as cellular structures and are thinner than altostratus clouds. These clouds commonly form through convection and often have ice virga precipitating from the cloud base.

Apart from the traditionally observed midlevel clouds that are optically thick, optically thin midlevel clouds also exist. These thin altostratus and thin altocumulus clouds do not obscure the disk of Sun or Moon for a surface observer. Thin ice clouds form in the midlevels of the troposphere as a result of glaciation of altocumulus clouds (*Sassen et al.*, 2003; *Sassen and Khvorostyanov*, 2008), as residuals of briefly lived clouds (*Hobbs and Rangno*, 1998), and those formed under the influence of topography over mountainous terrain. These thin midlevel clouds are least studied because of the limitations of the ground-based measurements and satellite passive sensors.

Although midlevel clouds cover up to 22% of the Earth's atmosphere (*Warren et al.*, 1986, 1988), they rarely produce precipitation and severe weather (*Gedzelman*, 1988). Therefore studies often neglect midlevel clouds. Studies show that most general circulation models underpredict midlevel cloud occurrence (*Zhang et al.*, 2005; *Illingworth et al.*, 2007). Observational studies show that these clouds are under-reported as midlevel clouds are often obscured by high level or low level clouds when observed from the top of atmosphere or surface, respectively. Furthermore, optically thin midlevel clouds are difficult to identify with passive sensors (*Zhang et al.*, 2005; *Wyser et al.*, 2008). The other challenge in understanding midlevel clouds is associated with the phase of the cloud particles. The intermediate altitudes (~2 – 10 km) of these clouds allows them to contain ice, water or mixed-phase particles depending on the local environmental conditions. Although much has been learned about water clouds and ice clouds, the complex microphysics of mixed-phase clouds makes the modeling of the midlevel cloud processes more challenging (*Sun and Shine*, 1995).

1.3 Cloud classification based on observational technique

Despite the substantial efforts and significant progress made over the past few decades, understanding of cloud types still remains a challenge. Partly this is due to the classification of clouds that can vary widely with the observational technique. For climate studies,

it is important to understand clouds in terms of their radiative effects. However different cloud observing techniques and strategies have different biases. Cloud climatologies derived from surface observations rely on the visual inspection of cloud base altitude. While cloud base heights of low level clouds can be estimated with good accuracy, the discrimination between middle and high clouds may depend more on morphology. There are three main height classes: low (0 – 2 km), middle (2 – 4 km in higher latitudes above 60°, 2 – 6 km at lower latitudes), and high. The first contemporary cloud climatology was prepared by compiling surface observations from world wide weather stations and yielded the result that midlevel clouds cover up to 22% of the time (*Warren et al.*, 1986, 1988). However, this estimate of 22% is a lower bound as low level clouds often obscure midlevel clouds from surface observers.

Cloud climatologies derived from passive satellite remote sensing observations rely on the cloud top pressure and cloud optical depth to classify clouds. Passive satellites measure the radiances at visible/infrared wavelengths that are compared with model simulated radiances to identify and derive cloud properties, such as visible optical depth, τ. Using passive satellite data, midlevel clouds are categorized as those forming between the 680 hPa and 440 hPa pressure levels (~3 km to 7 km) and as altocumulus (τ <3.6), altostratus (3.6 <τ <23) and nimbostratus (τ >23) clouds. Midlevel clouds are observed about 19% of the time (*Rossow and Schiffer*, 1999). Again this estimate represents a lower value as thinner (and therefore dimmer) midlevel clouds are obscured when they occur above thicker (and brighter) low level clouds and over snow- and ice-covered surfaces.

Active sensors, such as lidars and radars that identify both cloud top and base provide more accurate and sensitive measurements of thin clouds. Using lidar or radar remote sensing over the surface or airborne platform, several investigations have reported midlevel clouds over the tropics (*Yasunaga et al.*, 2006; *Ansmann et al.*, 2009; *Seifert et al.*, 2010; *Riihimaki et al.*, 2012), midlatitudes (*Heymsfield et al.*, 1991; *Field*, 1999; *Fleishauer et al.*, 2002; *Hogan et al.*, 2003; *Smith et al.*, 2009) and high-latitudes (*Hobbs and Rangno*, 1998; *Shupe et al.*, 2008, 2011). Active satellite measurements of the global distribution of altostratus and altocumulus clouds has shown these these clouds are prevalent over the polar regions (*Sassen and Wang*, 2012). These studies group optically thin and thick clouds as a single category. However, the lidar measurement of thick clouds suffers from the fact that the lidar beam does not completely penetrate the cloud. Thus in satellite measurements of thick

clouds the cloud tops are measured accurately while the cloud bases are ambiguous, and in ground-based measurements of thick clouds the cloud bases are measured accurately while the cloud tops are ambiguous. A comprehensive study that focuses on the occurrence and properties of thin midlevel clouds is still lacking. Such a study would provide a consistent view of these clouds and their role in the Earth's climate system.

Lampert et al. (2009) reported a case study of a thin ($\tau < 0.03$) midlevel ice cloud during a airborne field campaign in the 2006 – 2007 winter over Svalbard. Based on this field campaign they indicated that such clouds could be common over the Arctic region. Interest in Arctic midlevel clouds has also prompted a multi-year investigation of these clouds using a lidar at the Arctic Facility for Atmospheric Remote Sensing (AFARS), at the University of Alaska Fairbanks (64.86° N, 147.84° W). Optically thin midlevel ice clouds were observed 15% of the time over the AFARS station (*Kayetha*, 2014).

1.4 Objective and structure of the dissertation

The current study focuses on understanding the prevalence and properties of optically thin midlevel ice clouds as measured by a satellite-borne lidar. This dissertation presents a study of thin midlevel clouds as measured by the CALIOP lidar on the CALIPSO satellite over four years (2006 – 2010). This CALIPSO data allows us to consistently characterize these clouds globally, determine their relative occurrence amongst all clouds, and identify individual clouds that can be used to assess the radiative impact of these clouds on the Earth's surface.

This dissertation consists of five chapters. In Chapter 2, we review ground-based and satellite-based lidar measurements of clouds over AFARS from publicly available data archive (www.rainbow.gi.alaska.edu) . We confirm that both ground-based and satellite-based measurements provide a consistent view of optically thin midlevel clouds. In Chapter 3, we develop and implement logic-based rules to classify tropospheric clouds as detected and characterized by CALIPSO. This categorization, provides a holistic view of all cloud categories (optically thin and optically thick) and their global occurrence. We investigate the cloud macrophysical properties, geographic, seasonal, and day-night variations. We also investigate the horizontal spatial scales of the clouds. In Chapter 4, we determine the radiative properties of thin midlevel clouds over the Arctic. We use a freely available radiative transfer model *libRadtran* (www.libradtran.org) to calculate the radiative forcing

of these clouds. Finally in Chapter 5, we present a summary of our findings, conclusions that emphasize the role of these Arctic clouds in the Earth system, and our recommendations for future work.

Chapter 2
Instruments, data processing and data products

2.1 A-Train constellation

The CALIPSO satellite flies in a Sun-synchronous retrograde orbit (~705 km altitude) around the Earth's surface at a speed of about 7 km/s. CALIPSO along with Aqua, Aura, GCOM-W1, OCO-2 and CloudSat composes the Afternoon-Train constellation of satellites. The Afternoon Train, or A-Train, constellation cross the Earth's equator near local afternoon (~1:30 pm) and midnight (~1:30 am). The A-train travels northward (ascending) during the day half-orbit and southward (descending) during the night half-orbit. For a single day the satellite typical has up to 14 orbital tracks and repeats the equivalent ground track every 16 days. The purpose of the A-train constellation of satellites is to achieve simultaneous measurements of Earth's constituents from several instruments onboard with a minimum time lag ranging from a few seconds to a few minutes. The CALIPSO and CloudSat joined the A-train in June 2006 and since then provide continuous observations of clouds and aerosols over the Earth's atmosphere at global scales.

2.2 CALIPSO

The CALIPSO payload consists of three co-aligned, near-nadir viewing instruments: a dual wavelength Cloud-Aerosol Lidar with Orthogonal Polarization (CALIOP), an Imaging Infrared Radiometer (IIR), and a high-resolution Wide Field Camera (WFC). The purpose of the two passive instruments (i.e., IIR and WFC) is to provide additional information and meteorological context of the lidar's narrow field-of-view (FOV) measurements. The CALIOP lidar includes two identical laser transmitters, each equipped with a beam expander and a beam steering system, to ensure alignment between the transmitter and receiver. CALIOP employs an Nd:YAG laser to generate pulses of 110 mJ energy at both 532 nm and 1064 nm wavelengths with a pulse length of 20 ns. The lidar pulse repetition rate is 20.16 Hz. This repetition rate allows for a sampling of the complete atmospheric column every ~333 m on the ground. The emitted laser pulses are directed through beam expanders with an angular divergence of 100 rad to achieve a transmitted laser beam diameter of ~70 m on the surface of the Earth. The transmitted laser beam is linearly polarized and a beam splitter is used in the receiver subsystem to separate the parallel and perpendicular components of the returned signal for the 532 nm channel. The other components

of the receiver subsystem are a 1 m diameter telescope and three detectors - one for 1064 nm channel and two for the parallel and perpendicular polarization of the 532 nm channel.

Once a laser pulse is produced and transmitted the receiver equipped with a wide telescope measures the intensity of light backscattered from the atmospheric constituents. Depending on the scattering regime of the atmospheric constituents (clouds, aerosols, molecules, etc) the returned signals at the receiver are in the order of six magnitudes. Onboard detectors-photomultiplier tubes (PMTs), which provide high dynamic range are used to capture the returned signals at 532 nm channel, while an avalanche photodiode (APD) is used for the 1064 nm channel. To reduce the contamination of the returned signals by the solar background light, an etalon with a passband of 35 pm is used along with a dielectric interference filter in the 532 nm channels, while an interference filter alone is used for the 1064 nm channel. The analog signals from each detector are digitized at 10 MHz (corresponding to a 15 m range interval) starting when the laser pulse reaches an altitude of 115 km. The signals acquired between altitudes of 112 km and 97 km and between 80 km and 65 km, where the backscattering is insignificant, are averaged to obtain the solar background and DC signal level. The samples acquired below 40 km, for the 532 nm channels, and 30 km for the 1064 nm channel, are recorded and preprocessed (i.e., averaging and background subtraction) before they are downlinked to the ground-receiving station.

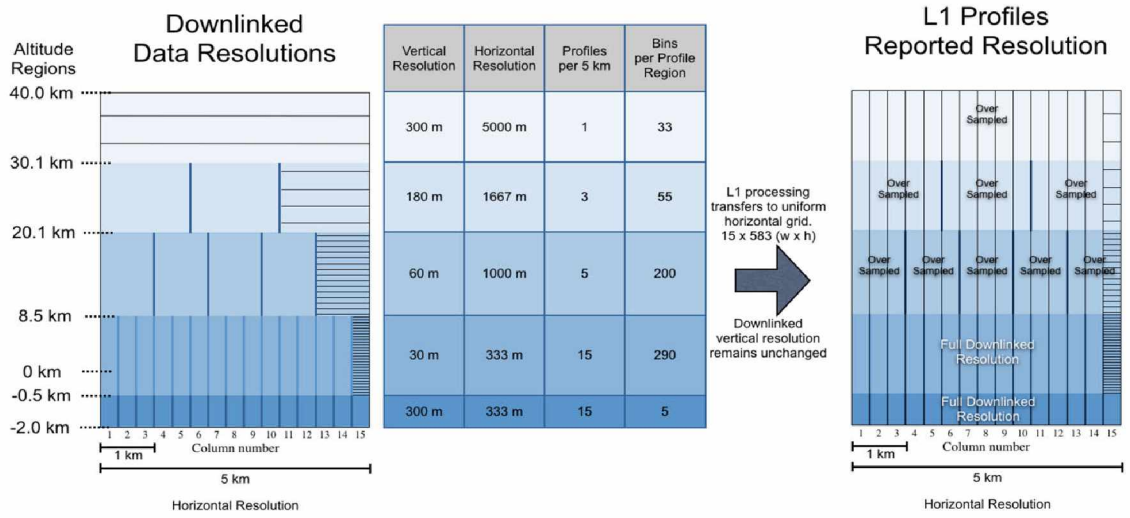

Figure 2.1: CALIPSO downlinked data resolution.

Figure 2.1 shows the downlinked data resolution with the averaging scheme implemented to produce calibrated backscattering profiles, which are distributed as Level-1 data products to the end users. To reduce the bandwidth of telemetry an altitude-dependent onboard averaging scheme is implemented. This averaging scheme owes to the fact that the atmosphere is more spatially uniform with increasing altitude and thus signals from higher levels in the atmosphere tend to be very weak, requiring more samples to be averaged to achieve the required signal-to-noise ratio (SNR) (*Winker et al.*, 2009).

2.2.1 Theoretical description on the working of lidar

The theoretical description on the working of lidar can be given through a lidar equation based on the particle scattering assumption. The lidar equation serves as a basis to relate the laser remote sensing field to the received photon counts (or in terms of laser power), light propagation in the atmosphere and the physical interaction between light and atmospheric constituents. The commonly used lidar equation for elastic scattering of light can be written as (*Measures*, 1992; *Silfvast*, 2004):

$$N_S(\lambda,r) = \left[\frac{P_L(\lambda)\Delta t}{\frac{hc}{\lambda}}\right] \mathrm{x} \left[\beta(\lambda,r)\Delta r\right] \mathrm{x} \frac{A}{r^2} \mathrm{x} \left[\eta(\lambda).T^2(\lambda,r).G(r)\right] + N_B\Delta t \tag{2.1}$$

where, $N_S(\lambda,r)$ is received number of photons from range r and wavelength λ, h is planck's constant, c is the velocity of light, Δt is the time interval of the laser pulse, $P_L(\lambda)$ is power of the laser transmitted, $\beta(\lambda,r)$ is volume backscatter coefficient, A is the area of the receiver, $T^2(\lambda,r)$ is two-way atmospheric transmittance, $\eta(\lambda)$ is optical efficiency of laser system, $G(r)$ is geometrical gain of receiver, and N_B is background photon counts.

A more general form of lidar equation used for lower atmosphere by a monostatic lidar under isotropic scattering assumption can be written as (*Scotland et al.*, 1971):

$$P(\lambda,r) = \frac{C(\lambda)}{r^2} \mathrm{x} \left[\beta_a(\lambda,r) + \beta_m(\lambda,r)\right] \mathrm{x} \exp\left[-2\int_0^r \left(\sigma_a(\lambda,r) + \sigma_m(\lambda,r)\right).dr\right] \tag{2.2}$$

where, $P(\lambda,r)$ is the returned backscattering power, C is the constant derived for the instrument, λ is operating wavelength of lidar, r is the distance of the target from lidar, σ_m, σ_a are the absorption coefficients of atmospheric molecules and particles, and β_m, β_a are the backscatter coefficients due to atmospheric molecules and particles.

The backscattering coefficient (β) represents the amount of light scattered in the backward direction from a volume of scatterers and depends on the particle phase function and scattering cross-section (square of the particle size/diameter to the scattering efficiency). The absorption coefficient (σ) represents the total quantity of light energy removed from the incident field and depends on the particle extinction cross-section. The backscatter and absorption coefficients, which are the unknown quantities in the lidar equation (2.2), can be derived from inversion methods by assuming a value for extinction-to-backscatter ratio (referred as lidar ratio, S) for any given scatterers (*Fernald et al.*, 1972; *Klett*, 1981). The other method for estimating the lidar ratio is to choose a clear air altitude range in the lidar profile where the returned signal is only due to the molecular scattering. Then the molecular (Rayleigh) volume backscattering is calculated as the product of number density of molecules and backscattering cross-section for air (*Measures*, 1992).

$$\beta_m(r,\lambda) = N(r) \times \sigma_m^R(\lambda) \tag{2.3}$$

where, $N(r)$ is the atmospheric number density at altitude r, and $\sigma_m^R(\lambda)$ is the molecular backscattering cross-section at wavelength (λ).

For a mixture of atmospheric gases below 100 km altitude, the molecular backscattering cross-section as estimated by *Collis and Russell* (1976) is:

$$\sigma_m^R(\lambda) = 5.45\text{x}\left[\frac{550}{\lambda(\text{nm})}\right]^4 \text{x}10^{-28} cm^2 sr^{-1} \tag{2.4}$$

For a standard atmosphere, the number density of molecules at any altitude r can be calculated as:

$$N(r) = N_A \times \frac{T_0}{T(r)} \times \frac{P(r)}{P_0} \tag{2.5}$$

where, N_A ($2.69\text{x}10^{19}$ molecules/cm^3), T_0 (273.15 K), P_0 (1013.25 mb) are the number density, temperature, and pressure at sea level, and $N(r), T(r), P(r)$ are the number density, temperature, and pressure at altitude r, respectively.

Thus the volume molecular backscattering at any altitude can be estimated using the temperature and pressure fields based on the equation 2.3. Once the molecular contribution

in the returned signal is known, the backscattering due to other atmospheric constituents (clouds or aerosols) can be computed. The other parameter that can be derived from the returned signal, through polarization channel is the depolarization ratio, which allows for the discrimination of the shape of scatterers as spherical or non-spherical. The linear depolarization ratio (LDR, denoted as δ) is defined as the ratio of the perpendicular to the parallel-polarized backscattered signals.

The parameter δ is used to infer the phase of the cloud. For instance, liquid water droplets of spherical shape retain the polarization state of the incident light, whereas the light incident on non-spherical particles undergoes multiple internal reflections, and produces depolarization of the light (*Liou and Scotland*, 1971). The corresponding δ values of commonly encountered hydrometeors in the atmosphere as reported by *Scotland et al.* (1971) and *Sassen* (1991) are: water droplets ~0.0, ice crystals and snowflakes ~0.5, and rimed ice and particles with complex surfaces have values more than 0.6.

2.2.2 CALIOP data processing

The operational processing of space-borne lidar data requires several assumptions for the calibration and retrieval of lidar ratio. The complete description of the calibration algorithms adopted for CALIPSO data are given in *Powell et al.* (2009). To produce calibrated profiles of attenuated backscatter for the three different channels, the returned signals along with the ancillary geophysical and meteorological data such as surface elevation (GTOPO30), temperature and pressure profiles of the atmosphere available through Global Modeling and Assimilation Office (GMAO) models are used as inputs. The CALIOP 532 nm parallel channel is calibrated by averaging signal over the 30 – 34 km altitude range where the aerosol loading is assumed to be insignificant and the obtained scattering is only due to molecules. The molecular backscattering in the calibrated region is computed using the density profiles from GMAO model (*Rienecker et al.*, 2008) and a known Cabannes backscatter cross-section (e.g., *She* (2001)). Due to the higher levels of noise associated with solar background signals, the calibration technique used during the nighttime cannot be used for daytime measurements. The daytime calibration constants for the version 3 of CALIPSO data are derived by a set of latitudinal- and time-dependent scale factors (*Powell et al.*, 2010). These scale factors are derived using attenuated scattering ratios calculated over cloud-free regions between 8 – 12 km altitudes. The calibration constants obtained

for the parallel channel are then transferred to the perpendicular channel using a pseudo-polarizer which allows for the electro-optical gain between the parallel and perpendicular channels.

Due to the nature of backscattering in the atmosphere which spans several orders of magnitude, the detection of features in CALIPSO data is challenging. A specifically designed algorithm called the Selective Iterated Boundary Locator (SIBYL) has been developed for this purpose by the CALIPSO team. The SIBYL algorithm starts at the top of the atmospheric profile at 40 km, which is a relatively clear air region, and compares the measured attenuated backscattering signal with the modeled data to determine a background signal and hence estimate an attenuated scattering ratio. The accuracy of the background signal obtained depends on the quality of the ancillary meteorological data obtained through GMAO models and the assumptions made. However, in practice the lidar signal is always contaminated with some amount of noise despite being well calibrated. Thus an optimum value of threshold signal is chosen to maximize the likelihood of detecting a feature successfully and eliminate the spurious detections due to noise. Then the algorithm scans the entire profile for signals above the background to identify it as any feature (i.e., clouds, aerosols or surface). Having identified the features in the single profile, the algorithm then uses successive horizontal averaging at 1 km, 5 km, 20 km and 80 km to identify more weakly scattering features (e.g, thin cloud and aerosol layers). The features detected at one averaging resolution are removed from the profile before the profile is averaged again. Thus features found at high spatial resolutions (i.e., with less averaging) will not be included in the profiles of attenuated scattering ratios scanned at coarser resolutions (i.e., more averaging). The algorithm runs iteratively until all the possible features are identified in the data. This procedure is essential because relatively weak scattering features (thin cirrus, thin aerosol layers) require extensive averaging of profiles to achieve sufficient SNR for their detection. The SIBYL algorithm records the identified features along with their descriptors such as layer-integrated signal backscatter and transmittance before it passes to the next step of processing. The Figure 2.2 shows the complete modules of algorithms used for the CALIPSO data processing.

The next step in CALIPSO data processing includes the Scene Classification Algorithms (SCA), which use the descriptors from SIBYL as input and classifies the features as atmospheric or non-atmospheric. The non-atmospheric features include Earth's surface and

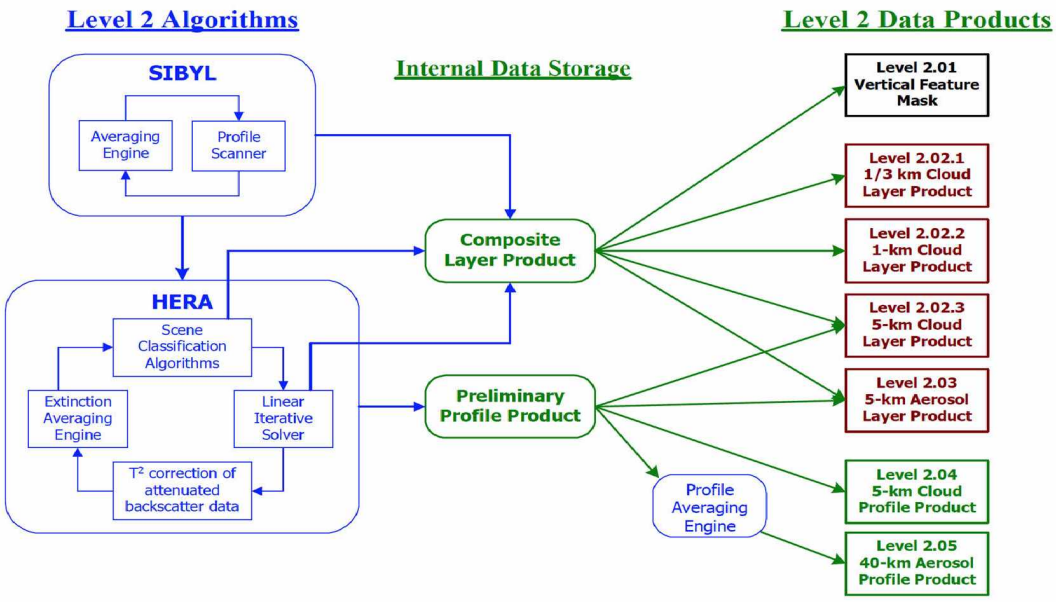

Figure 2.2: CALIPSO data processing work-flow (*Vaughan et al.*, 2005).

sub-surface. Then the atmospheric features are classified as either cloud or aerosol primarily based on the layer mean value of the 532 nm attenuated backscatter coefficient and the attenuated color ratio (ratio of attenuated backscatter coefficients measured at 1064 nm and 532 nm). This algorithm is referred as Cloud-Aerosol Discrimination (CAD) and is used to separate the cloud and aerosol layers identified at resolution of 5 km, 20 km and 80 km based on the statistical analysis for the priori probabilities of their detection (*Liu et al.*, 2009). Here the detection and removal of low level clouds in the single profile (333 m) resolution at 1064 nm optimizes the process of separating cloud and aerosol layers (*Vaughan et al.*, 2009). The classification of all the identified features along with their confidence flags are provided in CALIPSO vertical feature mask (VFM) product as 16-bit number. The interpretation or definitions for these classification flags are provided in Table 2.1.

If the feature is classified as a cloud, the SCA will then determine if it is an ice cloud or water cloud using the backscatter, depolarization layer height, and temperature information. The cloud phase discrimination algorithm used for CALIPSO data was developed by *Hu et al.* (2009) and classifies the cloud as either 'water', 'ice', 'mixed-phase' or 'unknown' along with the confidence flags as 'high', 'medium', 'low' or 'none'. The subsequent procedure of identifying aerosol subtypes are based on the algorithms developed by *Omar et al.* (2005, 2009). CALIOP aerosol models are primarily derived from the clustering analysis

Table 2.1: CALIPSO VFM data product description.

Bit	Field Description	Bit Interpretation
1 - 3	Feature Type	0 = invalid (bad/missing) 1 = clear air 2 = cloud, 3 = aerosol 4 = stratospheric feature 5 = surface, 6 = subsurface 7 = no signal/attenuation
4 - 5	Feature Type QA	0 = none, 1 = low, 2 = medium, 3 = high
6 - 7	Ice/Water Phase QA	0 = unknown, 1 = randomly oriented ice 2=water, 3 = horizontally oriented ice
8 - 9	Ice/Water Phase QA	0 = none, 1 = low, 2 = water
10 - 12	Feature Subtype If feature type=aerosol, bits 10-12 will specify the aerosol type	0 = not determined 1 = clean marine, 2 = dust 3 = polluted continental 4 = clean continental 5 = polluted dust, 6 = smoke, 7 = other
	If feature type=cloud, bits 10-12 will specify the cloud type	0 = low overcast, transparent 1 = low overcast, opaque 2 = transition stratocumulus 3 = low, broken cumulus 4 = altocumulus (transparent) 5 = altostratus (opaque) 6 = cirrus (transparent) 7 = deep convective (opaque)
	If feature type = Polar Stratospheric Cloud, bits 10-12 will specify PSC classification	0 = not determined 1 = non-depolarizing PSC 2 = depolarizing PSC 3 = non-depolarizing aerosol 4 = depolarizing aerosol 5 , 6 = spare, 7 = other
13	Cloud/Aerosol Type QA	0 = not confident, 1 = confident
14 - 16	Horizontal averaging required for detection	1=333 m, 2=1 km, 3=5 km, 4=20 km, 5=80 km

of the multi-year AERONET (Aerosol Robotic Network) data archive which determines characteristic aerosol types in terms of their physical and optical properties. The features identified in CALIPSO data as aerosols are then classified as one of the six subtypes: desert dust, polluted dust, smoke, clean continental, polluted continental, or marine. The lidar ratios computed for the features (clouds and aerosols) in these procedures are then passed on to the third step of processing referred as Hybrid Extinction Retrieval Algorithms (HERA), which performs the retrieval of extinction profiles at both 532 nm and 1064 nm.

2.2.3 CALIPSO data products

The data obtained from CALIPSO is made available for scientific research through NASA Langley Research Center (http://eosweb.larc.nasa.gov). Several data products are provided based on the geophysical variables retrieved for the observed cloud and aerosol layers. Since the beginning of the CALIPSO mission, several versions of data products have been released with improvements in the quality of the products with each successive release. Depending on the validation of the data products a data maturity flag is included in the naming of the product as Beta, Provisional, Validated Stage1, etc. These maturity flags indicate the status of data product validation using independent measurements. In the current thesis CALIPSO Version-3 data products are used, which are provided with improved quality mainly for daytime calibration (*Powell et al.*, 2009) and cloud-aerosol discrimination (*Liu et al.*, 2009).

A summary of the data products currently available is provided in the Table 2.2. While cloud layer products are provided at three horizontal resolutions 333 m, 1 km and 5 km. The aerosol layer products are provided at only 5 km resolution. This is because more sample averaging is required to attain sufficient SNR to identify aerosol layers. While using these cloud layer products it should be realized that 5 km data product provides a highly processed representation of the atmosphere. All data products are provided as separate files for the data acquired during day and night times. The day and night times in the orbital overpass are identified by using the lighting conditions at an altitude of 24 km.

2.3 CloudSat

The satellite CloudSat joined the A-train constellation and has been operational since June 2006. CloudSat carries a cloud profiling radar (CPR) operating at 94 GHz. The CPR measures energy backscattered by any hydrometeors (clouds or precipitation) within 1.5 km across-track x 1.7 km along-track footprint. The pulse repetition frequency of CPR is 4.3 kHz, which conveniently allows the radar to measure up to 35 km altitude from the surface. The pulse width 3.2 μs of the radar energy provides a vertical resolution of 480 m. However the data is oversampled to create range bins of 240 m before it is downlinked to the ground receiving station. The minimum detectable signal of the CPR is –30 dBZ (*Stephens et al.*, 2008).

Table 2.2: CALIPSO data products description.

Product ID	**Description**
CAL_LID_L1-ValStage1	Geolocated and calibrated attenuated back-scattering along with the meteorological and elevation data obtained through GMAO models.
CAL_LID_L2-VFM-ValStage1	Feature masks over 5 km horizontal and native vertical resolutions along with the feature class and their confidence level for the estimates.
CAL_LID_L2_333mCLay-ValStage1	Cloud layer properties derived at single shot resolutions. The parameters included are integrated attenuated backscatter, cloud midlayer temperature, lidar depolarization ratio, cloud top height, column reflectance and cloud base height.
CAL_LID_L2_01kmCLay-ValStage1	Cloud layer properties derived at 1 km horizontal averaging resolution.
CAL_LID_L2_05kmCLay-Prov	Cloud layer properties derived at 1 km horizontal averaging resolution. Cloud layer properties derived essentially at averaging 5 km horizontal resolution. Also the cloud properties derived at 20 km and 80 km resolutions are downscaled and provided.
CAL_LID_L2_05kmCPro-Prov	Cloud profile properties derived essentially at 5 km horizontal resolutions. The parameters included are backscatter coefficient, extinction coefficient, and depolarization ratio profiles.
CAL_LID_L2_05kmALay-Pro	Aerosol layer properties derived from 5 km, 20 km and 80 km averaging resolutions. The parameters include integrated attenuated backscatter, lidar depolarization ratio, column reflectance and aerosol optical thickness.
CAL_LID_L2_05kmAPro-Prov	Aerosol profile properties derived from 5 km, 20 km and 80 km averaging resolutions. The parameters include backscatter coefficients, depolarization ratio profile, and extinction coefficients.
CAL_LID_L3_APro_AllSky-Beta	532nm Extinction coefficient, column aerosol optical depth, aerosol layer properties.

The operating principle of CPR is similar to that of the lidar with the exception of the wavelengths used and the radar equation can be written as (*Sassen*, 1987):

$$P(r) = \frac{C}{r^2}.\eta.\exp\left[-2\int_0^r \left(k_a + k_i + k_w\right).dr\right] \tag{2.6}$$

where, $P(r)$ is the averaged returned power, λ, C is operating wavelength and constant of

the radar system, r is the distance from the target to the radar, η is the radar reflectivity, and k_a, k_i, k_w are the extinction coefficients for moist air, ice and water particles.

At Rayleigh scattering wavelengths, the radar reflectivity can be defined as the sum of the backscattering coefficients per unit volume and can be expressed as,

$$\eta = \frac{\pi^5}{\lambda^4} . |K|^2 \int_0^\infty N(D) . D^6 dD \tag{2.7}$$

where, $|K|^2$ is the dielectric constant for either ice or water particles, D is the diameter of the particle, and N is the particle concentration in the diameter interval from D to $(D+dD)$.

Thus the radar reflectivity is related to the sixth power of particle size and inversely related to the fourth power of the wavelength used. In other words, the radar can detect only relatively large particles and the shortest wavelength used for remote sensing in the microwave region of the spectrum possesses sensitivity to most cloud particles.

2.4 Arctic Facility for Atmospheric Remote Sensing

The AFARS station is located at the University of Alaska Fairbanks campus (64.86° N, 147.84° W) in Interior Alaska. A vertically pointing cloud polarization lidar (CPL) operating at 694 nm was deployed at AFARS for high-cloud measurement from 2004 – 2014. The CPL generates laser pulses through a ruby crystal every 10 sec with peak energy 1.5 J and pulse width 25 ns. Instruments at AFARS are usually operated during the local noon (~2300 UTC) times for about 2 – 3 hrs depending on the cloud conditions over the station. The AFARS operator categorizes the clouds primarily by observing the cloud height, color, texture and appearance of the sky through the cloud. The operator provides a description of the cloud type observed during the AFARS operations in the website along with the lidar data set. The AFARS operator and principal investigator, Prof. Kenneth Sassen, maintains the data set (returned power after background subtraction) collected through CPL in the National Science Foundation funded website (http://rainbow.gi.alaska.edu) for public use. In our earlier study (*Kayetha*, 2014), we used ~8 years of AFARS lidar data set to derive the climatological macrophysical properties of ice clouds over the AFARS station.

2.5 Comparison of CALIOP and AFARS lidars

Here we provide a direct comparison of data sets from CALIOP and a ground-based ruby lidar. For this purpose, a data set from a high-resolution ground lidar operated at the Arctic Facility for Atmospheric Remote Sensing (AFARS) station is used. This chapter illustrates the characteristics of the measurements made from the AFARS and CALIOP lidars under various atmospheric conditions. In order to compare the data sets obtained from two different lidars, it is imperative to understand their abilities and signal characteristics. Table 2.3 provides an overview of the AFARS and CALIOP lidar specifications. From the perspective of zenith looking ground-based lidar, the volume of the atmosphere sampled is small (narrow FOV) and is localized. However, from the satellite perspective, which is several hundreds of kilometers away from the targets and moving at high speed, the volume of atmosphere sampled for each laser shot is small (very narrow swath) over large horizontal distance. Thus, the signal characteristics obtained from these two platforms are expected to differ. This scenario is more complicated for the daytime measurements than the nighttime measurements, due to the higher daytime solar background.

Table 2.3: Technical specifications of lidars employed with AFARS and CALIPSO.

	AFARS	**CALIPSO**
Platform	Ground	Space-orbit: About 705 km altitude above earth's surface moving at 7 km/s speed
Wavelength	694 nm ($\parallel$, $\perp$)	532 nm ($\parallel$, $\perp$), 1064 nm
Pulse energy	1.5 J	110 mJ
Repetition rate	0.1 Hz	20.16 Hz
Pulse width	25 ns	20 ns
Range resolution: Vertical	6 m	30 m (0 to 8 km altitude) 60 m (>8km altitude)
Horizontal		333 m
Beamwidth/FOV: Transmitter	0.5 mrad	100 mrad
Receiver:	1 - 3 rad	130 mrad
Receiver: Telescope	28 cm diameter	1m diameter
Altitude range of measurement	0.5 - 14 km	0 - 30 km

A calculation of the photons received (or power received) by the two lidars from a typical altitude in the troposphere (say 10 km) is shown below. Here we assume the two-way transmittance of light from the satellite altitude to the target at 10 km (~250 mb) altitude is four times the two-way transmittance of light from a ground-based lidar. This assumption

seems to be reasonable as the altitude increases above 10 km the atmosphere becomes more homogeneous than the lower atmosphere.

From equation 2.1, we can write:

$$\frac{N_{S(AFARS)}}{N_{S(CALIPSO)}} = \left(\frac{P_{L(AFARS)}.\lambda_{AFARS}}{P_{L(CALIPSO)}.\lambda_{CALIPSO}}\right)x\left(\frac{\beta_{AFARS}.\Delta r}{\beta_{CALIPSO}.\Delta r}\right)x\left(\frac{A_{AFARS}}{r^2_{AFARS}}.\frac{r^2_{CALIPSO}}{A_{CALIPSO}}\right)x\left(\frac{T^2_{AFARS}}{T^2_{CALIPSO}}\right)$$

$$= \left(\frac{1.5x694}{0.11x532}\right)x\left(\frac{532}{694}\right)^4 x\left(\frac{28}{100}\right)^2 x\left(\frac{705-10}{10}\right)^2 x\left(\frac{1}{4}\right)$$

$$= (17.79)x(0.345)x(0.0784)x(4830.25)x(0.25)$$

$$= 581 \tag{2.8}$$

From this calculation we see that the ratio of photons received (or power received) per shot by the AFARS lidar is about 581 times greater than the power received by the CALIOP lidar under similar atmospheric conditions from a target at altitude of 10 km above the surface. The critical factor contributing for such high ratio is the distance of targets from the receiver. Even if the power transmitted by the laser system is as similar to the power transmitted by CALIOP, the inverse relation to the distance still causes a relatively high ratio. Thus, it can be said that ground-based and air-borne lidar systems can always achieve high resolution and precise signals from the targets in the troposphere and can be used for validating the performance of space-based lidars. This is not unexpected and well known, however, our purpose of this demonstration is to weigh the advantages and limitations of each measurement platform before the actual comparison of their measurements. Further, it should be noted that the backscattering observed from the AFARS and CALIOP lidar will vary due to the difference in their wavelengths. Recall, backscattering of atmospheric constituents is inversely related to the fourth power of wavelength used (equation 2.3). Thus, the backscattering observed by the CALIOP and AFARS lidar can be estimated to vary on the order 3:

$$\beta\alpha\frac{1}{\lambda^4}$$

$$\frac{\beta_{CALIOP}}{\beta_{AFARS}} = \left(\frac{694}{532}\right)^4 = 2.898 \tag{2.9}$$

2.6 Data used and methodology

For this study, we used six independent days of AFARS observations from the years 2006 and 2007. Our criteria for selecting these days are to include three representative conditions observed by the AFARS lidar: clear skies, high level (cirrus, cirrostratus) clouds and low/midlevel (cumulus, altocumulus, and altostratus) clouds. We have estimated the volume (Rayleigh) backscattering due to molecules (equation 2.3) over the AFARS station using radiosonde measurements available from the nearest meteorological station. The nearest meteorological station is located at the Fairbanks International Airport about 4.9 km away from the AFARS station where radiosondes are launched at 0000 (local noon) and 1200 UTC (local night) every day. Radiosonde data obtained from such meteorological stations worldwide are maintained as a open database in the website http://weather.uwyo.edu/upperair/sounding.html for public use. Table 2.4 shows the details of the AFARS and corresponding CALIPSO observations used in the current study.

Table 2.4: Details of AFARS and CALIPSO observations used in the current study.

	AFARS		**CALIPSO nearest overpass**			
			Day		**Night**	
Date	Time (UTC)	Observations	Time (UTC)	Distance (km)	Time (UTC)	Distance (km)
Sep 21, 2006	2218 - 0122	Clear, Cirrus	2223	8	1326	433
Oct 24, 2006	2129 - 2220	Clear	2306	480	1230	176
Oct 25, 2006	0105 - 0330	Cirrus Altostratus Altocumulus	2306	480	1230	176
Jan 27, 2007	2103 - 2300	Cirrostratus Altocumulus	2223	10	1326	430
Jan 30, 2007	2057 - 2301	Cirrostratus Altostratus Altocumulus	2254	338	1218	319
Feb 14, 2007	2127 - 2240	Altostratus Altocumulus	2211	143	1314	294
May 16, 2007	2051 - 2300	Cirrus	2153	346	1255	98

An averaged profile of the lidar returned signal for the AFARS observation period is extracted for each day. These profiles are range-corrected and normalized to the estimated Rayleigh molecular backscatter to convert the returned power of CPL to attenuated backscattering profiles. The nearest CALIPSO orbit over the AFARS station is determined

for our selected days and a range-corrected backscattering profile of 5 km horizontal resolution (average of 15 profiles) for the 532 nm channels are extracted from the Level 1B data product. For the CALIPSO profiles used, we also make an assessment of the corresponding features identified along with their quality assurance (QA) flags available from the data product.

To assess the overall cloud conditions over the AFARS and its surroundings, we generated MODIS (MODerate resolution Imaging Spectroradiometer) true color and IR-band (11.77 – 12.27 μm) images. MODIS data is freely available for public use and can be downloaded from the website http://ladsweb.nascom.nasa.gov. The images obtained from IR band (gray-scaled) should be interpreted as: the brighter (white) the feature the colder it is and the darker (black) the feature the warmer it is. To understand the pertaining synoptic conditions of over the region surface-, mid- and upper-level maps have been produced using a reanalysis data set. The MERRA (Modern Era Retrospective analysis for Research and Applications) reanalysis daily data set provided by NASA is used for this purpose. MERRA data sets provide sea level pressure (SLP) and several other meteorological parameters such as geopotential height, wind, temperature, relative humidity, and vertical pressure velocity at about 42 pressure levels ranging from 1000 – 0.01 mb (*Lucchesi*, 2012). These data sets are freely available and can be downloaded from http://disc.sci.gsfc.nasa.gov/daacbin/DataHoldings.pl.

We further demonstrate the lidar signal characteristics made from the two distinct measurement platforms under clear skies, high level and middle or low level cloud conditions with our selected case studies. Though the AFARS observations are limited to daytime measurements, our illustration includes both day and night observations available from satellite measurements. This helps in understanding the evolution and persistence of typical cloud systems over the sub-Arctic region. We also show the differences in Rayleigh estimates derived from the radiosonde and CALIPSO provided GMAO model data. However, because of the difference in the wavelength of AFARS and CALIOP lidars these cannot be directly compared. A discussion of temperature profiles (inversely related to density) from these two data sets will be provided later.

2.7 Results and discussion

2.7.1 Clear skies

2.7.1.1 Case study 1: September 21, 2006

For the day on September 21, 2006 the AFARS observations were available for up to 3 hours starting from 2218 UTC. The nearest CALIPSO orbital overpass was approximately 8 km from the AFARS station at 2223 UTC. The prevailing synoptic and cloudy conditions over the AFARS station for the local day and night times are shown in the Figure 2.3 and Figure 2.4.

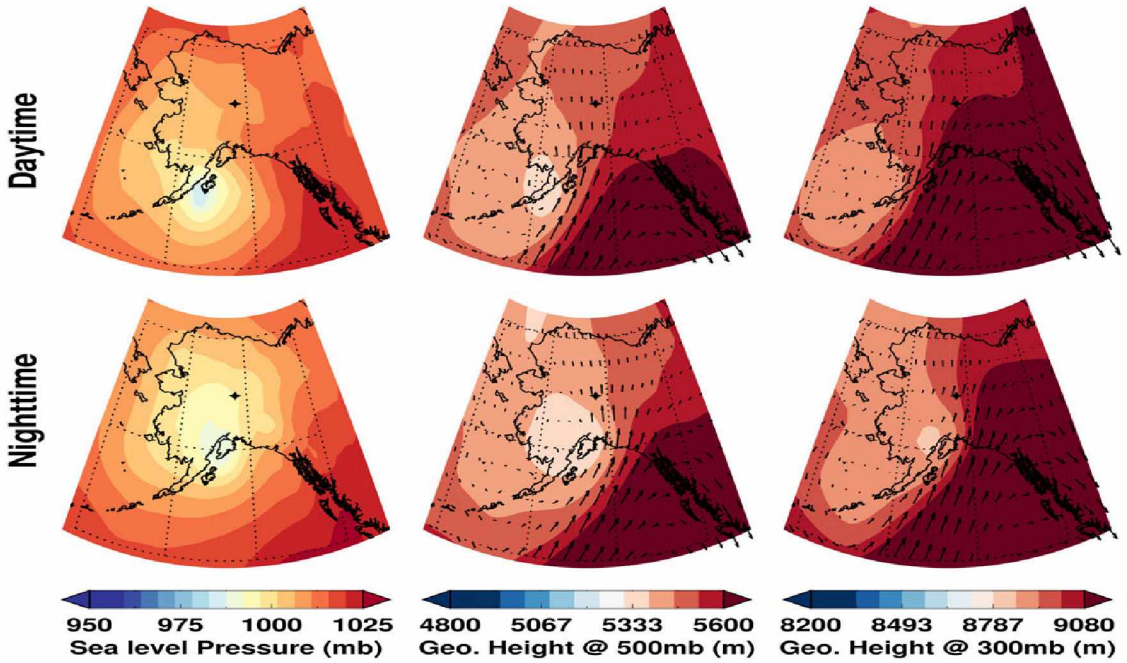

Figure 2.3: Synoptic meteorological conditions over Alaska on September 21, 2006 during both local day and night.

A surface low-pressure system (SLP ~980 mb) is located to the southwest of Alaska supporting the upper level ridge towards the Interior Alaska. This ridge in the mid and upper levels of atmosphere advects warm moist air from the North Pacific Ocean to the Interior Alaska. The wind is southerly into the Interior, which supports the formation of clouds due to the topographic enhancement along the Alaska Range (~6190 m high). The Alaska Range acts as a barrier and effectively blocks the direct passage of air to the Interior region

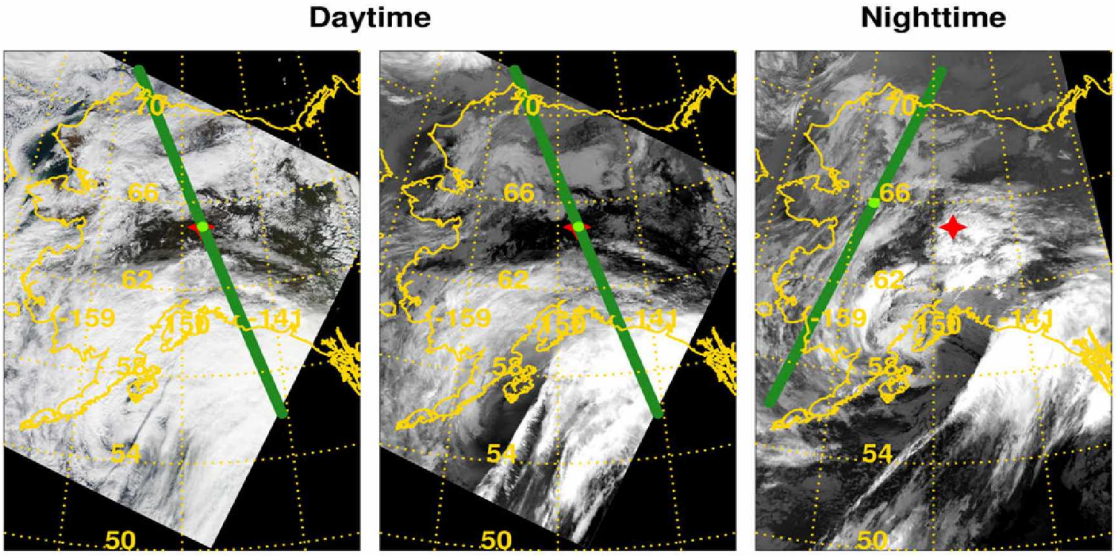

Figure 2.4: MODIS true color and IR imagery (left to right) showing cloudy conditions and the overlaid CALIPSO orbit (green) over Alaska on September 21, 2006 during both local day and night.

of Alaska. The MODIS true color and IR imagery for the daytime clearly shows that clouds formed along the Alaska Range due to the cyclonic system, which slowly progresses into the Interior with time. The thick cloud band observed in the IR imagery is formed along the ridge from North Pacific Ocean extending towards the southeastern part of Alaska due to synoptic uplift and cooling of the warm moist air. By night, the surface low-pressure system is displaced towards Interior from the southwest and weakens (SLP ~990 mb), while the upper level warm air advection towards the Interior by southerly winds continues. This causes much of the low/midlevel clouds formed along the Alaska Range to be dissipated and remain as concentrated cloud masses over certain regions. The IR imagery for night clearly depicts the concentrated cloudy regions over the southern and Interior Alaska. Subsequent movement of the thick cloud band downstream of the upper level ridge towards the continental states is also observed.

The corresponding AFARS, CALIPSO and CloudSat observations for September 21, 2006 are shown in Figure 2.5. The AFARS lidar observed clear skies and advecting cirrus clouds over the station. The AFARS lidar returned power is display as gray-scale image, where white signifies high power. Initially the AFARS lidar observed clear skies and with time could capture the cirrus clouds advecting over the Interior Alaska from the south

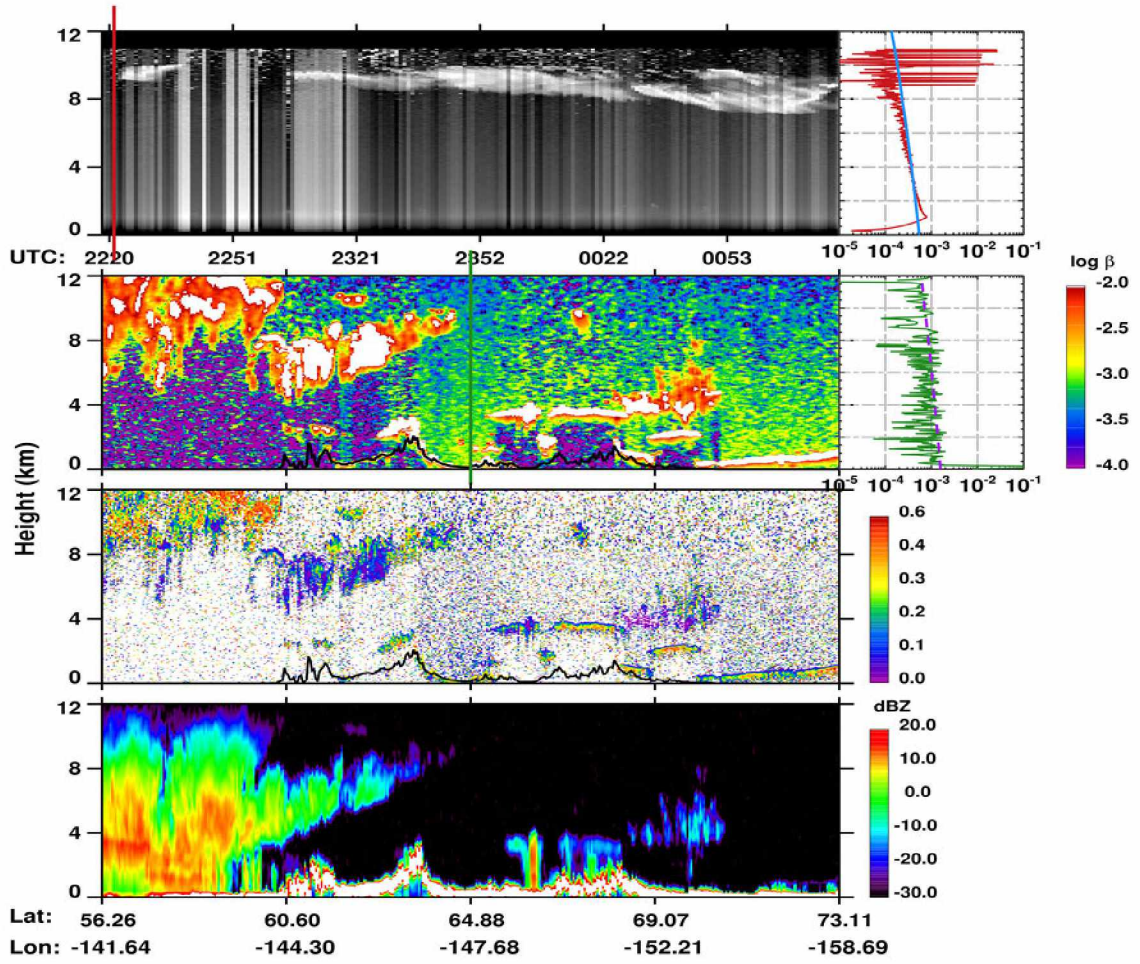

Figure 2.5: AFARS lidar returned power, CALIPSO total attenuated backscattering, CALIPSO linear depolarization ratio and CloudSat radar reflectivity data displays (top to bottom) and profiles during the satellite overpass on September 21, 2006 local day. Also shown is the corresponding wavelength Rayleigh estimates derived from radiosonde (solid line-blue) and CALIPSO provided model data (dashed line-purple).

formed due to the cyclonic system. Data set from radiosonde and MERRA confirms the winds in upper atmosphere to the Interior as southerly. The wind speed at the cirrus cloud altitude (~9 km) is found to be 25 m/sec from radiosonde data. Considering the AFARS observations from 2305 – 0122 UTC, it appears that cirrus clouds with minimum horizontal scale of 265 km has been observed over the Interior Alaska. The CALIPSO and CloudSat orbital transect near the AFARS station clearly shows the deep clouds formed due to the cyclonic system over southern Alaska and the midlevel clouds formed north of Alaska (65^{o} – 70^{o} N, latitude) due to local meteorological conditions. The nearest

observation of the satellites to the AFARS station (green line) is placed in the middle of the data display to show complete satellite observations to the north and south of AFARS, having a total stretch of 1505 km horizontal scale (5 km x 301 profiles).

The clouds observed by the CALIPSO and CloudSat (Figure 2.5) clearly illustrate the complementary nature of simultaneous lidar and radar observations. The way visible light and microwaves interact with hydrometeors is quite dissimilar. Light scattering from clouds is proportional to the cloud particle diameter D^2, such that even smallest hydrometeors in the particle size distribution contribute to backscattering. Strong backscattering also leads to strong attenuation of the visible light, thus causing loss of signals after penetration in dense clouds. However, microwave scattering is proportional to D^6 and radar wavelength λ^{-4}. This means the radar signal attenuation in clouds is generally weak and most clouds that are too optically thick to be penetrated by lidar pulses are optically thin to the radar. Here, it can be observed that the (cumulonimbus) clouds formed in the cyclonic system are dense enough to completely attenuate the CALIOP signals after penetrating few kilometers of cloud. However, the CloudSat could detect the deep precipitating clouds down to the surface level. The δ clearly shows the ice particles formed along upper levels of the cloud system. The updrafts induced in the cyclonic system provide favorable conditions for the air to saturate and form ice particles, which gradually grow to large sizes and precipitate. The other type of clouds observed in this orbital transect over the Interior region show high backscattering at the cloud top altitudes and loss of signals thereafter, while CloudSat can detect the hydrometeors down to the surface level. This is the typical characteristic of altocumulus type of clouds that has supercooled liquid layer along the cloud top and precipitating ice virga from the cloud base.

Comparison of the single backscattering profiles (Figure 2.5) at the time of the satellite overpass shows that the backscattering measured by both the lidars during clear skies follows the expected Rayleigh molecular scattering. Here, it is critical to understand that despite the limitations imposed on CALIOP lidar because of its measurement platform (as discussed in section 2.5), the observed molecular scattering over the AFARS station agrees reasonably well with the estimated Rayleigh molecular scattering. We observe that the AFARS backscattering profile has high values below 1 km altitude and then follows the

molecular scattering above. The CALIPSO backscattering profile has also high values near the surface. The surface elevation of the region around the AFARS station is 218 m. The high backscattering observed in AFARS profile is due to the lidar transmitter and receiver overlap region and should be ignored, this is a typical characteristic of any bistatic lidar. For the down-looking CALIOP lidar the high backscattering observed near the surface indicates the energy transmitted after hitting the surface, which caused the abrupt increase in backscattering values. It is important to identify such surface returns for a down-looking lidar, to assess the atmosphere as opaque or transmissive for the visible (532 nm) light used. In presence of clouds or aerosols in the atmosphere the transmission of light till the surface is limited due to extinction. *Platt et al.* (1980) estimated that clouds with visible optical depths higher than 3 can completely absorb the light. In other words, only clouds with visible optical depth limited to 3 can be observed using both AFARS and CALIOP lidars.

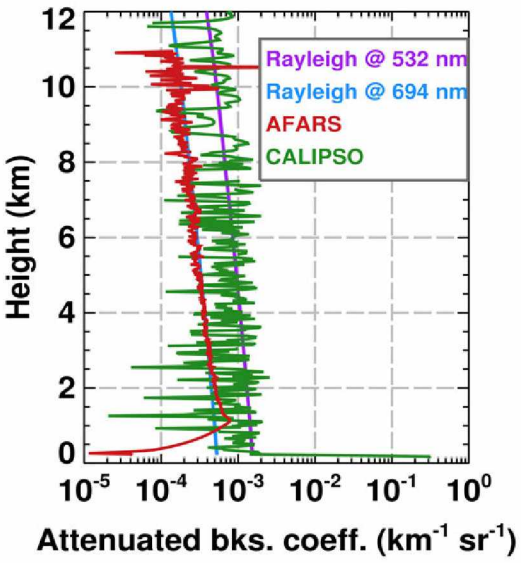

Figure 2.6: Averaged profile for the AFARS observation period and the nearest CALIPSO total attenuated backscattering profile on September 21, 2006 during local day.

The averaged backscattering profile obtained for the entire AFARS observation period (~3 hours) during local daytime is compared with the nearest CALIPSO profile as shown in Figure 2.6 and the features provided by CALIPSO data product in Table 2.5. As discussed earlier, it is now clearly shown that the ratio of Rayleigh molecular scattering at AFARS and CALIOP wavelengths is 2.9, which is consistent with the theoretical value shown in

Table 2.5: The CALIPSO identified features and QA flags for the nearest profile to the AFARS station on September 21, 2006 local day.

Property/Description	**Value**
Surface elevation (km)	0.135
Number of cloud layers	0
Horizontal averaging (km)	-
Cloud top altitude (km)	-
Cloud base altitude (km)	-
Transparency flags (0-Transparent/1-Attenuated)	0
Feature type	-
Feature subtype	-
Feature type QA	-
Ice/water phase	-
Ice/water phase QA	

equation 2.10. The AFARS backscattering profile typically follows the Rayleigh estimated profile until it reaches the altitude of 8 km thereafter the signal shows more backscattering than we expect from molecules alone. This is because of the contribution from the observed cirrus cloud. However, the CALIPSO profile near the AFARS station around 2223 UTC has only a molecular contribution. Since the cirrus clouds observed over AFARS are eventually formed and advected over the region after the passage of the satellite. Thus the data product show no cloud features that are identified from this backscattering profile.

That night, the CALIPSO orbit is found to be ~433 km west of the AFARS station and captured the clouds formed in the cyclonic system that moved towards the central and western parts of the Alaska. The corresponding CALIPSO and CloudSat observations and the nearest profile to the AFARS station are shown in the Figure 2.7 and the features provided by CALIPSO data product in Table 2.6. As described earlier, a similar behavior of lidar signal attenuation and radar signals down to the surface level can be observed with the deep clouds formed in the cyclonic system. $\delta < 0.1$ are common in the cloud and occur mostly towards the cloud base. These are supercooled liquid droplets that contribute high backscattering values up to 10^{-2} km^{-1} sr^{-1}. The cloud system shown in the data display spans about 1250 km at horizontally.

The nearest CALIPSO backscattering profile shows that the lidar pulse was completely absorbed by the cloud mass. The lidar signal penetrates 2 km altitude and below that

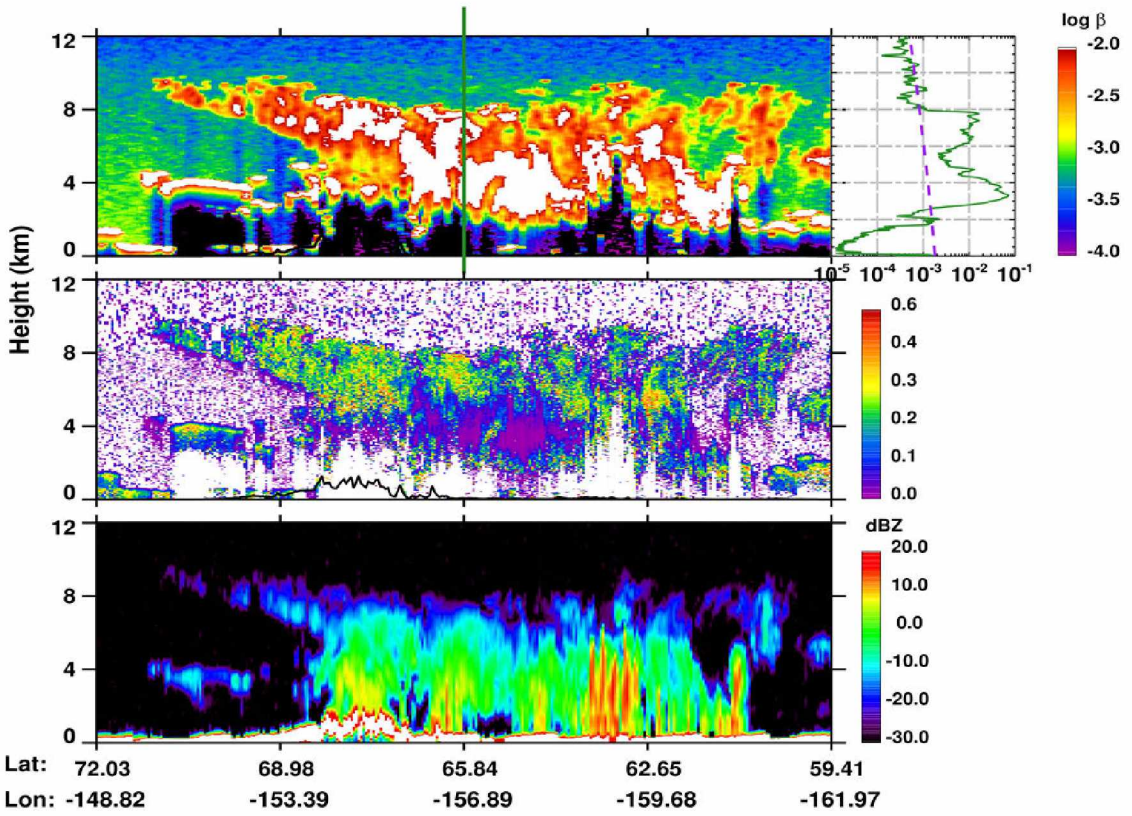

Figure 2.7: CALIPSO total attenuated backscattering (and profile), linear depolarization ratio and CloudSat radar reflectivity for the nearest overpass to the AFARS station on September 21, 2006 during local night.

Table 2.6: The CALIPSO identified features and QA flags for the nearest profile to the AFARS station on September 21, 2006 local night.

Property/Description	**Value**
Surface elevation (km)	0.072
Number of cloud layers	1
Horizontal averaging (km)	5
Cloud top altitude (km)	8.06
Cloud base altitude (km)	2.46
Transparency flags (0-Transparent/1-Attenuated)	1
Feature type	Cloud
Feature subtype	Deep convective
Feature type QA	High
Ice/water phase	Mixed-phase
Ice/water phase QA	High

no strong surface reflection is observed. From the CALIPSO backscattering profile the cloud top altitude can be identified at ~8 km and cloud base at ~2 km. These estimated cloud altitudes can be confirmed from the data product retrievals (Table 2.6). Also as the observed δ show values ranging 0.1 – 0.6 within the cloud, it can be identified as mixed-phase cloud with ice particles in the upper levels of the cloud and supercooled liquid droplets near the cloud base. Above the cloud top altitude the backscattering agrees well with the estimated Rayleigh scattering. Since there is no strong surface returns in this profile and the signal at lower levels is less than the estimated Rayleigh scattering, it can be said that the observed cloud base is not the true cloud base and is only an apparent cloud base.

2.7.1.2 Case study 2: October 24, 2006

For the day on October 24, 2006 AFARS observations were available for up to 1 hour starting from 2129 UTC and again on October 25, 2006 from 0105-0330 UTC (this indicates the same day as October 24 for the local AFARS time). The prevailing synoptic and cloud conditions are shown in the Figure 2.8 and Figure 2.9.

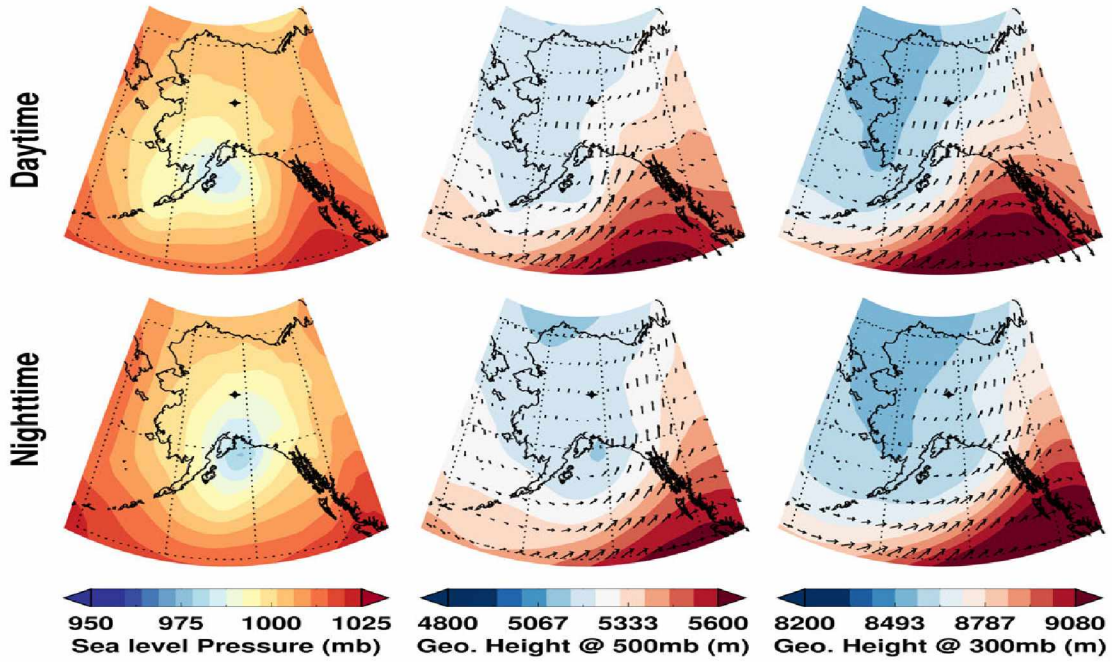

Figure 2.8: Synoptic meteorological conditions over Alaska on October 24, 2006 during both local day and night.

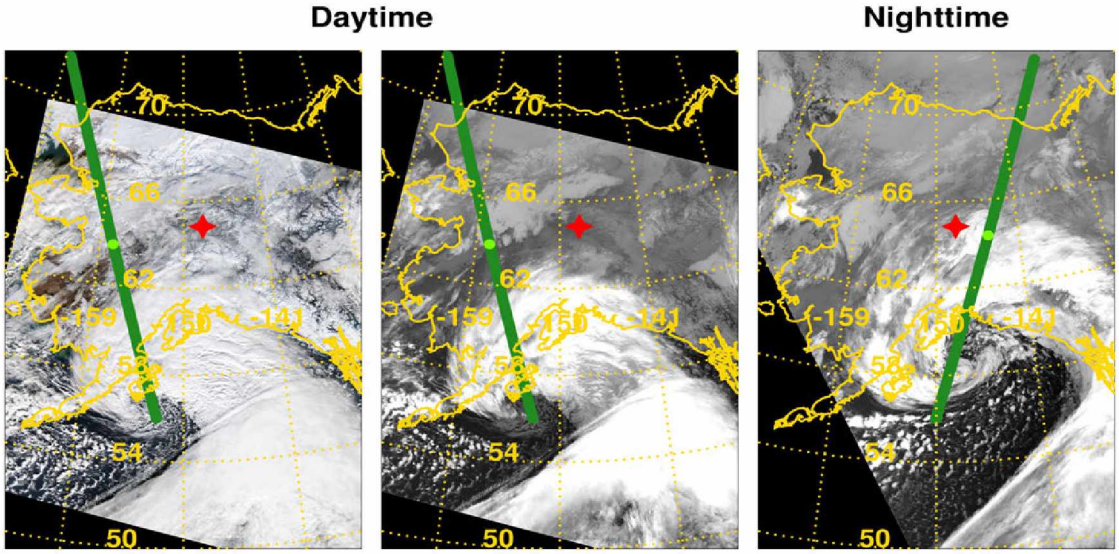

Figure 2.9: MODIS true color and IR imagery (left to right) showing cloudy conditions and the overlaid CALIPSO orbit (green) over Alaska on October 24, 2006 during both local day and night.

For this case the synoptic conditions observed over the Alaska appears to be quite similar to that observed over the day of September 21, 2006 except that the upper level ridge is not deeply extended towards the Interior region but rather towards the continental United States. The deep clouds formed in the cyclonic system over southern Alaska and thick cloud band formed along the North Pacific ridge can be clearly observed in the MODIS imagery. Over the Interior regions mostly clear skies prevail until the clouds formed in the cyclonic system move inwards. The other types of midlevel and low level clouds formed due to local meteorological conditions can be observed over the northwestern parts of Alaska (seen as gray patches in IR imagery). By night, the North Pacific ridge moves towards the continental states and the corresponding movement of clouds along the upper level ridge can be observed.

The corresponding AFARS, CALIPSO and CloudSat observations for October 24, 2006 are shown in Figure 2.10. Initially the AFARS lidar observed clear skies and with time capture the cirrus clouds advecting over the Interior Alaska from the south formed due to the cyclonic system. The southerly winds in the upper levels of atmosphere can be confirmed from both radiosonde and MERRA data sets. The deep clouds formed in the cyclonic system extend to 8 km altitude, which slowly with time move to the Interior region by

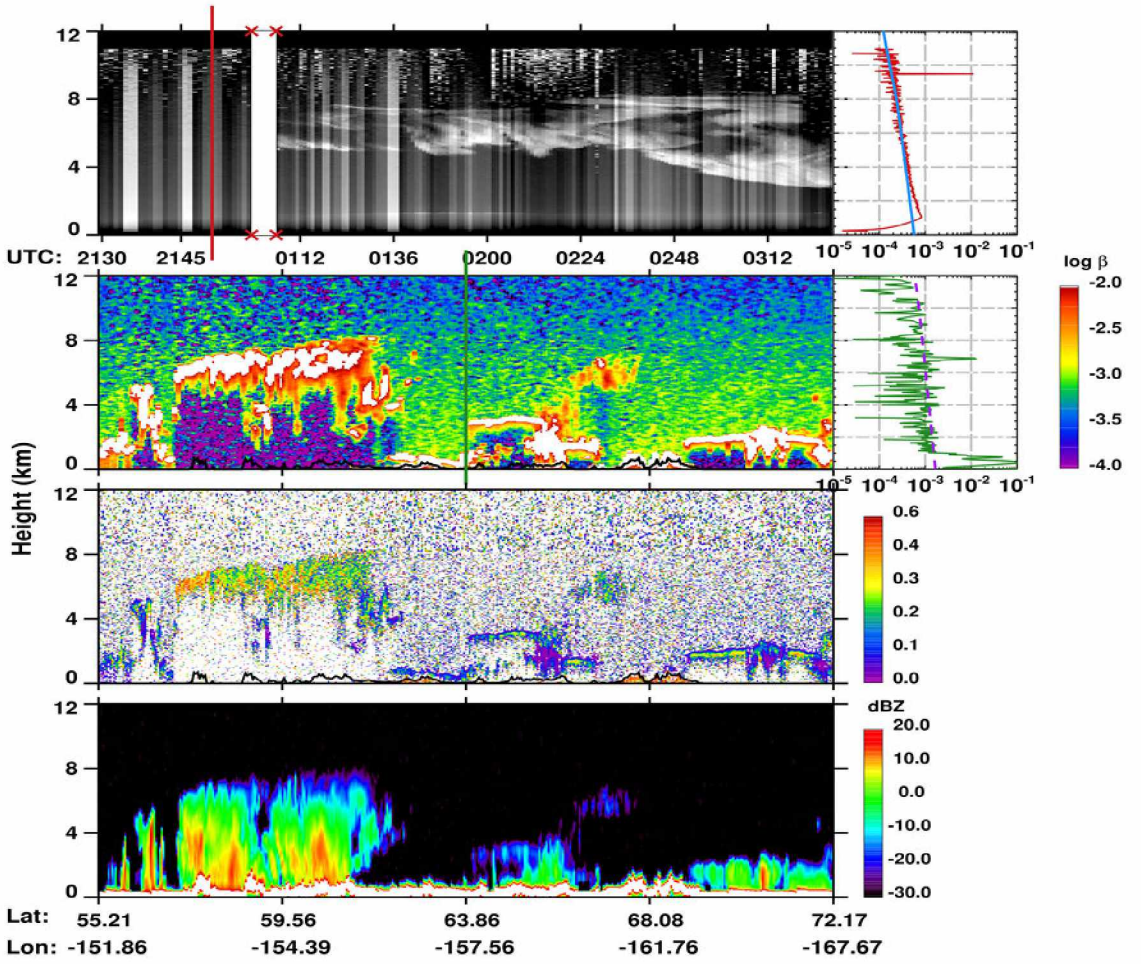

Figure 2.10: AFARS lidar returned power, CALIPSO total attenuated backscattering, CALIPSO linear depolarization ratio and CloudSat radar reflectivity data displays (top to bottom) and profiles during the satellite overpass on October 24, 2006 local day. Also shown is the corresponding wavelength Rayleigh estimates derived from radiosonde (solid line-blue) and CALIPSO provided model data (dashed line-purple).

the upper level winds and are captured by AFARS lidar with similar cloud top altitude. As the cloud mass get thicker over the Interior the AFARS lidar signal is attenuated and could only detect the cloud base (after 0312 UTC). Observation of AFARS backscattering profile in clear skies typically follows the estimated molecular backscattering. The abrupt backscattering increase (spike) in the AFARS profile is due to random electronic noise in the signal. In the CALIPSO-CloudSat orbital overpass, at near 68° N latitude a cloud is observed from 6 – 7.5 km altitude. It is observed that the radar reflectivity for this cloud does not exceed –15 dBZ whereas, for the other types of clouds the radar reflectivity

is observed with high values up to 20 dBZ extending till the surface level. The small values of microwave scattering observed by CloudSat indicate the small-sizes of the cloud particles, which cannot precipitate. In other words, threshold radar reflectivity can be determined and used to identify clouds as precipitating or non-precipitating types of clouds.

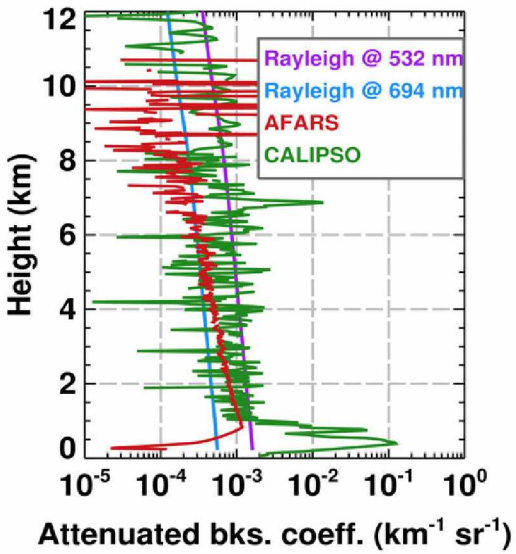

Figure 2.11: Averaged profile for the AFARS observation period and the nearest CALIPSO total attenuated backscattering profile on October 24, 2006 during local day.

Table 2.7: The CALIPSO identified features and QA flags for the nearest profile to the AFARS station on October 24, 2006 local day.

Property/Description	**Values**	
Surface elevation (km)	0.04	
Number of cloud layers	2	
Horizontal averaging (km)	80	5
Cloud top altitude (km)	1.83	0.48
Cloud base altitude (km)	1.37	0.27
Transparency flags	0	0
(0-Transparent/1-Attenuated)		
Feature type	Cloud	Cloud
Feature subtype	Low overcast	Low overcast
Feature type QA	None	High
Ice/water phase	Unknown	Water
Ice/water phase QA	None	High

The averaged backscattering profile obtained for the entire AFARS observation period (~3 hrs) during local daytime is compared with the nearest CALIPSO profile as shown in Figure 2.11 and features identified are provided in Table 2.7. The AFARS profile follows the estimated molecular backscattering until 5 km altitude after which a clear increase in backscattering (contributed by cloud) is observed. It can be confirmed from the data display that the cloud base altitude for the observation period is on average about 5 km. Above the cloud base no clear cloud top can be identified from the averaged profile as for a brief time during the observation period the AFARS lidar signal got attenuated. The CALIPSO backscattering profile typically shows molecular contribution with an exception of increase in backscattering below 1 km altitude. The increase in backscattering near surface levels should be the combined contribution from low-lying clouds and multiple scattering effects from the surface. Thus, it is important to have accurate surface elevation information in order to avoid any misinterpretation of features while using satellite lidar data. The data product shows the surface elevation as 0.04 km and identifies two cloud layers detected at 80 km and 5 km horizontal averaging. Observation of CALIPSO data display clearly shows the low level cloud at the altitudes 1.3 – 1.8 km near the AFARS station, but the same cannot be identified in the backscattering profile alone. It should be noted that the QA flags for the cloud detected at 80 km resolution is 'none' while for the cloud detected at 5 km resolution is 'High'. This indicates the low SNR values in the CALIOP signals, which is not sufficient to identify the cloud layer.

That night, the CALIPSO orbit is found to be ~176 km west of the AFARS station and captured the clouds formed in the cyclonic system that moved towards the central and southern parts of the Alaska. The corresponding CALIPSO and CloudSat observations and the nearest profile to the AFARS station are shown in the Figure 2.12 and the features identified by CALIPSO in Table 2.8.

For this case the CALIPSO-CloudSat observes both the clouds formed in the cyclonic system and low-overcast clouds in the northern parts (72^{o} – 67^{o} N latitude) of Alaska. As expected, CALIOP lidar attenuation effects and the high radar reflectivity from the precipitating cloud mass can be clearly observed. The nearest CALIPSO backscattering profile to the AFARS station shows three (approximately 1 km, 4 km, 5 – 6 km) regions of enhanced backscattering. While the data product confirms our observation from the

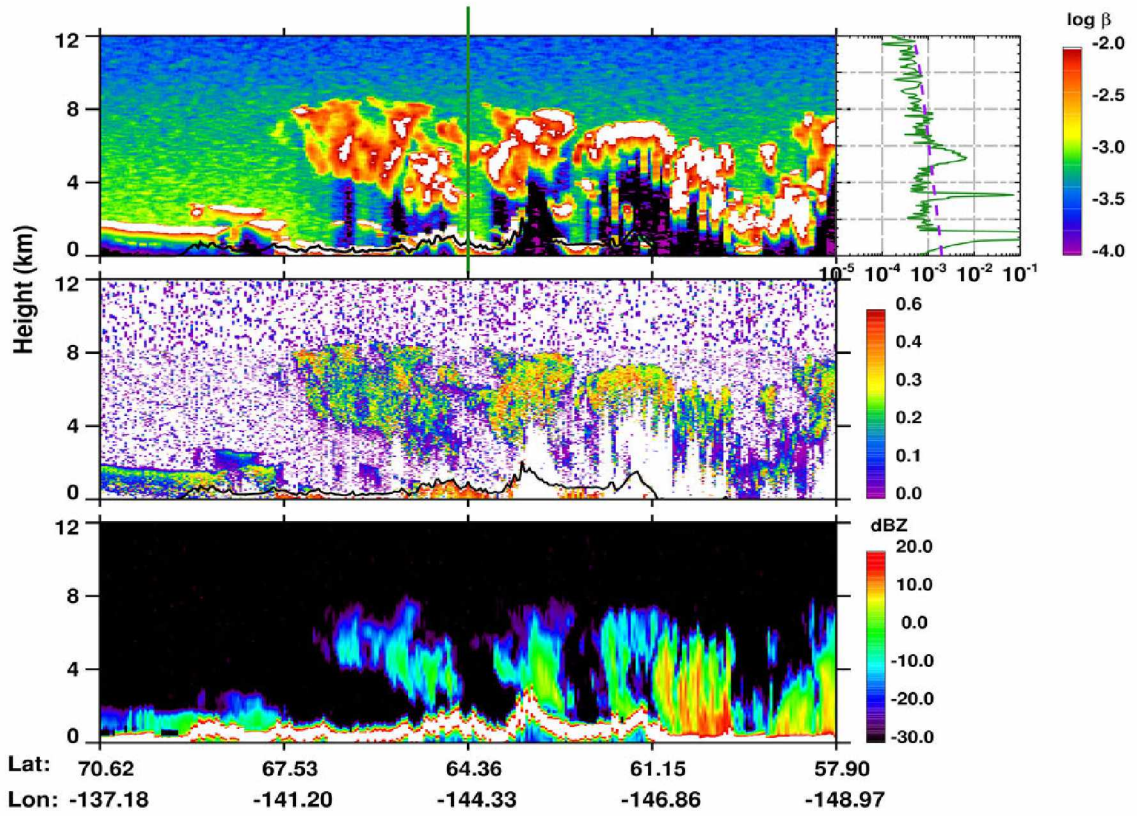

Figure 2.12: CALIPSO total attenuated backscattering (and profile), linear depolarization ratio and CloudSat radar reflectivity (top to bottom) for the nearest overpass to the AFARS station on October 24, 2006 during local night.

Table 2.8: The CALIPSO identified features and QA flags for the nearest profile to the AFARS station on October 24, 2006 local night.

Property/Description	**Value**
Surface elevation (km)	0.979
Number of cloud layers	1
Horizontal averaging (km)	5
Cloud top altitude (km)	6.11
Cloud base altitude (km)	4.85
Transparency flags	0
(0-Transparent/1-Attenuated)	
Feature type	Cloud
Feature subtype	Cirrus
Feature type QA	High
Ice/water phase	Ice
Ice/water phase QA	High

data display (Figure 2.12) that a cloud is detected at 4.8 – 6.1 km altitude and the low level enhanced backscattering is from the surface. However, the feature observed in the profile at 3.8 km altitude is categorized as 'aerosol' detected at 20 km averaging resolution. This seems to be reasonable as the observed δ for this feature is < 0.1 and the CloudSat do not detect its presence. Recall, the particle size dependence on microwave scattering. Thus, aerosol particle sizes are too small to be sensitive for radar signals.

Thus, from these two case studies it is now confirmed by AFARS lidar signals that CALIPSO can capture the estimated molecular scattering in the absence of clouds or aerosols.

2.7.2 High level clouds

2.7.2.1 Case study 3: January 30, 2007

For the day on January 30, 2007, AFARS observations were available for up to 2 hours starting from 2254 UTC. The prevailing synoptic and cloud conditions are shown in the Figure 2.13 and Figure 2.14.

During daytime, a surface low-pressure system (SLP ~980 mb) is formed around the Aleutian Islands and most inland regions of the Alaska are under high surface pressure. The upper level ridge from the North Pacific Ocean extends deep in to the Interior region of Alaska. The deep extended ridge provides synoptic uplift of the air mass through the southerly winds to the Interior causing favorable conditions for high amounts cirrus clouds. While the low-pressure system caused cloudiness over the southwestern parts of Alaska, the upper level ridge caused cloudiness towards northern Alaska and over the Beaufort Sea that can also be confirmed from the MODIS imagery. By night, the cyclonic system weakens and moves from the Aleutian Islands towards western Alaska, while the upper level air mass flows along the North Pacific ridge persists. This caused the clouds to move and be concentrated over the northwestern parts of the Alaska.

The corresponding AFARS, CALIPSO and CloudSat observations for January 30, 2007 are shown in Figure 2.15. For this day, the AFARS lidar observed an altostratus cloud 3 – 4 km altitude and cirrostratus cloud extending above from 7 km altitude. Here, the AFARS

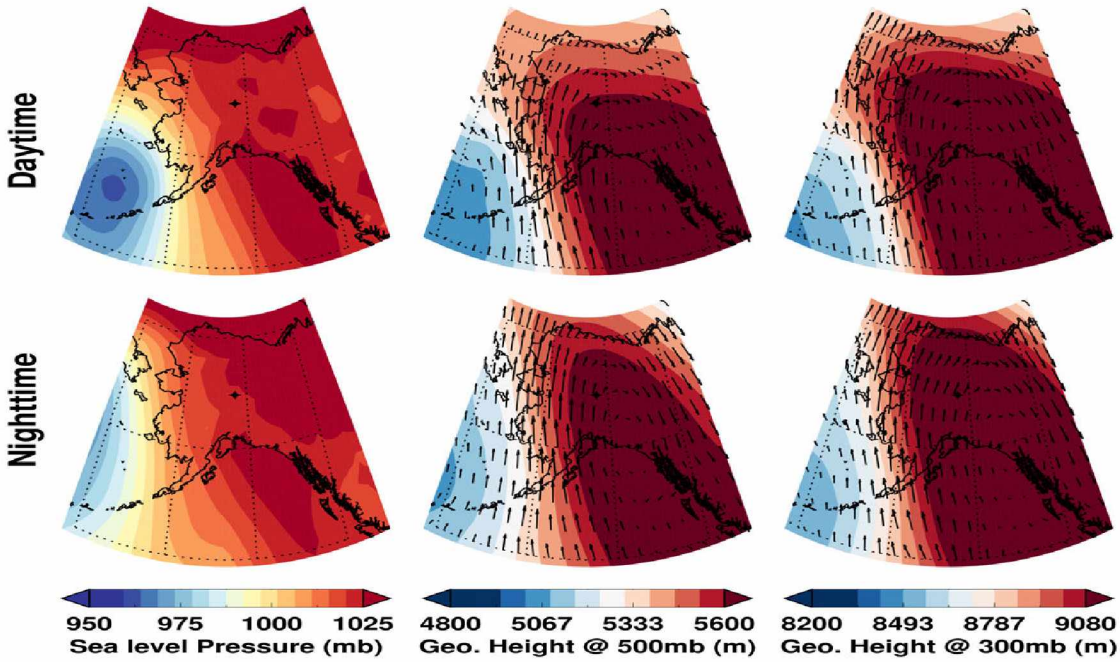

Figure 2.13: Synoptic meteorological conditions over Alaska on January 30, 2007 during both local day and night.

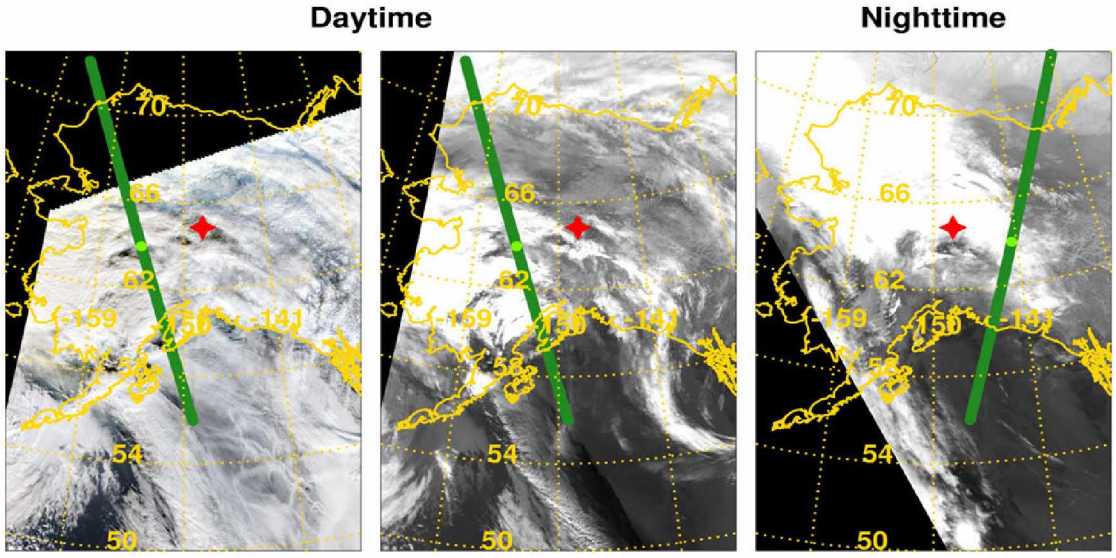

Figure 2.14: MODIS true color and IR imagery (left to right) showing cloudy conditions and the overlaid CALIPSO orbit (green) over Alaska on January 30, 2007 during both local day and night.

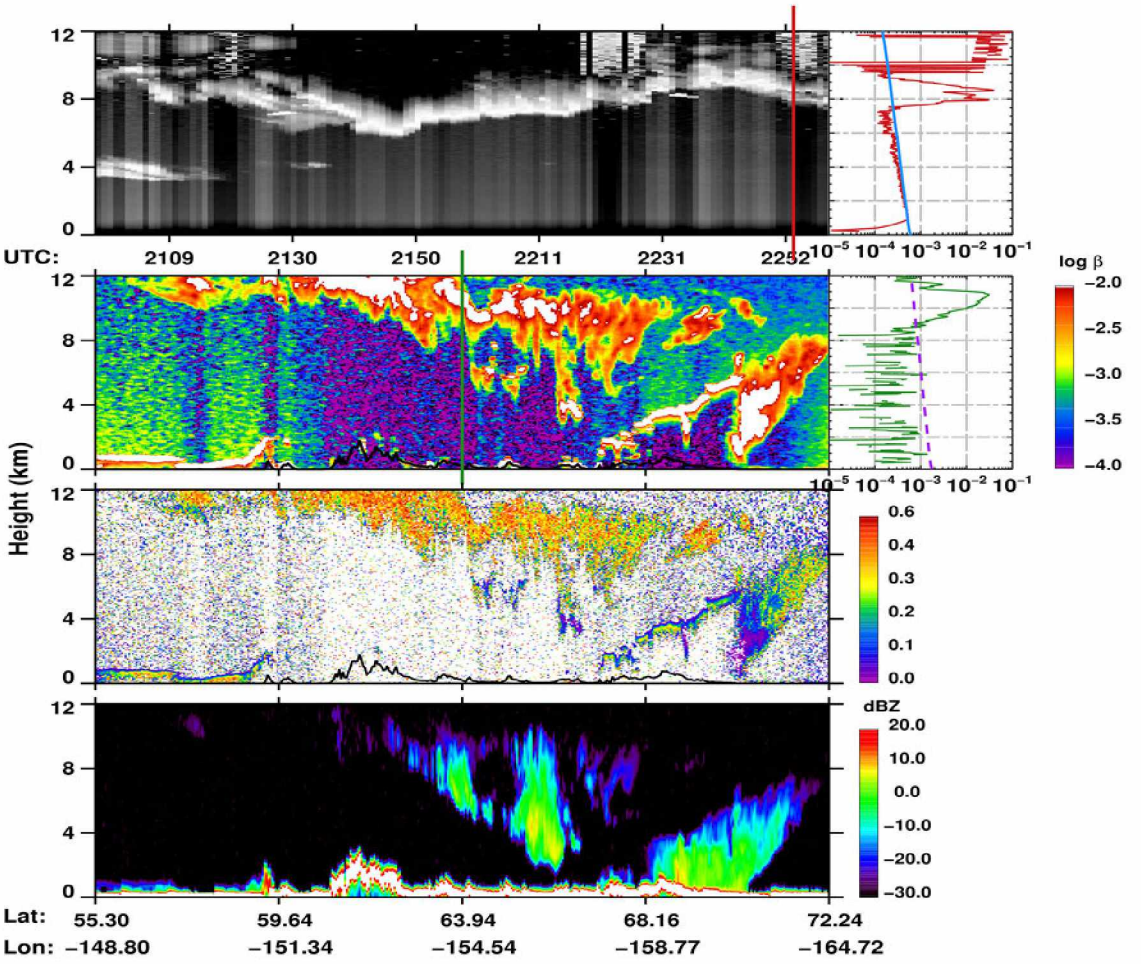

Figure 2.15: AFARS lidar returned power, CALIPSO total attenuated backscattering, CALIPSO linear depolarization ratio and CloudSat radar reflectivity data displays (top to bottom) and profiles during the satellite overpass on January 30, 2007 local day. Also shown is the corresponding wavelength Rayleigh estimates derived from radiosonde (solid line-blue) and CALIPSO provided model data (dashed line-purple).

lidar clearly shows the attenuation effect caused by the opaque cirrostratus cloud. Thus, it should be noted that for the cirrostratus type of cloud observed here the true cloud top altitude cannot be determined. The AFARS backscattering profile shows only molecular contribution till 7.5 km altitude after which it detects backscattering contribution from the cloud. The AFARS lidar signal attenuation caused by the cloud can be identified as the sudden fall of backscattering to values less than the estimated molecular backscattering. CALIPSO data shows that the high level clouds extends above 12 km altitude. This is a typical characteristic of lidar remote sensing from ground and airborne or satellite

platforms, that for a optically thick cloud satellite lidar can detect only true cloud top (apparent cloud base) while ground-lidar can detect only true cloud base (apparent cloud top).

The high δ values observed for the upper level clouds indicates the presence of ice crystals that are smaller in size and are completely undetected by the CloudSat. The synoptic uplift of air provides favorable conditions to attain high ice-supersaturation and initiates the formation of ice particles through homogeneous nucleation from the cloud top zones (*Sassen*, 2002). As the ice particles grow in size their fall speed increases and allows the ice particles to escape from the latent heat released during this process that promotes further growth of ice through secondary generating mechanisms such as accretion and riming. These ice-particle generating processes are responsible for their complex shapes (*Hallett and Mossop*, 1974; *Pruppacher and Klett*, 1997) which produces high δ. Thus, for most ice clouds, particles along the cloud top nucleation zones are smaller in size, which clearly went undetected by the CloudSat for the case shown here. The other clouds observed by CALIPSO over the latitudes 68° – 72° N can be identified as supercooled liquid topped stratiform clouds. The high backscattering at the cloud top, low depolarization and subsequent attenuation of CALIOP signals indicates supercooled liquid layer.

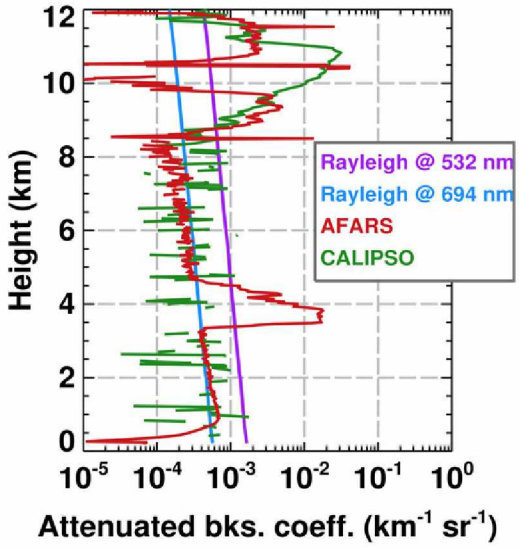

Figure 2.16: Averaged profile for the AFARS observation period and the nearest CALIPSO total attenuated backscattering profile on January 30, 2007 during local day.

Table 2.9: The CALIPSO identified features and QA flags for the nearest profile to the AFARS station on January 30, 2007 local day.

Property/Description	**Value**
Surface elevation (km)	0.185
Number of cloud layers	1
Horizontal averaging (km)	5
Cloud top altitude (km)	11.6
Cloud base altitude (km)	9.1
Transparency flags (0-Transparent/1-Attenuated)	1
Feature type	Cloud
Feature subtype	Deep convective
Feature type QA	High
Ice/water phase	Ice
Ice/water phase QA	High

The averaged backscattering profile obtained for the entire AFARS observation period (~3 hours) during local daytime is compared with the nearest CALIPSO profile as shown in Figure 2.16 and the features identified are provided in Table 2.9. From the AFARS backscattering profile, the contribution of the altostratus cloud from 3 – 5 km altitude is clearly evident. Thereafter the observed backscattering follows the molecular contribution and shows increase in backscattering values starting from 7 km altitude, which is contributed by the cirrostratus cloud. The CALIPSO backscattering profile shows increased backscattering from 11.5 – 9 km altitude and thereafter is attenuated and shows only background noise. This is also in agreement with the data product retrieval that shows cirrus cloud at a similar altitude and flags the profile as attenuated.

That night, the CALIPSO orbit is found to be ~319 km west of the AFARS station and captured the cirrus clouds over the Interior Alaska. The corresponding CALIPSO and CloudSat observations and the nearest profile to the AFARS station are shown in the Figure 2.17 and the features identified by CALIPSO in Table 2.10. As described earlier, the cirrus cloud observed here with CALIPSO was not detected by CloudSat. This is due to the small size distributions of the cloud particles, which cannot contribute to scattering at microwave wavelengths. From the analysis of ground-based lidar observations, *L'Ecuyer et al.* (2008) estimated that for ice clouds, which are detected only by lidar and not by radar, the equivalent effective radius of the particle does not exceed 30 micron. However, the estimated particle size is not strictly fixed and varies with the particle number concentration. This

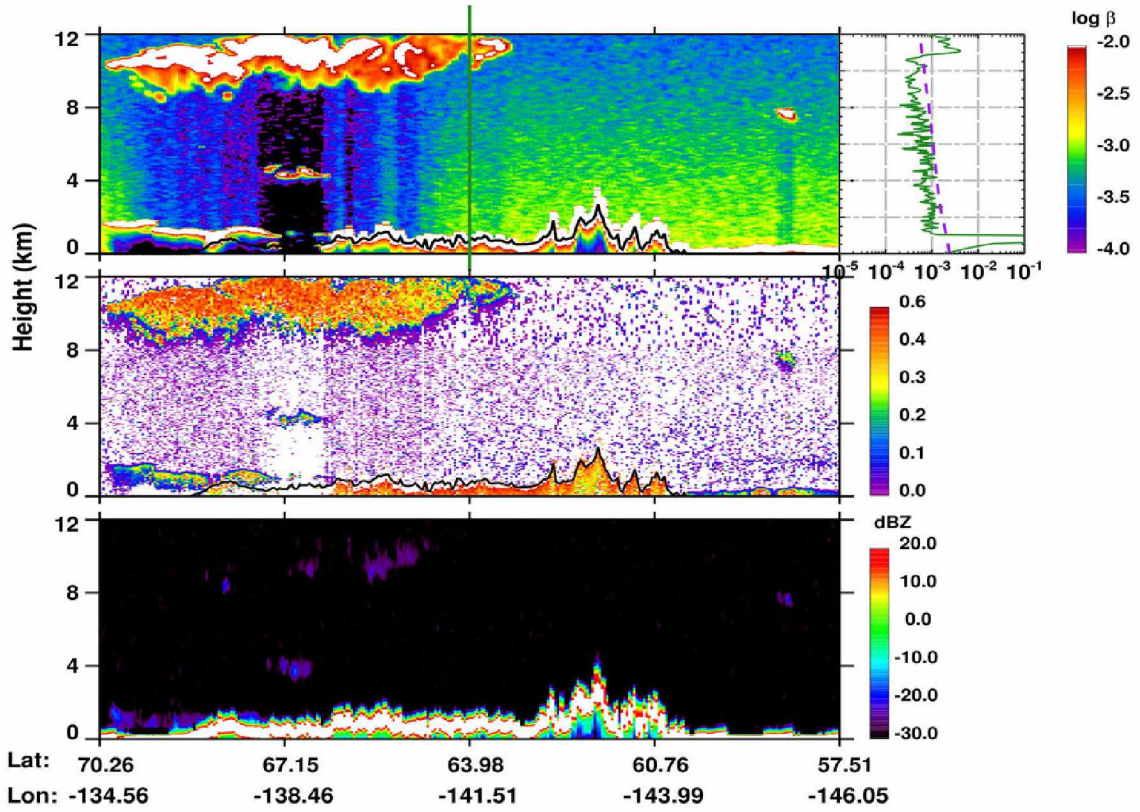

Figure 2.17: CALIPSO total attenuated backscattering (and profile), linear depolarization ratio and CloudSat radar reflectivity (top to bottom) for the nearest overpass to the AFARS station on January 30, 2007 during local night.

Table 2.10: The CALIPSO identified features and QA flags for the nearest profile to the AFARS station on January 30, 2007 local night.

Property/Description	**Value**
Surface elevation (km)	0.73
Number of cloud layers	1
Horizontal averaging (km)	5
Cloud top altitude (km)	12.3
Cloud base altitude (km)	10.6
Transparency flags	0
(0-Transparent/1-Attenuated)	
Feature type	Cloud
Feature subtype	Cirrus
Feature type QA	High
Ice/water phase	Ice
Ice/water phase QA	High

estimation of the ice particle size appears to represent typical optical depths for clouds as 0.1 – 0.2, which is in agreement with *Comstock et al.* (2002). Thus, it appears that when thin clouds, with optical depth < 0.2 are composed primarily of small particles they can be detected by lidar and not by radar. The CALIPSO backscattering profile shows more backscattering than the estimated molecular scattering from the altitude around 10.5 km due to the presence of the cirrus cloud. The cirrus cloud altitude and the observed surface returns in the backscattering profile are in agreement with the data product retrievals.

2.7.2.2 Case study 4: May 16, 2007

For the day on May 16, 2007 AFARS observations were available for up to 2 hours starting from 2050 UTC. The nearest CALIPSO orbital overpass is found to be around 346 km away from the AFARS station around 2153 UTC. The prevailing synoptic and cloudy conditions over the AFARS station are shown in the Figure 2.18 and Figure 2.19.

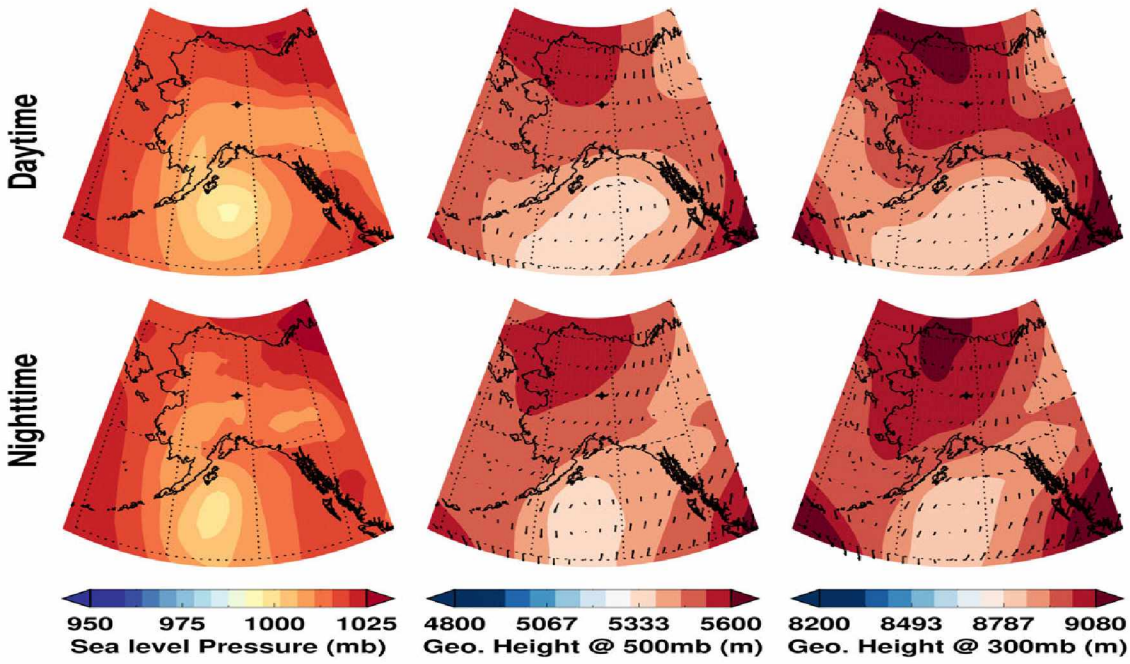

Figure 2.18: Synoptic meteorological conditions over Alaska on May 16, 2007 during both local day and night.

The synoptic maps at surface and upper levels of the atmosphere for May 16, 2007 show a low-pressure system (SLP ~990 mb) over the Gulf of Alaska and a high-pressure system

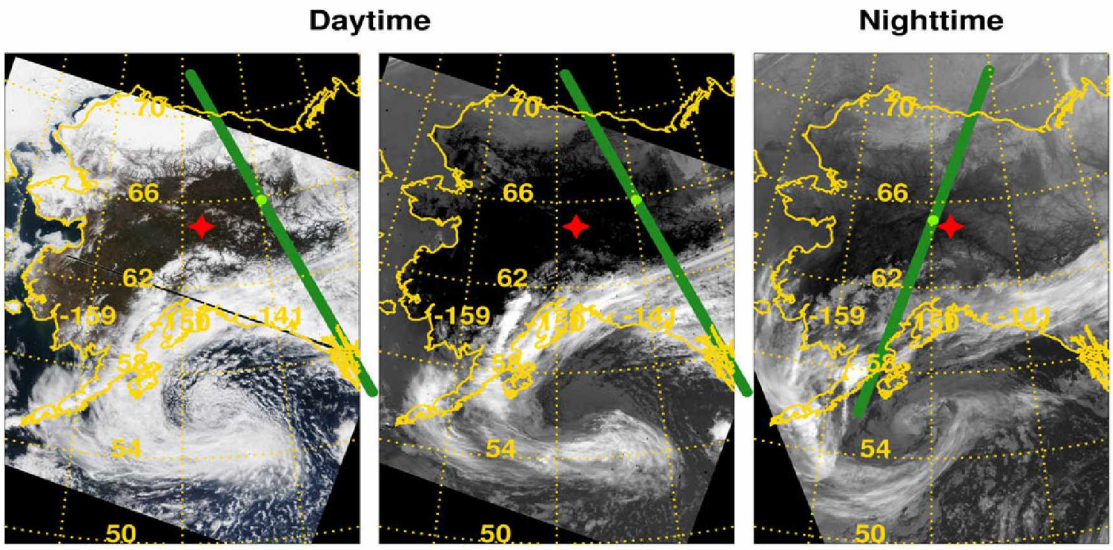

Figure 2.19: MODIS true color and IR imagery (left to right) showing cloudy conditions and the overlaid CALIPSO orbit (green) over Alaska on May 16, 2007 during both local day and night.

from Beaufort Sea extending to the Interior regions. While most of the Interior regions are observed to have clear sky conditions, the relatively cold moist air masses from the Beaufort Sea reaches the Interior through north-northeasterly flow. This resulted in the formation of relatively thin cirrus clouds over the Interior as captured by the AFARS lidar. IR imagery do not have the ability to identify the relatively thin clouds over the Interior (formed during the daytime) and only shows the cloud band formed as a result of cyclonic system over the Gulf of Alaska. However, by night the cyclonic system weakens and moves towards the North Pacific Ocean, the continued northerly flow in the upper levels of atmosphere promoted the growth of thin clouds. This can be now observed in the IR imagery as gray patches that are extending to Interior from northerly flow.

The corresponding AFARS, CALIPSO and CloudSat observations for May 16, 2007 are shown in Figure 2.20. For this day, the AFARS lidar observed a thin cirrus cloud layer at 9 – 10 km altitude with very weak returned power. The AFARS lidar operator identified these clouds as 'subvisual' cirrus. Thin cirrus clouds with visible optical depths limited to 0.03 are categorized as 'subvisual' cirrus (*Sassen and Cho*, 1992). The data display show that apart from cirrus cloud there are two other layers in the troposphere seen as

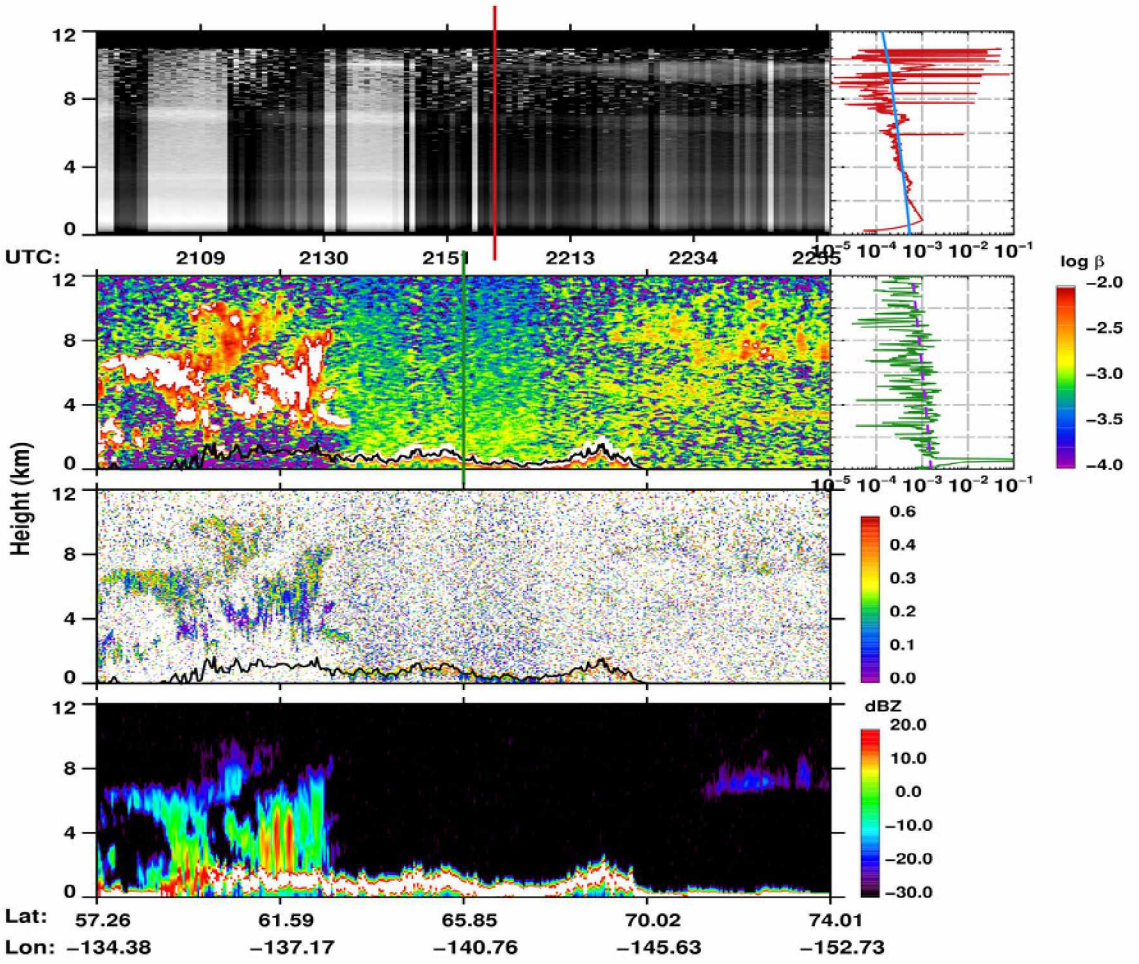

Figure 2.20: AFARS lidar returned power, CALIPSO total attenuated backscattering, CALIPSO linear depolarization ratio and CloudSat radar reflectivity data displays (top to bottom) and profiles during the satellite overpass on May 16, 2007 local day. Also shown is the corresponding wavelength Rayleigh estimates derived from radiosonde (solid line-blue) and CALIPSO provided model data (dashed line-purple).

returned power at 8 km and 3 – 4 km altitudes. The AFARS operator reported these as aerosol layers. The single AFARS backscattering profile drawn from the time when no cloud is observed, clearly shows an increase in backscattering indicating the contribution from these aerosol layers. The nearest CALIPSO-CloudSat orbital overpass for this day detected clouds associated with the cyclonic system over the southern regions, clear skies over the Interior, and thin cloud layers to the north of the AFARS station. The thin clouds at 7 – 10 km altitude detected by CALIPSO over 70° – 74° N latitude shows weak backscattering compared to the other type of clouds. Thus, it can be now confirmed that

the prevailing northerly winds transported these thin cloud masses to the Interior, which is later captured by AFARS.

The CALIPSO orbital overpass along the region 70° – 72° N latitude (Figure 2.20) clearly detected the aerosol layers around 3 – 5 km altitudes, seen as yellow patches in the CALIPSO backscattering data display. We have confirmed these layers as aerosols by observing their presence in the CALIPSO VFM product (not shown here) and their absence in the CloudSat data display, as expected. We generated a 5-day back trajectory of air mass along the identified altitudes using HYSPLIT (Hybrid Single Particle Lagrangian Integrated Trajectory) model available through National Oceanic and Atmospheric Administration-Air Resources Laboratory (https://ready.arl.noaa.gov/HYSPLIT.php) to investigate the source of these aerosols.

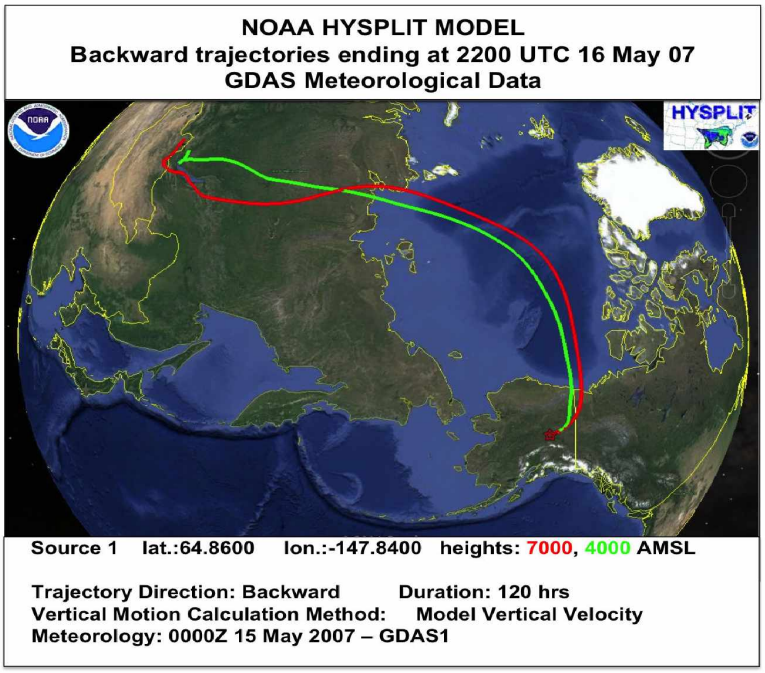

Figure 2.21: HYSPLIT model backward trajectories of an air mass starting from the AFARS station (star mark) at 2200 UTC, 16 May 2007.

The HYSPLIT backward trajectories (Figure 2.21) confirm that the aerosols observed for this day over Alaska originated from the arid Gobi Desert in Asia. The synoptic flow (Figure 2.18) observed for this day is consistent with the obtained air mass trajectories. Long-range transports of dust particles from Asia and smoke aerosols from Siberian forest

fires to Alaska are not uncommon during spring season (March-April-May). Several studies (e.g., *Sassen* (2005), *Sassen and Khvorostyanov* (2008) and *Atkinson et al.* (2013)) have reported notable episodes of aerosol transport from Asia and eastern Russia to the Alaska. Under favorable conditions, these aerosols can initiate ice cloud formation in the midlevels of the troposphere.

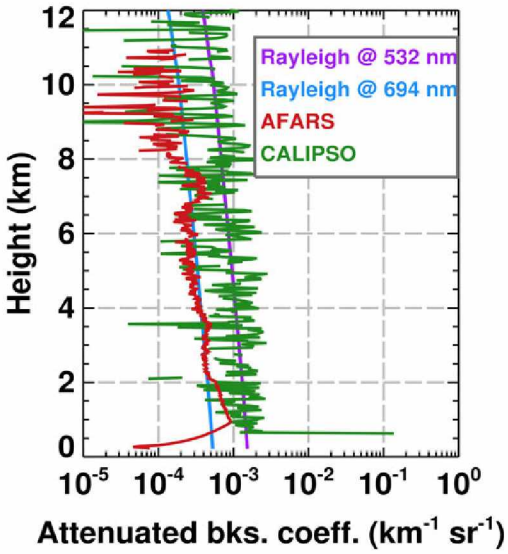

Figure 2.22: Averaged profile for the AFARS observation period and the nearest CALIPSO total attenuated backscattering profile on May 16, 2007 during local day.

The averaged backscattering profile obtained for the entire AFARS observation period (~3 hours) during local daytime is compared with the nearest CALIPSO profile in Figure 2.22. The features identified by CALIPSO are presented in Table 2.11. The AFARS backscattering profile shows the aerosol layers as regions of enhanced backscattering at altitudes of 3 – 4 km and 7 – 8 km. Since the thin cirrus cloud observed at 9 km altitude is only present for a brief time during the observation period, the averaged profile shows the cirrus cloud signal embedded in the noise levels. The nearest CALIPSO backscattering profile, which is ~340 km away to the east of the AFARS station, observed clear skies. Thus, the CALIPSO backscattering profile follows the estimated molecular scattering with a peak backscattering at the surface indicating the atmosphere is optically transparent, which is in agreement with the data product retrievals.

Table 2.11: The CALIPSO identified features and QA flags for the nearest profile to the AFARS station on May 16, 2007 local day.

Property/Description	Value
Surface elevation (km)	0.607
Number of cloud layers	0
Horizontal averaging (km)	-
Cloud top altitude (km)	-
Cloud base altitude (km)	-
Transparency flags (0-Transparent/1-Attenuated)	0
Feature type	-
Feature subtype	-
Feature type QA	-
Ice/water phase	-
Ice/water phase QA	

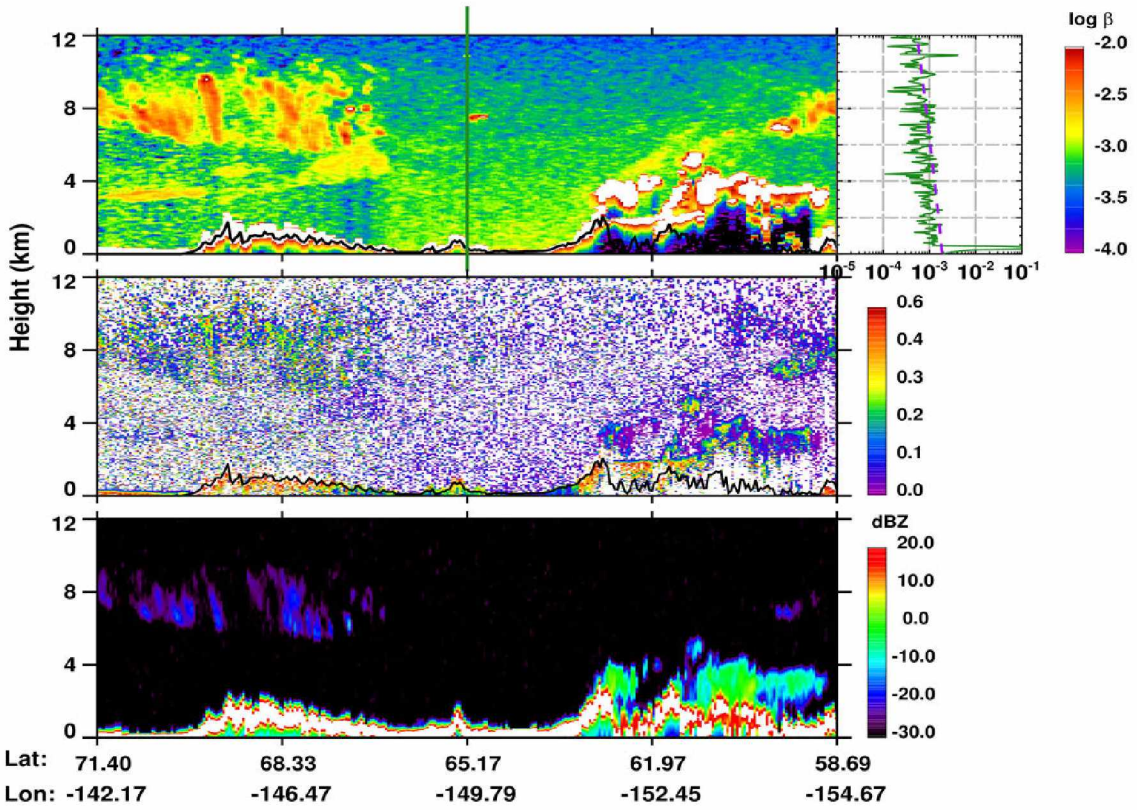

Figure 2.23: CALIPSO total attenuated backscattering (and profile), linear depolarization ratio and CloudSat radar reflectivity for the nearest overpass to the AFARS station on May 16, 2007 during local night.

That night, the CALIPSO orbit is found to be ~98 km west of the AFARS station and detected the cirrus clouds, clear skies and clouds formed in the cyclonic system. The corresponding CALIPSO and CloudSat observations and the nearest profile to the AFARS station are shown in the Figure 2.23 and the features identified by CALIPSO in Table 2.12. For this case, CALIPSO detected similar conditions as observed during daytime: the high level clouds to the north of the AFARS station, clear skies over the Interior and clouds formed due to the cyclonic system in the southern regions. The enhanced CALIPSO backscattering at 4 – 6 km altitudes can be identified as aerosol layers ($\delta < 0.1$ in lidar and not detected in CloudSat), which is also confirmed by CALIPSO VFM data product (not shown here). The nearest CALIPSO backscattering profile to the AFARS station captures only clear skies and follows the estimated molecular backscattering along with the surface returns. The data product flags this backscattering profile as transparent with no cloud/aerosol features and is in agreement with our observation. For this case, it is interesting to note that CALIPSO has not observed any aerosol layers over the Interior Alaska while it is ~340 km to the east and ~98 km to the west of the AFARS station during its day and night orbital overpasses. However, AFARS lidar during its local daytime operations had identified transient/diffuse aerosol layers. This shows that the aerosol layers are streamlined in the prevailing northerly winds in the upper levels of the troposphere.

Table 2.12: The CALIPSO identified features and QA flags for the nearest profile to the AFARS station on May 16, 2007 local night.

Property/Description	**Value**
Surface elevation (km)	0.357
Number of cloud layers	0
Horizontal averaging (km)	-
Cloud top altitude (km)	-
Cloud base altitude (km)	-
Transparency flags (0-Transparent/1-Attenuated)	0
Feature type	-
Feature subtype	-
Feature type QA	-
Ice/water phase	-
Ice/water phase QA	

These two case studies confirm that high level optically thick cloud attenuates both the AFARS and CALIOP lidar signals after penetrating a few meters in the cloud. Only the true cloud top altitude can be identified from CALIOP and only true cloud base altitude can be identified from AFARS signals. For such cases, as a consequence the estimated Rayleigh molecular scattering is neither observed above the cloud with AFARS nor below the cloud with CALIOP signals. Thin cirrus cloud is observed by CALIOP lidar and is confirmed by the AFARS lidar (categorized as 'subvisual' type of cloud by AFARS operator). Diffuse aerosol layers has been observed by both AFARS and CALIOP lidars at midlevels of the troposphere over Alaska. These aerosol layers are consistent with the synoptic flow pattern and the HYSPLIT back trajectories indicates the aerosols as 'dust' particles that are transported from arid regions of Asia.

2.7.3 Mid/low level clouds

2.7.3.1 Case study 5: January 27, 2007

For the day on January 27, 2007 the AFARS observations were available for up to 2 hours starting from 2100 UTC. Around 2223 UTC the nearest CALIPSO orbital overpass was 10 km from the AFARS station. The prevailing synoptic and cloudy conditions over the Alaska for this day are shown in the Figure 2.24 and Figure 2.25.

The synoptic conditions observed for this day are similar to the conditions observed for the case of January 30, 2007. A surface low-pressure system over the Aleutian Islands and the upper level ridge extending to most of the Interior Alaska is observed. This caused extensive cloudiness over the southwestern parts of Alaska and the Gulf of Alaska regions. By night, the cyclonic system weakens and moves from the Aleutian Islands towards western Alaska, while the upper level air mass flows along the North Pacific ridge continues. This caused extensive deepening of the clouds throughout Interior Alaska. The deep clouds formed due to synoptic uplift of the airmass along the ridge are evident from the white patches of clouds in the IR imagery.

The corresponding AFARS, CALIPSO, and CloudSat observations for January 27, 2007 are shown in Figure 2.26. During the observation period the AFARS lidar captured altocumulus clouds around 3.0 – 4.5 km altitude and cirrostratus clouds from 6 – 10 km

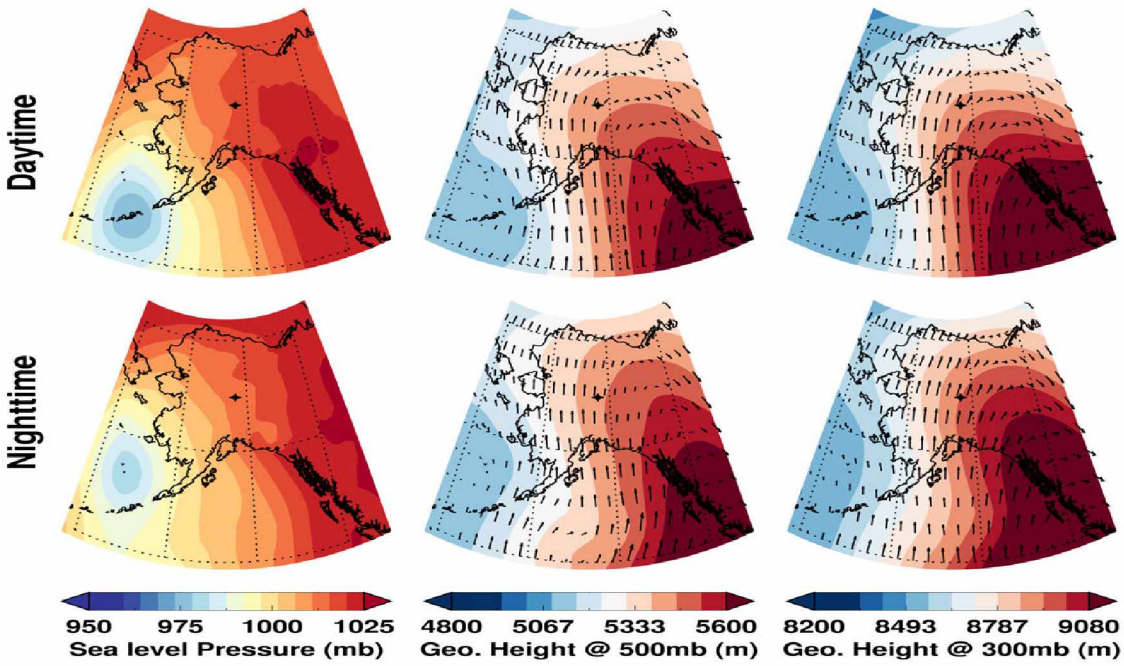

Figure 2.24: Synoptic meteorological conditions over Alaska on January 27, 2007 during both local day and night.

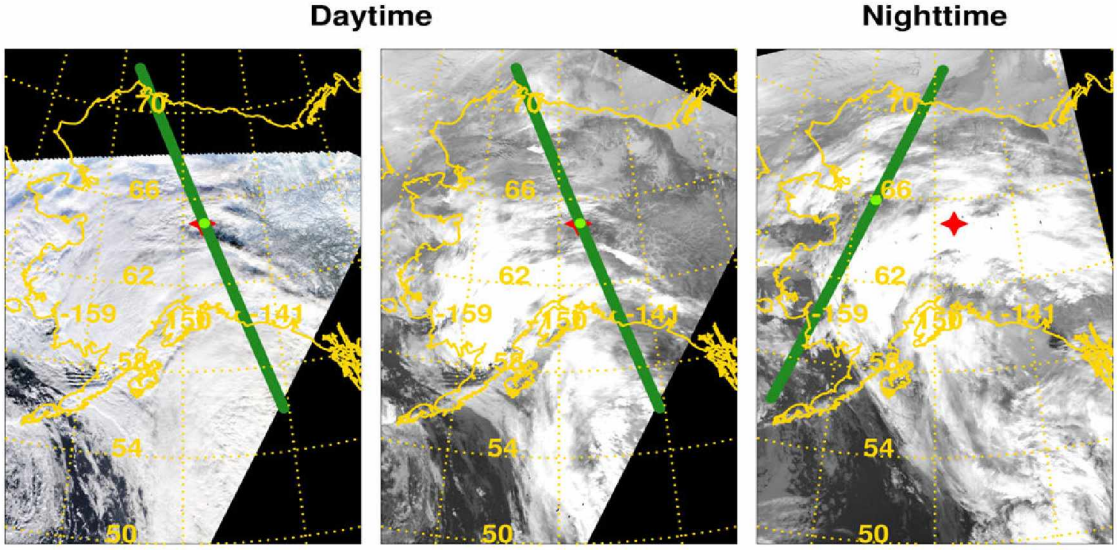

Figure 2.25: MODIS true color and IR imagery (left to right) showing cloudy conditions and the overlaid CALIPSO orbit (green) over Alaska on January 27, 2007 during both local day and night.

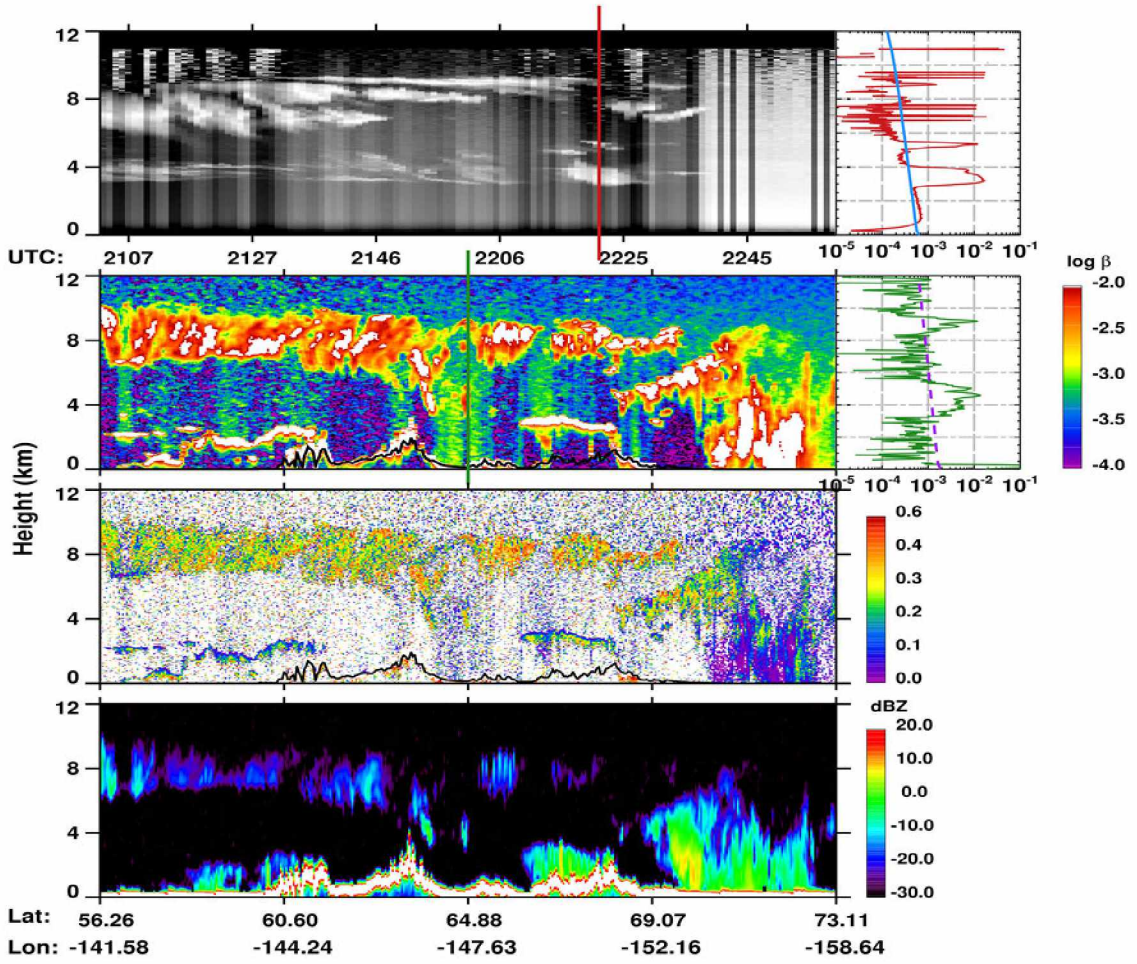

Figure 2.26: AFARS lidar returned power, CALIPSO total attenuated backscattering, CALIPSO linear depolarization ratio and CloudSat radar reflectivity data displays (top to bottom) and profiles during the satellite overpass on January 27, 2007 local day. Also shown is the corresponding wavelength Rayleigh estimates derived from radiosonde (solid line-blue) and CALIPSO provided model data (dashed line-purple).

altitude. A thin layer of supercooled liquid droplets are observed at the altocumulus cloud top that can be readily identified from linear depolarization data display (not shown here, AFARS lidar depolarization data displays for all days are available in www.rainbow.gi.alaska.edu). However, this thin supercooled liquid layer is not dense enough to completely attenuate the AFARS lidar pulses and the cirrostratus cloud layer could also be identified until 2220 UTC. After 2220 UTC, the altocumulus cloud layer becomes dense enough to attenuate the lidar pulse energy for a brief period until 2230 UTC. As well known, this is the typical limitation of cloud observations from a ground

lidar, that mid/low level clouds often block observation of high level clouds. The AFARS backscattering profile clearly shows the altocumulus cloud layers around 3 – 4 km and 5 km altitudes that eventually absorbed the lidar pulse energy. However, a small increase in backscattering embedded in the noise is observed at the cirrostratus cloud layer altitude. For the same time, the CALIPSO backscattering profile detects both the midlevel and high level cloud. Also the high backscattering values near the surface level shows that these clouds observed by CALIPSO are optically thin. The cirrus cloud band detected by CloudSat does not detect the cloud top altitude as detected by CALIPSO, because of the smaller particle sizes in the cloud top nucleation zones. Also it can be observed that CloudSat does not detect low level cloud over the 56° – 58° N latitudinal regions that are detected by CALIPSO. *Okamoto et al.* (2010) estimated that more than 10% of the low level clouds detected by CALIPSO have gone undetected by CloudSat because of the possible contamination from surface clutter that produces strong radar echoes (reflectivity) or due to the attenuation of radar pulses in optically dense clouds which considerably reduces the reflectivity near the surface. For this case, it is interesting to observe that both AFARS and CALIOP lidars illustrate the two commonly found midlevel cloud types, optically thin and optically thick cloud in a single observation.

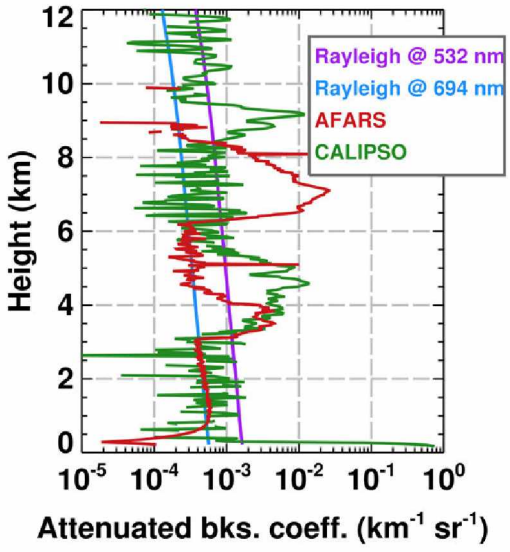

Figure 2.27: Averaged profile for the AFARS observation period and the nearest CALIPSO total attenuated backscattering profile on January 27, 2007 during local day.

The averaged backscattering profile obtained for the entire AFARS observation period (~3 hours) during local daytime is compared with the nearest CALIPSO profile in Figure 2.27 and the features identified by CALIPSO are provided in Table 2.13. The AFARS backscattering profile shows an increase in backscattering at 3 – 4.5 km and 6 – 9 km due to the contribution from altocumulus and cirrus cloud, respectively. Thereafter the AFARS averaged backscattering profile is observed to be much less than the estimated molecular scattering and shows attenuation effects, this is because of the brief period where AFARS lidar got attenuated by dense altocumulus cloud. The nearest CALIPSO backscattering profile clearly identifies enhanced backscattering at 8.5 – 9.5 km, 3.5 – 5.5 km and surface level due to the contribution from cirrus, midlevel cloud and surface returns, respectively. The estimated cloud top and base altitudes from the backscattering profile are in good agreement with the data product retrievals which also flags the backscattering profile as transparent.

Table 2.13: The CALIPSO identified features and QA flags for the nearest profile to the AFARS station on January 27, 2007 local day.

Property/Description	**Values**	
Surface elevation (km)	0.139	
Number of cloud layers	2	
Horizontal averaging (km)	5	5
Cloud top altitude (km)	9.4	5.36
Cloud base altitude (km)	8.4	3.63
Transparency flags (0-Transparent/1-Attenuated)	0	0
Feature type	Cloud	Cloud
Feature subtype	Cirrus	Altocumulus
Feature type QA	High	High
Ice/water phase	Ice	Ice
Ice/water phase QA	High	High

That night, the CALIPSO orbit is found to be ~430 km west of the AFARS station and captured the cirrus clouds and clouds formed in the cyclonic system. The corresponding CALIPSO and CloudSat observations and the nearest profile to the AFARS station are shown in the Figure 2.28 and the features identified by CALIPSO in Table 2.14. For this case, the CALIPSO-CloudSat observed deep clouds that are formed due to the continuous synoptic uplift of the air mass along the upper level North Pacific ridge. As expected the CALIOP signals were totally absorbed after penetrating a few meters in the cloud and

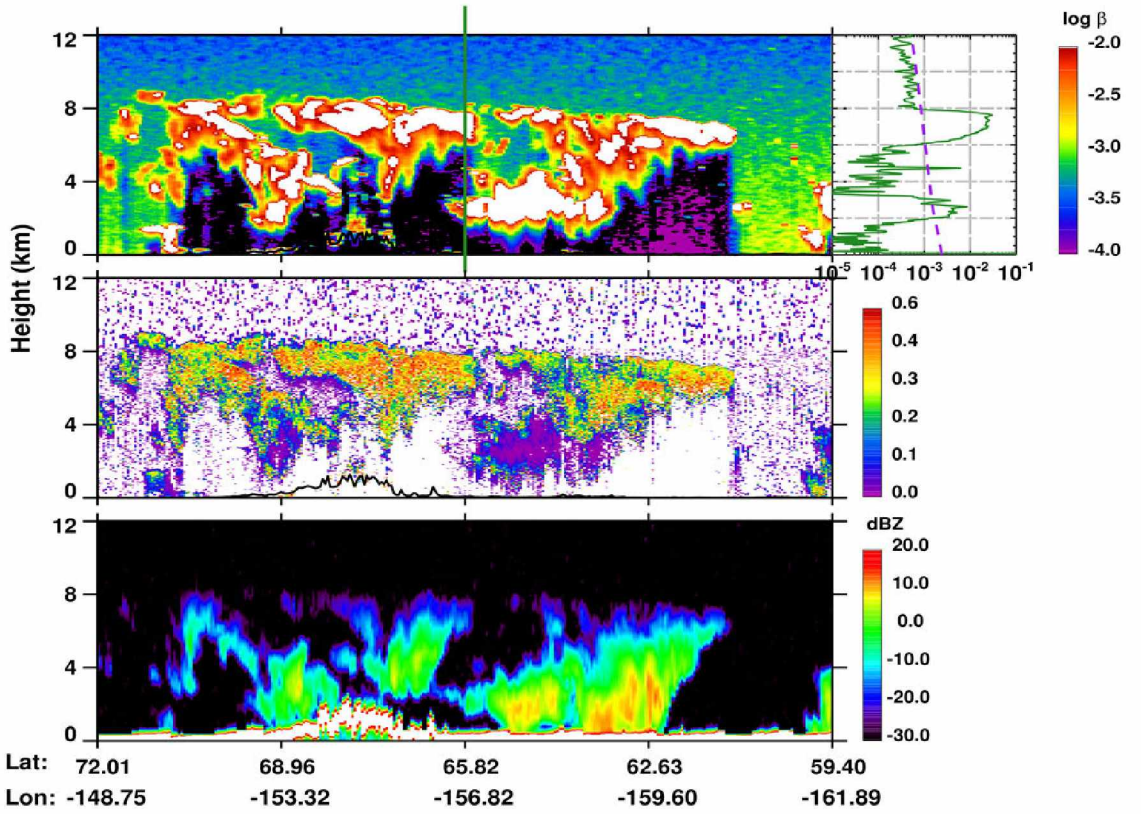

Figure 2.28: CALIPSO total attenuated backscattering (and profile), linear depolarization ratio and CloudSat radar reflectivity for the nearest overpass to the AFARS station on January 27, 2007 during local night.

only true cloud top is being identified, whereas the CloudSat observed radar echoes down to the surface level indicating precipitation from the clouds. Observation of δ, shows high values near the cloud top for most clouds indicating ice particles and low values < 0.1 for the cloud observed at 1 – 4 km altitude over 65^{o} – 63^{o} N latitudinal region indicating the supercooled liquid layer.

The nearest CALIPSO backscattering profile to the AFARS station captures the upper and midlevel cloud layers and also shows the effects of attenuation. From the observation of CALIPSO backscattering profile it is clear that there are two layers of enhanced backscattering indicating cloud layers at approximately 2 – 3 km and 6 – 8 km. These approximate cloud top and base altitudes are in agreement with the data product retrievals that show clouds identified at 5 km horizontal resolution. Apart from these two cloud layers,

Table 2.14: The CALIPSO identified features and QA flags for the nearest profile to the AFARS station on January 27, 2007 local night.

Property/Description	**Values**				
Surface elevation (km)	0.06				
Number of cloud layers	5				
Horizontal averaging (km)	5	20	20	5	20
Cloud top altitude (km)	7.94	6.02	4.4	3.2	1.83
Cloud base altitude (km)	6.02	5.25	2.82	1.86	0.93
Transparency flags (0-Transparent/ 1-Attenuated)	0	0	0	0	0
Feature type	Cloud	Cloud	Cloud	Cloud	Cloud
Feature subtype	Cirrus	Alto-cumulus	Alto-cumulus	Alto-cumulus	Low overcast
Feature type QA	High	High	None	None	None
Ice/water phase	Ice	Unknown	Unknown	Unknown	Unknown
Ice/water phase QA	High	None	None	None	

the data product reports more cloud layers at 20 km horizontal averaging that are consistent with the observations from the CALIPSO backscattering data display. CALIPSO data users should be cautioned about the use of multi-horizontal resolution scheme for detecting cloud layers, which leads to overlap of cloud layers detected at any resolution. For example, Table 2.5 shows a cloud layer detected at 5 km horizontal resolution that has its cloud top altitude within the cloud boundaries detected at 20 km horizontal resolution. Nonetheless, strongly scattering cloud layers are reported by the data product as we have observed from the associated backscattering profiles.

2.7.3.2 Case study 6: February 14, 2007

For the day on February 14, 2007 the AFARS observations were available for up to 2 hours starting from 2127 UTC. Around 2211 UTC the nearest CALIPSO orbital overpass was 143 km from the AFARS station. The prevailing synoptic and cloudy conditions over Alaska for this day are shown in the Figure 2.29 and Figure 2.30.

The synoptic maps for February 14, 2007 show a low-pressure system (SLP ~990 mb) near the Aleutian Islands. During daytime, while the high-pressure system over Beaufort Sea extends to the Interior region providing northerly winds, the upper level North Pacific ridge is completely over the continental states towards the southeastern parts of Alaska

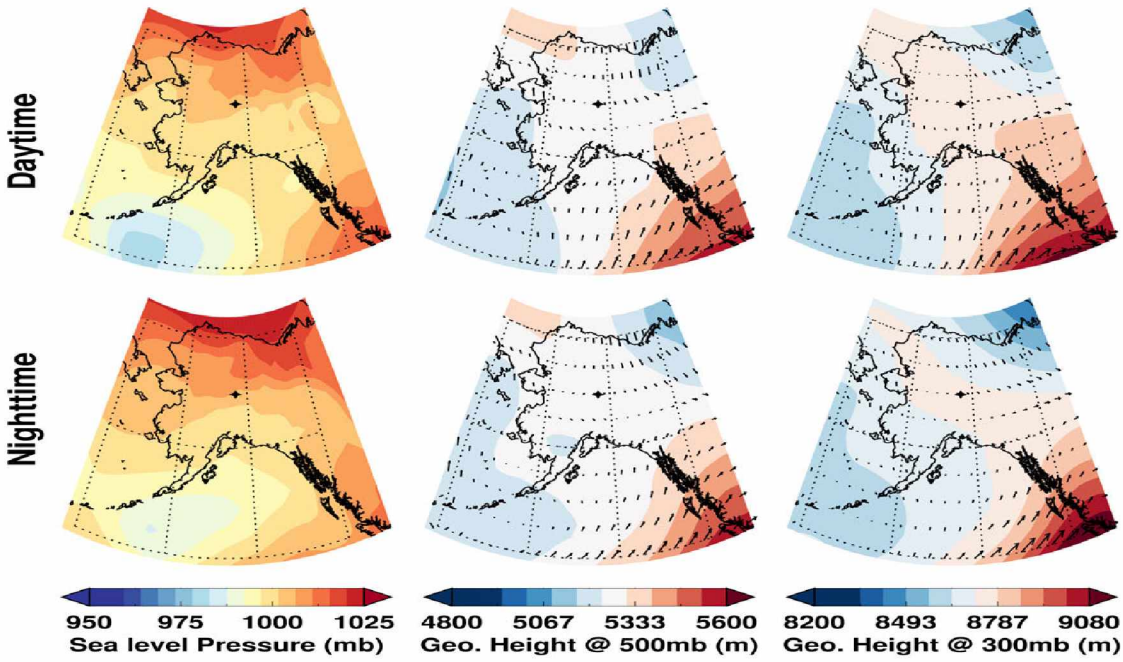

Figure 2.29: Synoptic meteorological conditions over Alaska on February 14, 2007 during both local day and night.

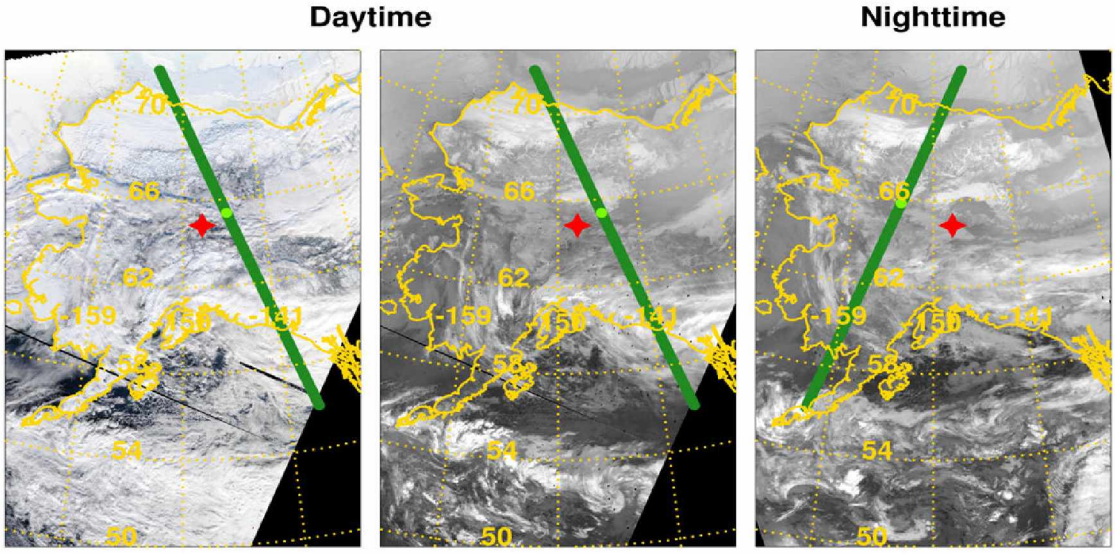

Figure 2.30: MODIS true color and IR imagery (left to right) showing cloudy conditions and the overlaid CALIPSO orbit (green) over Alaska on February 14, 2007 during both local day and night.

with southwesterly winds. This caused clouds along the frontal zone that is clearly seen in the MODIS imagery over the southeastern parts of Alaska extending towards Canada and the continental United States. The clouds formed due to the cyclonic system are also seen in the MODIS imagery near the Aleutian Islands. Over Interior Alaska, the relatively cold moist air provided by the northerly winds forms thin clouds under local meteorological conditions that are seen as dim shades of white color in the MODIS imagery. Similar conditions are observed during night for this day.

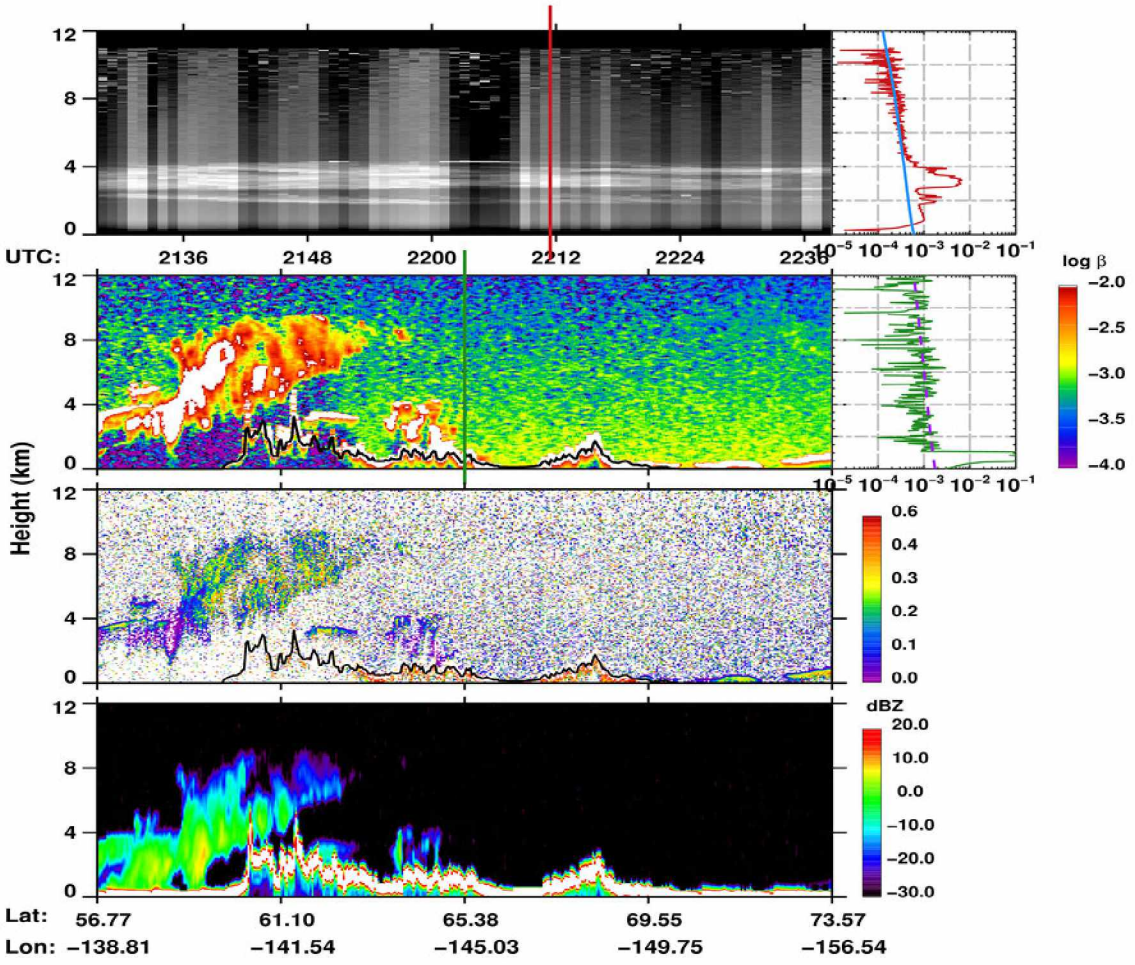

Figure 2.31: AFARS lidar returned power, CALIPSO total attenuated backscattering, CALIPSO linear depolarization ratio and CloudSat radar reflectivity data displays (top to bottom) and profiles during the satellite overpass on February 14, 2007 local day. Also shown is the corresponding wavelength Rayleigh estimates derived from radiosonde (solid line-blue) and CALIPSO provided model data (dashed line-purple).

The corresponding AFARS, CALIPSO and CloudSat observations for February 14, 2007 are shown in Figure 2.31. For this day, the AFARS lidar observed optically thin midlevel cloud at 2 – 4 km altitude. Observation of AFARS lidar signals show the effect of attenuation for a brief time 2202 – 2208 UTC due to the presence of thin supercooled liquid layer at the cloud top, which can be identified by the high returned power. *Kayetha* (2014) showed the prevalence of optically thin midlevel ice clouds over the AFARS station and observed that these clouds occur ~2 km lower than the cirrus cloud altitudes in the midlevels of the troposphere. The single AFARS profile shown here, clearly identifies the two thin cloud layers and thereafter follows the molecular scattering. The nearest CALIPSO-CloudSat orbital overpass observes deep clouds formed along the frontal zone over the southeastern parts of Alaska and the midlevel clouds formed in the Interior region at 63° – 65° N latitude, which are eventually captured by the AFARS lidar. From the CALIPSO δ, the location of ice, mixed-phase, and supercooled liquid particles can be clearly identified within the cloud. The deep clouds observed by CloudSat show radar echoes extending to the surface level, as expected.

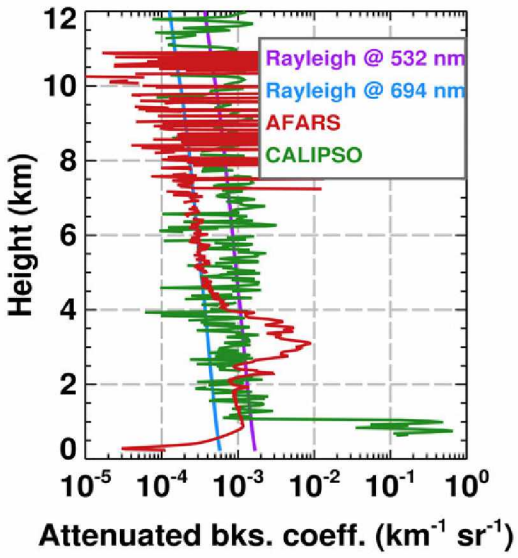

Figure 2.32: Averaged profile for the AFARS observation period and the nearest CALIPSO total attenuated backscattering profile on February 14, 2007 during local day.

The averaged backscattering profile obtained for the entire AFARS observation period (~3 hrs) during local daytime is compared with the nearest CALIPSO profile as shown

Table 2.15: The CALIPSO identified features and QA flags for the nearest profile to the AFARS station on February 14, 2007 local day.

Property/Description	**Value**
Surface elevation (km)	0.60
Number of cloud layers	0
Horizontal averaging (km)	-
Cloud top altitude (km)	-
Cloud base altitude (km)	-
Transparency flags (0-Transparent/1-Attenuated)	0
Feature type	-
Feature subtype	-
Feature type QA	-
Ice/water phase	-
Ice/water phase QA	

in Figure 2.32 and features identified are provided in Table 2.15. The AFARS profile clearly captures the backscattering contribution from the midlevel cloud. The cloud top and base altitudes can be estimated as 2 and 4 km, respectively. Above the cloud top altitude the decrease in backscattering is due to the AFARS lidar signal attenuation for brief time during the observation period. However, the nearest CALIPSO profile captures clear sky and follows the estimated molecular backscattering. Thus, the data product retrievals, which flag the backscattering profile as thin with no cloud/aerosol features are in agreement with the CALIPSO observations.

That night, the CALIPSO orbit is found to be ~294 km east of the AFARS station and captured the cirrus clouds and clouds formed in the cyclonic system. The corresponding CALIPSO and CloudSat observations and the nearest profile to the AFARS station are shown in the Figure 2.33 and the features identified by CALIPSO in Table 2.16. The nighttime CALIPSO orbital overpass observes mostly clear skies over the Interior region and mid/high level clouds to the south of AFARS station. The nearest backscattering profile to the AFARS station captures clear skies and thus follows the estimated molecular backscattering. The high backscattering observed near the 300 – 400 m altitude indicates the returned signal from the surface. This can be confirmed from the data product retrievals, which shows the location surface elevation as 357 m. Also as expected, the data product shows the flags for the backscattering profile as transparent with no cloud/aerosol features.

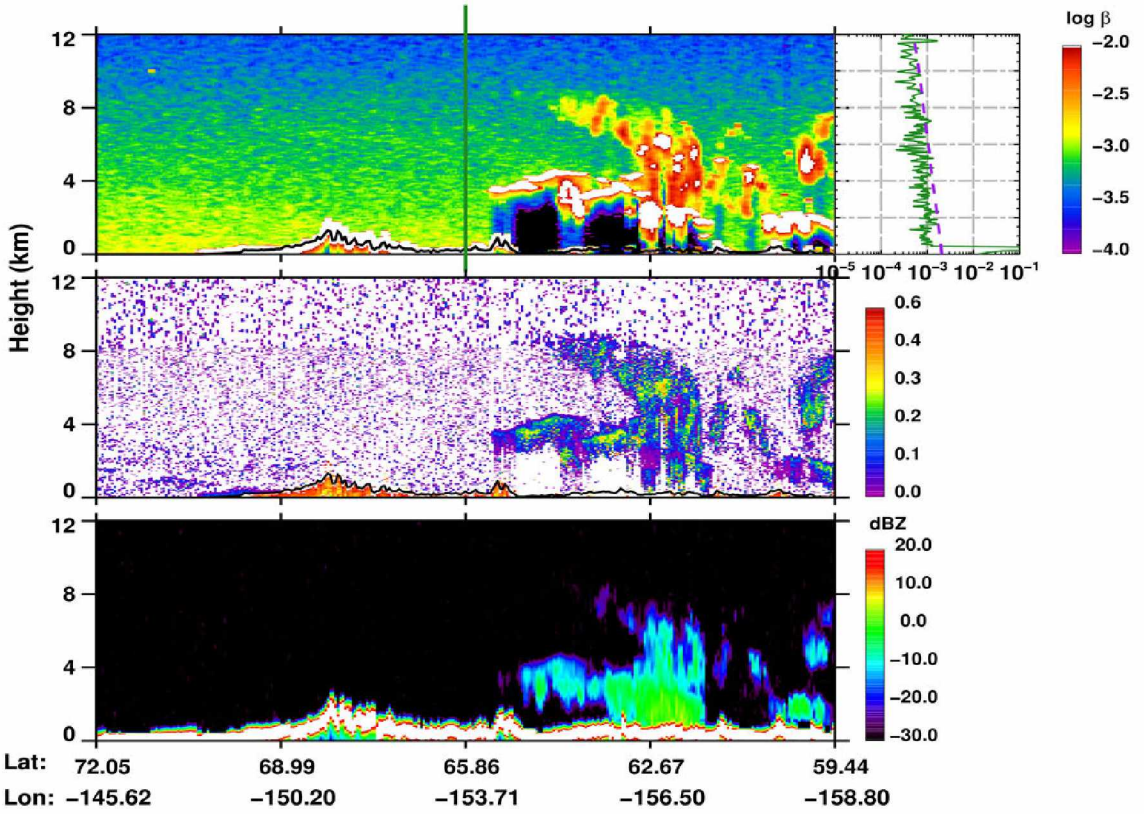

Figure 2.33: CALIPSO total attenuated backscattering (and profile), linear depolarization ratio and CloudSat radar reflectivity (top to bottom) for the nearest overpass to the AFARS station on February 14, 2007 during local night.

Table 2.16: The CALIPSO identified features and QA flags for the nearest profile to the AFARS station on February 14, 2007 local night.

Property/Description	**Value**
Surface elevation (km)	0.357
Number of cloud layers	0
Horizontal averaging (km)	-
Cloud top altitude (km)	-
Cloud base altitude (km)	-
Transparency flags	0
(0-Transparent/1-Attenuated)	
Feature type	-
Feature subtype	-
Feature type QA	-
Ice/water phase	-
Ice/water phase QA	

Thus, from these two cases studies it is now confirmed that optically thin midlevel clouds can be observed by both AFARS and CALIOP lidars.

2.7.4 Day-night differences in CALIOP signals

Here we provide a comparison of backscattering profiles obtained by CALIOP lidar during daytime and nighttime measurements. For this purpose we have selected the cases where CALIOP observed clear skies or does not have any backscattering contribution from clouds or aerosols above 2 km altitude. These include the daytime CALIPSO backscattering profiles used in the clear skies category (i.e., September 21, 2006 and October 24, 2006) and both day-night CALIPSO profiles from the case for February 14, 2007. In this comparison, we ignore the CALIPSO backscattering obtained below 2 km altitude in order to avoid specular/multiple scattering effects induced by the surface. The estimated molecular backscattering at CALIOP wavelength is calculated using the nearest local radiosonde measurements. Since the signal characteristics are influenced by the resolution of data, we calculate the integrated backscattering coefficient corresponding to the CALIPSO downlinked vertical resolutions and 5 km horizontal resolution. The vertical resolution of CALIPSO data for altitude range 2 – 8 km and 8 – 12 km are 30 m and 60 m, respectively.

On these two days the estimated molecular Rayleigh scattering from the radiosonde measurement for both day and night are identical. However, the calculated day-night ratio of the corresponding CALIOP molecular scattering signal is 1.26 (i.e. 26% greater in daytime than nighttime). *Vaughan et al.* (2005) provided pre-launch estimates of the minimum detectable backscattering that can be obtained by CALIOP signals at 10 km altitude for 5 km horizontal and 60 m vertical resolution as 13.2 x 10^{-4} km^{-1} sr^{-1} (daytime) and 9.24 x 10^{-4} km^{-1} sr^{-1} (nighttime), which gives a day-night ratio in detection threshold of 1.43 (i.e., 43% greater in daytime than nighttime).

2.7.5 Comparison of radiosonde and GMAO derived temperature

We now compare the temperature profiles obtained from the radiosonde and CALIPSO provided GMAO model data. For this purpose we have selected two days (September 21, 2006 and January 27, 2007) from the six days of AFARS observations used in this

study, where the CALIPSO overpass is within 10 km or less. As described in section 2.2.2, CALIPSO data processing algorithms highly depend on quality of GMAO model data for their calibration. Further CALIPSO data users rely on these temperature profiles to relate and identify cloud phase and cloud type. Thus, such comparisons are essential and required wherever possible to assess the quality of the modeled data.

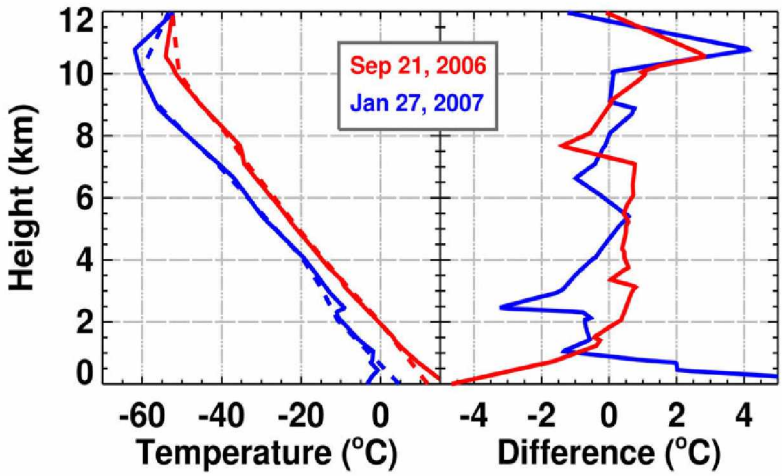

Figure 2.34: Temperature profiles from radiosonde (solid), GMAO model data (dashed) and the differences between the two data sets for the days, September 21, 2006 and January 27, 2007.

The temperature profiles and the differences observed from the two days of profiles are shown in Figure 2.34. The difference in temperature is high near the surface and tropopause level with an exception of a temperature inversion layer near 2 km altitude. The low level temperature inversions, which occur over Fairbanks about 95% of the time during winter (*Wendler and Nicpcon*, 1975), are clearly underestimated by the model data. For our interest of midlevel cloud altitudes (i.e., above 2 km till the tropopause level), the root mean square difference in the temperature profiles for the two days of data considered here is 1.1° C. The minimum and maximum difference in temperature from radiosonde and model data for the midlevel cloud altitudes are –3.2° C and 4.1° C, respectively. The observed differences here seem to be reasonable and insignificant considering the assumptions and uncertainties in the models for producing meteorological variables. However, studies (https://climatedataguide.ucar.edu/climate-data/atmospheric-reanalysis-overview-comparison-tables, (*Pandey and Kurtakoti*, 2014)) show that model

data agrees reasonably well with the in-situ data at certain locations and could vary with the geographic location, time and the meteorological variable used. Uncertainties in temperature introduce ambiguities in cloud classifications based on temperature. This will be explored more in Chapter 3.

2.8 Summary

The performance of ground-based lidar and satellite-borne lidar has been illustrated using three meteorological conditions (i.e., clear skies, high level cloud, and mid/low level cloud) over the AFARS station in interior Alaska. We present two examples of each condition to yield six case studies. The observed differences in CALIPSO and AFARS measurements are consistent with the spatial and temporal variations of meteorological conditions as evident in the MODIS imagery and the synoptic maps obtained through MERRA reanalysis data sets. The synergy of ground-based lidar and A-Train satellite observations is proven to be very useful in depicting the type of clouds present in Interior Alaska.

Our key findings in this Chapter are as follows:

1. From the case for clear skies over the AFARS station, we confirmed that CALIOP lidar can capture the estimated molecular scattering in the absence of cloud or aerosols.

2. Diffuse aerosol layers have been observed by both AFARS and CALIOP lidars at midlevels of the troposphere. These aerosol layers are consistent with the synoptic flow pattern and HYSPLIT back trajectories indicating the aerosols as 'dust' particles that are being transported from arid regions of Asia.

3. Optically thin cirrus clouds can be observed by both the AFARS and CALIOP lidars. The AFARS operator reported the optically thin cirrus cloud as subvisual cloud..

4. For the case of high level cloud occurrence, we confirmed that the presence of high level optically thick cloud attenuates both the lidar signals after penetrating a few meters in the cloud, such that only true cloud top altitude can be identified from CALIPSO and only true cloud base altitude can be identified from AFARS signals. For such cases, as a consequence the Rayleigh molecular scattering is not observed above (below) the cloud in the AFARS (CALIOP) signal.

5. Unlike traditional observed midlevel clouds, which are optically thick and attenuate the laser pulses, optically thin altocumulus and altostratus have been detected from both AFARS and CALIOP lidars.

6. Comparison of CALIOP backscattering obtained during clear sky conditions from two days of daytime and nighttime measurements showed higher values in daytime.

7. Comparison of temperature profiles for two days obtained from the local radiosonde and CALIPSO provided GMAO model data show RMS differences less than 1^{o} C.

Chapter 3
Clouds of the troposphere as observed by CALIOP lidar

In the previous chapter, we reviewed the capabilities of ground-based and satellite-borne lidars for observing clouds formed in the different levels of the troposphere. We confirmed that lidar measurements are consistent in detecting, identifying, and characterizing cloud types. In this chapter, we provide an overview of all clouds in the troposphere as observed globally by the CALIOP lidar. Here we develop and implement a cloud classification scheme based on logic-based rules derived from traditional knowledge on visual identification and previous studies of the clouds. The goal of this chapter is to identify and understand the properties of optically thin midlevel ice clouds in the context of all tropospheric clouds.

3.1 Data used and methodology

For the present study, we used four-years (12/01/2006 – 11/30/2010) of CALIOP lidar measurements. Among the several CALIPSO level 2 data products, we have used the 5 km-cloud layer product (CAL_LID_L2_05kmCLay-Prov-V3-01), which provides information on all of the clouds detected by the lidar. CALIPSO uses several signal-averaging schemes to identify clouds. The CALIPSO feature detection algorithm uses averaged signals over different resolutions (i.e. 5 km, 20 km and 80 km) to gain enough signal-to-noise ratio to detect even thin cloud and aerosol layers in the atmosphere that are otherwise difficult to detect (*Vaughan et al.*, 2005). All the clouds identified by the algorithm are provided in the 5 km-data product and are flagged as either 5 km, 20 km, or 80 km depending on the horizontal averaging used in identifying those clouds. For our analysis, we have selected only those clouds that are detected at 5 km resolution. These clouds are associated with relatively strongly scattering layers. This selection also allows us to avoid most aerosol layers that could have been misidentified as cloud layers at coarse resolutions.

3.1.1 Cloud classification

As we discussed in Chapter 1, the WMO uses cloud base altitude range to categorize a cloud as either a low, mid or high level cloud. These altitudes vary with geographic location and spans the range ~2 km to 7 km, 8 km and 10 km above the ground level in the polar, midlatitude, and tropical regions, respectively. The algorithm used to classify clouds

in the current study is shown in Figure 3.1. Our algorithm uses both cloud top and cloud base temperatures and altitudes that are reasonable at all latitudinal regions. The CALIOP lidar can identify the clouds and aerosols up to 30 km altitude in the atmosphere. Thus our algorithm initially employs a maximum allowable cloud top height as 1 km above the local tropopause level to avoid the inclusion of stratospheric clouds. Since the location of the tropopause altitude over the polar regions with reanalysis data is often ambiguous, we used an allowable height of 12 km for the regions poleward of 60° N and 60° S. Then we identify the clouds with top altitudes less than 2 km above the ground level as 'Low level clouds (L)'. This choice of limiting cloud top altitudes within 2 km of the surface level separates the low-lying clouds that are often influenced by boundary-layer processes and surface fluxes. The clouds with top altitudes greater than 2 km of the ground level are classified into six distinct types based on the cloud top and base temperatures and optical transparency and attenuation of the lidar signal through the cloud layer.

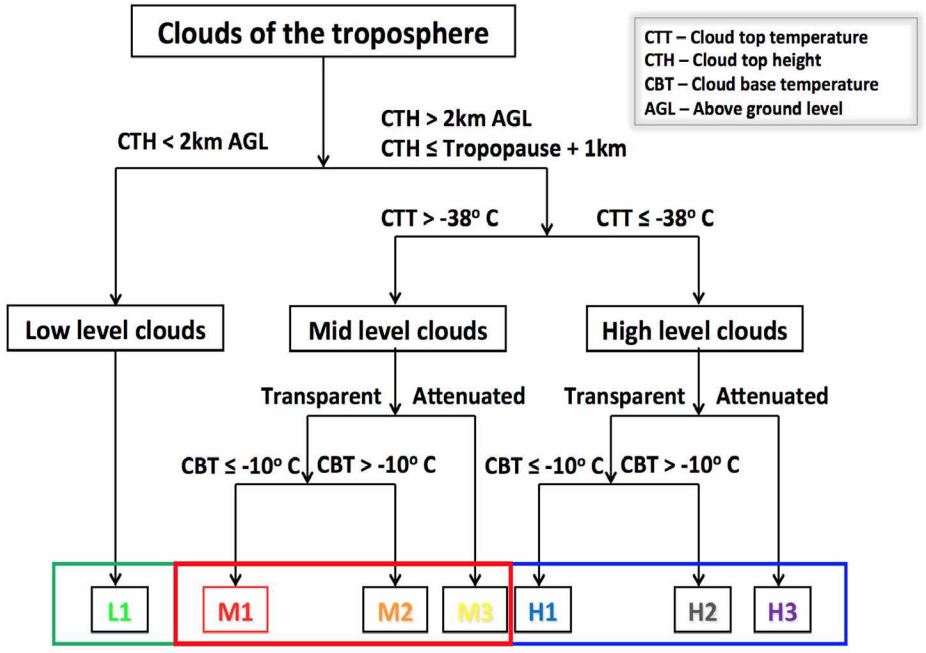

Figure 3.1: Logic-based rules used to categorize tropospheric clouds detected by CALIPSO. Midlevel (M1, M2, M3) clouds are highlighted with a red outline. High level (H1, H2, H3) clouds are highlighted with a blue outline. Low level (L1) clouds are highlighted with a green outline.

We then use a threshold cloud top temperature –38° C to discriminate between the clouds forming in the high level (denoted as H) and midlevel (denoted as M) of the troposphere. The choice of threshold cloud top temperature –38° C comes from the knowledge of the supercooled liquid droplets in the cloud. Studies show that as the cloud temperature reaches below –38° C the supercooled liquid droplets freeze homogeneously to initiate the formation of ice particles (*Sassen and Dodd*, 1988; *Pruppacher and Klett*, 1997; *Rosenfeld and Woodley*, 2000). Thus we classify the clouds with top temperature below –38° C as high level (i.e. cirrus) clouds.

After identifying a cloud as either low level, midlevel or high level, we then impose additional constraints based on optical transparency and cloud base temperature to place the clouds in subcategories. For this purpose we use the transparency flags of the cloud layers provided by the CALIPSO data product. The CALIOP data processing algorithm looks for a defined cloud/aerosol layer or surface returns below the identified cloud layer and flags it as either attenuated or transparent. The transparency criterion serves as a proxy to identify clouds with visible optical depths less than 3 – 4, beyond which the two-way attenuation of the laser pulse return will not exist (*Sassen*, 2002). However depending on the SNR of the signals, the CALIOP data processing algorithm retrieves the optical depth of thin clouds up to an optical depth of 6 (*Vaughan et al.*, 2009). Finally, after considering the cloud top temperature and optical transparency, we look for the cloud base temperature of –10° C to separate ice and water dominated clouds. The maximum cloud base temperature of –10° C is chosen to identify ice and water dominated clouds. Since studies show that clouds have a minimum ice particle concentration of 1 litre^{-1} below the temperature –10° C (*Morris and Braham*, 1968). Upon the initiation of ice particle formation, the available water vapor rapidly deposits to form ice particles. This growth of ice particles occurs because the equilibrium vapor pressure with respect to ice is less than the equilibrium vapor pressure with respect to water at the same subfreezing temperatures. Such a process where the ice crystals compete for the available water vapor and gain mass by depositional growth is referred as *Wegener-Bergeron-Findeisen (WBF)* process (*Wegener*, 1911; *Bergeron*, 1935; *Findeisen*, 1938). We categorize all the tropospheric clouds into seven types using logic-based rules that are based on these meteorological processes and thresholds. We refer to these seven cloud types as L1, M1, M2, M3, H1, H2 and H3 clouds. Table 3.1 shows our categories of tropospheric clouds along with their description. The M1 clouds

are the ice-dominated optically-thin midlevel clouds that are the primary focus of this study.

Table 3.1: Description of cloud types based on our logic-based rules.

Type	Cloud-phase	Description
L1	Water, Mixed-phase, Ice	Cumulus, stratus and stratocumulus types of clouds. All low-lying ice clouds, specifically over the polar regions.
M1	Ice, Mixed-phase	Optically thin altostratus and altocumulus types of clouds those are ice-dominated.
M2	Mixed-phase, Water	Optically thin altostratus and altocumulus types of clouds those are water-dominated.
M3	Mixed-phase, Water	Altostratus, altocumulus and nimbostratus types of clouds that attenuate lidar pulses after few meters of penetration.
H1	Ice	Optically thin cirrus types of clouds.
H2	Mixed-phase/ water, Ice	Optically thin cirrus types of clouds that extends till the lower levels (warm temperatures).
H3	Ice, Mixed-phase	Clouds with ice particles at the top altitudes and dense enough to attenuate the lidar pulses such as cumulonimbus types of clouds.

Examples showing the implementation of our cloud classification scheme on CALIPSO data are provided in Figures 3.2 and 3.3. These examples are drawn from the CALIPSO overpasses over the northern and southern hemisphere and show the occurrence of M1 clouds. The overall, cloud and synoptic meteorological conditions over the region are illustrated using MODIS IR imagery during the time of CALIPSO overpass (Figures 3.2a and Figure 3.3a). Recall, these two orbital overpasses span a horizontal length of 2825 km and 1405 km, respectively and show a varieties of high, mid, and low level clouds. Consider the case of northern hemisphere (Figure 3.2) where the synoptic conditions show a prevailing surface high pressure system. While the midtropospheric circulation (500 mb level) show a weak frontal zone where warm continental air from Eurasia meets the cold air over the western parts of the Arctic Ocean. MODIS imagery confirms the cloudiness along this frontal zone. Clouds along the frontal zone are lighter while the clouds formed over the Southern Alaska due to a low-pressure system over the region appear brighter. This shows that clouds along the frontal zone over the Arctic Ocean are present at lower or midlevels of the troposphere. In contrast to the scenario over the Arctic Ocean (Figure 3.2), M1 clouds are observed within the spiral deck of clouds formed in the low-pressure

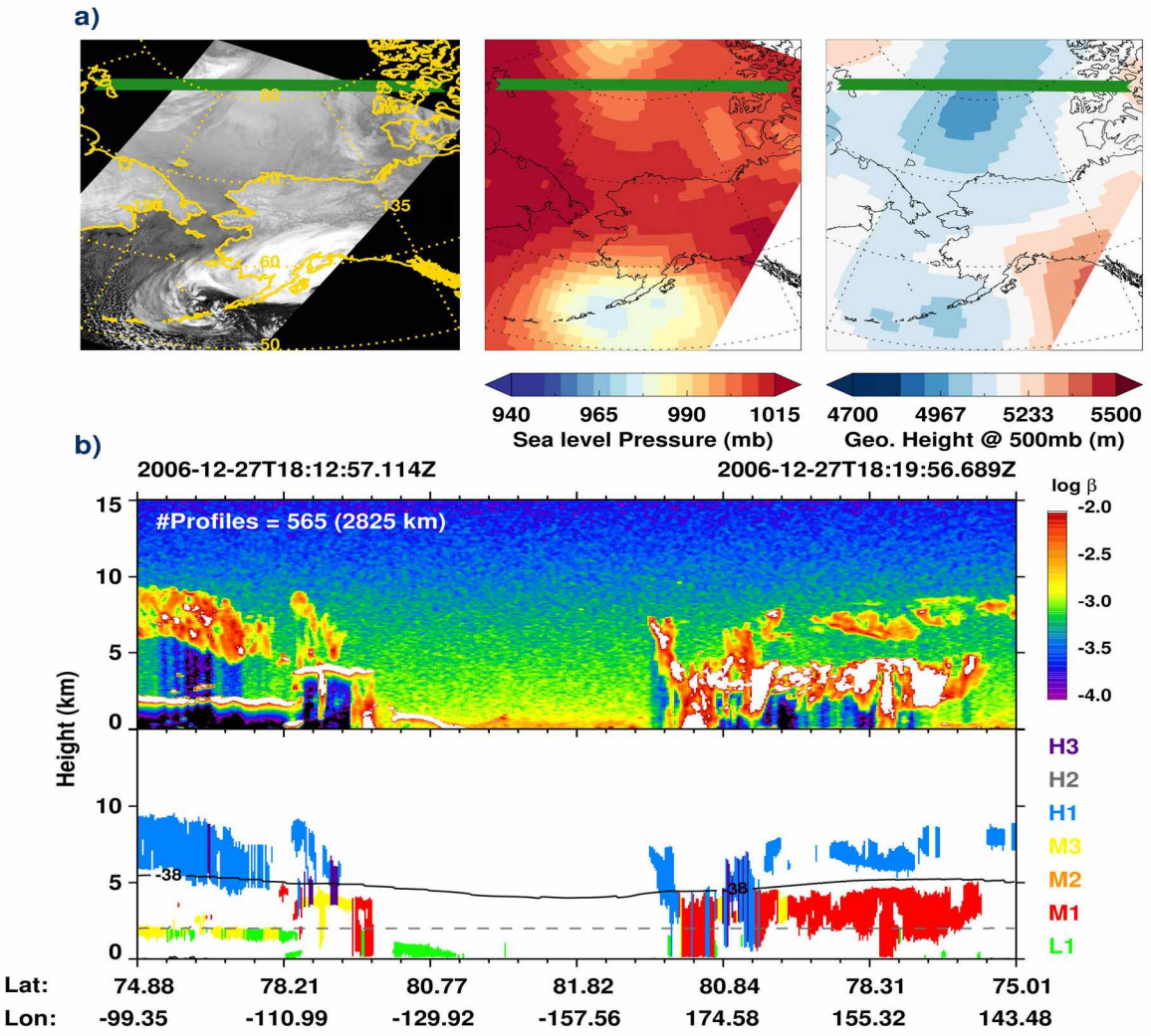

Figure 3.2: (a) MODIS IR imagery and Synoptic meteorological conditions derived from MERRA data, and (b) CALIPSO backscattering (above) and types of clouds (below) derived from our logic-based rules from an overpass (green) over the Arctic region on December 27, 2006. The dotted line indicates the 2 km altitude level above the surface and also shown is the temperature contour.

system over the Southern ocean (Figure 3.3). The rising warm air mass along the ridge pattern is responsible for the clouds at multiple layers. The meteorological conditions that are favorable for the formation of M1 clouds will be explored further in Chapter 4.

The visual inspection of CALIPSO backscattering images (Figure 3.2b and Figure 3.3b) show that our logic-based rules produces contiguous clouds. However, it can be noticed that a cloud type is sensitive to the temperature and optical transparency criteria used.

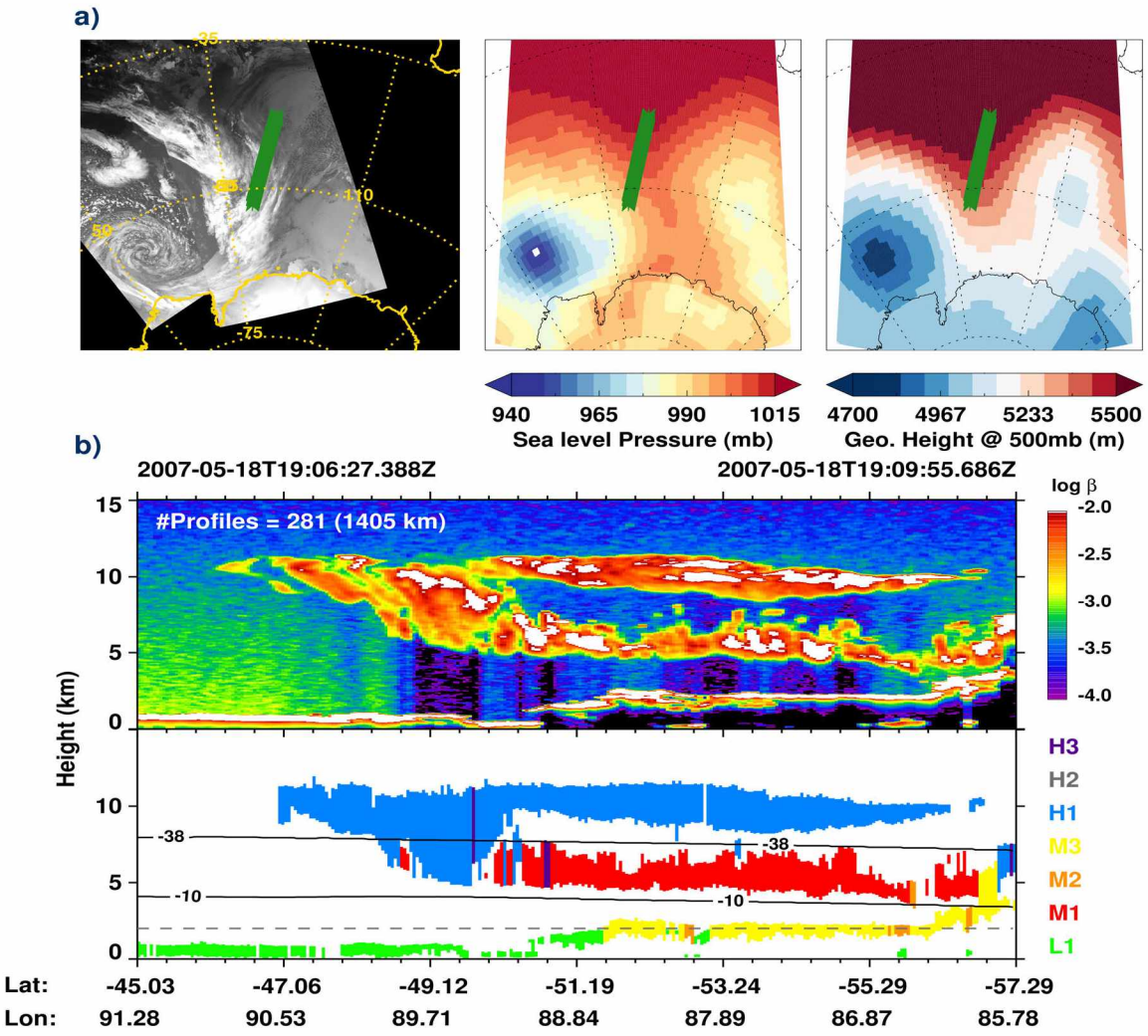

Figure 3.3: (a) MODIS IR imagery and Synoptic meteorological conditions derived from MERRA data, and (b) CALIPSO backscattering (above) and types of clouds (below) derived from our logic-based rules from an overpass (green) over the Southern ocean on May 18, 2007. The dotted line indicates the 2 km altitude level above the surface and also shown is the temperature contour.

For instance (Figure 3.3b), the thinner H1 clouds appear together with thicker H3 clouds. Similarly, embedded in the continuous M1 cloud are a few profiles of either H3, M2 or M3 clouds. The assignment of the specific cloud type depends on the temperature and optical attenuation of the cloud. However, the appearance of a change in cloud type over a single profile may reflect uncertainty in the lidar measurement and associated temperature estimates rather than a physical change in the clouds. To address this, we implement a successive profile method of identifying clouds over contiguous profiles and we conduct

a sensitivity analysis on temperature to see how our cloud type categorization depends on our specific temperature thresholds.

3.1.2 Cloud occurrence using successive profiles

Here we describe the implementation of a successive profile method where cloudy profiles of a type are treated as a single entity or cluster. With the successive profile analysis, we investigate clouds forming at a variety of spatial scales. After classifying clouds into seven types using our logic-based rules. An identified cloud type is counted as a valid cloud, only if the n successive profiles have the same cloud category within the same altitude range. The value of n has been chosen as 2, 5, 10, 20 and 100 that corresponds to 10 km, 25 km, 50 km, 100 km, and 500 km horizontal scales, respectively. Initially cloud statistics will be derived by counting all profiles (i.e. 1-profile, 5 km) that serve as reference of the cloud amounts. Then cloud statistics will be derived for two successive profiles and so on. The increasing number of successive profiles not only provides information on the spatial scales of the cloud but also eliminates the isolated cloudy profiles from the sample.

After counting the total number of valid clouds in each type, frequency of occurrence and fraction of clouds are calculated based on the total observations (profiles) divided by the value of n. The types of clouds obtained from the entire data set are binned into 2.5^{o} x 5^{o} latitude-longitude grids over the global scale. Cloud statistics are derived for an average of four years of binned data. Frequency of occurrence of a cloud type is defined as the number of cloudy profiles to the total number of profiles (clear + cloudy). Whereas, the fraction of clouds for any cloud type is defined as the ratio of the number of clouds identified as that particular type to the total number of clouds. While the frequency of occurrence gives information on the clouds formed with time, the fraction of clouds provides information on the dominant cloud type relative to all the tropospheric clouds.

Figure 3.4 illustrates the successive profile method with examples to derive cloud statistics. Here we consider three clouds of different spatial extents forming in different altitudes. The total number of profiles (observations) shown in this example are 22. Where, 19 are cloudy and the remaining 3 profiles show clear skies. Then the total number of clouds (including multiple layers) is 28 with a contribution of 6, 13 and 9 profiles from cloud-1, cloud-2 and cloud-3, respectively. Consider cloud-3 that was identified in 9 CALIPSO

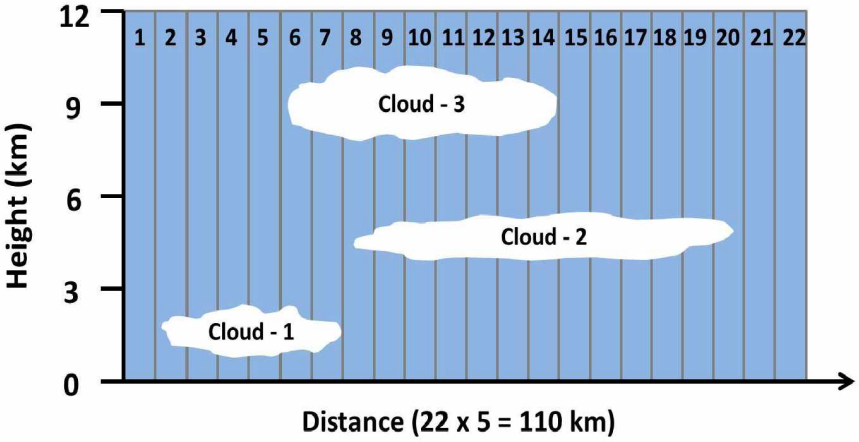

Frequency of occurrence

	1prf	2prf	5prf	10prf	20prf
Total profiles	22	11	4	2	1
Cloud-1 (%)	27	27	25	0	0
Cloud-2 (%)	59	55	50	50	0
Cloud-3 (%)	41	36	25	0	0

Fraction of clouds

	1prf	2prf	5prf	10prf	20prf
Total clouds	28	13	4	1	0
Cloud-1 (%)	21	23	25	0	0
Cloud-2 (%)	46	46	50	100	0
Cloud-3 (%)	32	31	25	0	0

Figure 3.4: Successive profile method used to derive the cloud statistics at different spatial scales.

profiles (9 x 5 km = 45 km). Then the number of valid cloudy profiles for cloud-3 at 1-profile, 2-profile, 5-profile sampling resolutions are 9, 4 and 1, respectively. This shows that while considering 2-profile sampling resolution only 4 clouds will be identified as valid clouds and one cloudy profile (i.e., 9 – 4 x 2 = 1) will be discarded from the statistics. Similarly while considering 5-profile sampling resolution the number of valid clouds will be one and the remaining four cloudy profiles (i.e., 9 – 5 x 1 = 4) will be discarded from the statistics. The calculation of frequency of occurrence and fraction of clouds are also presented in tabular form in the Figure 3.4. The total frequency of occurrence of all three clouds is 127% as multiple clouds appear in a single profile. The frequency of occurrence and fraction of cloud for cloud-3 at 1-profile sampling resolution are derived as 9/22 = 41% and 9/28 = 32%, respectively. Similarly, the frequency of occurrence and fraction of cloud for cloud-3 at 2-profile sampling resolution is 4/11= 36% and 4/13 = 31%, respectively. With this procedure we will determine the cloud statistics (frequency of occurrence and fraction of cloud) as a function of the horizontal extent and continuity of each cloud type.

Then we investigate the geographical distributions, seasonal variations and variation with

the altitude for our seven cloud types. Our analysis also highlights the diurnal variation (i.e. for satellite ascending orbits during daytime and descending orbits during nighttime) of all cloud type occurrences.

3.2 CALIPSO observations

3.2.1 Cloud statistics at 1-profile resolution

We first present the results based on 5 km spatial scale or single profile (1-profile) and the latter section discusses the change in cloud statistics based on increasing spatial scales. The frequency of occurrence and the percentage fraction of clouds for each category from the four years (12/01/2006 – 11/30/2010) of CALIPSO observations at 1-profile resolution are given in Table 3.2.

Table 3.2: Cloud statistics derived from four years (12/01/2006 - 11/30/2010) of CALIPSO observations at 1-profile resolution.

Type	Number of clouds	Frequency of occurrence (%)	Fraction of clouds (%)
H1	29,765,490	19.9	25.8
H2	123,208	<0.1	<0.1
H3	12,036,411	8.1	10.4
M1	10,630,100	7.1	9.2
M2	6,766,417	4.5	5.9
M3	23,820,078	15.9	20.6
L1	32,274,809	21.6	28.0
Total profiles = 149,479,672			
Total profiles with no clouds (clear sky) = 46,000,214			
Total number of valid clouds = 115,416,513			

Over the four years of data considered, the total number of profiles at the 5 km scale (1-profile) was 149,479,672. Of these, 31% of the profiles are in clear skies, which indicates on average that 69% of the Earth's surface is covered by clouds. The total number of cloudy profiles at 5 km resolution is 115,416,513. Among these clouds 36% of clouds are categorized as high level clouds (H1+H2+H3), while 36% are midlevel (M1+M2+M3), and 28% are low level (L1) clouds. The percentage of low level clouds represents a lower bound estimate. The presence of optically thick clouds in the higher levels of the troposphere can obscure the low level clouds by attenuating the lidar signal and thus preventing the detection of the low level clouds.

The global mean frequency of occurrence for the H1 clouds (i.e, traditional cirrus) is found to be 19.9% contributing to a mean fraction of 25.8% of all tropospheric clouds. Cirrus clouds mostly occur at a maximum temperature of -10^{o} C and therefore, there are only few cloud profiles categorized as H2 clouds. The global mean frequency of H2 clouds is <0.1% with a contribution of <0.1% to the total tropospheric cloud population. For the H3 attenuated ice clouds, the global mean occurrences are found to be 8.1% with a mean fraction of 10.4% of clouds. The optically thin H1 and H2 clouds form 26% of all tropospheric clouds, while the thicker H3 clouds form 10% of all tropospheric clouds.The global mean occurrence of M1 optically thin midlevel ice clouds are found to be 7.1% and these clouds represent 9.2% of all tropospheric clouds. The global mean occurrence of M2 optically thin midlevel water clouds is 4.5% and these clouds represent 5.9% of all tropospheric clouds. This observation shows that both ice- and water-dominated optically thin midlevel clouds exist which is consistent with earlier studies (*Wyser et al.*, 2008; *Sassen and Wang*, 2012; *Kayetha*, 2014). It is interesting to note that these least studied optically thin midlevel clouds contribute up to 15.1% of the total clouds. The other type of midlevel clouds are those that are are optically thick. These M3 clouds occur 15.9% of the time and represent 20.6% of the total clouds.

We further derived the cloud properties in terms of cloud top and base altitudes, temperatures, and the optical depth of the cloud as provided by the CALIPSO data product. This is done to provide the overall range of cloud properties as well as to ensure that cloud properties conform to our constraints imposed by the logic-based rules. Table 3.3 shows the global cloud properties for our seven cloud types derived from the four years of the data set used. The cloud top and bottom heights represent heights above mean sea level or altitude. Thus L1 clouds which lie below 2 km above ground level, are found up to 8.7 km above mean sea level, though on average they are found less than 1.5 km above the mean sea level.

For optically thin clouds (M1, M2, H1 and H2) the maximum optical depth of the clouds is 6. For optically thick clouds (H3, M3 and L1) the maximum optical depth of clouds is 10. It is interesting to note that five of the cloud types (i.e., L1, M1, M2, H1 and H2) have median optical depths less than 3, and these clouds represent 68.9% of all clouds in the troposphere. This indicates the prevalence of optically thin clouds at either high, mid and low levels of the troposphere. Additionally, the median optical depth of clouds is <1 for

Table 3.3: Cloud properties derived from 12/01/2006 – 11/30/2010 CALIPSO observations.

		Min.	Max.	Mean	Median	Std. dev.
	Cloud Top Height (km)	0.1	8.7	1.4	1.4	0.8
	Cloud Top Temperature (°C)	-69.0	44.6	-2.6	-1.8	14.0
L1	Cloud Base Height (km)	0.1	8.0	0.8	0.6	0.7
	Cloud Base Temperature (°C)	-67.6	47.0	-0.6	0.2	14.2
	Cloud Optical Depth	<0.1	8.4	2.3	2.6	1.4
	Cloud Top Height (km)	2.0	12.0	6.0	5.6	2.0
	Cloud Top Temperature (°C)	-38.0	-10.0	-27.4	-28.0	6.8
M1	Cloud Base Height (km)	0.1	11.3	4.7	4.5	2.3
	Cloud Base Temperature (°C)	-37.0	-10.0	-20.6	-20.5	6.0
	Cloud Optical Depth	<0.1	6.0	0.8	0.4	1.0
	Cloud Top Height (km)	2.0	11.7	4.5	4.5	1.6
	Cloud Top Temperature (°C)	-38.0	27.7	-5.8	-5.8	9.7
M2	Cloud Base Height (km)	0.1	7.8	3.5	3.6	1.6
	Cloud Base Temperature (°C)	-10.0	46.5	-0.4	-1.6	7.2
	Cloud Optical Depth	<0.1	6.0	1.2	0.6	1.3
	Cloud Top Height (km)	2.0	12.0	4.5	4.0	2.0
	Cloud Top Temperature (°C)	-38.0	26.0	-13.0	-13.7	13.0
M3	Cloud Base Height (km)	0.1	11.0	3.3	3.0	1.8
	Cloud Base Temperature (°C)	-31.0	40.0	-6.5	-7.5	11.4
	Cloud Optical Depth	6.0	9.0	7.7	7.8	1.2
	Cloud Top Height (km)	2.0	18.5	11.0	10.6	3.2
	Cloud Top Temperature (°C)	-87.5	-38.0	-58.0	-56.7	11.7
H1	Cloud Base Height (km)	0.1	17.0	8.5	8.3	3.2
	Cloud Base Temperature (°C)	-85.0	-10.0	-42.0	-40.0	13.0
	Cloud Optical Depth	<0.1	6.0	0.5	0.3	0.6
	Cloud Top Height (km)	3.5	17.8	9.0	9.0	2.3
	Cloud Top Temperature (°C)	-85.0	-38.0	-48.7	-47.0	8.3
H2	Cloud Base Height (km)	0.1	8.0	3.0	3.0	2.0
	Cloud Base Temperature (°C)	-10.0	24.0	-7.0	-7.7	3.0
	Cloud Optical Depth	<0.1	6.0	2.0	2.0	1.2
	Cloud Top Height (km)	2.0	19.0	11.0	11.0	3.0
	Cloud Top Temperature (°C)	-90.0	-38.0	-57.0	-56.0	11.0
H3	Cloud Base Height (km)	0.1	17.6	7.6	7.6	3.0
	Cloud Base Temperature (°C)	-85.0	16.0	-33.0	-33.0	12.4
	Cloud Optical Depth	6.0	10.4	8.7	8.5	1.0

M1, M2, and H1 clouds. This shows that optically thin clouds form in the midlevels of the troposphere with similar optical depths to cirrus clouds.

For L1 clouds, the minimum cloud temperature is –69° C. This is because ice clouds can

form in the lower polar troposphere in winter. The maximum cloud top height of L1 clouds is 8.7 km. As we noted earlier, this is due to the low-lying clouds formed over the mountainous terrain, which can be confirmed from the low values of the mean and median altitudes. The observation of the cloud top altitudes and temperatures for our seven cloud types seems to follow the local tropopause level.

For M1 clouds the mean of cloud top and base height are 6.0 km and 4.7 km, respectively. The mean cloud top and base height of M2 clouds are 4.5 km and 3.5 km, respectively. This observation owes to the fact that M1 clouds are ice-dominated and found at higher altitudes than water-dominated M2 clouds. Recall, for optically thick clouds the true cloud base can not be identified and the value reported here is apparent cloud base, the mean cloud top and base height of M3 clouds are 4.5 km and 3.3 km, respectively. In view of the lidar probing from the top of the atmosphere, this suggests that the presence of M3 cloud does not obscure the M1 clouds, but may obscure the lower-lying L1 clouds. For H3 clouds, the mean top and base altitude is 11.0 km and 7.6 km, respectively. Similarly the presence of H3 clouds at altitudes of 7.6 km and 11.0 km could obscure L1, M1, M2 and M3 clouds. Considering the presence of optically thick clouds (H3 and M3), it can be estimated that M1 and L1 clouds could be two times greater than the cloud amounts observed here.

However, different cloud types are formed in association with varying meteorological conditions and they also vary widely with the geographical location. Thus the geographic distribution of clouds will provide more information on the cloud amounts that are underestimated due to the presence of optically thick clouds at higher levels of the troposphere.

The global distribution of fraction of clouds and frequency of occurrences derived at 1-profile resolution (5 km spatial scale) are shown in Figures 3.5 and 3.6. H1 and L1 clouds are dominantly present over the tropical regions. However, while H1 clouds are mostly concentrated along the convergence zone especially over the Indian ocean, L1 clouds are observed along the oceanic regions where air masses descend (subsidence regions) as a part of the general circulation of the atmosphere. Over the tropical regions H1 clouds are found to occur more than 40% of the time, while over the midlatitude storm tracks and in the polar regions they occur with lower frequency (~25%). The geographical distribution of H3 cloud occurrences are similar to the H1 clouds but occur less frequently. The H3 cloud occurrences are dominant over the tropical regions for about 20% of the observation

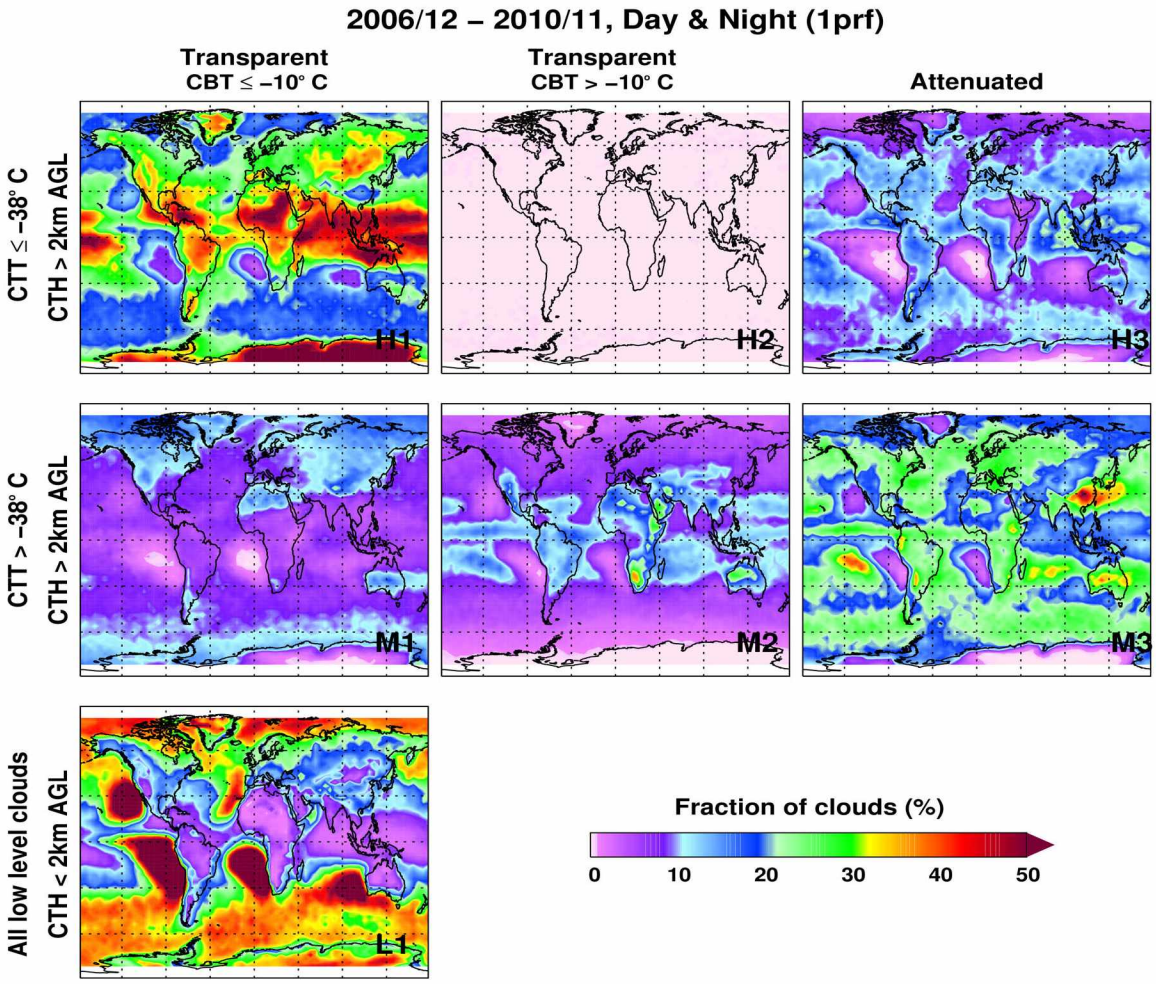

Figure 3.5: Fraction of clouds derived from CALIPSO data (Day and night) at 1-profile resolution.

period, while their occurrences vary from 10 – 15% along the midlatitude storm tracks. M1 clouds are found to have maximum occurrences up to 15% in the polar regions. M1 clouds occur less frequently along the midlatitude storm tracks and in tropical regions. M1 clouds occur more frequently over the Tibetan plateau, indicating orography could play a role in M1 cloud formation. The global distribution of M2 clouds is found to have maximum occurrences of up to 30% over the tropical region and are found less frequently over the midlatitudes. While M1 clouds occur mostly over the polar regions extending into the midlatitude regions, M2 clouds have concentrated occurrences over the tropical regions. This seems to be reasonable and owes to the maximum cloud base temperature of –10° C used to discriminate M1 and M2 clouds. M3 clouds occur 20% of the time over the

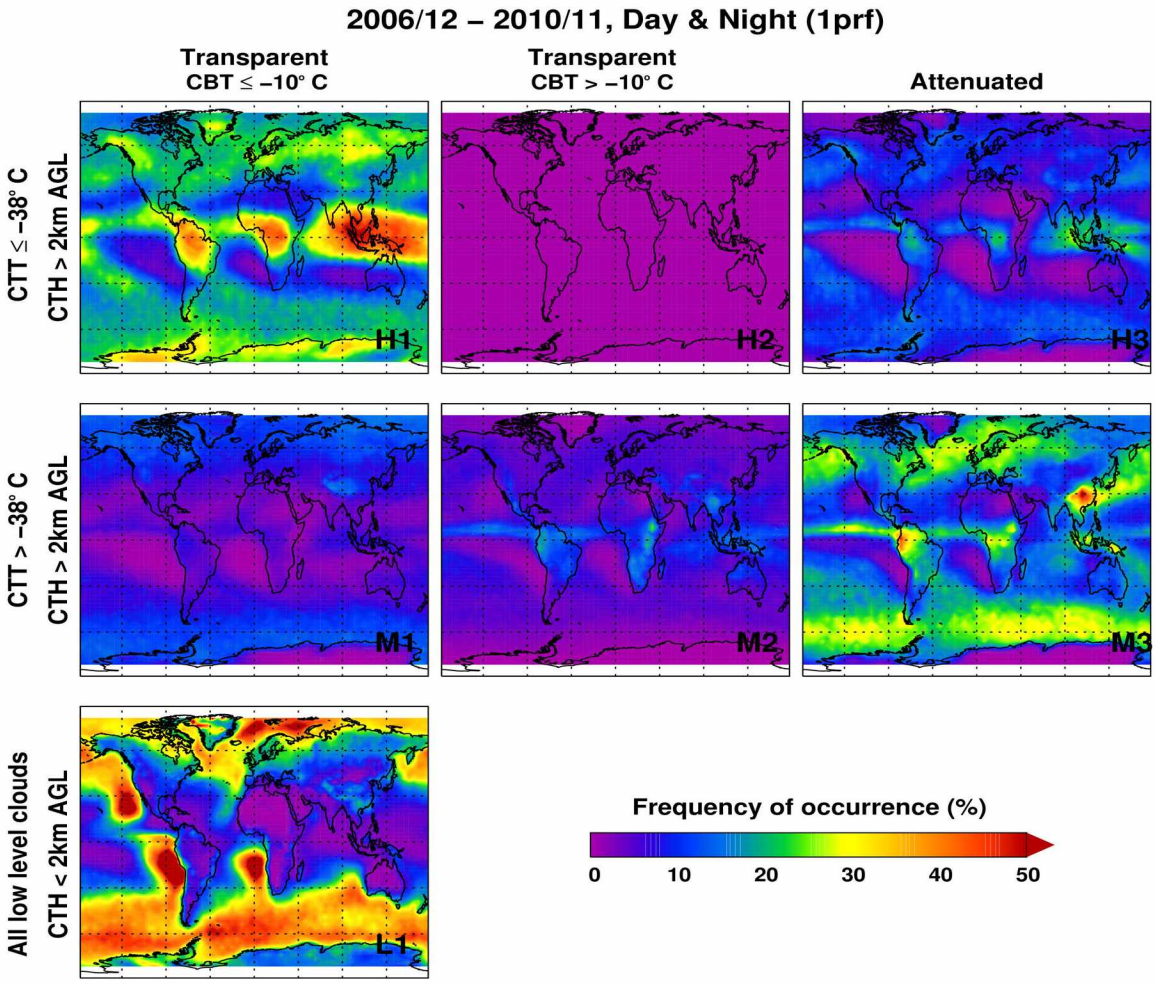

Figure 3.6: Frequency of cloud occurrences derived from CALIPSO data (Day and night) at 1-profile resolution.

midlatitudes extending into the polar regions. M3 clouds have an frequency of occurrence of up to 40% over the northern South America and eastern parts of China. Unlike M1 and M2 clouds, M3 clouds occur over both land and oceanic regions, where high occurrences of up to 25 – 30% are found over the Southern, Pacific, and Atlantic Oceans. In the lower levels of the troposphere (i.e. below 2 km of the surface level) clouds are dominantly observed over the oceanic regions. L1 cloud occur more frequently over oceans (35%) than land (10%). Recall, L1 clouds are obscured by H3 and M3 clouds. These are base reference observations that have been derived at 1-profile resolution, i.e. all the cloudy profiles in the data set are treated as valid clouds. Now we will investigate the sensitivity of the threshold temperatures used and the day versus night differences in these cloud occurrences.

3.2.2 Sensitivity of cloud types to temperature

In Chapter 2, we provided a comparison of temperature derived from local radiosonde measurement and GMAO model data. The differences in temperature derived from these data sets are up to 2° C in the troposphere. Thus we introduce a 2° C jitter in the temperature criteria used for in our cloud classification scheme. This procedure results in nine scenarios by changing the cloud top/base temperatures as shown in Table 3.4.

Table 3.4: Scenarios considered after introducing 2° C change of temperature in the cloud classification scheme.

Scenario	**0**	**1**	**2**	**3**	**4**	**5**	**6**	**7**	**8**
CTT (°C)	-38	-40	-36	-38	-40	-36	-38	-40	-36
CBT (°C)	-10	-10	-10	-12	-12	-12	-8	-8	-8

The scenario-0 is the default cloud top or base temperature used in the current work. Consider the scenario-1, where the threshold cloud top temperature used to categorize high and midlevel clouds is –40° C. Then the clouds which have been categorized as high level clouds in the scenario-0 will now be placed as midlevel clouds and so on. This sensitivity test is performed to determine how cloud statistics might change with threshold temperatures. The complete results of temperature sensitivity are presented in Table 3.5. Since the cloud type L1 is based on the cloud top height criteria above the ground level, L1 cloud amounts do not change. For the remaining cloud types, with change in temperature the cloud amounts show little changes. These changes are expected owing to the cloud top and base temperatures used in our classification scheme. Overall the change in cloud statistics for all scenarios is <1%. The results for M1 cloud are shown in Figure 3.7. Therefore we

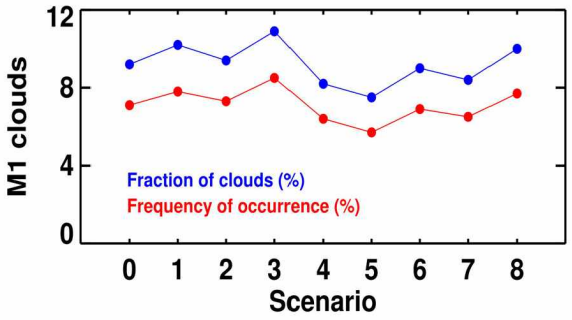

Figure 3.7: Temperature sensitivity for M1 cloud statistics.

Table 3.5: Cloud statistics derived for all the scenarios considered.

Cloud Type	Scenario	0	1	2	3	4	5	6	7	8
L1	Frequency of occurrence (%)	22	22	22	22	22	22	22	22	22
	Fraction of clouds (%)	28	28	28	28	28	28	28	28	28
M1	Frequency of occurrence (%)	7	8	7	8	7	6	7	7	8
	Fraction of clouds (%)	9	10	9	11	8	8	9	8	10
M2	Frequency of occurrence (%)	5	5	5	4	5	5	4	5	4
	Fraction of clouds (%)	6	6	7	5	6	7	5	7	5
M3	Frequency of occurrence (%)	16	16	16	16	16	16	16	16	16
	Fraction of clouds (%)	21	21	21	21	20	20	20	21	21
H1	Frequency of occurrence	20	19	19	19	21	21	21	20	20
	Fraction of clouds (%)	26	25	25	25	26	26	27	26	26
H2	Frequency of occurrence (%)	<0.1	<0.1	<0.1	<0.1	<0.1	<0.1	<0.1	<0.1	<0.1
	Fraction of clouds (%)	<0.1	<0.1	<0.1	<0.1	<0.1	<0.1	<0.1	<0.1	<0.1
H3	Frequency of occurrence (%)	8	8	8	8	8	8	8	8	8
	Fraction of clouds (%)	10	10	10	10	11	11	11	10	10

see that the change of 2^o C temperature does not have any significant effect on the cloud statistics derived and we conclude that the cloud classification based on temperatures is robust.

3.2.3 Day-night difference in cloud occurrences

The observations presented so far are from the combined (daytime and nighttime) observations of the CALIOP lidar. We now present the differences in the cloud occurrences during the daytime and nighttime observations. Table 3.6 provides the global mean frequency of occurrences for all cloud categories and the (night-day) differences at 1-profile

resolution. The day-night differences in frequency of occurrences for H1 clouds are high, up to 6.2%. This is expected and owes to the lower SNR in the daytime observations than in nighttime. For the remaining clouds the differences in frequency of occurrences are low and insignificant at global scales.

Table 3.6: Global mean frequency of occurrences of clouds derived from day and night observations at 1-profile resolution.

	Frequency of occurrence (%)			
Type	**Day & Night**	**Day**	**Night**	**Night-Day**
H1	19.9	17	23.2	6.2
H2	<0.1	<0.1	0.14	0.11
H3	8.1	8.0	8.1	0.1
M1	7.1	7.6	6.6	-1.0
M2	4.5	4.2	4.8	0.6
M3	15.9	16.4	15.3	–1.1
L1	21.6	22.6	20.4	–2.2

We further examine the day-night differences in cloud occurrences over the geographical distribution rather than the global average values. The day-night differences in frequency of cloud occurrences over the global distribution at 1-profile resolution is shown in Figure 3.8. H1 cloud occurrences show pronounced day-night differences in the tropical region (up to 25% during daytime and 40% during nighttime). H1 clouds occur more often during nighttime than in daytime over the midlatitude storm tracks and in the polar regions, especially over Greenland, Antarctica, and eastern Eurasia. Regionally, the H3 cloud occurrences do not show any pronounced day-night differences except for the region over the Indian ocean where there is small increase in daytime cloud occurrences (15%-daytime, 12%-nighttime). Optically thin midlevel M1 clouds show a slight increase in daytime cloud occurrences (10%-daytime, 7%-nighttime) over Greenland, Tibet, and the Southern Ocean, while M2 clouds show a small increase in nighttime occurrences (6%-daytime, 10%-nighttime) over the tropics. The optically attenuating midlevel (M3) clouds show an increase in nighttime cloud occurrences (15%-daytime, ~25%-nighttime) particularly over the northern South America and central Africa. For the low-lying (L1) clouds, regional enhancements in daytime cloud occurrences (40%-daytime, 35%-nighttime) are observed particularly over the North Atlantic sector of the Arctic Ocean and over the Southern Ocean. Now we will investigate the day-night differences in cloud occurrences at the 2-profile resolution. Recall, with 2-profile sampling resolution, the cloudy profiles

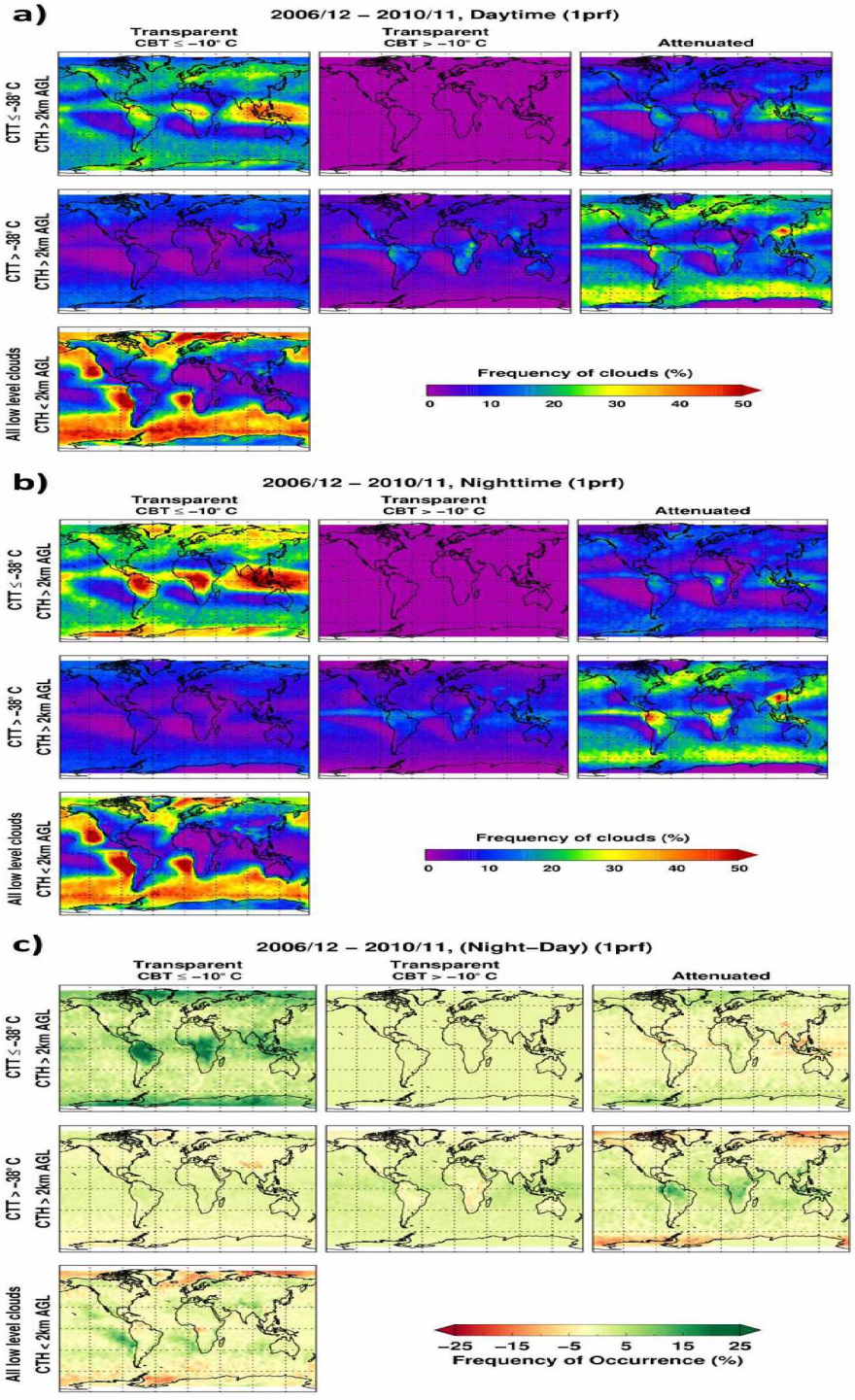

Figure 3.8: Frequency of clouds derived from (a) daytime, (b) nighttime, and (c) nighttime-daytime CALIPSO observations at 1-profile resolution.

are counted as valid clouds only if two successive profiles have similar cloud types. Thus at 2-profile sampling resolution the isolated cloudy profiles due to our logic-based rules or spurious cloud layer detection due to CALIOP cloud detection algorithm should be eliminated and provides more reliable information.

Table 3.7: Global mean frequency of occurrences of clouds derived from day and night observations at 2-profile resolution.

	Frequency of occurrence (%)			
Type	**Day + Night**	**Day**	**Night**	**Night-Day**
H1	16.7	13.6	20.3	6.7
H2	<0.1	<0.1	<0.1	0.0
H3	6.8	6.7	7.1	0.4
M1	4.5	4.3	4.0	-0.3
M2	2.3	2.0	2.6	0.6
M3	13.0	13.4	12.5	-0.9
L1	17.1	18.2	15.9	–2.3

The day-night differences in global mean frequency of cloud occurrences for all cloud categories at the 2-profile resolution are given in Table 3.7. The day-night differences in frequency of occurrences for H1 clouds are still high, up to 6.7%. While for the remaining clouds the differences in frequency of occurrences are found to be quite low or similar to the differences observed at 1-profile resolution.

The day-night differences in global distribution of cloud occurrences at 2-profile resolution are shown in Figure 3.9. At 2-profile resolution, regional differences observed at the 1-profile resolution still exist for H1, M3 and L1 cloud occurrences. The remaining clouds (i.e. H2, H3, M1, and M2) do not show any significant differences in frequency of daytime and nighttime occurrences. Recall the ratio of daytime and nighttime measurement of clear skies with CALIOP is about 1.2 (Chapter 2). It is apparent that the SNR is lower during daytime than nighttime. Consistent with the CALIOP signal characteristic that daytime measurements are contaminated with high solar background noise, the observation of high frequency of occurrence for optically thin H1 clouds during nighttime is in good agreement. Similarly, we expect the same behavior (i.e. high occurrences in nighttime) for at least the other optically thin cloud categories such as M1 and M2, but clearly this is not the case. For the case of optically thick cloud categories (i.e. H3 and M3), regionally high daytime occurrences are observed for H3 clouds while high nighttime occurrences are observed for M3 clouds. Although regional daytime occurrences for few cloud types

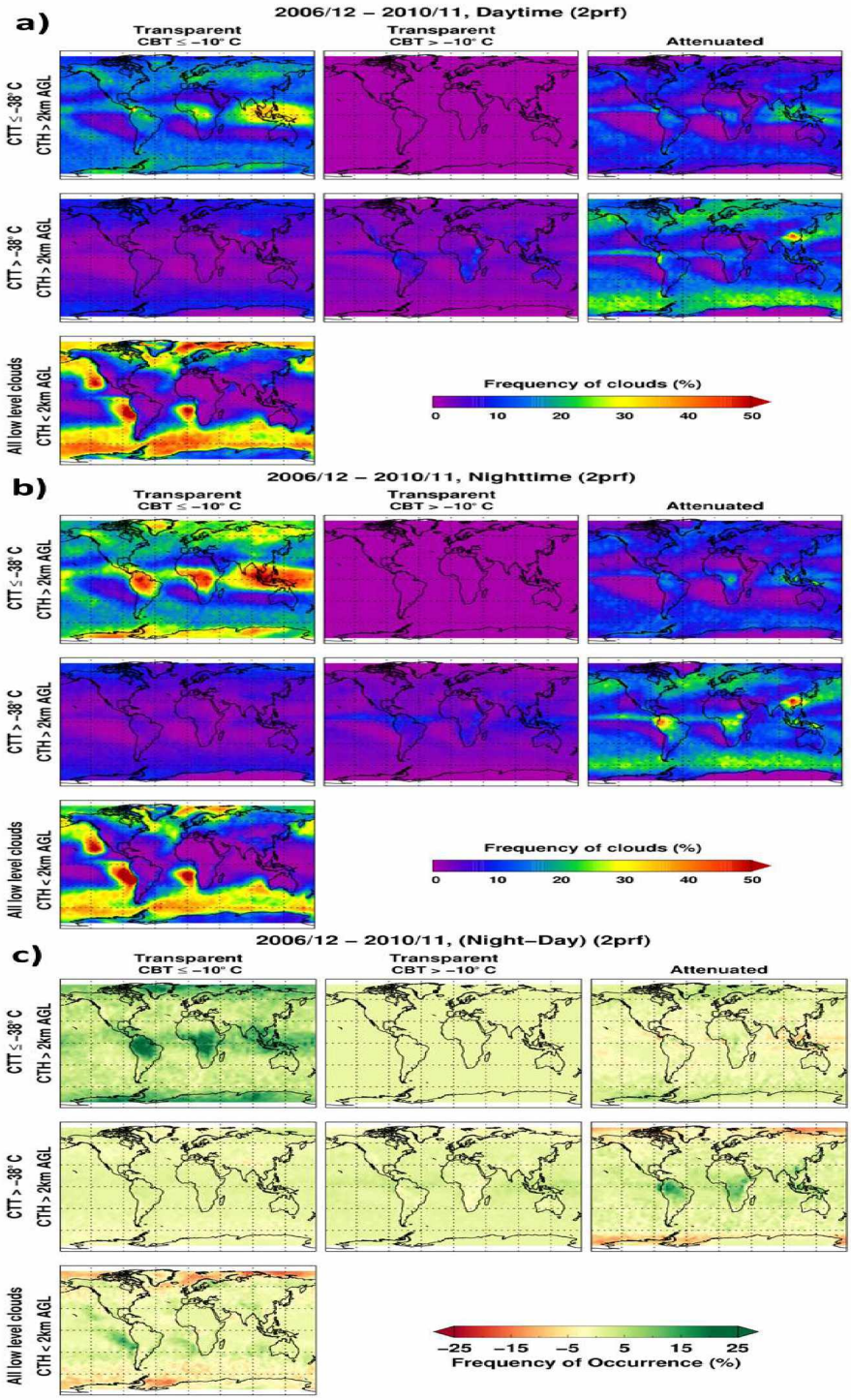

Figure 3.9: Frequency of clouds derived from (a) daytime, (b) nighttime, and (c) nighttime-daytime CALIPSO observations at 2-profile resolution.

are high there is no basis for us to derive a meteorological context merely on these observations that drives the cloudiness. Thus we conclude the that observed day-night differences are high only for H1 clouds (~6%) and are not significant for other clouds. Thus hereafter the results presented will be based on 2-profile resolution or higher.

3.3 Global distribution of clouds

Here, we present results based on 2-profile resolution or a 10 km spatial scale. The frequency of occurrence and the fraction of clouds for each category from the four years (12/01/2006 – 11/30/2010) of CALIPSO observations at 2-profile resolution are provided in Table 3.8. For the four years of data considered, the total number of profiles are divided by two and amounts to 74,739,836 (i.e., at 10 km spatial scale or 2-successive profiles). We have used a total of 45,328,950 valid cloudy profiles to determine the frequency of occurrence and fraction percentage of clouds.

Table 3.8: Cloud statistics derived from four years (12/01/2006 - 11/30/2010) of CALIPSO observations at 2-profile resolution.

Type	**Number of clouds**	**Frequency of clouds (%)**	**Fraction of clouds (%)**
H1	12,520,659	16.7	27.6
H2	27,994	<0.1	<0.1
H3	5,141,715	6.8	11.3
M1	3,371,498	4.5	7.4
M2	1,728,463	2.3	3.8
M3	9,713,249	12.9	21.4
L1	12,825,372	17.1	28.2
Total profiles = 74,739,836			
Total number of valid clouds = 45,328,950			

The global distribution of fraction of cloud types and their frequency of occurrences derived at 2-profile resolution are shown in Figures 3.10 and 3.11. The fraction of clouds clearly shows high amounts of H1 and L1 clouds in the tropics. The low L1 cloud amounts particularly over the Indian ocean and surroundings might be due to the presence of H3 or M3 clouds that prevents the detection of low-lying clouds. The frequency of occurrences show that H1 and L1 clouds are dominantly formed over the tropical regions. However while H1 clouds are mostly concentrated along the convergence zone especially over the Indian ocean, L1 clouds are observed along the oceanic regions where air masses decend

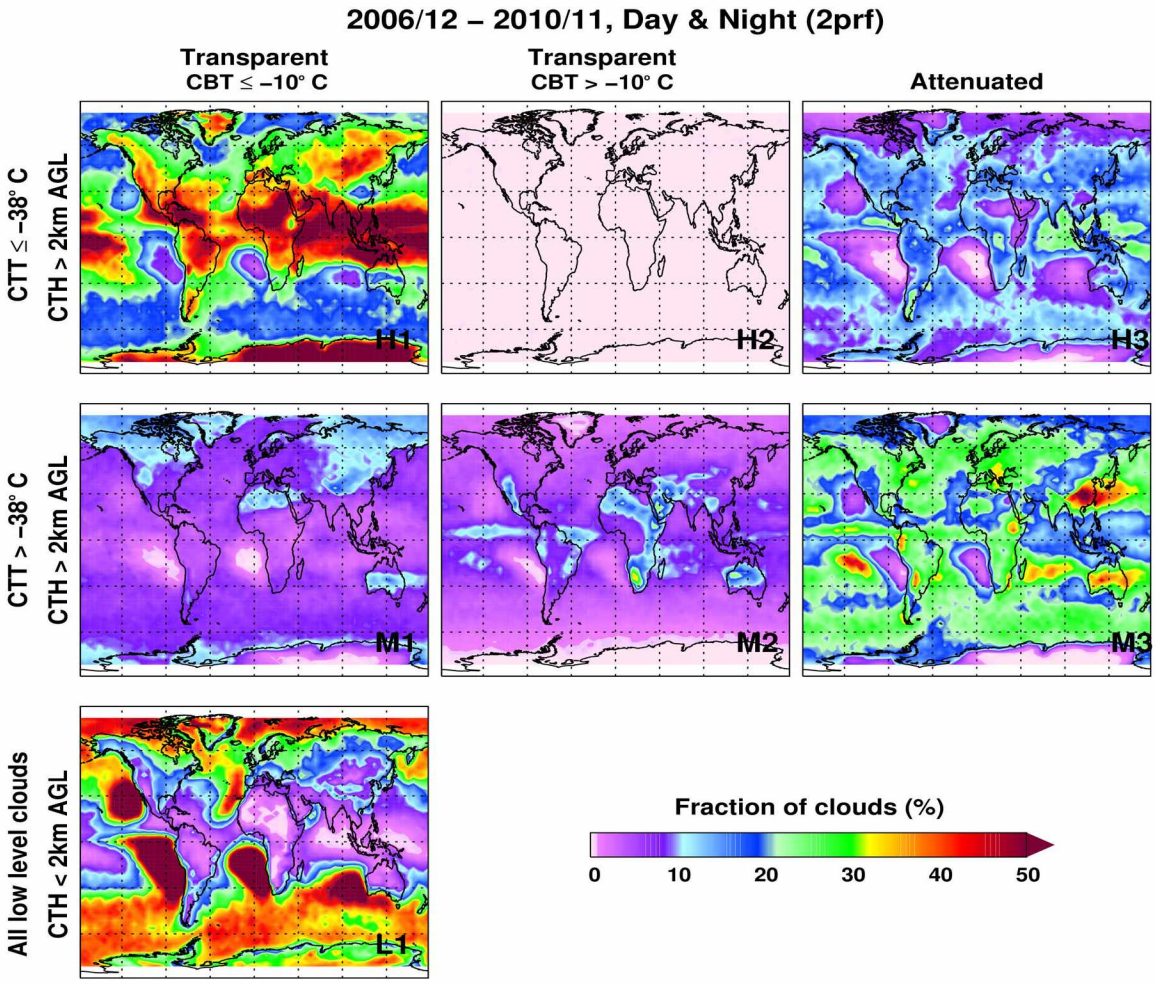

Figure 3.10: Fraction of clouds derived from CALIPSO data (Day and night) at 2-profile resolution.

(subsidence regions) as a part of atmospheric general circulation. Over the tropical regions H1 clouds occur more than 40% of the time, while over the midlatitude storm tracks and in the polar regions they are relatively less abundant (~25%). The geographical distribution of H3 cloud occurrences is found to be similar to that of H1 clouds, but with lower frequencies. The H3 cloud occurrences are dominant over the tropical regions for about 20% of the observation period, while their occurrences vary from 10 – 15% along the midlatitude storm tracks. Optically thin midlevel ice-dominated (M1) clouds occur most commonly (up to 15%) over the polar regions. M1 cloud occurrences along the midlatitude storm tracks and tropical regions are apparent but are relatively lower (5 – 10%). M1 clouds occur more frequently over Tibet (>10%), indicating orography could play a role

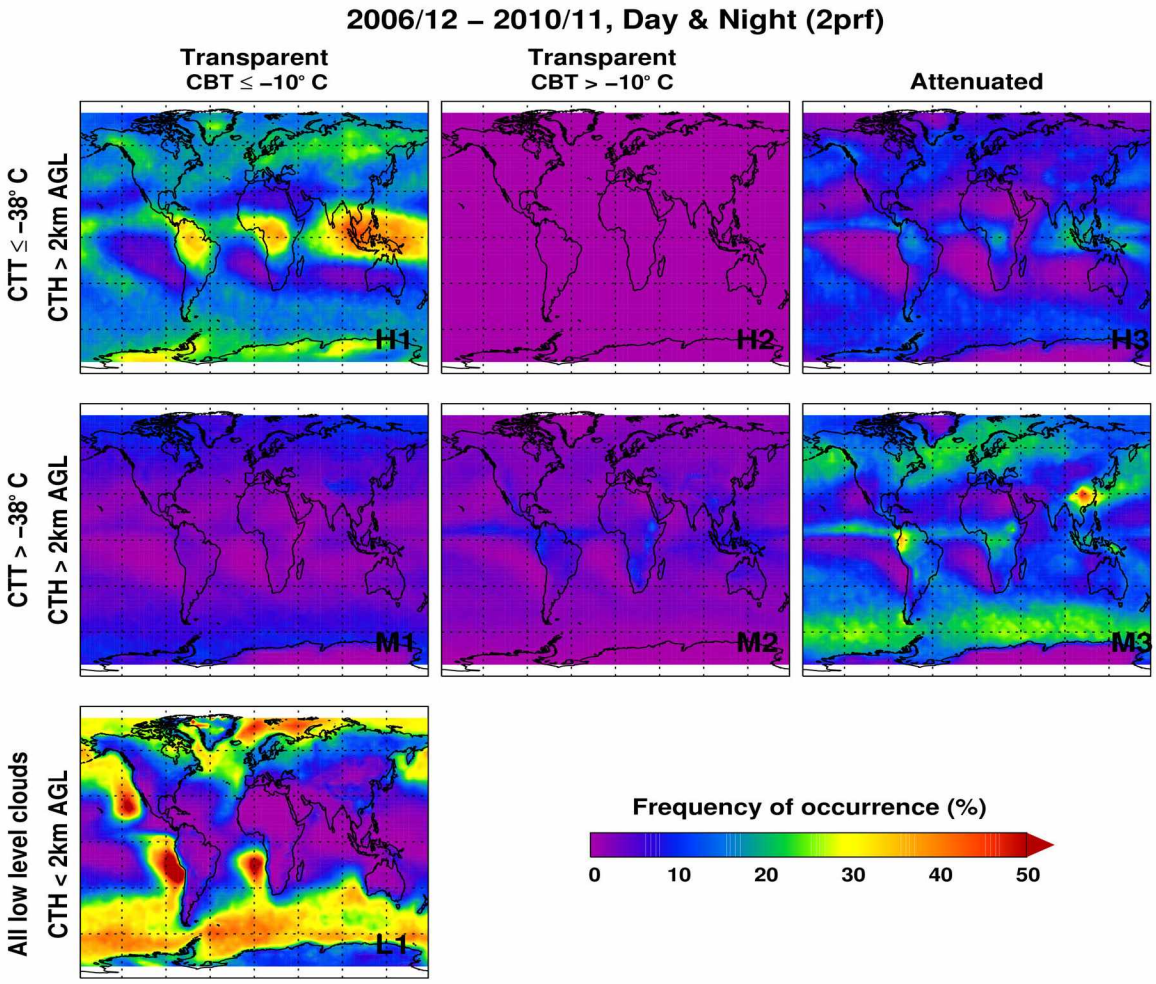

Figure 3.11: Frequency of occurrence of clouds derived from CALIPSO data (Day and night) at 2-profile resolution.

in the M1 cloud formation. Optically thin water-dominated)M2) clouds occur more frequently (15 – 20%) over the tropics and less frequently over the midlatitudes (up to 5%). While M1 clouds occur mostly over the polar regions extending into midlatitudes, M2 clouds occur in patches in the tropics. This observation seems to be reasonable and owes to the maximum cloud base temperature –10° C used in discriminating M1 and M2 clouds. The attenuated midlevel (M3) clouds occur 20% of the time over the midlatitudes extending into the polar regions. M3 clouds occur up to 40% of the time over northern South America and eastern parts of China. Also a noticeable difference in M3 cloud occurrences over land and oceans is noted, where high occurrences of up to 25 – 30% are observed over the Southern, Pacific, and Atlantic Oceans. The low level (L1) clouds of the troposphere

(i.e. below 2 km of the surface level) clouds occur most commonly over the oceans. The L1 cloud occurrences show a striking contrast between land (10%) and ocean (35%).

3.4 Seasonal variation in cloud occurrences

3.4.1 High level clouds

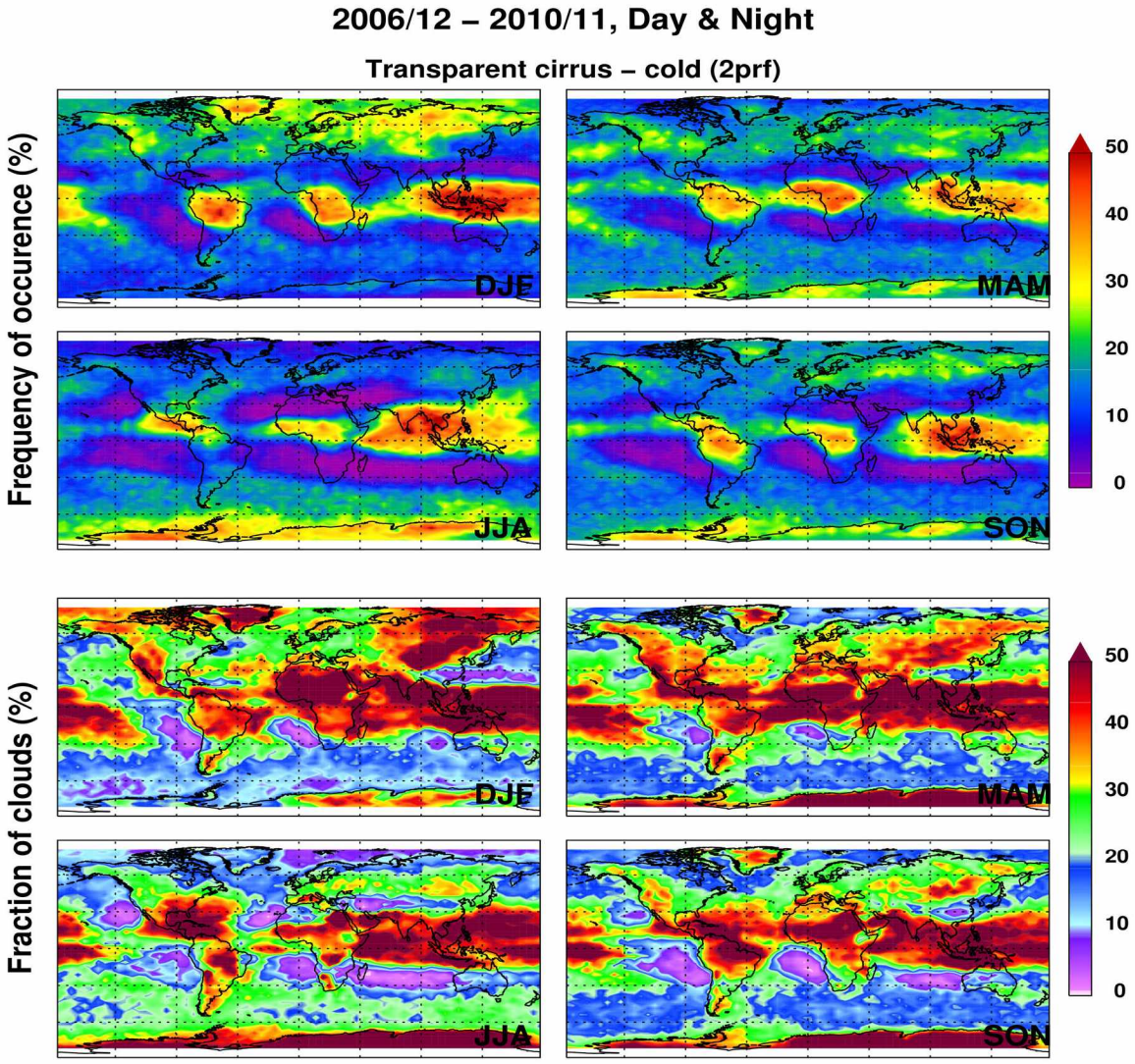

Figure 3.12: Seasonal variation in frequency of occurrence and fraction of clouds for H1 clouds.

The seasonal variation in the geographical distribution of H1 cloud occurrences and fraction of clouds is shown in Figure 3.12. During the months of December-January-February

(DJF), H1 clouds are found more than 40% of the time over the Arctic. During the transitional seasons (March-April-May, MMA and September-October-November, SON), H1 clouds occur less often (15 – 20%) over the polar regions and often more (> 30%) over the northern and southern midlatitudinal regions. During the months of June-July-August (JJA), H1 clouds show high occurrences of up to 40% of the time over the Antarctic region. From this observation it is clear that H1 clouds are found to occur most commonly over the polar regions during the winter seasons (DJF-northern, JJA-southern). These clouds are likely formed in association with the upper-level atmospheric circulation and regional weather patterns. The arid regions such as northern Africa, western China and Australia where subsidence of air masses prevail, H1 clouds have minimum occurrences particularly evident for the months JJA. Over the tropical regions, it is observed that H1 clouds occur dominantly up to 50% of the time along the convergence zone throughout the seasons. Here these clouds are likely formed with the upper-atmospheric humidification induced by strong updrafts associated with deep convection. Also evident is the influence of regional monsoons on the H1 cloud occurrences particularly over the Indian Ocean (*Sassen et al.*, 2009). Orographically formed H1 clouds are observed particularly over Greenland, Tibet, and the Rocky mountains during DJF.

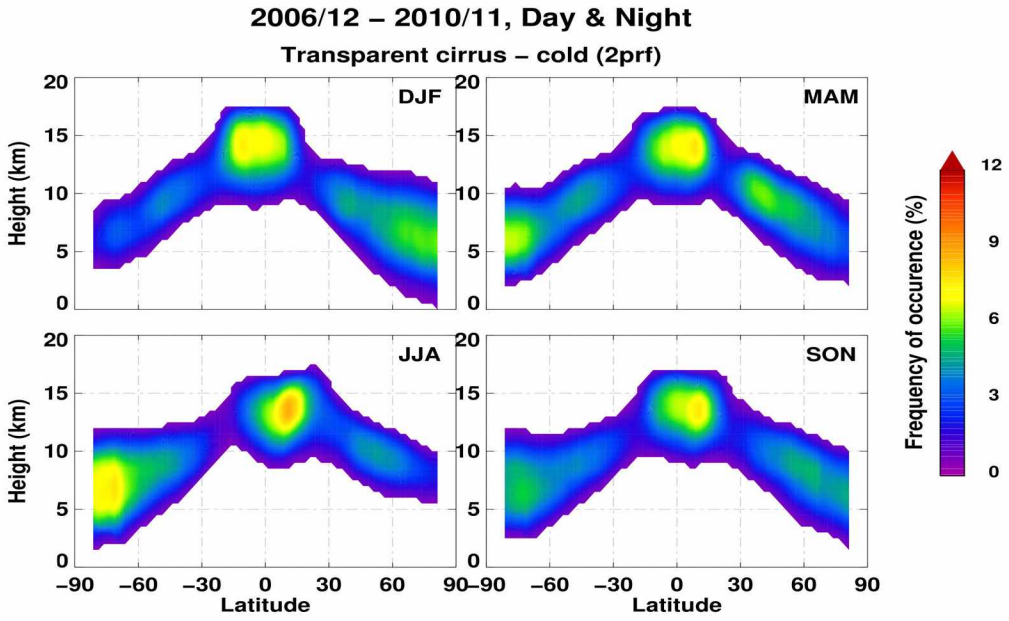

Figure 3.13: Zonally averaged frequency of occurrence of H1 clouds with the altitude.

The zonally averaged frequency of occurrences of H1 clouds with altitude is shown in Figure 3.13. The occurrence of H1 clouds follows the Hadley-cell circulation, where the lowest occurrences corresponds to regions of subsidence throughout the seasons. H1 clouds are found to be associated with the tropopause level over the temperate regions. Over the tropical regions cloud occurrences are found up to 17 km altitude and up to 12 km altitude over the polar regions. Recall that due to the ambiguity in tropopause altitude and temperature with GMAO model data, we used a limit of 12 km altitude for the regions poleward of 60^{o} N and 60^{o} S. However this observation is consistent with the cloud climatologies derived from ground-based lidar measurements over the midlatitudes and sub-arctic regions that show cirrus cloud top altitudes are seasonally independent and only vary with the regional tropopause level (*Sassen and Campbell*, 2001; *Kayetha*, 2014). H1 clouds occur more commonly over Antarctica in the southern winter than over the Arctic in the northern winter. This is due to the fact that Antarctica is significantly colder than the Arctic in winter.

The seasonal variation in the global distribution of H3 cloud occurrences and fraction of clouds is shown in Figure 3.14. H3 clouds also have cloud top temperatures that are cold enough to initiate ice particle formation through homogeneous freezing of particles. These clouds are optically dense enough to attenuate the lidar pulses. H3 cloud fractions contribute up to 20% of the tropospheric clouds over the tropics. Seasonality of the cloud occurrences and percentage fraction of clouds are consistent with the latitudinal migration of convergence zone. The influence of the monsoon systems is clearly evident with increased cloudiness over the Indian Ocean during the summer (JJA). The geographical and seasonal distribution of H3 clouds is similar to H1 clouds but with relatively less cloudiness (up to 20% over the tropics and < 10% over the midlatitudes and polar regions). This shows that H1 clouds are likely formed in association with H3 clouds.

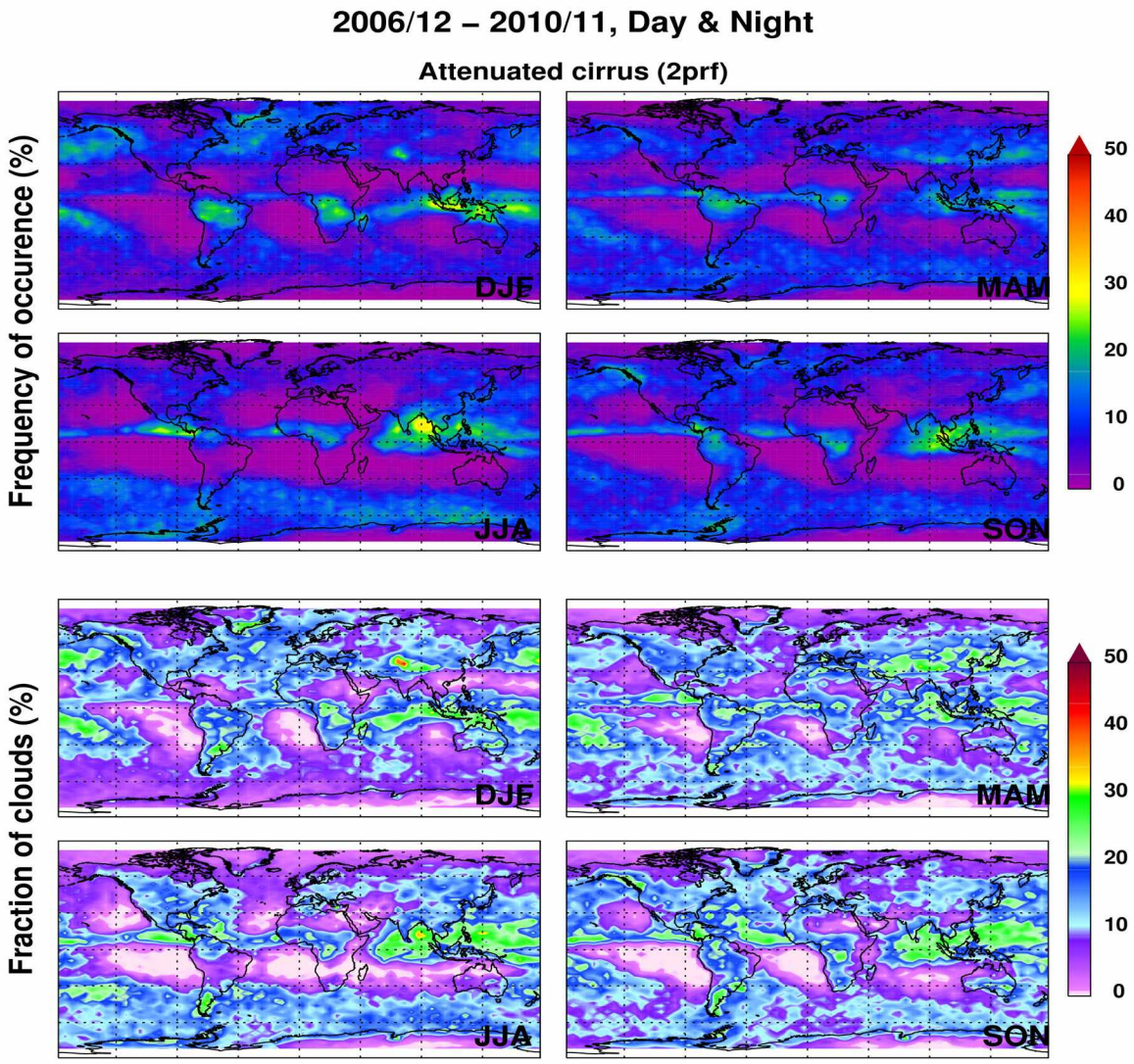

Figure 3.14: Seasonal variation in frequency of occurrence and fraction of clouds for H3 clouds.

3.4.2 Midlevel clouds

The seasonal variations in M1 cloud occurrences and fraction of M1 clouds are shown in Figure 3.15. High amounts of M1 cloud occurrences varying from 10 – 15% were found over polar regions extending into the midlatitudes. M1 cloud occurrences are maximum during the months of DJF and minimum during the months JJA, in both hemispheres with an exception of few high altitude regions such as Greenland and Tibet. Occurrences of M1 clouds along the midlatitude storm tracks are evident throughout the seasons but are quite

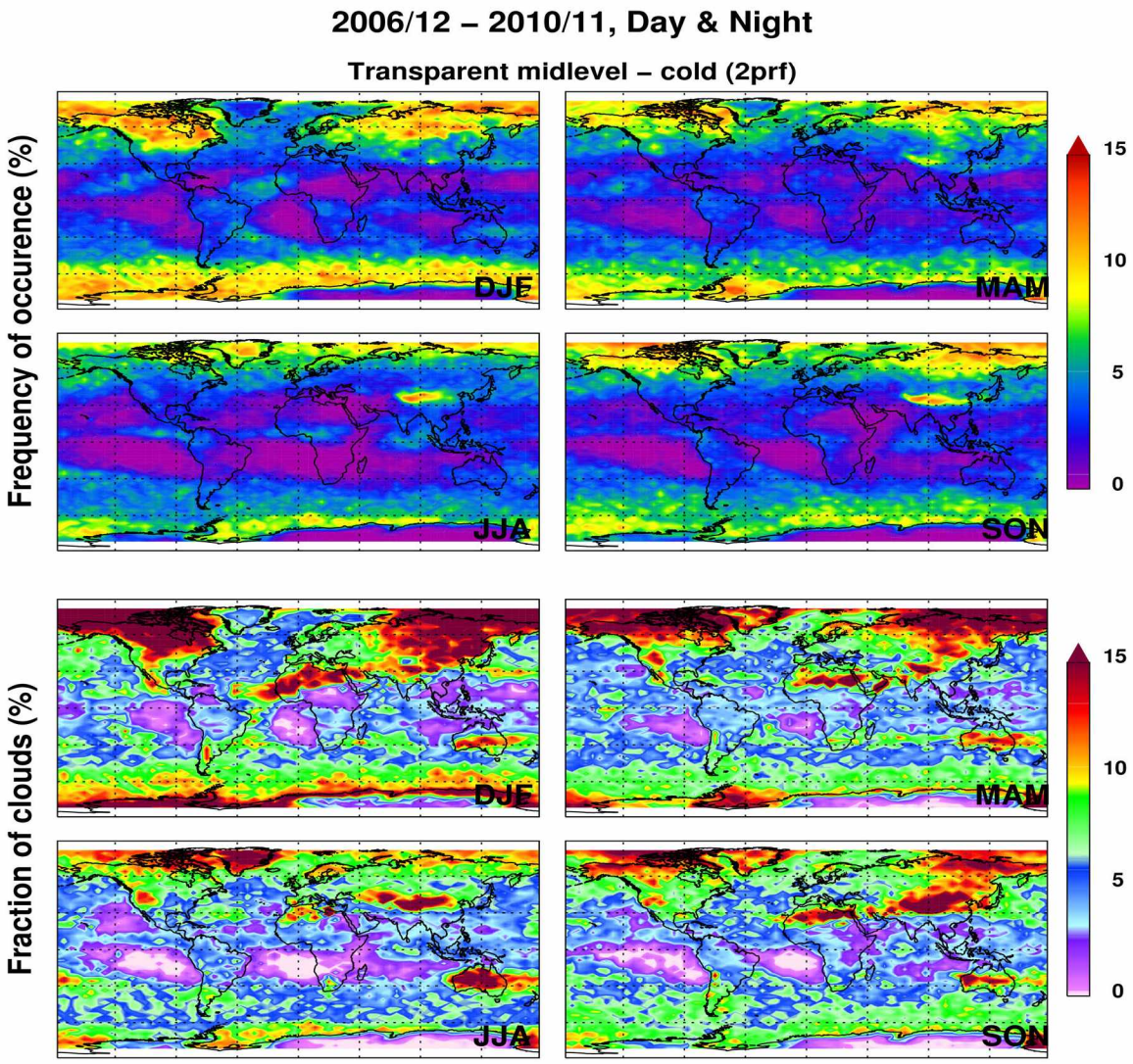

Figure 3.15: Seasonal variation in frequency of occurrence and fraction of clouds for M1 clouds.

low particularly for the months of JJA. Recall our result could be biased low for the regions where optically thick clouds have dominant occurrences that also include prominent storm track regions. No seasonal symmetry in M1 cloud occurrences is observed. M1 clouds occur most commonly over both the Arctic and the Southern Ocean during northern winter (DJF) indicating that M1 clouds form through a variety of processes. Over the tropics, M1 cloud occurrences are found to be minimum (5%) and are concentrated along the convergence zone, resembling the altocumulus cloud distribution (*Sassen and Wang*, 2008). The fraction of clouds clearly shows that M1 clouds are more abundant in the northern than

in the southern hemisphere. This can be related to the availability of ice nuclei for the formation of M1 cloud. Studies (*Sassen*, 2005; *Sassen and Khvorostyanov*, 2008) show that dust particles from the arid regions act as effective ice nuclei and can initiate the formation of ice through heterogeneous nucleation of particles in clouds even at warmer temperatures (–15^{o} C). Specifically the occurrence of high fraction of M1 clouds over arid regions in Africa, China, and Australia supports the assertion that M1 clouds here are likely formed by such a process. Over the northern hemisphere M1 clouds are most common along the western Arctic extending into the midlatitudes and less common in the synoptically active North Pacific and Atlantic Oceans, where cloud droplets easily grow to large sizes and produce precipitation. We will see later that it is consistent with the M3 clouds in this region. Over the southern hemisphere, M1 clouds are found over Southern Ocean surrounding Antarctica. Specifically M1 clouds are limited to western Antarctica leaving the eastern parts almost devoid of these types of clouds.

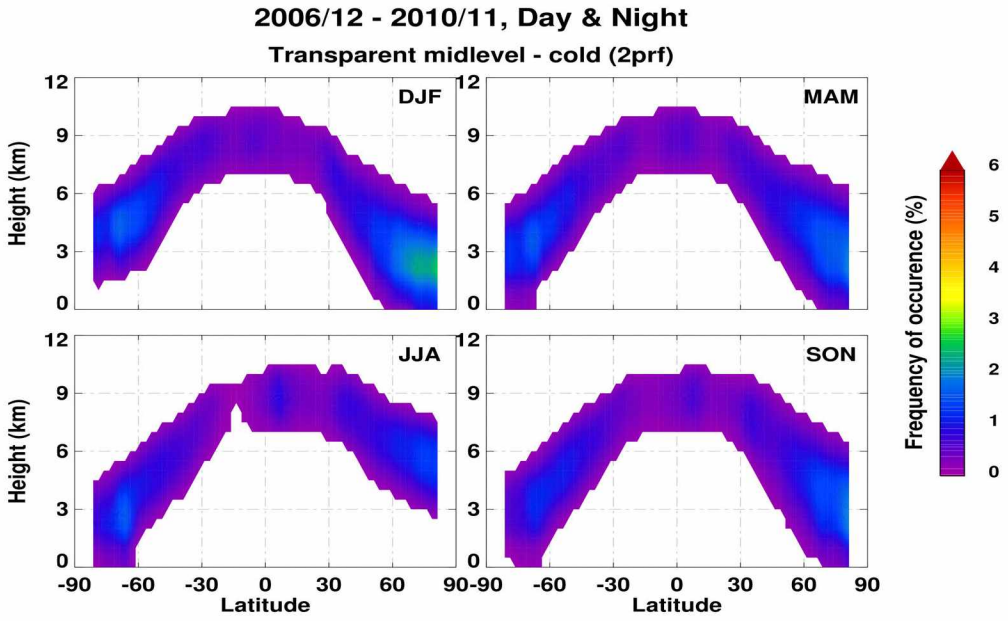

Figure 3.16: Zonally averaged frequency of occurrence of M1 clouds with altitude.

The zonally averaged frequency of occurrences of M1 clouds with altitude is shown in Figure 3.16. The M1 cloud occurrences are high (up to 8%) in the middle altitudes of the

troposphere over the polar regions during DJF months. There is a general dependence of cloud occurrences on the atmospheric circulation (Hadley-cell) pattern, where ascending and descending air motions influence the cloudiness. Over the tropical regions M1 cloud occurrences are limited to 7 – 10 km altitude, while the tropopause level varies from 16 – 18 km altitude. This observation further supports the assertion that M1 clouds here are formed through detrainment of deep convective towers that extend into the upper atmosphere (*Folkins et al.*, 2000).

Table 3.9: Average macrophysical properties of M1 clouds over the latitudinal belts derived from four years of CALIPSO observations.

Latitudinal Belt	**Cloud top**		**Cloud base**		**Cloud thickness**	**Relative occurrences**
	Height (km)	**Temp. (° C)**	**Height (km)**	**Temp. (° C)**	**(km)**	(%)
90N - 60N	4.6 ± 0.3	-27.6 ± 0.5	3.2 ± 0.4	-21 ± 0.5	1.4 ± 0.1	29
60N - 30N	6.4 ± 0.3	-27.5 ± 0.4	5.2 ± 0.3	-20 ± 0.3	1.2 ± 0.1	18
30N - 30S	8.8 ± 0.1	-26.5 ± 0.5	7.7 ± 0.1	-19 ± 0.5	1.0 ± 0.1	15
60S - 30S	6.2 ± 0.2	-27.5 ± 0.2	5.1 ± 0.2	-20 ± 0.2	1.0 ± 0.0	18
90S - 60S	4.2 ± 0.2	-28.8 ± 0.5	3.0 ± 0.3	-22 ± 0.4	1.2 ± 0.0	20

We further present the macrophysical properties of M1 clouds derived over the latitudinal belts in Table 3.9. Here the relative occurrences shown are derived as the ratio of M1 clouds that occur in each latitudinal belt to the global M1 cloud amounts. M1 clouds are more abundant in northern (~47%) than in southern hemisphere (~38%) extratropical regions (poleward of 30^{o} latitude). As mentioned earlier, this can be related to the availability of ice nuclei for the M1 cloud formation. Further, the average M1 cloud thickness increases from tropical to polar regions in both hemispheres. The average M1 cloud thickness is higher in the Arctic (1.4 km) than any other region. This observation is consistent with the thin midlevel ice cloud climatology derived from ground-based lidar observations, that reported average thin midlevel ice cloud thickness as 1.7 km over the sub-Arctic region (*Kayetha*, 2014).

The seasonal variations in M2 cloud occurrences and fraction of M2 clouds are shown in Figure 3.17. M2 clouds occur most commonly over the tropics with a frequency of up to 15%. Clouds occur along the midlatitude storm tracks with lower frequencies (5%) than in

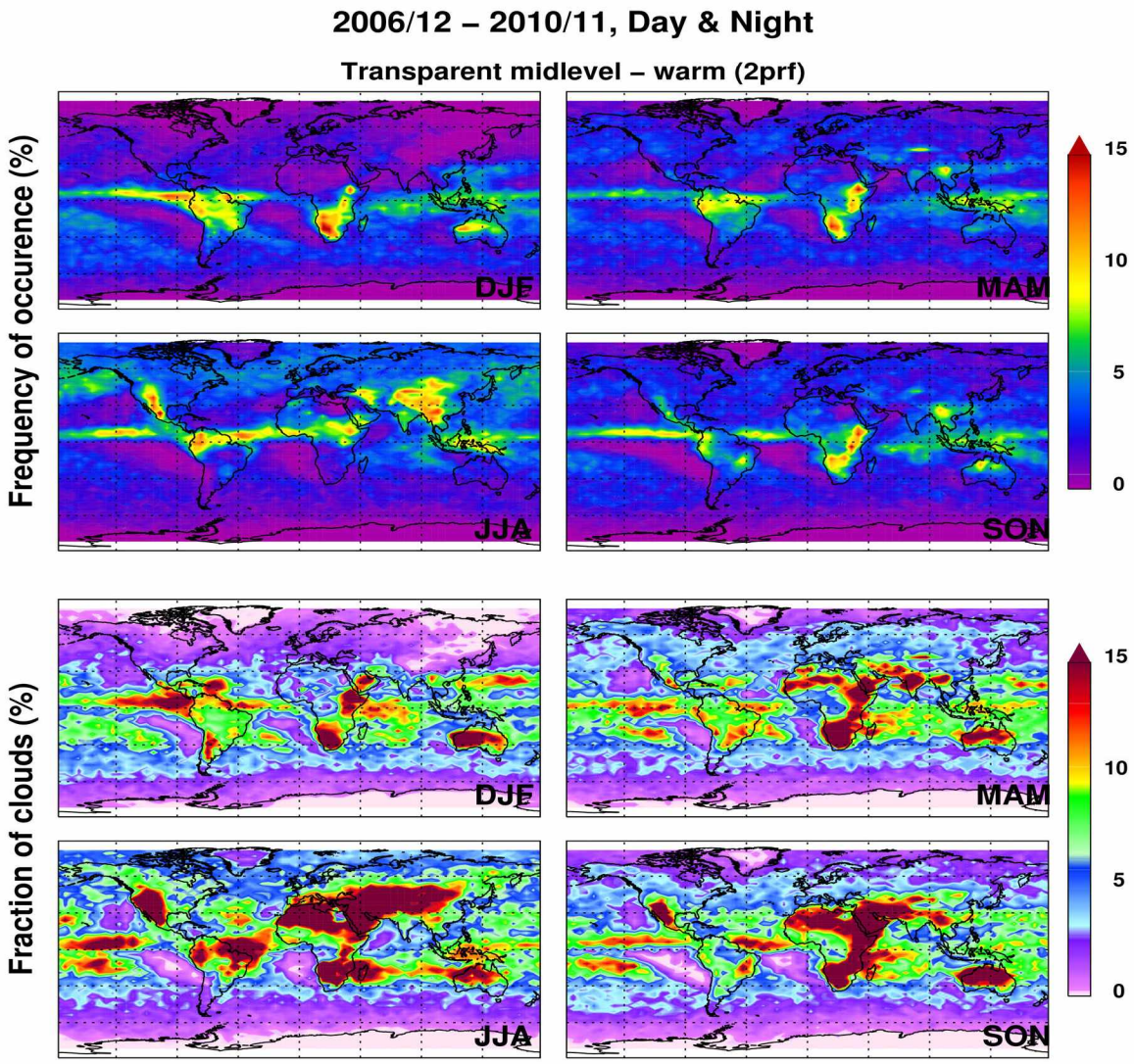

Figure 3.17: Seasonal variation in frequency of occurrence and fraction of clouds for M2 clouds.

the tropics. During the summer, the M2 cloud occurrences increase at midlatitudes in both hemispheres. The increase in the northern hemisphere (12%) is more pronounced than in the southern hemisphere. The seasonal distribution of M2 clouds shown here is similar to the distribution of altocumulus cloud (*Sassen and Wang*, 2008, 2012). Traditional altocumulus clouds have a supercooled liquid layer at the cloud top, and the cloud eventually glaciates and produces ice virga. These altocumulus clouds are optically thick. However, M2 clouds are water-dominated and are not dense enough to attenuate the lidar pulses.

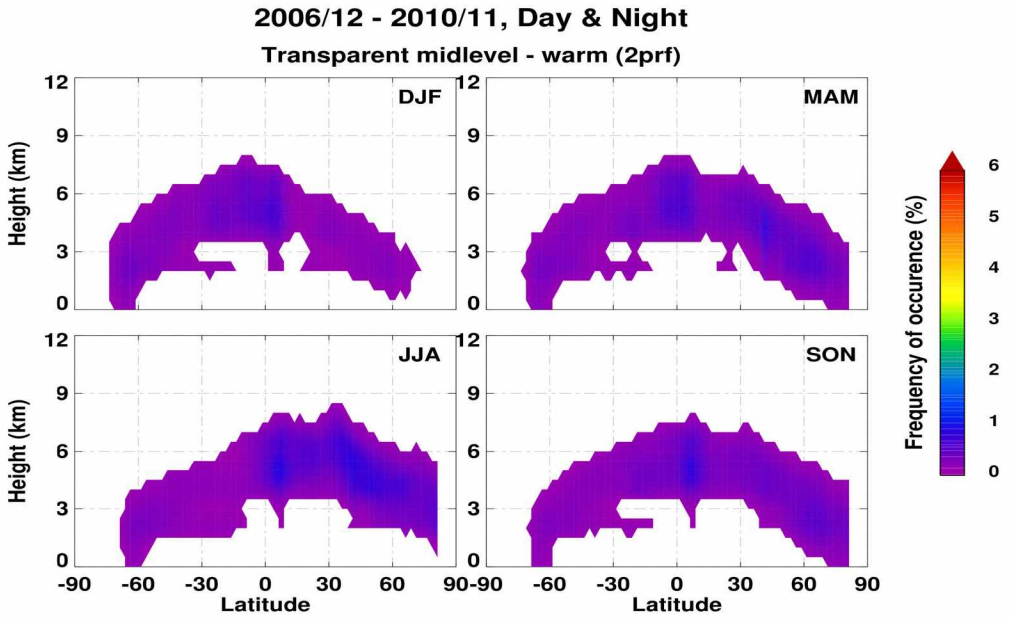

Figure 3.18: Zonally averaged frequency of occurrence of M2 clouds with altitude.

The zonally averaged frequency of occurrences of M2 clouds with altitude is shown in Figure 3.18. Similar to the global distribution of M2 clouds, the zonal distribution with altitude show maxima over the tropics in the middle atmosphere. M2 clouds are found at relatively lower altitudes compared to the M1 clouds.

The seasonal variation in frequency of occurrence and fraction of M3 clouds is shown in Figure 3.19. The M3 cloud occurrence is maximum (up to 30%) over the midlatitudes extends to the polar region in summer. Note that the M3 clouds shown here are traditionally referred to as altostratus and altocumulus clouds, which are optically thick. A noticeable feature throughout the seasons is the occurrence of M3 clouds over the eastern parts of Tibet. This feature is consistent with the global distribution of midlevel clouds (*Sassen and Wang*, 2012) and reflects the atmospheric circulation that leads to air mass convergence in the lower troposphere over Tibet (*Duan and Wu*, 2005).

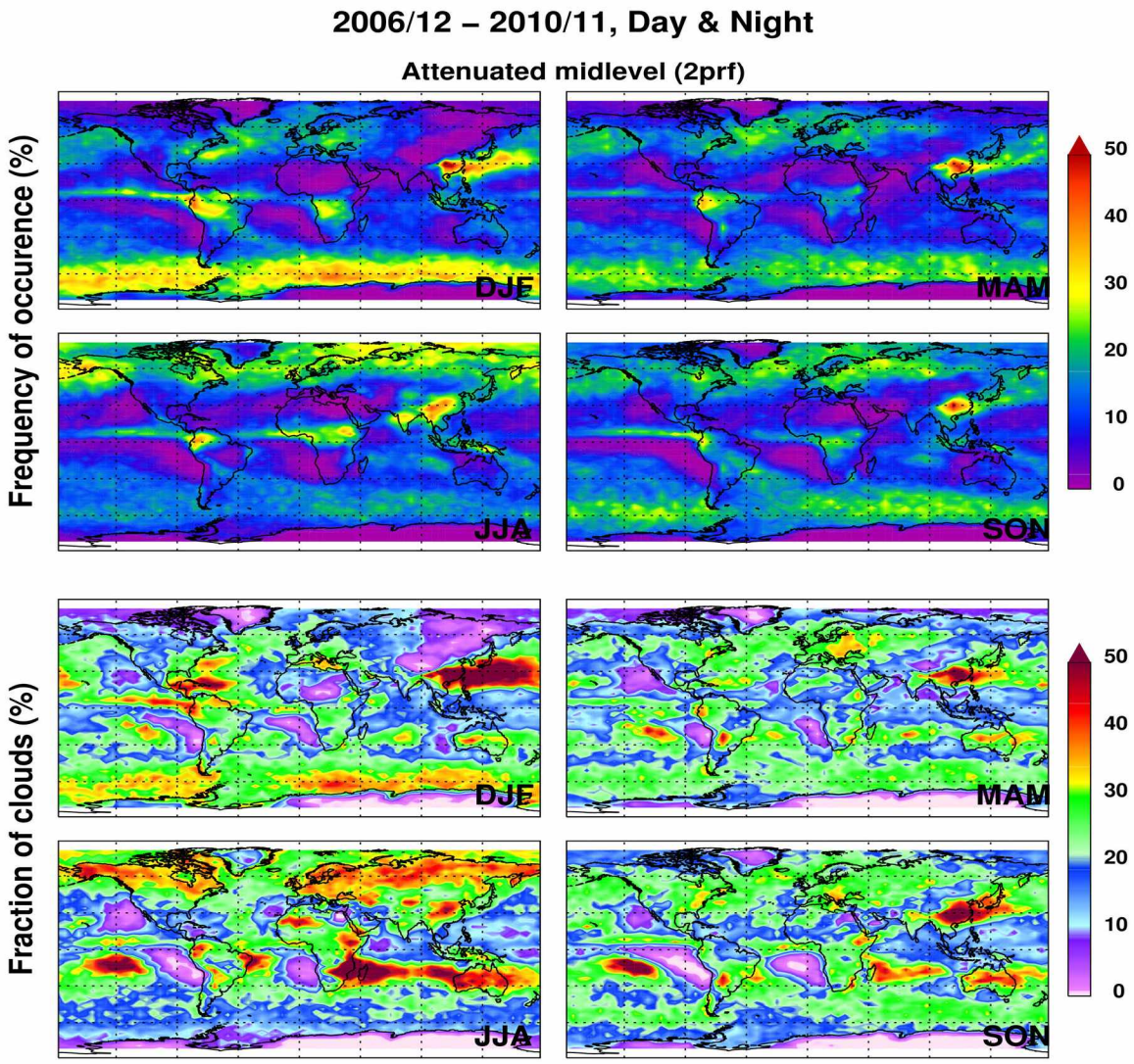

Figure 3.19: Seasonal variation in frequency of occurrence and fraction of clouds for M3 clouds.

3.4.3 Low level clouds

The seasonal variations in L1 cloud occurrences and fraction of L1 clouds is shown in Figure 3.20. L1 clouds show maximum occurrences in the summer hemisphere. Throughout the seasons, L1 clouds are dominantly formed over the oceans and thus show higher occurrences over in the Southern Hemisphere than the Northern Hemisphere. This shows that the low level cloud occurrences are biased due to the presence of optically thick clouds in the higher levels of the troposphere. Studies using CALIPSO data have shown similar fea-

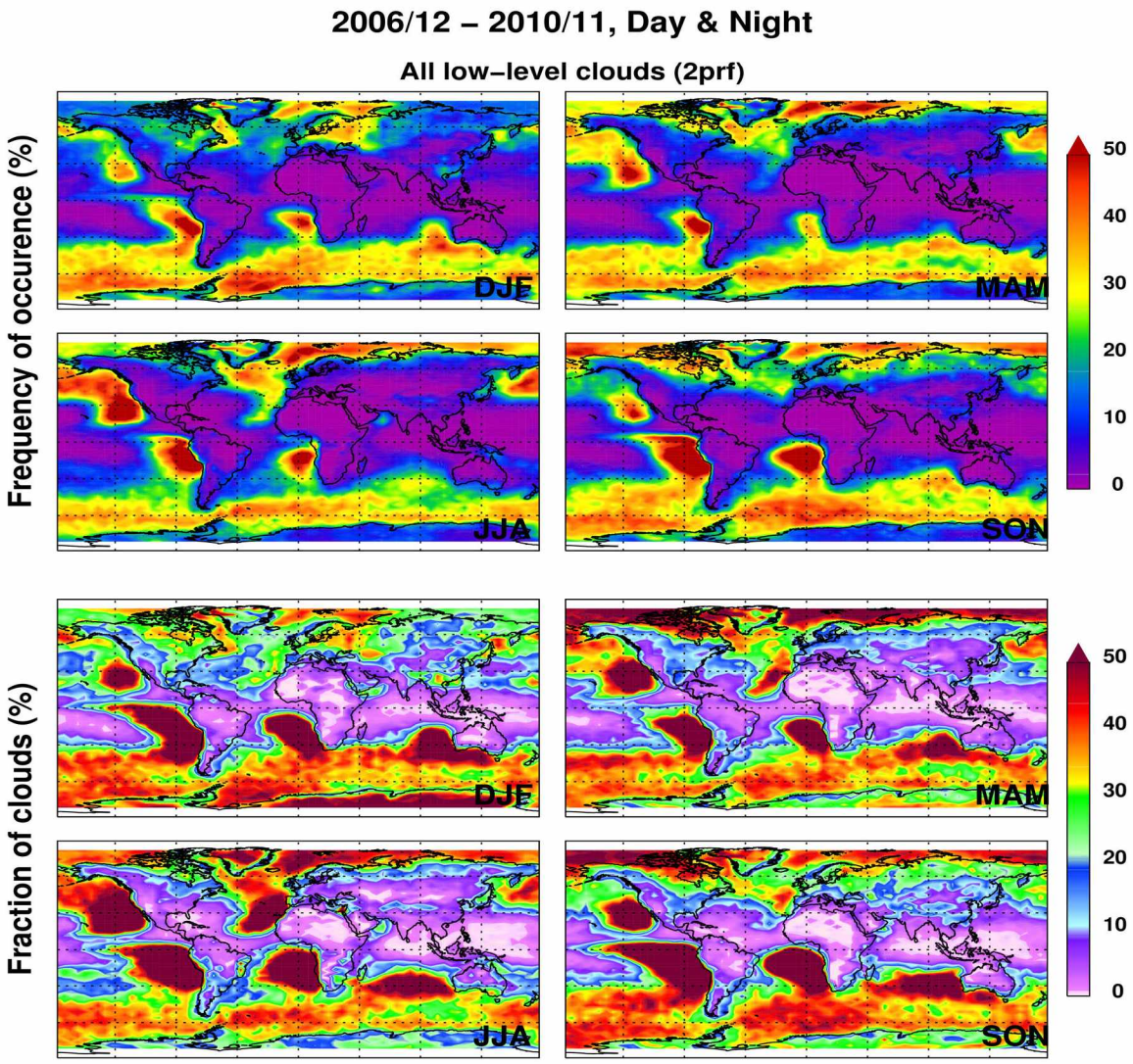

Figure 3.20: Seasonal variation in frequency of occurrence and fraction of clouds for L1 clouds.

tures over the tropical trade wind regions (*Kahn et al.*, 2008; *Marchand et al.*, 2008). However *Zhao and Di Girolamo* (2007) shows that low level cloud amounts detected by CALIOP lidar over the tropics are similar to some satellite retrievals but less than others (e.g. ISCCP). L1 clouds are likely formed through local weather processes and convection through the readily available moisture over the oceanic surfaces.

3.5 Spatial scales of cloud types

We have determined the number of clouds present at different scales in the CAIPSO data set. The total number of clouds detected decreases with increasing scale from 45,328,950 clouds at 2-profile (10 km) resolution to 1,153,447 clouds at 20-profile (100 km) resolution. The global mean fraction of clouds derived from CALIPSO observations at different spatial scales is shown in Figure 3.21. We see that with increasing spatial scale, the relative fraction of the different clouds changes.

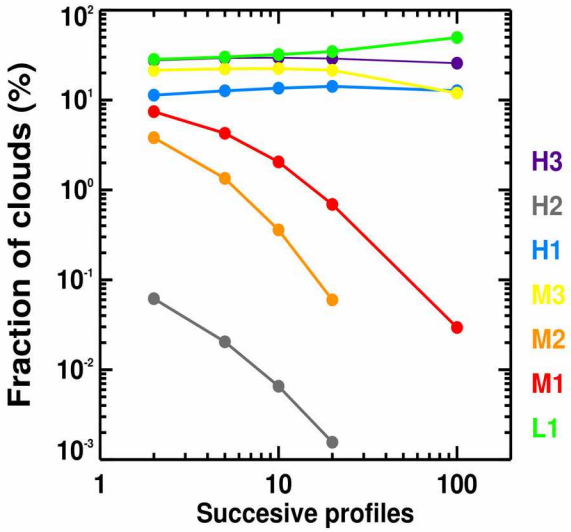

Figure 3.21: Global mean fraction of clouds derived from CALIPSO observations at different spatial scales.

The global mean fraction of clouds for L1 clouds is found to increase, while for H1, H3, and M3 clouds is found to be consistent with increasing spatial scales. For M1 and H2 clouds the fraction of clouds decreases exponentially with increasing spatial scales. For M1 clouds the fraction of clouds is 7.4%, 4.2%, 2.0%, and <0.1% at 2-profile (10 km), 5-profile (25 km), 10-profile (50 km), and 20-profile (100 km) resolution, respectively. A break point is defined as a decrease in cloud fraction by up to 50% due increasing spatial scale. The break point for the fraction of M1 clouds is 25 km. At larger scales the M1 cloud fraction decreases more rapidly with scale. At the largest spatial scale of 500 km, only five M1 clouds are found amongst a total of 16,951 clouds. These five M1 clouds identified at 500 km spatial scale will be hereafter referred to as *distinct* M1 clouds and will be explored further in Chapter 4.

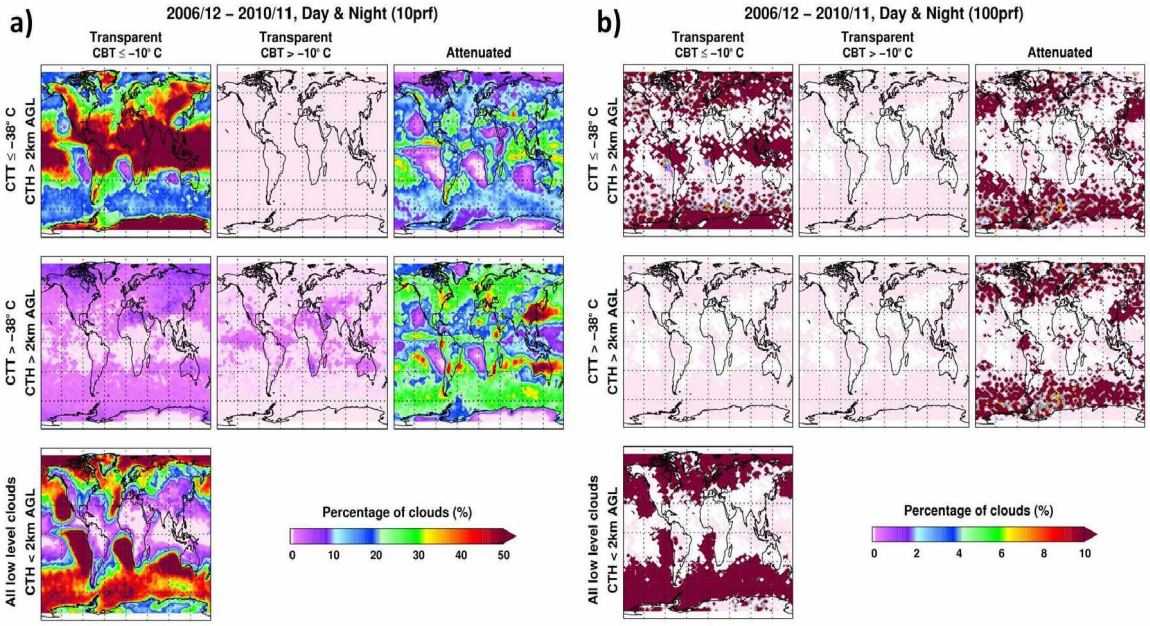

Figure 3.22: Global distribution of fraction of clouds derived from CALIPSO observations at (a) 10-profile (50 km) and (b) 100-profile (500 km) resolutions.

We next examine the geographical distribution of clouds at different spatial scales. The global distribution of fraction of clouds at 10-profile and 100-profile resolutions is shown in Figure 3.22. Note the color coding for cloud distribution at 10-profile and 100-profile occurrences have a maximum value of 50% and 10%, respectively. In comparison to the 2-profile resolution, the distribution of cloud occurrences has similar features. Additionally at the 100-profile resolution, the fraction of clouds decreases and shows H1 clouds up to 2% over Antarctica and the tropics and L1 clouds over the Southern Ocean and the subsidence regions in the tropics. This shows that the prevalence of H3 and M3 clouds is associated with synoptic-scale processes, while H1 and L1 clouds are also formed in association with large-scale atmospheric circulation and regional weather patterns.

We next examine the global distribution of M1 cloud amounts at different spatial scales. The global distribution of M1 clouds at different spatial scales are shown in Figure 3.23. The maximum value for each spatial scale shown varies from 15% to 2%. The distribution of M1 clouds at different spatial scales shows consistent features but suggests reduced cloud amounts with increasing spatial scales. In the Arctic, with the exception of the North Atlantic sector of the Arctic Ocean, M1 clouds occur and contribute >2% of the clouds at

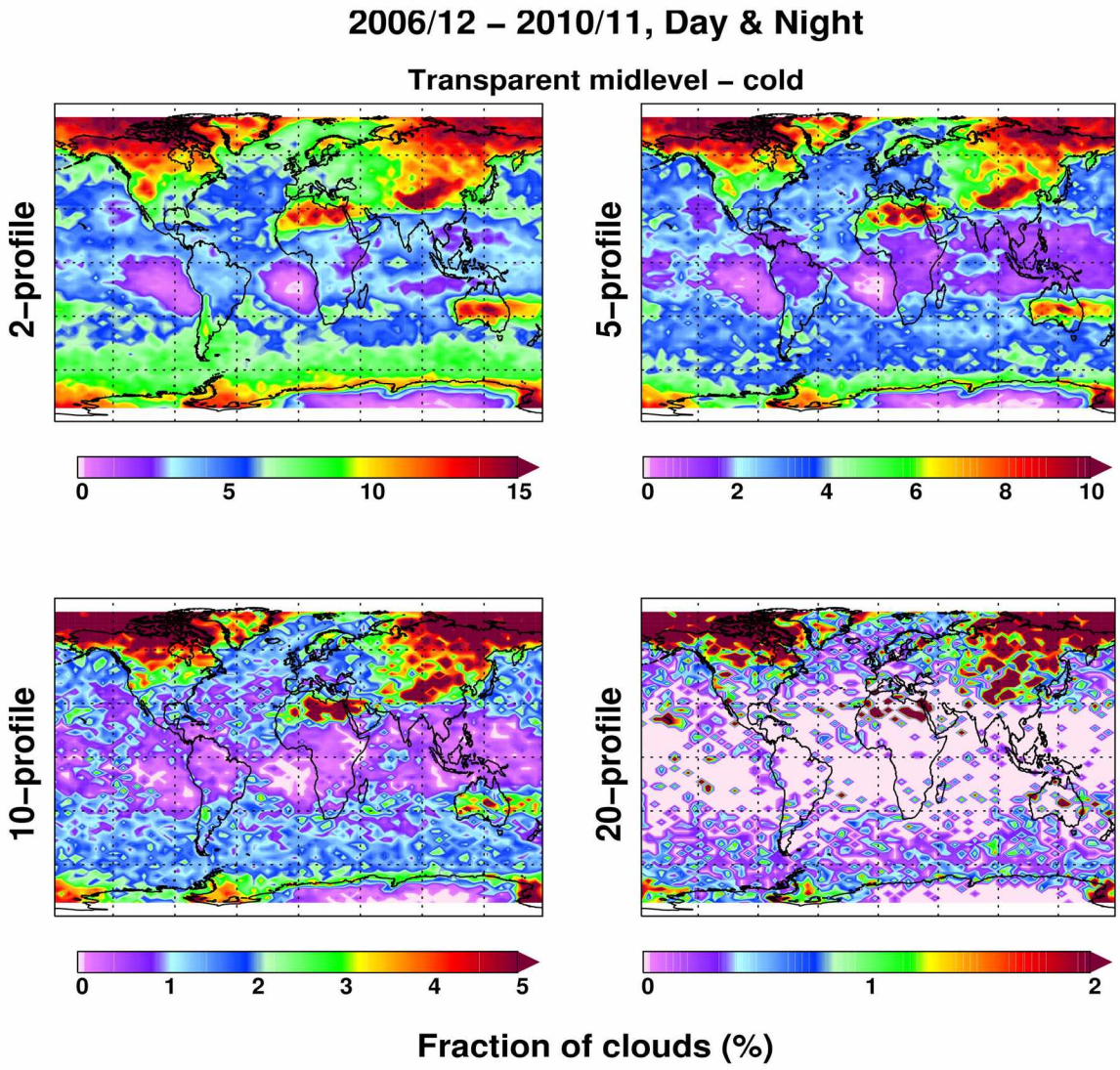

Figure 3.23: Fraction of M1 clouds at different spatial scales.

any spatial scales shown here. Thus it is now confirmed that M1 clouds preferentially occur in the Arctic at all spatial scales.

3.6 Cloud distribution and general meteorology

The characteristic patterns of the global distribution of cloud types are found to be consistent with the classical climate regimes produced by the large-scale atmospheric circulation (*Randall*, 2015). In the tropics where the circulation is dominated by mean upward motions and deep convective activity, high amounts of H1 clouds are found. Embedded in these regions is the highest concentration of dense precipitating systems (optically thick) observed

as H3 clouds. The subtropics are dominated by mean downward motions with convection confined to the boundary layer have high amounts of L1 clouds over oceans. Whereas over the drier land, the downward motion regimes (i.e. deserts) show low amounts of high and midlevel clouds and a complete lack of L1 clouds reflecting low amounts of moisture in the atmosphere. Over the midlatitudes, where large scale cyclonic systems dominate the general circulation, there are high amounts of optically thin (H1) and optically thick clouds (H3 and M3). However the frequencies of H1 and M3 clouds are found to be higher than H3 clouds.

The traditionally referred cirrus clouds are categorized as H1 type according to the classification scheme used in the present study. From the observations presented in the current study it is clear that the global distribution of H1 clouds shows high occurrences in the tropics. Seasonally the H1 cloud occurrences are high in the winter hemispheres. These observations are in agreement with cirrus cloud studies that use a compilation of surface observations, and ground-based and satellite measurements (*Stone*, 1957; *Cox*, 1971; *Warren et al.*, 1986; *Sassen and Campbell*, 2001; *Sassen et al.*, 2009; *Kayetha*, 2014). Our H1 cloud occurrences can be related to the two dominant cirrus cloud formation mechanisms: produced through synoptic activity and clouds associated with deep convective activity. Depending on the local environmental conditions these processes provide favorable conditions for the cloud particles to grow to large sizes that would eventually precipitate (H3 clouds) or survive as optically thin (H1) clouds. Thus the geographical distribution and seasonal variation in H3 cloud occurrences resembles that observed for the H1 clouds, indicating that partly H1 clouds are formed with H3 clouds. H2 clouds, high level optically thin clouds that extend to warmer temperatures of up to -10^{o} C, are found to have very low occurrences <0.1%. This shows that in practice no cirrus clouds are found at temperatures of -10^{o} C or higher.

Midlevel clouds are generally formed through large-scale processes that provide sufficient uplift of air masses to reach supersaturation and condense as clouds. Regional weather patterns and topography also play a crucial role in the formation and maintenance of these clouds. But so far, midlevel cloud studies have treated optically thin and thick clouds as a single category. However, with our logic-based rules we have categorized the midlevel clouds as M1 (optically thin and ice-dominated), M2 (optically thin and water-dominated) and M3 (optically thick) cloud categories. As stated earlier the focus of the current study is

to understand the prevalence of optically thin midlevel ice clouds. The ice dominated M1 clouds have high occurrences over the polar regions, while water dominated M2 clouds have high occurrences over the tropics. M1 clouds are likely formed through scenario such as the following: (a) Ice crystal sedimentation from the upper level cirrus types of clouds that seeds the lower layer triggering the formation of ice in it. Once an ice particle forms in a cloud the available water vapor can quickly be transformed to ice crystals through the WBF process and remain in the atmosphere until it dissipates. Depending on the availability of water vapor and the updraft velocities these clouds remain optically thin or their particles grow to larger size particles that can attenuate visible light and become M3 clouds. (b) Ice crystal remnants of midlevel stratiform clouds. Midlevel stratiform clouds containing supercooled liquid layers at their cloud top leave remnants of ice crystals when the environmental conditions cease to support the upward transport of water that formed the cloud (c) The availability of ice nuclei over certain arid regions can activate the formation of clouds even at warmer temperatures. The optically thin water dominated M2 clouds occur primarily over the tropical convergence zone. M2 clouds are formed through the detrainment of deep convective clouds over the relatively stable layers of the troposphere.

In comparison to the altostratus cloud distribution (*Sassen*, 2002) derived from the combined CALIPSO-CloudSat algorithm (*Wang*, 2011) which includes both optically thin and attenuated midlevel clouds, M1 clouds identified here show a reciprocal pattern of cloud occurrences. For instance, the altostratus clouds reported therein occur commonly (>40% of observations) at high latitude regions during winter in either hemisphere, where M1 clouds are found to be minimum over these regions. This indicates that the majority of the altostratus clouds reported over such regions are optically thick and attenuate the lidar pulses. It is likely that synoptically induced uplift of airmasses over such topography resulted in updraft velocities and ice-supersaturation that allowed cloud particles to easily reach large sizes that would eventually precipitate. Otherwise without synoptic forcing the weaker uplift of airmasses along the mountainous terrain would provide conditions where supercooled liquid droplets would glaciate and remain as ice crystals. Such ice crystal clouds are often observed upwind of mountain regions that are often subvisual or diffuse by appearance (*Sassen and Campbell*, 2001). M1 clouds are likely observed under quite stable atmospheric conditions with low wind speeds where cold air masses reach ice-saturation and form as cloud. This finding is consistent with the observation of sub-

visual midlevel ice cloud reported under similar atmospheric conditions (*Lampert et al.*, 2009).

In comparison to the midlevel mixed-phase stratiform (altocumulus) clouds that remain as ice cloud layers after the depletion of supercooled liquid layer should share some characteristics with the M1 clouds. Such mixed-phase stratiform clouds are dominantly formed over the polar regions in the summer hemisphere (*Zhang et al.*, 2010), which is not in agreement with the M1 cloud occurrences as observed here. However, the M2 and M3 cloud distribution shows agreement with the altocumulus cloud distribution. This provides further evidence that M1 clouds derived here are formed through a variety of processes as discussed above.

In reference to the current cloud classification schemes implemented for remote sensing observations, these optically thin midlevel clouds are broadly categorized as altostratus clouds (*Sassen and Wang*, 2012). Such a classification scheme could be misleading in assessing the net radiative effect of midlevel clouds and should be improved by including visual traits of the cloud types. Unlike the M1 clouds studied here, the classic or standard altostratus clouds are those that obscure the disk of Sun or Moon for a surface observer. This means that the lidar pulses operating in visible wavelengths will be completely extinguished.

3.7 Summary

Four years of CALIPSO data have been used to identify optically thin midlevel ice clouds. For this purpose, the tropospheric clouds detected by CALIPSO have been categorized in seven classes based on logic-based rules derived from previous studies. Our logic-based rules use cloud top temperatures and altitudes to identify high, mid, and low level clouds. Additionally, the ability of CALIOP lidar signals to penetrate the clouds has been used to separate optically thin and thick clouds. A sensitivity test has been performed to assess the change in cloud statistics to the threshold temperatures used in the cloud classification scheme. The global distribution of the seven cloud categories along with the seasonal variations and day-night differences in cloud occurrences have been investigated. Further, the spatial scales of all cloud categories have been examined. We have focused on optically thin midlevel ice clouds that are referred as M1 clouds. The possible mechanisms for the formation of M1 clouds are discussed.

Our key findings in this Chapter are as follows:

1. The global mean occurrence of M1 clouds is 4.5% and represents 7.3% of all tropospheric clouds detected by CALIPSO.

2. M1 clouds occur most commonly in the polar regions and during Arctic midwinter. M1 clouds occur 19% of the time.

3. In polar regions M1 clouds occur most commonly (both hemispheres) in the DJF months. However, there is no hemispheric symmetry in M1 cloud occurrences indicating that these clouds are formed through a variety of local processes.

4. Small day-night differences in M1 cloud occurrences are observed regionally.

5. M1 clouds can extend to large scales of 500 km, though they primarily occur at smaller spatial scales with median scale of 25 km.

6. M1 clouds are commonly found over Greenland and Tibet, particularly during the JJA months suggesting orographic formation.

Chapter 4
Radiative impacts of thin midlevel clouds over the Arctic

In the previous chapter, we identified optically thin midlevel (M1) ice clouds by applying a logic-based rule scheme to the CALIPSO data. We determined the frequency of occurrence, geographical distribution and seasonal variation of M1 clouds. Additionally, we investigated the spatial extents of the M1 clouds by looking for continuity in the clouds over progressively larger numbers of CALIPSO profiles. We found that while M1 clouds could extend to 500 km, the median extent of these clouds was 25 km. In this chapter, our goal is to estimate the radiative impact of these clouds. For this purpose we use cloud characteristic information from CALIPSO and meteorological data from reanalysis to represent the cloud in the model. The resolution of cloud measurements is 5 km (single profile) and of the reanalysis data is 50 – 60 km (0.5° latitude x 0.6° longitude). To analyze the radiative properties of M1 clouds, we choose case studies of distinct clouds with large spatial extent (500 km). We made this choice for several reasons. Firstly, the clouds are mature and we are not identifying small transient clouds that are evolving. Secondly, the scale of clouds matches the scale of the reanalysis data. Finally, the large scales of the cloud supports the plane-parallel assumption of the radiative transfer code. In the four years of CALIPSO data we found five cases of such large M1 clouds. These five cases were found in the Arctic in the months of December, February and March.

In this chapter we first review several key studies of Arctic clouds to provide a context for understanding the role of M1 clouds in the atmospheric radiation budget. We then describe the open-access radiative transfer model that we use in this study and we validate the model using previous published studies. We then present our five case studies of the M1 clouds and determine the radiative impact of these distinct M1 clouds. We then discuss these results in the context of all M1 clouds. Finally, we summarize our key results.

4.1 Arctic clouds and their radiative effects

In the Arctic, clouds are known to show great variability in the radiative transfer of energy. The annual Arctic cloud fraction amounts to around 50 – 80% with predominant low level clouds up to 70% of the time from spring to fall (*Curry et al.*, 1990; *Curry and Ebert*, 1992; *Intrieri et al.*, 2002; *Shupe and Intrieri*, 2004). Cloud amounts over the Arctic are higher during summer to fall and lower during winter. The presence of clouds generally leads to an

increase of energy reaching the surface and a net warming effect in winter, spring, and fall. In summer, clouds produce a net cooling effect (*Intrieri et al.*, 2002; *Shupe and Intrieri*, 2004). During the winter, the large solar zenith angle and the increased surface reflectivity due to the snow cover and sea ice enhances the surface warming effect. During summer months although the Arctic is much cloudier than in winter, the longer solar insolation periods and decrease in surface albedo cancels the effect of cloud longwave radiation and induces a net cooling effect. Additionally in the Arctic, the frequent temperature inversions, the usually clean and dry atmosphere, intrusion of sporadic aerosol loading provides unique conditions for the Arctic clouds. Examples include the formation of liquid-topped mixed-phase clouds in the boundary layer (*Intrieri et al.*, 2002; *Turner*, 2005), the formation of multiple cloud layers (*Verlinde et al.*, 2007; *Luo et al.*, 2008) and the formation of optically thin clouds in winter (*Wyser et al.*, 2008).

The cloud radiative forcing (CRF) at a given altitude z is defined as the difference of the net irradiances (F) in cloudy and clear sky conditions (*Ramanathan et al.*, 1989):

$$CRF(z) = \left[F^{\downarrow}(z) - F^{\uparrow}(z)\right]_{cloudy} - \left[F^{\downarrow}(z) - F^{\uparrow}(z)\right]_{clear} \tag{4.1}$$

Where, $F^{\downarrow}$ is the downwelling irradiance, and $F^{\uparrow}$ is the upwelling irradiance.

A positive (negative) value of CRF is interpreted as the clouds have a warming (cooling) effect at the altitude z. In practice radiative transfer calculations are done separately for the solar (F_{SW}) and thermal infrared spectral ranges (F_{LW}). Thus the net radiative forcing at an altitude z, due to clouds can be written as:

$$CRF(z) = CRF_{SW}(z) + CRF_{LW}(z) \tag{4.2}$$

Studies at stations in the Arctic have shown that the longwave radiation forcing under clear sky conditions varies from –25 W/m^2 (cooling) in winter to –50 W/m^{2}in summer. Similarly the shortwave forcing under clear sky conditions vary from 0 W/m^2 during winter to 52 W/m^2 (warming) (*Dong et al.*, 2010). While the shortwave cloud radiative forcing (CRF_{SW}) is a function of cloud transmittance, surface albedo and solar zenith angle, the longwave cloud radiative forcing (CRF_{LW}) depends on the cloud temperature, height and emissivity (*Shupe and Intrieri*, 2004). The interaction of clouds with both shortwave and

longwave radiation determines the net radiative effect of the clouds on the Earth's surface. A study by *Curry and Ebert* (1992) uses satellite observations and ground measurements obtained through field campaigns to provide the annual cycle of radiative fluxes over the Arctic ocean as: (a) the CRF_{LW} is a minimum of 40 W/m^2 during winter and increases monotonically to reach a maximum of 80 W/m^2 in summer, (b) the CRF_{SW} decreases monotonically with the increasing solar energy to reach a –100 W/m^2 during summer as the albedo effect increases with increasing cloudiness. Thereafter, studies on radiative properties of Arctic clouds at various weather stations reported a similar annual cycle (*Shupe and Intrieri*, 2004; *Dong et al.*, 2010).

In terms of cloud composition and microphysical properties, the annual mean of CRF_{LW} for liquid clouds and ice clouds over the Arctic region is reported to be 52 W/m^2 and 16 W/m^2, while the annual mean CRF_{SW} is –21 W/m^2 and –3 W/m^2, respectively (*Shupe and Intrieri*, 2004). Studies show that CRF_{LW} is particularly sensitive to cloud water path (CWP) <30 g/m^2 but insensitive to higher CWPs, while CRF_{SW} decreases with increase in CWPs (*Slingo*, 1989; *Ebert and Curry*, 1993; *Shupe and Intrieri*, 2004). In other words, for optically thin clouds CRF_{LW} plays a major role in determining the net radiative effect particularly during the prolonged winter nighttime when there is no source of shortwave radiation.

Cloud radiative forcing is also altered by the indirect effect of aerosols. Aerosols alter the cloud particle concentration and size that leads to an increase in cloud thermal emissivity and solar albedo (*Twomey*, 1977). Aerosol intrusions from midlatitudes to the Arctic are not uncommon, particularly between the winter and spring periods. These aerosols are often referred to as *Arctic Haze* and are concentrated mostly in the lower few kilometers and sometimes are observed as high as 7 km in the Arctic atmosphere (*Shaw*, 1995). The cloud radiative forcing due to the indirect effects of aerosols is found to vary from 12.2 W/m^2 (warming) during February to –11.8 W/m^2 (cooling) during the month of August (*Zhao and Garrett*, 2015). Overall, the indirect effect of aerosols increases the CRF_{LW} by ~5.2 W/m^2 under cloudy conditions (*Garrett and Zhao*, 2006; *Lubin and Vogelmann*, 2006).

In the Arctic, the interaction of radiation with the surface albedo leads to a positive feedback. *Wyser et al.* (2008) used measurements from the 'Surface Heat Budget of the Arctic Ocean' experiment (SHEBA) to show that during winter when most of the region is covered by sea ice or snow the monthly average mean broadband albedo exceeds 0.7, while

during summer the average monthly broadband albedo in the Arctic reaches a minimum of 0.3. The decrease in surface albedo allows more solar radiation to be absorbed by the surface under clear sky conditions. This results in enhanced snow and sea ice melt leading to more surface warming (*Kay et al.*, 2008).

We now investigate the role of M1 clouds in the radiative transfer over the Arctic, based on five case studies.

4.2 Data used and methodology

The day and location where distinct M1 clouds are identified are shown in Figure 4.1 and Table 4.1.

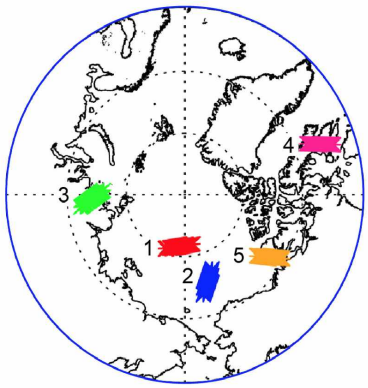

Figure 4.1: Locations of distinct M1 clouds in the Arctic.

Table 4.1: Distinct M1 clouds identified from the CALIPSO observations.

	Date	Location	Time (UTC)
Case-1	March 9, 2007	Arctic Ocean	1906
Case-2	March 10, 2007	Chukchi Sea	1456
Case-3	December 1, 2007	Kara Sea coast	0531
Case-4	December 6, 2007	Baffin Bay	0739
Case-5	February 14, 2009	Beaufort Sea	2021

All the identified cases of distinct M1 clouds occur during the cold season over the Arctic oceanic surface. Thus, the radiative transfer simulations of the observed M1 clouds will be performed using the spectral albedo for the surface type sea ice. For these cases, we used reanalysis meteorological data (i.e., temperature, pressure, relative humidity and O_3 density profiles) obtained from the CALIPSO data product to represent the atmosphere

in model simulations. Since the M1 clouds considered here are distinct with large spatial scales up to 500 km the use of reanalysis data is reasonable and we do not require meteorological data from local radiosonde measurements. The simulations use cloud parameters derived from the CALIPSO data product that includes the cloud top and base altitudes and optical depth. Additionally, we use the daily MERRA reanalysis data set and MODIS imagery to investigate the synoptic and cloudy conditions over the region of M1 cloud occurrence.

4.3 Radiative transfer simulations

The radiative forcing of thin midlevel clouds presented here are calculated from the *libRadtran* (*lib*rary for *Rad*iative *tran*sfer) radiative transfer package (*Mayer and Kylling*, 2005). LibRadtran is a software package designed to calculate the radiative quantities such as radiances, irradiances at user-defined altitudes within the atmosphere using input data of the extraterrestrial radiation, the atmosphere (pressure, temperature, humidity, O_3, N_2,O, and CO_2, profiles) and surface properties. This package is freely available and suitable for computing radiative effects of aerosols and clouds under user-defined boundary conditions (www.libradtran.org).

4.3.1 Model inputs

The meteorological data such as pressure, temperature, relative humidity and ozone number density profiles obtained from the CALIPSO data product have been used as inputs to the model to represent the atmospheric conditions for the observed clouds. For the atmospheric data above 30 km altitude the standard subarctic winter profiles are used (*Anderson et al.*, 1986). The aerosol microphysical properties of maritime type for the winter season represent the background aerosol conditions for the simulations. At 1 μm, the maritime aerosol has an aerosol optical thickness of 0.11 and an angstrom exponent of 0.63 (*Shettle*, 1989). The surface spectral albedo plays a crucial role in the simulation of radiative transfer in the solar spectral range. The *libRadtran* software provides an option to input any measured surface albedo or to use a standard library of spectral albedo values. These standard values are taken from International Geosphere-Biosphere Programme (IGBP) database based on the geographical location (latitude and longitude). The IGBP database categorizes the global surface into seventeen types (1-evergreen needle forest, 2-evergreen broad forest, 3-deciduous needle forest, 4-deciduous broad forest, 5-mixed

forest, 6-closed shrubs, 7-open shrubs, 8-woody savanna, 9-savanna, 10-grassland, 11-wetland, 12-cropland, 13-urban, 14-crop mosiac, 15-permanent ice/snow, 16-desert, 17-ocean water) and provides spectral albedo of these surface types derived from satellite measurements (*Belward and Loveland*, 1996). For our simulations, we used a modified spectral albedo of the surface-type 15 (*permanent ice/snow*) that we have validated (complete details are provided in Section 4.3). The simulations in the solar spectral range (290 – 4000 nm) were performed with the discrete ordinate radiative transfer solver DISORT version 2.0 (*Stamnes et al.*, 1988). The DISORT radiative transfer equation (RTE) solver assumes a 1D plane-parallel atmosphere and uses an even number of discrete streams of radiation in each hemisphere, each one representing a different direction (e.g., *Petty* (2006)). A complete description of the RTE is provided in the Appendix. We used extraterrestrial solar irradiance spectrum by *Gueymard* (2004) as input for simulations in solar spectral range. The solar zenith angle (from CALIPSO data) and day of the year for which simulation were conducted is provided to the model to correct the computed quantities for Sun-Earth distance. To account for the gaseous absorption, we use the LOWTRAN band model as adopted from SBDART (*Ricchiazzi et al.*, 1998). The IR (4000 – 100000 nm) simulations were performed using a two-stream radiative solver (*Kylling et al.*, 1995). The flowchart showing the entire inputs and options chosen for radiative calculations is presented in Figure 4.2.

In addition to the above described options, for the radiative calculations of the cloudy conditions, cloud optical properties must be provided to the model. If no measurements of cloud optical properties are available, the user can provide cloud microphysical properties (top/base altitudes, CWC, R_{eff}) to the model. These microphysical properties are then converted to optical properties by the user specified parameterizations. The libRadtran software provides a library of cloud optical properties suitable for computing radiative properties of ice clouds (*Fu*, 1996; *Fu et al.*, 1998; *Yang et al.*, 2000; *Key et al.*, 2002; *Baum et al.*, 2005a,b) and water clouds (*Hu and Stamnes*, 1993). For the case of ice clouds, in addition to the cloud microphysical properties the ice crystal shape must also be specified. For the present work, we have used the Yang parameterization (*Yang et al.*, 2000) for ice clouds. *Yang et al.* (2000) provides optical properties of ice crystals suitable for computing radiative quantities over the wavelength range 0.2 – 100 μm. For the case of mixed-phase clouds, the ice-phase and water-phase optical properties are input to the model which are then internally combined by the *libRadtran* pack-

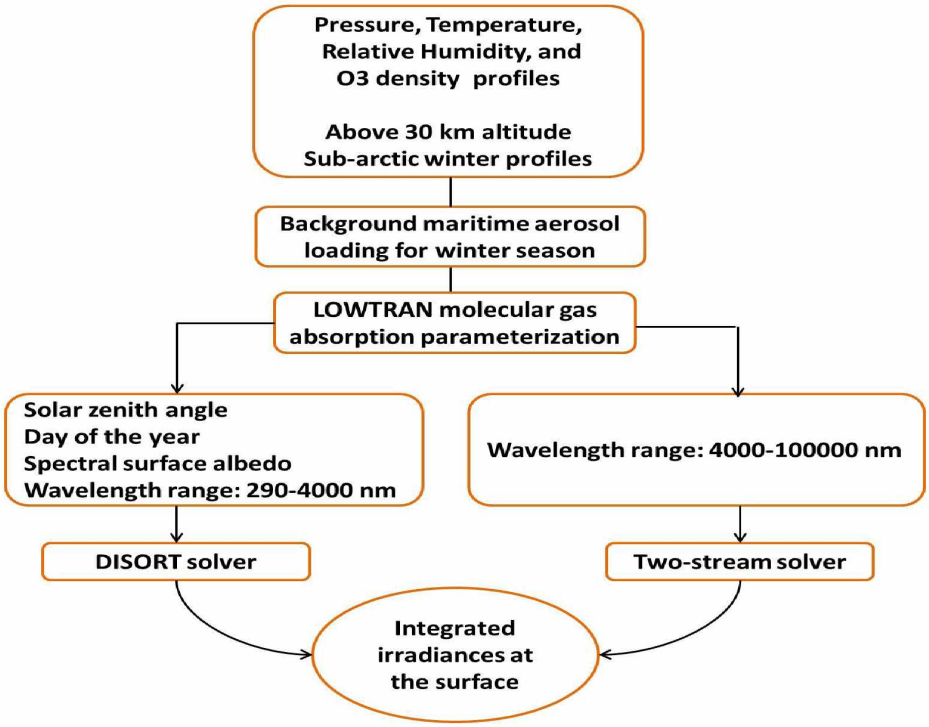

Figure 4.2: Flowchart showing the inputs provided and options chosen for the simulations with libRadtran.

age. The complete details of various options available in the libRadtran model along with examples on how to run simulations are provided in the software documentation (http://www.libradtran.org/doku.php?id=documentation).

For this current study, we carried out radiative transfer simulations assuming the identified M1 cloud as: (a) pure ice cloud consisting of solid-column shaped crystals, (b) pure water cloud consisting of small spherical droplets, and (c) mixed-phase cloud with varying ice fraction from 100 to 0%. To do this, we initially estimated the effective radius of the cloud particle based on previous studies that reported in-situ measurements of optically thin midlevel clouds (*Hobbs and Rangno*, 1998; *Lampert et al.*, 2009). These studies reported thin altocumulus clouds with small water droplets not exceeding 20 μm in size and thin altostratus clouds consisting solely of ice particles (columns with rounded edges) with maximum size up to 100 μm. Further the measured liquid/ice water content for these clouds was reported to have an average value of 0.01 g m^{-3} with an maximum value of 0.45 g m^{-3}. With this information we have chosen an effective radius of 30 μm and 60 μm for ice clouds and 10 μm and 20 μm for water clouds, respectively. For the case of mixed-

phase clouds, the total optical depth (τ) of the cloud is due to the contribution of ice and water particles. Assuming an ice optical fraction of 80% and water optical fraction of 20% the ice water path (IWP) and liquid water path (LWP) are estimated with their mode of optical depths, i.e. 0.8 x τ and 0.2 x τ, respectively. By keeping the optical depth of the cloud constant, we have varied the ice optical fraction from 100% (pure ice cloud) to 0% (pure water cloud).

Table 4.2: Description of the cloud microphysics used in the radiative transfer simulations.

Cloud phase		**R_{eff} (μm)**	**Max. CWP (g m^{-2})**	**Max. CWC (g m^{-3})**
Ice	Solid-column	30	109.9	0.10
		60	219.8	0.20
Water	Spheres	10	40.0	0.04
		20	80.0	0.08
Mixed	60μm column + 10μm sphere	ice frac.80 + water frac.20	146.5 +6.7 = 153.2	0.15
		ice frac.60 + water frac.40	110 + 13.3 = 123.3	0.12
		ice frac.40 + water frac.60	73.3 + 20 = 93.3	0.093
		ice frac.20 + water frac.80	36.7 + 26.7 = 63.4	0.063

Table 4.2 shows the cloud microphysical properties chosen for the radiative simulations. From Chapter 3, we know that the cloud optical depth in visible wavelengths does not exceed 6 for optically thin clouds. We can calculate the maximum cloud water path (CWP) of the M1 clouds for the assumed R_{eff}. From CWP, we calculate the maximum cloud water content (CWC) based on the average M1 cloud thickness (1.0 km, reported in Chapter 3). Thus, the maximum cloud water content used for the radaitive transfer simulations of M1 clouds does not exceed 0.2 g m^{-3} and is within the range of water content reported for similar clouds.

4.4 Validation of model simulations

To validate the model simulations, we compare our results with a recent study that presents radiative transfer simulations with measured spectral albedo over sea ice (*Lampert et al.*, 2009). *Lampert et al.* (2009) present a case study of a subvisible and glaciated cloud at an altitude of ~3 km over the Barents Sea south of the Svalbard on 10 April, 2007.

This study was a part of the Arctic Study of Tropospheric Aerosol, Clouds and Radiation (ASTAR 2007) campaign and used airborne remote sensing and in-situ sensors to capture the microphysical properties of the observed clouds. The data obtained from ASTAR 2007 were published in a paper and a dissertation (i.e. *Lampert et al.* (2009); *Andre* (2009)). On 10 April, 2007 they observed an subvisible midlevel cloud (3.2 – 2.6 km) and a cirrus cloud (7.0 – 6.5 km). They reported that cirrus clouds consist of column shaped crystals with R_{eff} about 60 μm and an optical depth 0.03. Their radiative transfer simulation uses a spectral albedo measured from an albedometer over the sea ice surface (complete details about spectral albedo are presented in *Andre* (2009)). Our objective is to reproduce the results reported in *Lampert et al.* (2009) and validate our use of libRadtran. To achieve this, we used meteorological data for the day April 10, 2007 from radiosonde measurements and performed a initial simulation by using the original IGBP spectral albedo of the surface type *permanent ice/snow*.

Table 4.3: Validation of radiative transfer simulations with *Lampert et al.* (2009).

	SW			**LW**			**SW + LW**
	$F^{\downarrow}$	$F^{\uparrow}$	F_{net}	$F^{\downarrow}$	$F^{\uparrow}$	F_{net}	F_{net}
Lampert et al. (2009)	351.7	193.0	158.7	184.7	273.1	-88.4	70.3
Original IGBP albedo	358.5	248.7	109.8	187.0	282.5	-95.5	14.3
Modified albedo	354.6	196.2	158.4	187.0	282.5	-95.5	63.0

Table 4.3 provides the radiative transfer simulations presented in *Lampert et al.* (2009) and our results. In our simulation we first used the IGBP spectral albedo provided by the model and found the net radiative forcing to be much lower (14 W/m^2) than the Lampert value (70 W/m^2). This is primarily because of the high albedo values of the *permanent ice/snow* that produced higher amounts of $F^{\uparrow}_{SW}$. To investigate this further, we then changed the spectral albedo to the values of *sea ice* available from *Andre* (2009). Figure 4.3a shows the original IGBP provided spectral albedo of the surface type *permanent ice/snow* and its modified fit to the surface type *sea ice*. The resolution of the IGBP spectral albedo is defined by the wavelength bands of the correlated-k u/Liou parameterization. The permanent snow and ice spectral albedo have higher values in the visible region of the solar spectral range than with the sea ice surface. This change in albedo values has contributed to a change of about 15% in the upward shortwave irradiance. The spectral albedo for other

surface types over the Arctic region is available through *Andre* (2009) (Figure 4.3b). While the albedo over the open sea water varies ~0.1, the albedo observed over the sea ice or permanent ice surfaces approach 1.0. Then we performed a simulation by using the modified spectral albedo fit. We now find that the results obtained (63.0 W/m^2) are reasonably consistent with the simulations reported (70.3 W/m^2) in *Lampert et al.* (2009). This result highlights the importance of surface albedo in radiative transfer calculations which varies highly with surface types. However, by using the modified spectral albedo our results are consistent with the *Lampert et al.* (2009) and we have obtained a spectral albedo that conforms to the surface type sea ice that will be used for our simulations of M1 cloud case studies.

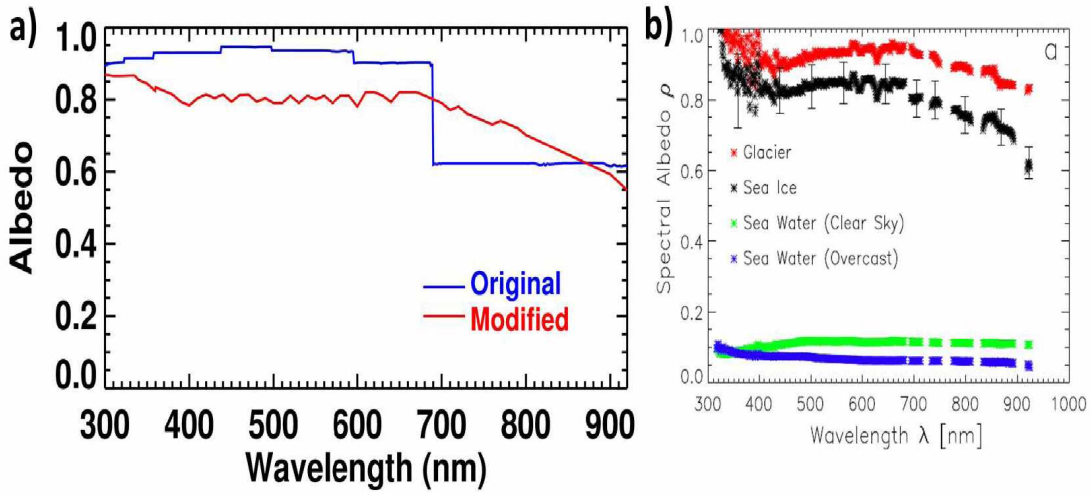

Figure 4.3: (a) Spectral albedo for the surface type sea ice used in the simulations. (b) Spectral albedo for various surface types as reported by *Andre* (2009).

4.5 Radiative transfer: Case studies

Initially we present, the synoptic meteorological and cloud conditions over the region and then the results from our simulations for each of the five clouds.

4.5.1 Case 1: March 9, 2007

On March 9, 2007 CALIPSO detected a distinct M1 cloud over the Arctic ocean during its orbital overpass at 1906 UTC. The prevailing synoptic and cloud conditions over the region of M1 clouds are shown in Figures 4.4 and 4.5.

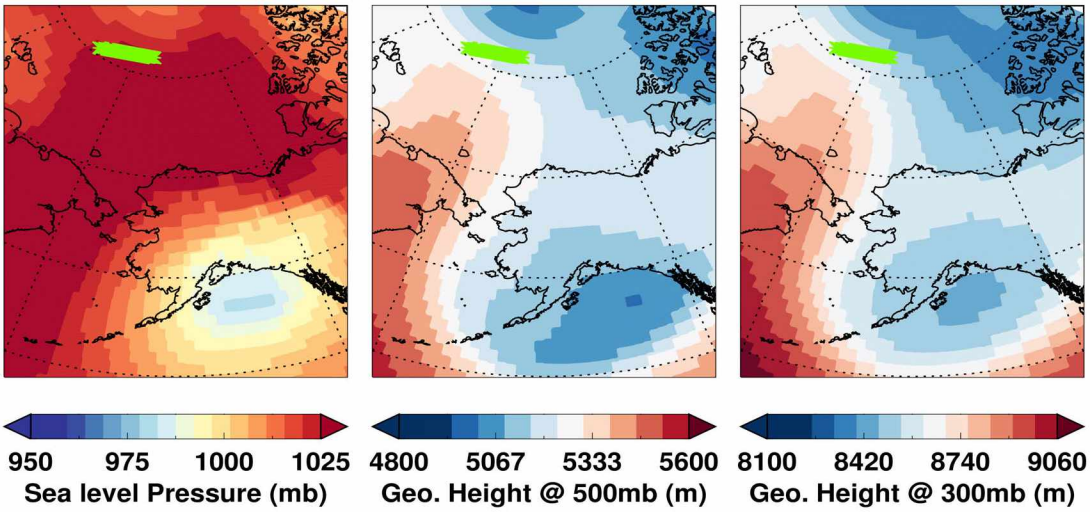

Figure 4.4: Synoptic meteorological conditions over a portion of the Arctic region on March 9, 2007 during a CALIPSO overpass (green).

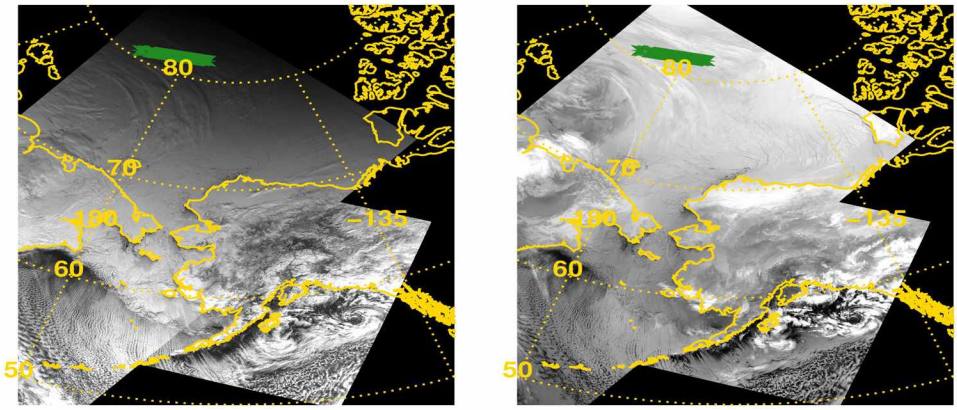

Figure 4.5: MODIS visible (left) and IR imagery (right) showing cloudy conditions and the overlaid CALIPSO orbit (green) on March 9, 2007.

A surface high pressure system prevails over the Arctic Ocean extending into the Beaufort Sea and the East Siberian Sea. The middle (500 mb) and upper (300 mb) atmospheric circulation pattern shows a ridge over eastern Siberia that transports warm moist air from the Pacific to the Arctic Ocean. The warm air mass from the Pacific and the cold air mass from Arctic Ocean form a frontal zone where the M1 clouds are observed. The MODIS IR imagery clearly depicts the clouds formed along the ridge over eastern Siberia and thin clouds over the Arctic Ocean along the frontal zone. While the clouds along the frontal

zone appear lighter, the clouds over eastern Siberia appear much brighter in the IR imagery. This indicates that clouds along the frontal zone are at mid or low levels of the atmosphere with comparable temperatures as the prevailing surface. Since it is local nighttime over the region, the MODIS visible band could not capture the features clearly.

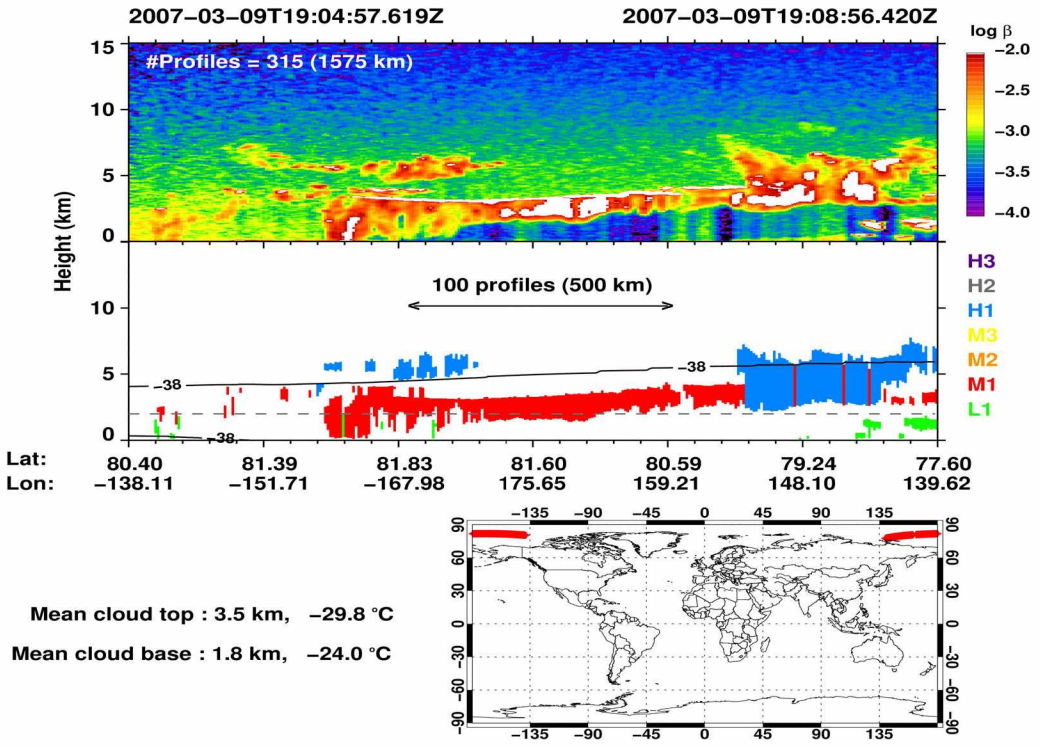

Figure 4.6: CALIPSO backscattering and cloud category masks derived for March 9, 2007.

The corresponding CALIPSO observations for daytime on March 9, 2007 are shown in Figure 4.6. The visual inspection of CALIPSO backscattering show patches of cloud regions with high backscattering values (> 10^{-2} km^{-1} sr^{-1}), indicating the presence of supercooled liquid droplets. However, the liquid layer in the cloud is not dense enough to extinguish the lidar pulses. Table 4.4 shows the properties of 100 profiles of the observed M1 cloud. The M1 cloud top altitude ranges from 3.1 – 4.4 km and the base altitude ranges from 0.6 – 2.8 km. For the 100 profiles of M1 cloud, the average top and base altitude is 3.5 km and 1.8 km, respectively. The M1 cloud has a relatively flat cloud top, while the cloud base varies in height. This variability is also reflected in the cloud base temperatures that have a higher standard deviation (1.3° C) than the cloud top temperatures (0.3° C). The cloud

optical depth derived from the CALIPSO data product shows a mean value of 1.4, with a few M1 cloudy profiles reaching optical depths as high as 5. The observed M1 cloud spans a horizontal length of 500 km, where the solar zenith angle (SZA) for the time of cloud observation varied from 91° – 95°. With the above derived cloud properties as inputs to the model, we performed our radiative simulations.

Table 4.4: Properties derived from the distinct M1 cloudy profiles observed on March 9, 2007.

		Min.	Max.	Mean	Median	Std. dev.
Cloud top	Height (km)	3.1	4.4	3.5	3.4	0.3
	Temperature (°C)	-35.2	-28.0	-30.0	-30.0	0.9
Cloud base	Height (km)	0.6	2.8	1.8	1.7	0.4
	Temperature (°C)	-29.0	-22.0	-24.0	-24.0	1.3
Optical depth		0.2	5.4	1.4	1.1	1.0
Solar zenith angle		91	95.4	93.0	93.0	1.2

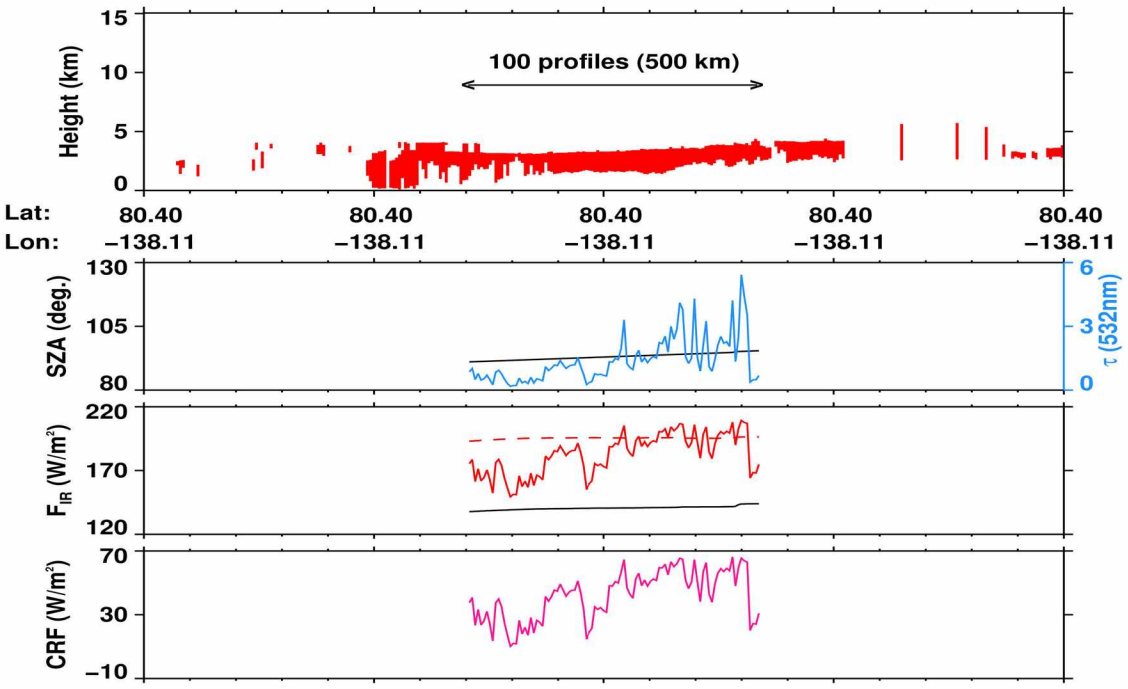

Figure 4.7: Cloud category masks, simulated irradiances (upwelling - dashed, downwelling - solid) and cloud radiative forcing for March 9, 2007.

Our radiative transfer simulations, where we assumed that the observed M1 cloud on March 9, 2007 was a pure ice cloud with ice crystals effective radius of 30 μm, are shown in Figure 4.7. Since the SZA over the region of M1 cloud occurrence is greater than 90^o, the irradiances in the solar spectral range is zero. Therefore, the radiative transfer due to the presence of M1 cloud is associated with the thermal or longwave radiation alone. As expected, in the longwave range the upwelling irradiance is only due to the emission from the Earth's surface. The other component $F^{\downarrow}_{cloud,LW}$ varies with the optical depth of the cloud (τ is directly proportional to the CWP), and so the cloud radiative forcing varies with the optical depth. For the profiles where M1 cloud optical depth is greater than 3, it is observed that $F^{\downarrow}_{cloud,LW}$ is equal to or greater than the $F^{\uparrow}_{cloud,LW}$. Overall the presence of M1 cloud induces an increase in $F^{\downarrow}_{LW}$ component.

Table 4.5: Radiative transfer simulations for the M1 clouds observed on March 9, 2007.

		SW			**LW**			**SW + LW**	**CRF**
		$F^{\downarrow}$	$F^{\uparrow}$	F_{net}	$F^{\downarrow}$	$F^{\uparrow}$	F_{net}	F_{net}	**W/m^2**
Clear sky		0	0	0	140.6	195.3	-54.7	-54.7	
Ice cloud	30 μm columns	0	0	0	182.6	195.3	-12.7	-12.7	42.0
	60 μm columns	0	0	0	182.9	195.3	-12.4	-12.4	42.3
Water cloud	10 μm spheres	0	0	0	182.8	195.3	-12.5	-12.5	42.2
	20 μm spheres	0	0	0	185.0	195.3	-10.3	-10.3	44.4
Mixed-phase	ice frac. 0.8 water frac. 0.2	0	0	0	183.0	195.3	-12.3	-12.3	42.4
	ice frac. 0.6 water frac. 0.4	0	0	0	183.0	195.3	-12.3	-12.3	42.4
	ice frac. 0.4 water frac. 0.6	0	0	0	183.0	195.3	-12.3	-12.3	42.4
	ice frac. 0.2 water frac. 0.8	0	0	0	183.0	195.3	-12.3	-12.3	42.4

The complete results of all the scenarios considered (ice, water, mixed-phase) for the observed M1 clouds on March 9, 2007 are provided in Table 4.5. It is interesting to observe that the CRF of M1 cloud is insensitive to the cloud phase. This could be attributed to the low optical depths of the observed M1 cloud. Overall, irrespective of the cloud phase the observed M1 cloud has a net warming effect. The average warming effect at the surface derived for eight cloud microphysical scenarios is 42.5 W/m^2.

4.5.2 Case 2: March 10, 2007

On March 10, 2007 CALIPSO detected a distinct M1 cloud over the Chukchi Sea during its orbital overpass at 1456 UTC. The prevailing synoptic and cloud conditions over the region of M1 clouds are shown in Figures 4.8 and 4.9.

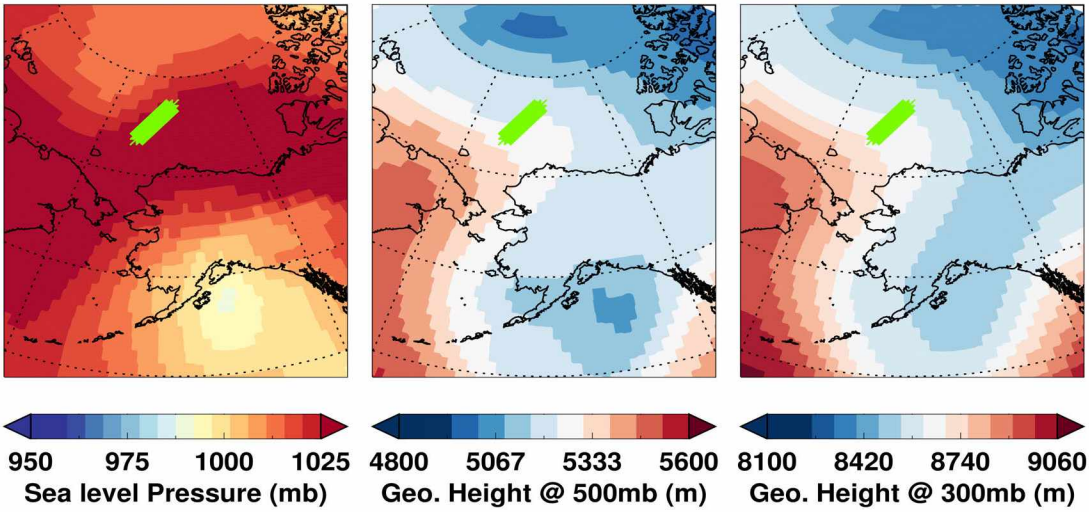

Figure 4.8: Synoptic meteorological conditions over a portion of the Arctic region on March 10, 2007 during a CALIPSO overpass (green).

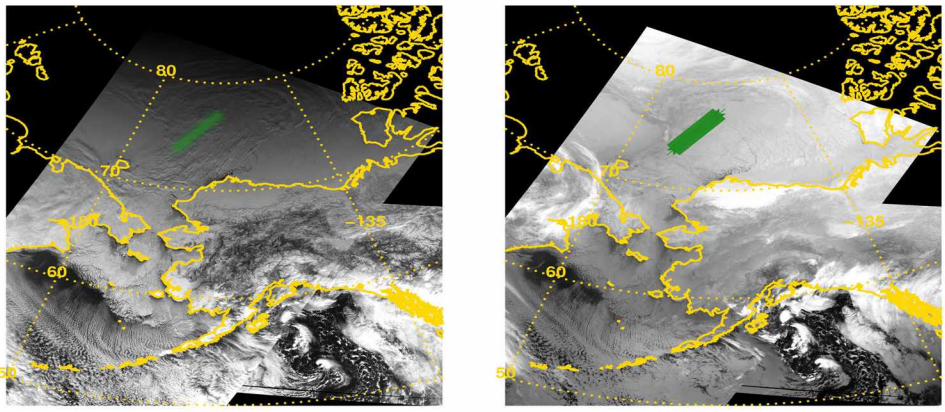

Figure 4.9: MODIS visible (left) and IR imagery (right) showing cloudy conditions and the overlaid CALIPSO orbit (green) on March 10, 2007.

The meteorological conditions observed for this day are similar to those observed for Case 1 (March 9, 2007). The surface high pressure system extends throughout central Alaska and

Northern Canada. The middle and upper atmospheric circulation shows a ridge pattern over eastern Siberia. This promotes cloudiness along the frontal zone. While the clouds formed along the ridge can be clearly identified, the M1 clouds are difficult to identify from MODIS IR imagery. This highlights the limitations of passive remote sensors in detecting optically thin clouds.

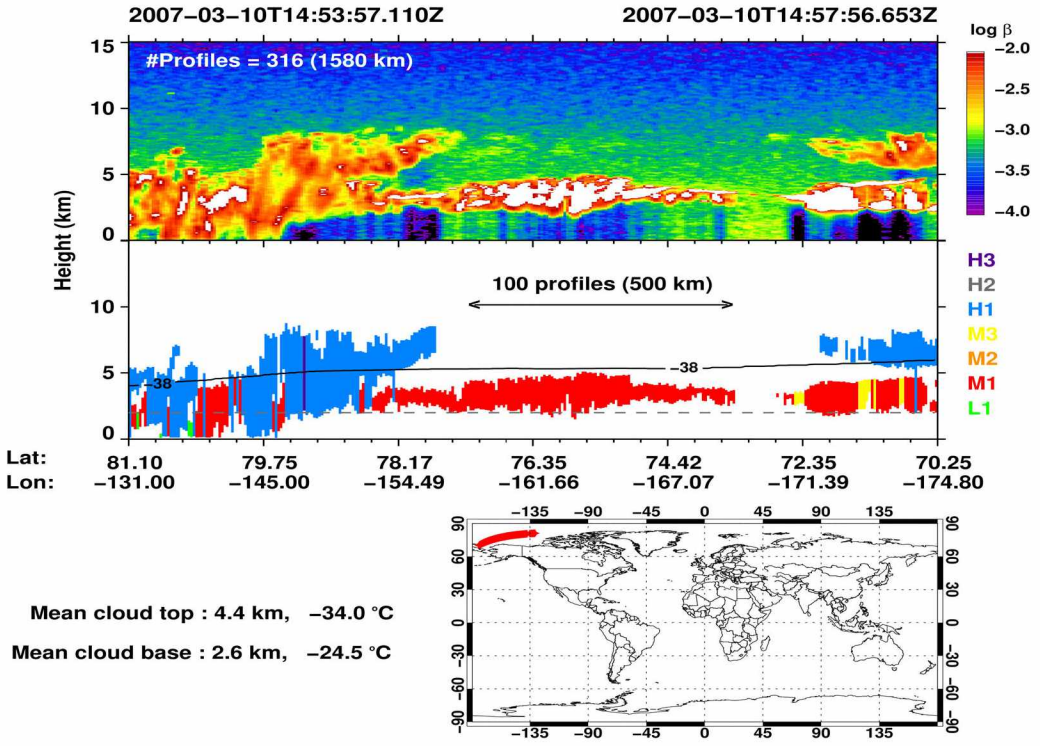

Figure 4.10: CALIPSO backscattering and cloud category masks derived for March 10, 2007.

The corresponding CALIPSO observations for the day of March 10, 2007 are shown in Figure 4.10. The M1 cloud forms as a layer along with an upper level H1 (cirrus) cloud. Table 4.6 shows the properties derived from the 100 profiles of the observed M1 cloud. The M1 cloud displays both relatively flat top and base altitudes with a mean value of 4.4 km and 2.6 km, respectively. The mean optical depth of the M1 cloud is 1.1. The SZA over the M1 cloud occurrence is 100° – 104°.

Table 4.6: Properties derived from the distinct M1 cloudy profiles observed on March 10, 2007.

		Min.	Max.	Mean	Median	Std. dev.
Cloud top	Height (km)	3.6	5.0	4.4	4.4	0.4
	Temperature (°C)	-37.0	-28.6	-34.0	-34.7	2.0
Cloud base	Height (km)	1.5	3.5	2.6	2.6	0.4
	Temperature (°C)	-29.4	-22.0	-24.6	-24.6	1.6
Optical depth		0.05	4.5	1.1	0.8	1.0
Solar zenith angle		100	104	102	102	1.2

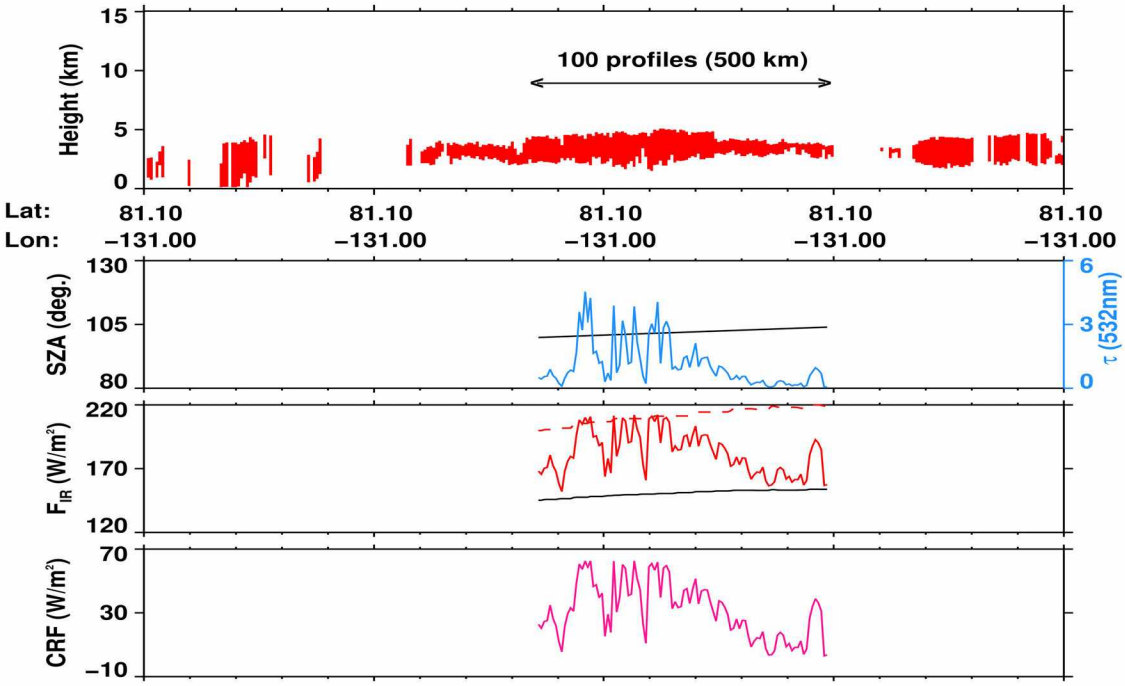

Figure 4.11: Cloud category masks, simulated irradiances (upwelling - dashed, downwelling - solid) and cloud radiative forcing for March 10, 2007.

Our radiative transfer simulations, where we assumed that the observed M1 cloud on March 10, 2007 was a pure ice cloud with ice crystals effective radius of 30 μm, are shown in Figure 4.11. As expected, we see that $F^{\downarrow}_{cloud,LW}$ increases with optical depth. Occasionally for the profiles where M1 cloud optical depth reaches 3, then $F^{\downarrow}_{cloud,LW}$ equals $F^{\uparrow}_{cloud,LW}$. The complete results of all the scenarios considered (ice, water, mixed-phase) for the observed M1 clouds on March 10, 2007 are provided in Table 4.7. For all the scenarios considered,

Table 4.7: Radiative transfer simulations for the M1 clouds observed on March 10, 2007.

		SW			LW			SW + LW	CRF
		$F^{\downarrow}$	$F^{\uparrow}$	F_{net}	$F^{\downarrow}$	$F^{\uparrow}$	F_{net}	F_{net}	W/m^2
Clear sky		0	0	0	150.7	211.6	-60.9	-60.9	
Ice cloud	30 μm columns	0	0	0	182.3	211.6	-29.3	-29.3	31.6
	60 μm columns	0	0	0	182.4	211.6	-29.2	-29.2	31.7
Water cloud	10 μm spheres	0	0	0	182.4	211.6	-29.2	-29.2	31.7
	20 μm spheres	0	0	0	184.1	211.6	-27.5	-27.5	33.4
Mixed-phase	ice frac. 0.8 water frac. 0.2	0	0	0	182.5	211.6	-29.1	-29.1	31.8
	ice frac. 0.6 water frac. 0.4	0	0	0	182.5	211.6	-29.1	-29.1	31.8
	ice frac. 0.4 water frac. 0.6	0	0	0	182.5	211.6	-29.1	-29.1	31.8
	ice frac. 0.2 water frac. 0.8	0	0	0	182.5	211.6	-29.1	-29.1	31.8

the presence of M1 cloud imposes a net warming effect. The average warming effect at the surface derived for eight cloud microphysical scenarios is 32 W/m^2.

4.5.3 Case 3: December 1, 2007

On December 1, 2007 CALIPSO detected a distinct M1 cloud over the Kara Sea coast during its orbital overpass at 0531 UTC. The prevailing synoptic and cloud conditions over the region of M1 clouds are shown in Figures 4.12 and 4.13.

A surface high pressure system extends from the Arctic Ocean to central Eurasia. The middle and upper level atmospheric circulation show an amplified ridge pattern along 90^o E. MODIS IR imagery clearly depicts the clouds (bright) formed along the ridge where positive vorticity advection uplifts the air mass and the air reaches supersaturation. The M1 clouds (relatively lighter) form downstream of the ridge pattern where negative vorticity advection prevails with sinking motion of air masses. This indicates that the observed M1 cloudiness is due to the mixing of cold air masses from the surrounding region at lower levels of the troposphere.

The corresponding CALIPSO observations for the day of December 1, 2007 are shown in Figure 4.14. The M1 clouds form as an isolated layer in the atmosphere with no other clouds in the region. Table 4.8 shows the properties derived from the 100 profiles of the

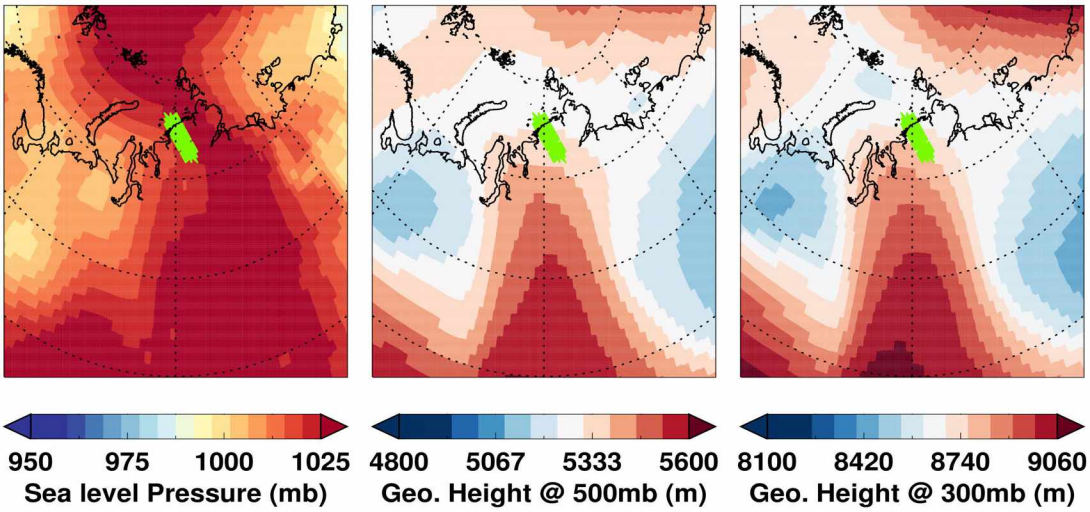

Figure 4.12: Synoptic meteorological conditions over a portion of the Arctic region on December 1, 2007 during a CALIPSO overpass (green).

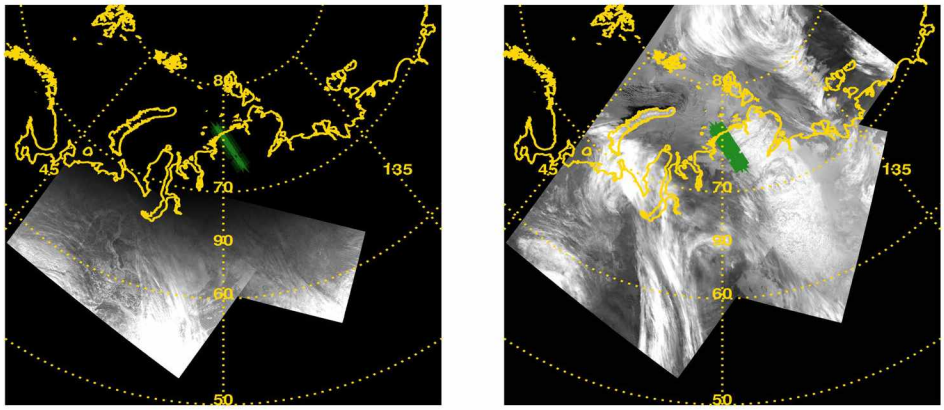

Figure 4.13: MODIS visible (left) and IR imagery (right) showing cloudy conditions and the overlaid CALIPSO orbit (green) on December 1, 2007.

observed M1 cloud. The mean of the M1 cloud top and base altitudes is found to be 4.4 km and 1.4 km, respectively. While the cloud top altitude is relatively flat, the cloud base altitudes vary greatly reaching a minimum altitude of 0.2 km above the surface level. Although the CALIPSO derived optical depth of the cloud show values as high as 6.0 for few profiles, the mean optical depth of the cloud is found to be 1.1. The SZA over the M1 cloud is 94^{o} – 98^{o}, and thus the thermal effect alone determines the net radiative effect of the cloud.

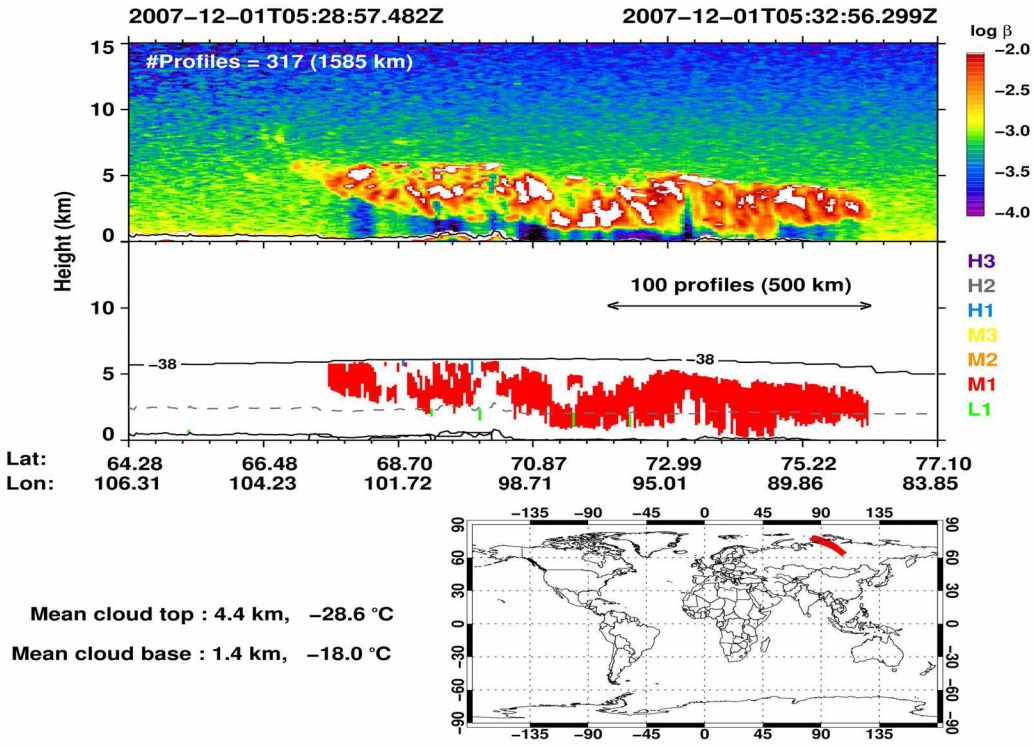

Figure 4.14: CALIPSO backscattering and cloud category masks derived for December 1, 2007.

Table 4.8: Properties derived from the distinct M1 cloudy profiles observed on December 1, 2007.

		Min.	Max.	Mean	Median	Std. dev.
Cloud top	Height (km)	2.8	5.3	4.4	4.4	0.5
	Temperature (°C)	-33.0	-20.8	-28.6	-29.0	2.5
Cloud base	Height (km)	0.2	3.8	1.4	1.3	0.8
	Temperature (°C)	-29.0	-13.0	-18.0	-16.4	4.0
Optical depth		0.05	6.0	1.1	1.0	1.0
Solar zenith angle		94	98	96	96	1.2

Our radiative transfer simulations, where we assumed that the observed M1 cloud on December 1, 2007 was a pure ice cloud with ice crystals effective radius of 30 μm, are shown in Figure 4.15. Although the $F^{\downarrow}_{cloud,LW}$ increase with respect to the optical depth, $F^{\downarrow}_{cloud,LW}$ never reaches the value of $F^{\uparrow}_{cloud,LW}$. This confirms that the previously (for Case 1 and Case 2) observed $F^{\downarrow}_{cloud,LW} = F^{\uparrow}_{cloud,LW}$ is purely a coincidence. Recall that while $F^{\uparrow}_{cloud,LW}$ depends

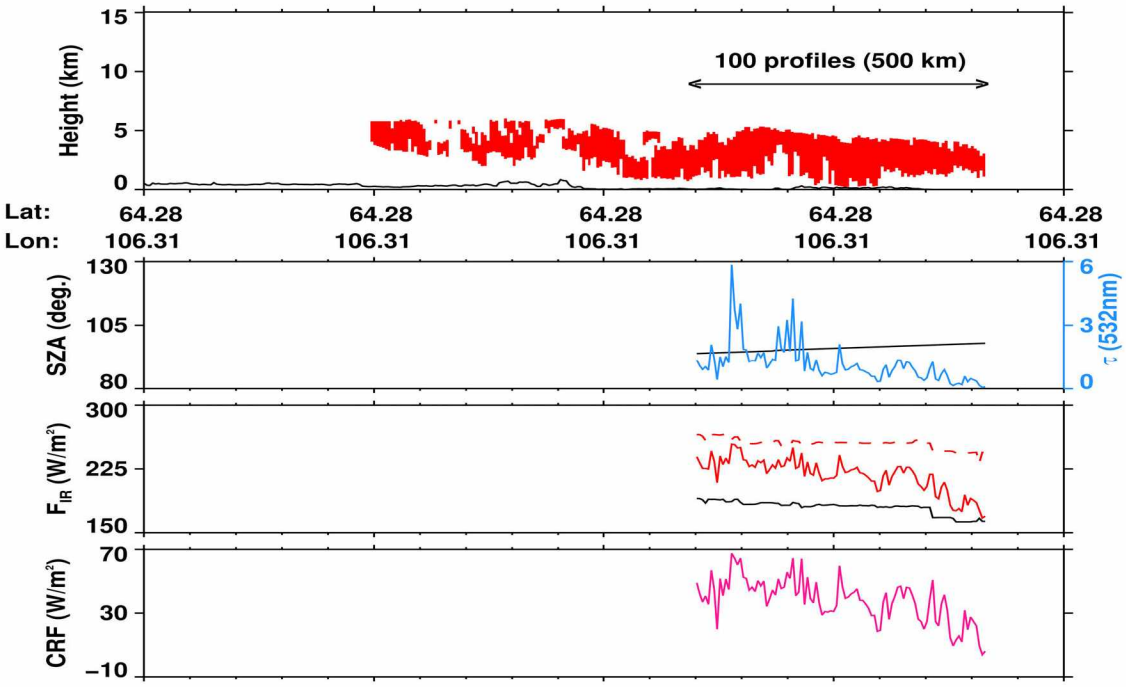

Figure 4.15: Cloud category masks, simulated irradiances (upwelling - dashed, downwelling - solid) and cloud radiative forcing for December 1, 2007.

Table 4.9: Radiative transfer simulations for the M1 clouds observed on December 1, 2007

		SW			LW			SW + LW	CRF
		$F^{\downarrow}$	$F^{\uparrow}$	F_{net}	$F^{\downarrow}$	$F^{\uparrow}$	F_{net}	F_{net}	W/m^2
Clear sky		0	0	0	180.0	254.6	-74.6	-74.6	
Ice cloud	30 μm columns	0	0	0	218.0	254.6	-36.6	-36.6	38.0
	60 μm columns	0	0	0	218.1	254.6	-36.5	-36.5	38.1
Water cloud	10 μm spheres	0	0	0	217.5	254.6	-37.1	-37.1	37.5
	20 μm spheres	0	0	0	220.0	254.6	-34.6	-34.6	40.0
Mixed-phase	ice frac. 0.8 water frac. 0.2	0	0	0	218.0	254.6	-36.6	-36.6	38.0
	ice frac. 0.6 water frac. 0.4	0	0	0	218.0	254.6	-36.6	-36.6	38.0
	ice frac. 0.4 water frac. 0.6	0	0	0	218.0	254.6	-36.6	-36.6	38.0
	ice frac. 0.2 water frac. 0.8	0	0	0	217.7	254.6	-36.9	-36.9	37.7

on the surface emission (temperature), $F^{\downarrow}_{cloud,LW}$ also depends on the cloud temperature and water content. The complete results of all the scenarios considered (ice, water, mixed-

phase) for the observed M1 clouds on December 1, 2007 are provided in Table 4.9. For all these scenarios, the presence of M1 clouds results in a net warming effect. The average warming effect at the surface derived for eight cloud microphysical scenarios considered is 38.1 W/m^2. For the case of pure water cloud, the CRF is relatively higher than in other scenarios.

4.5.4 Case 4: December 6, 2007

On December 6, 2007 CALIPSO detected a distinct M1 cloud over Baffin Island during its orbital overpass at 0739 UTC. The prevailing synoptic and cloud conditions over the region of M1 clouds are shown in Figures 4.16 and 4.17.

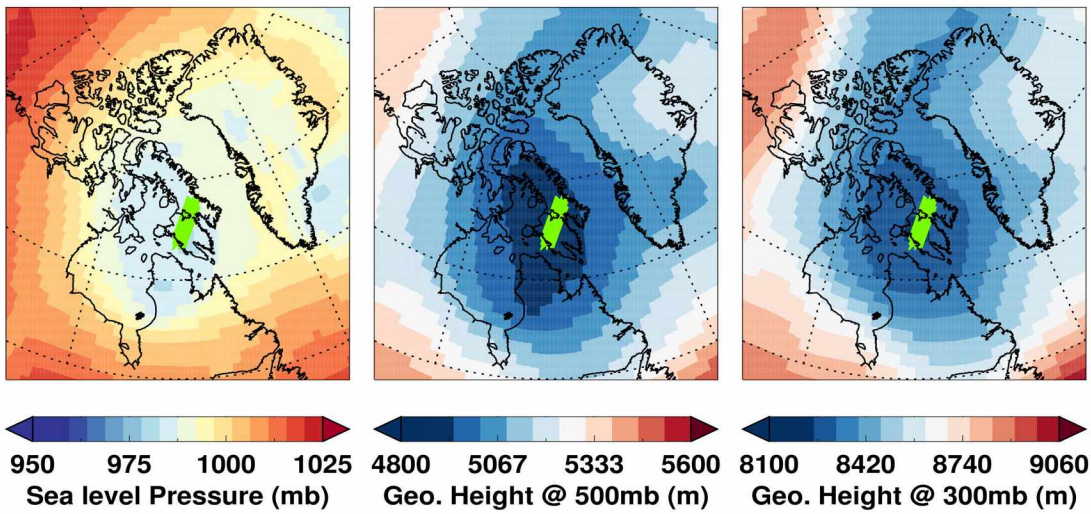

Figure 4.16: Synoptic meteorological conditions over a portion of the Arctic region on December 6, 2007 during a CALIPSO overpass (green).

While a surface low pressure system (980 mb) prevails, the middle and upper atmosphere circulation shows the core of the polar vortex over Baffin Island. This is a typical winter atmospheric circulation over the Arctic region, where the cold air from the Arctic Ocean extends towards Greenland and Baffin Island. MODIS IR imagery shows high amount of cloudiness over Greenland, while scattered thin clouds are present over Baffin Bay and the Canadian Archipelago. Overall, the observed low pressure system is not intense enough to produce thick clouds.

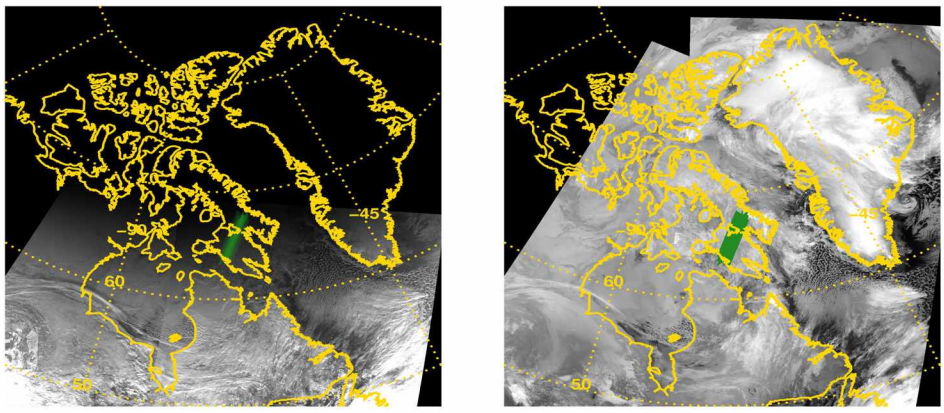

Figure 4.17: MODIS visible (left) and IR imagery (right) showing cloudy conditions and the overlaid CALIPSO orbit (green) on December 6, 2007.

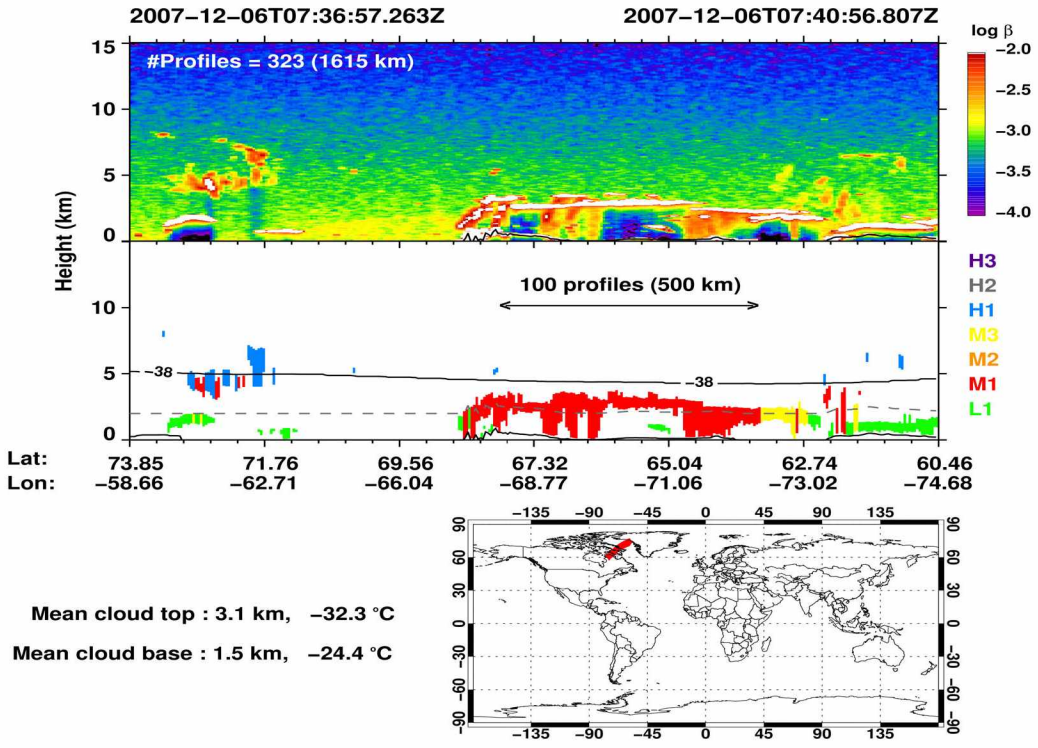

Figure 4.18: CALIPSO backscattering and cloud category masks derived for December 6, 2007.

The corresponding CALIPSO observations for the day of December 6, 2007 is shown in Figure 4.18. M1 cloud is formed as an isolated layer in the atmosphere with no other clouds

present. Table 4.10 shows the properties derived from the 100 profiles of the observed M1 cloud. The mean of the M1 cloud top and base altitudes is 4.4 km and 1.4 km, respectively. While the cloud top altitude is relatively flat, the cloud base altitudes vary greatly reaching a minimum altitude of 0.2 km above the surface level. Although the CALIPSO derived optical depth of the cloud show values as high as 6.0 in few profiles, the mean cloud optical depth is 1.1. The SZA over the region of M1 cloud occurrence varies from 94° – 98°.

Table 4.10: Properties derived from the distinct M1 cloudy profiles observed on December 6, 2007.

		Min.	Max.	Mean	Median	Std. dev.
Cloud top	Height (km)	2.3	3.7	3.0	3.0	0.4
	Temperature (°C)	-35.0	-27.0	-32.3	-33.2	2.3
Cloud base	Height (km)	0.1	2.8	1.4	1.7	1.0
	Temperature (°C)	-32.0	-14.4	-24.4	-25.0	4.6
Optical depth		0.4	6.0	2.0	2.0	1.2
Solar zenith angle		126	130	128	128	1.0

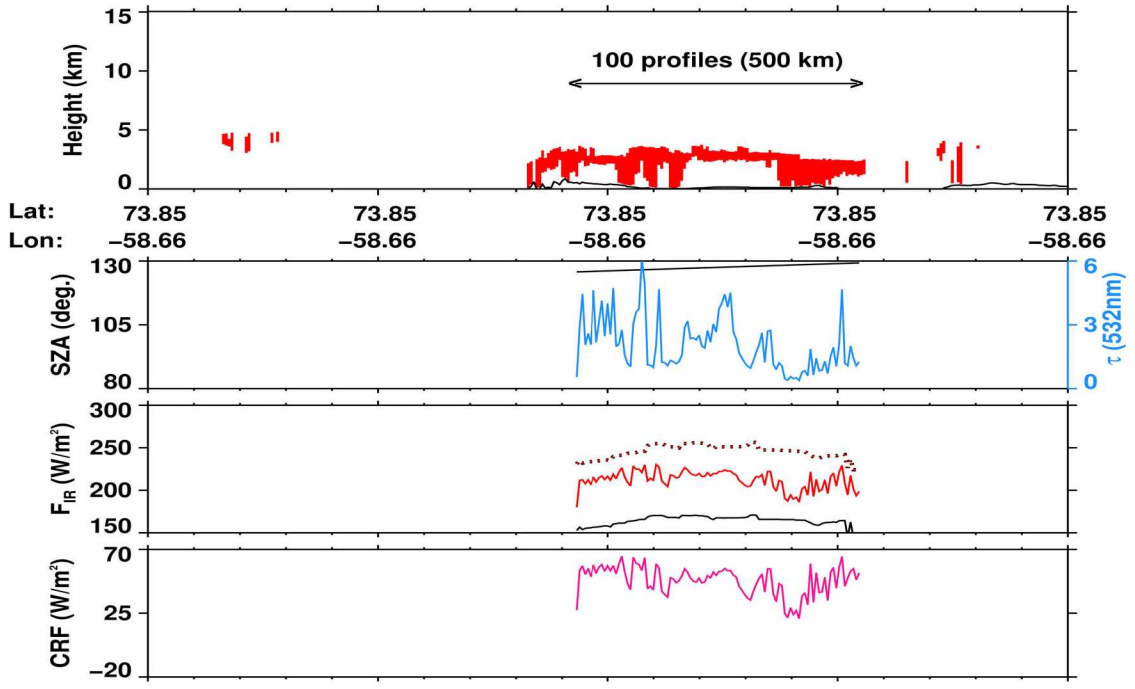

Figure 4.19: Cloud category masks, simulated irradiances (upwelling - dashed, downwelling - solid) and cloud radiative forcing for December 6, 2007.

Table 4.11: Radiative transfer simulations for the M1 clouds observed on December 6, 2007.

		SW			LW			SW + LW	CRF
		$F^{\downarrow}$	$F^{\uparrow}$	F_{net}	$F^{\downarrow}$	$F^{\uparrow}$	F_{net}	F_{net}	W/m^2
Clear sky		0	0	0	164.0	245.2	-81.2	-81.2	
Ice cloud	30 μm columns	0	0	0	212.1	245.2	-33.1	-33.1	48.1
	60 μm columns	0	0	0	212.2	245.2	-33.0	-33.0	48.2
Water cloud	10 μm spheres	0	0	0	212.3	245.2	-32.9	-32.9	48.3
	20 μm spheres	0	0	0	214.0	245.2	-31.2	-31.2	50.0
Mixed-phase	ice frac. 0.8 water frac. 0.2	0	0	0	212.3	245.2	-32.9	-32.9	48.3
	ice frac. 0.6 water frac. 0.4	0	0	0	212.4	245.2	-32.8	-32.8	48.4
	ice frac. 0.4 water frac. 0.6	0	0	0	212.4	245.2	-32.8	-32.8	48.4
	ice frac. 0.2 water frac. 0.8	0	0	0	212.4	245.2	-32.8	-32.8	48.4

Our radiative transfer simulations, where we assumed that the observed M1 cloud on December 6, 2007 was a pure ice cloud with ice crystals effective radius of 30 μm, are shown in Figure 4.19. The $F^{\downarrow}_{cloud,LW}$ increases with respect to the optical depth resulting in an increase in the CRF. The complete results of all the scenarios considered (ice, water, mixed-phase) for the observed M1 clouds on December 6, 2007 are provided in Table 4.11. The average warming effect at the surface derived for eight cloud microphysical scenarios considered is 48.5 W/m^2. Compared to previous cases (i.e., Case 1, Case 2, Case 3), the warming effect observed in Case 4 is considerably higher. This is attributed to the higher water vapor content in the atmosphere. The clear sky net irradiance shows lower amounts of cooling (up to 81 W/m^2) at the surface, compared to other cases.

4.5.5 Case 5: February 14, 2009

On February 14, 2009 CALIPSO detected a distinct M1 cloud over the Beaufort Sea during its orbital overpass at 2021 UTC. The prevailing synoptic and cloud conditions over the region of M1 clouds are shown in Figures 4.20 and 4.21. The surface high pressure system prevails over the Canada and extends towards the Beaufort Sea. The middle and upper atmospheric circulation shows that cold air from the Arctic Ocean extends towards Siberia, while a ridge pattern brings warm moist air from the North Pacific Ocean over central Alaska towards the Beaufort Sea. While the cold air outbreak from the Arctic Ocean shows

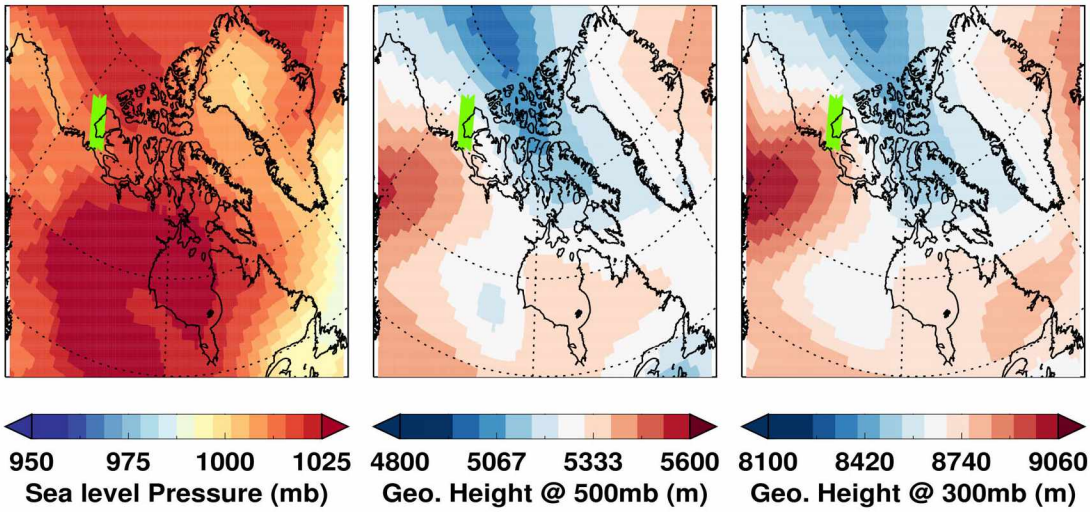

Figure 4.20: Synoptic meteorological conditions over a portion of the Arctic region on February 14, 2009 during a CALIPSO overpass (green).

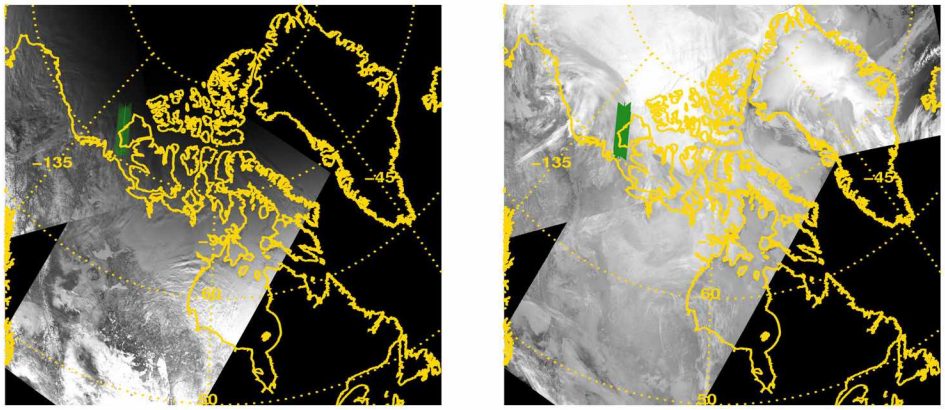

Figure 4.21: MODIS visible (left) and IR imagery (right) showing cloudy conditions and the overlaid CALIPSO orbit (green) on February 14, 2009.

extensive cloudiness (IR imagery), the M1 cloud is detected along the leading edge of the downstream of the ridge.

The corresponding CALIPSO observations for the day of February 14, 2009 are shown in Figure 4.22. M1 clouds formed as a muti-layered cloud system with thin layers extending along a portion of the system. The visual inspection of CALIPSO backscattering shows the presence of a supercooled liquid layer at the M1 cloud top altitude. However, the super-

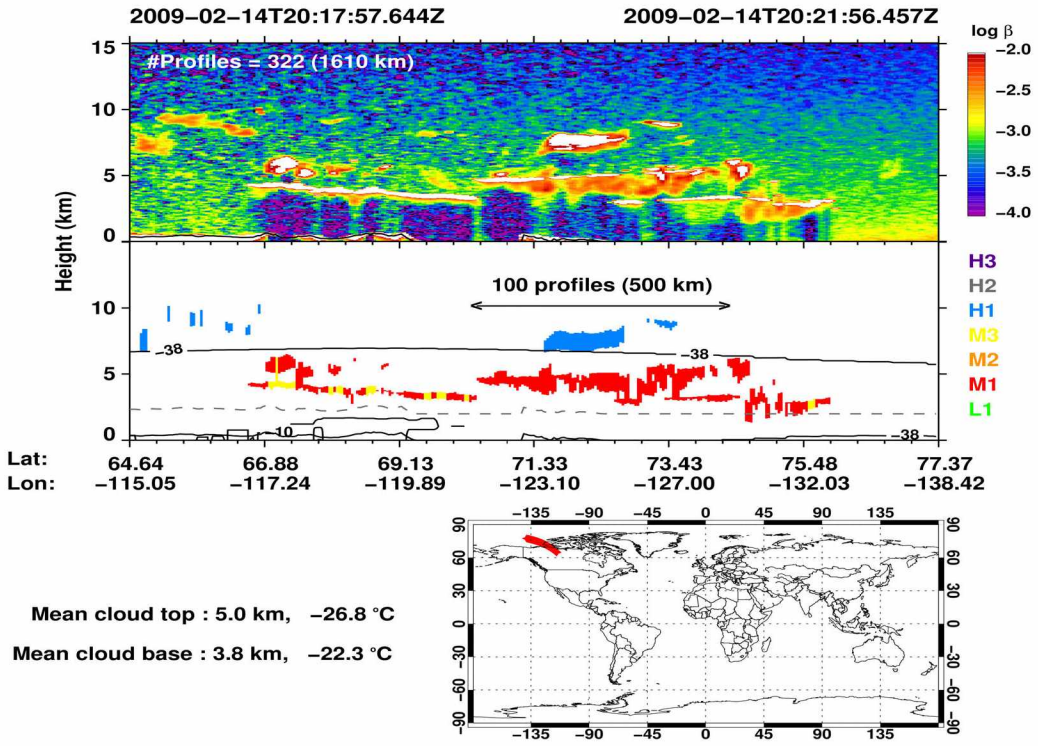

Figure 4.22: CALIPSO backscattering and cloud category masks derived for February 14, 2009.

Table 4.12: Properties derived from the distinct M1 cloudy profiles observed on February 14, 2009.

		Min.	Max.	Mean	Median	Std. dev.
Cloud top	Height (km)	3.1	5.8	5.0	5.0	0.6
	Temperature (°C)	-33.0	-21.4	-27.0	-26.0	3.0
Cloud base	Height (km)	2.6	5.2	3.4	3.8	0.6
	Temperature (°C)	-30.0	-19.0	-22.3	-21.6	2.5
Optical depth		0.06	4.0	1.0	0.6	1.0
Solar zenith angle		83	87	85	85	1.2

cooled liquid layer is not dense enough to completely attenuate the lidar pulses. Table 4.12 shows the properties derived from the 100 profiles of the observed M1 cloud. The mean of the M1 cloud top and base altitudes is found to be 5.0 km and 3.4 km, respectively. Here, the M1 cloud optical depth for the observed 100 profiles varies from 0.06 – 4.0 with mean and median values of 1.0 and 0.6, respectively. In comparison to the previous four cases, the median of the M1 cloud optical depth (0.6) is the lowest for Case 5. The SZA

over the region of M1 cloud occurrence varied from 83° – 87°. Thus, the irradiances in the solar spectral range might be low but not absolute zero and it allows us to investigate how the radiative transfer of solar energy through M1 cloud will influence net radiation at the surface.

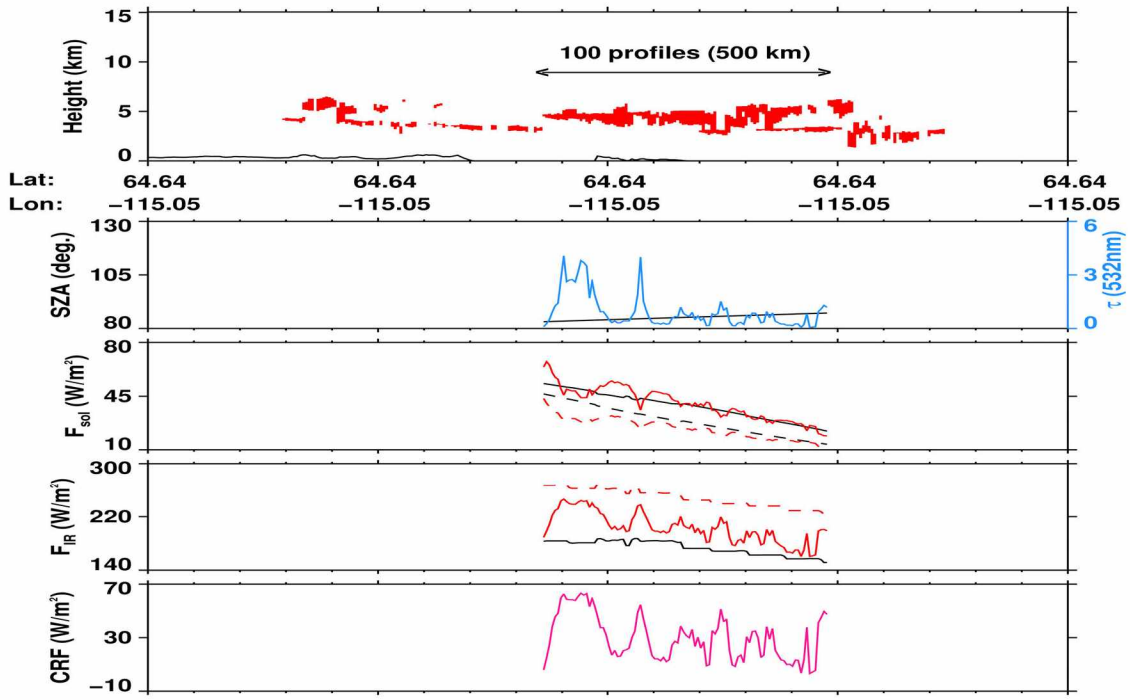

Figure 4.23: Cloud category masks, simulated irradiances (upwelling - dashed, downwelling - solid) and cloud radiative forcing for February 14, 2009.

Our radiative transfer simulations, where we assumed that the observed M1 cloud on February 14, 2009 was a pure ice cloud with ice crystals effective radius of 30 μm, are shown in Figure 4.23. The trend in solar irradiance component is consistent with the trend in the solar zenith angle (i.e., the incident solar radiation increases with increasing SZA).With respect the cloud optical depth, SW irradiance decreases and LW irradiance increases as the optical depth increases. In other words, clouds with higher optical depths reflect more radiation back to space and the net solar radiation at the surface is reduced. However, the warming induced by solar radiation is less than the cooling due to thermal radiation. Thus, the M1 cloud occurrence produces a net warming effect at the surface. The complete results of all the scenarios considered (ice, water, mixed-phase) for the observed M1 clouds on February 14, 2009 are provided in Table 4.13. Under clear sky conditions, the solar

irradiance warms the surface by 24.0 W/m^2, while the thermal irradiance cools the surface by 75.0 W/m^2 to produce a net cooling of 51.0 W/m^2 at the surface. In the presence of M1 cloud the $F^{\downarrow}$ decreases in the SW component and increases in the LW component. However, it is found that for all the M1 cloud scenarios the decrease in heating from the SW component is less than the increase in heating from the LW component producing a net warming effect. The average warming effect at the surface derived for the eight cloud microphysical scenarios is 23.3 W/m^2.

Table 4.13: Radiative transfer simulations for the M1 clouds observed on February 14, 2009

		SW			**LW**			**SW + LW**	**CRF**
		$F^{\downarrow}$	$F^{\uparrow}$	F_{net}	$F^{\downarrow}$	$F^{\uparrow}$	F_{net}	F_{net}	**W/m^2**
Clear sky		53.0	29.0	24.0	173.5	248.5	-75.0	-51.0	
Ice cloud	30 μm columns	40.6	24.0	16.6	203.4	248.5	-45.1	-28.5	22.5
	60 μm columns	40.5	24.1	16.4	203.4	248.5	-45.1	-28.7	22.3
Water cloud	10 μm spheres	43.0	25.0	18.0	203.3	248.5	-45.2	-27.2	23.8
	20 μm spheres	43.0	25.0	18.0	205.1	248.5	-43.4	-25.4	25.6
Mixed-phase	ice frac. 0.8 water frac. 0.2	41.0	24.2	16.8	203.5	248.5	-45.0	-28.2	22.8
	ice frac. 0.6 water frac. 0.4	41.3	24.3	17.0	203.5	248.5	-45.0	-28.0	23.0
	ice frac. 0.4 water frac. 0.6	41.8	25.0	16.8	203.5	248.5	-45.0	-28.3	22.7
	ice frac. 0.2 water frac. 0.8	42.2	24.6	17.6	203.5	248.5	-45.0	-27.5	23.5

4.6 Discussion

Out of the five cases studies presented here, four cases (i.e., Case 1, 2, 3, 5) are associated with a high-pressure ridge. In these cases the M1 clouds are found along the leading downstream edge of the ridge pattern. At this location in the ridge we expect to find conditions with weaker ascent that supports the formation of thinner clouds than found along the upstream edge of the ridge where we would expect to find stronger ascent and thicker clouds. The remaining case (i.e., Case 4) is associated with a weak low pressure system. There is a lack of thick clouds over the low pressure system as the warm air sector of the trough appears too weak to provide sufficient moisture and ascent to form thick clouds.

In general the radiative forcing of a cloud depends on its macrophysical (altitude, temperature, thickness) and microphysical (cloud phase, CWC, particle size distribution, particle

habit) properties. Additionally, the surface cloud radiative properties depend on the surface albedo. The radiative transfer simulations of the M1 clouds show a net warming effect for all the five case studies. In comparison to the annual mean of CRF_{LW} for liquid and ice clouds (*Shupe and Intrieri*, 2004), the CRF_{LW} due to M1 clouds is consistent owing to their low optical depths.

We investigate radiative transfer simulations of the observed M1 clouds with varying optical depth. The CALIPSO data product used for the current study reports an uncertainty in the retrieval of optical depth by a factor of 2 (*Vaughan et al.*, 2009). We have chosen Case 5, where both solar and longwave components contribute in the net irradiance for this purpose. We performed sensitivity simulations by varying the optical depth of the M1 cloud by a factor of 2 (2τ and $\tau/2$) and the SZA. This is done to investigate the radiative effects of M1 clouds under sunlight conditions. Table 4.14 shows the results of the radiative transfer simulations with varying optical depth and SZA.

Table 4.14: Radiative transfer simulations with varying optical depth of M1 cloud and the SZA in Case-5

		SW			**LW**			**SW + LW**	**CRF**
		$F^{\downarrow}$	$F^{\uparrow}$	F_{net}	$F^{\downarrow}$	$F^{\uparrow}$	F_{net}	F_{net}	**W/m^2**
SZA = 70°	Clear sky	354.2	197.3	156.9	173.5	248.5	-75.0	81.9	
	Ice cloud (τ)	292.7	171.4	121.3	203.4	248.5	-45.1	76.2	-5.7
	Ice cloud (2τ)	265.6	159.9	105.7	214.4	248.5	-34.1	71.6	-10.3
	Ice cloud ($\tau/2$)	315.0	180.7	134.3	193.1	248.5	-55.4	78.9	-3.0
SZA = 80°	Clear sky	144.6	79.3	65.3	173.5	248.5	-75.0	-9.7	
	Ice cloud (τ)	110.3	64.9	45.4	203.4	248.5	-45.1	0.3	10.0
	Ice cloud (2τ)	100.0	60.6	39.4	214.4	248.5	-34.1	5.3	15.0
	Ice cloud ($\tau/2$)	119.8	68.9	50.9	193.1	248.5	-55.4	-4.5	5.2
SZA = 90°	Clear sky	0	0	0	173.5	248.5	-75.0	-75.0	
	Ice cloud (τ)	0	0	0	203.4	248.5	-45.1	-45.1	29.9
	Ice cloud (2τ)	0	0	0	214.4	248.5	-34.1	-34.1	40.9
	Ice cloud ($\tau/2$)	0	0	0	193.1	248.5	-55.4	-55.4	19.6

As expected, the $F^{\downarrow}_{SW}$ radiation decreases and $F^{\uparrow}_{LW}$ radiation increases with the increase in optical depth of the cloud. Within the uncertainty level of CALIPSO optical depth retrievals the CRF due to M1 cloud is found to vary 40% and shows a net warming effect. We performed additional sensitivity simulations by the varying the optical depth of clouds to obtain a threshold value where the net CRF is negligible, i.e., radiative forcing at clear sky conditions is equal to forcing due to the cloud. Here, cloud optical depth as low as 0.004

produces similar forcing as under clear sky conditions. Additionally, it is found that at lower SZA (70°), M1 clouds have a net cooling effect. This cooling gradually decreases out to produce a net warming effect with increasing SZA. Beyond 90° (i.e., when the Sun is at the horizon), any increase in SZA does not have any effect on the CRF. In other words at SZA >90°, CRF is entirely dependent on the LW component that is determined by cloud optical depth and temperature. For instance under no sunlight conditions (SZA >90°), the use of the original optical depth produced a warming effect of 30.0 W/m^2. The change in CRF with increasing optical depth by factor of 2 is ~1.2 W/m^2, while with decreasing optical depth by factor of 2 is 16.3 W/m^2. This clearly shows the significance of optically thin clouds over the Arctic, especially during the wintertime where solar zenith angle is high for prolonged periods.

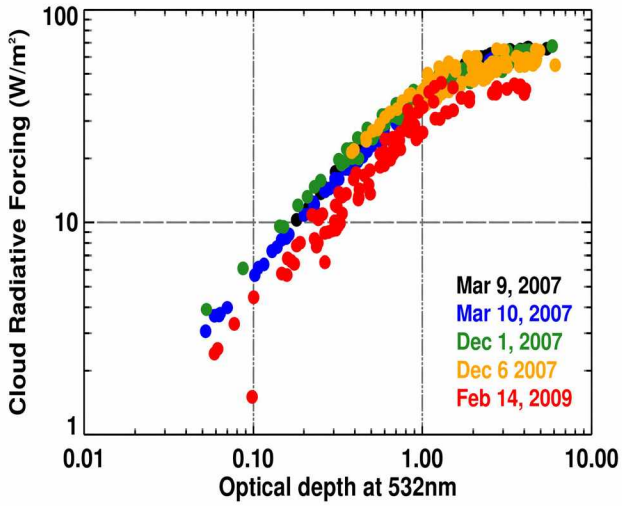

Figure 4.24: Variation of M1 cloud radiative forcing with optical depth.

In our radiative analysis of each of the five clouds we determined the radiative properties at 5 km resolution at each of the CALIPSO profiles, and then averaged the CRF over the entire cloud. We plot the variation of CRF with optical depth for the five clouds in Figure 4.24. The CRF associated with the sunlight cloud (i.e., Case 5) is lower due to blocking of solar shortwave radiation by the cloud. In general we see that the CRF due to M1 clouds increases exponentially with optical depth for optical depths up to 1 (i.e. from approximately 4 W/m^2 to 50 W/m^2 between 0.1 and 1). For optical depths between 1 and 6 the CRF increases less rapidly with optical depth (i.e, from approximately 50 W/m^2

to 60 W/m^2 between 1 and 6). This is consistent with previous studies that show that CRF_{LW} varies exponentially with the optical depth for thin clouds (*Stephens*, 1978; *Shupe and Intrieri*, 2004). The mean M1 cloud optical depths for the five cases are 1.1, 0.8, 1.0, 2.0 and 0.6, respectively. For these optical depths, the CRF varies from 20 W/m^2 to 60 W/m^2.

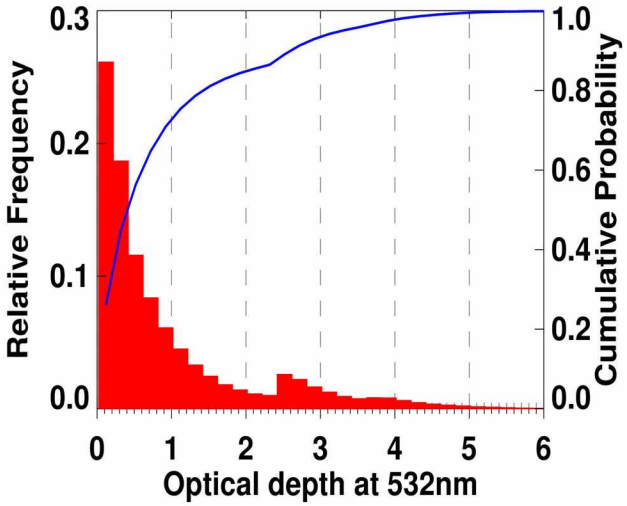

Figure 4.25: Probability density function of M1 cloud optical depths derived from four years of CALIPSO data.

We calculated the optical depth for M1 clouds over the entire four year CALIPSO data set at a spatial scale of 10 km (i.e., 2-profile). As we found in Chapter 3, the optical depths are between 0 and 6 (Table 3.3). We show the probability density function and cumulative distribution function of the M1 cloud optical depth in Figure 4.25. The median optical depth is 0.4 which corresponds to a CRF_{LW} of 20 W/m^2. We see that 20% of the clouds have an optical depth greater than 1.0 (the average of our five case studies), and these clouds have a CRF_{LW} of over 40 W/m^2 during the polar night. In Chapter 3, we saw that 50% of M1 clouds are found in the polar regions (Table 3.9), and thus we conclude that these clouds make a significant contribution to the atmospheric radiation budge during the polar night.

4.7 Summary

Five case studies of distinct M1 clouds spanning a horizontal extent of 500 km were identified from four years of CALIPSO data. These distinct clouds are likely thin altostratus with

relatively flat tops. Radiative transfer simulations of these M1 clouds were performed using reanalysis meteorological data. The dependence of CRF_{SW}, CRF_{LW} on the observed M1 cloud characteristics has been investigated.

Our key findings in this Chapter are as follows:

1. During nighttime, M1 clouds have a warming effect at the surface. For the five case studies presented here the warming effect varies between 23 and 48 W/m^2.

2. During daytime, M1 clouds have a net cooling effect due to reflection of shortwave radiation. For this study during winter days (solar zenith angle < 70^o) the cooling effect varies between 3 and 10 W/m^2.

3. The optical depth of M1 clouds is less than 1.0 for 80% of these clouds. For these M1 clouds the radiative forcing is insensitive to the cloud phase.

Chapter 5
Summary, conclusions and future work

From a climate perspective, understanding the cloud radiative effects are important. The accurate identification of cloud type and its composition takes the foremost step in this process. Evolving studies from ground and satellite measurements of clouds show that cloud properties vary widely not only with geographical location but also with its altitude of occurrence in the troposphere. Thus, identifying cloud types solely based on the genera (altitude range of occurrence) of clouds could lead to spurious inference on the role of a cloud type. The current dissertation focuses on the midlevel ice clouds, specifically ones that are optically thin where lidar pulses pass through the clouds. The research presented here can be summarized as two major parts: (a) the occurrence and properties of optically thin midlevel ice clouds, and (b) the radiative effects of these clouds.

5.1 Summary

In Chapter 2, we compare ground-based and satellite lidar measurements using six case studies over the AFARS station. Our criteria for selecting these case studies was to observe all the representative conditions over AFARS that include clear skies, high, mid and low level clouds. This was done to understand the lidar signal characteristics and its ability to identify optically thin clouds. The formation of different types of clouds over the AFARS station has been investigated. This study was supported by local radiosonde data from Fairbanks International Airport, synoptic maps derived from the MERRA reanalysis data, and MODIS imagery. We established that optically thin clouds are measured consistently by both the ground-based and satellite-based lidars. We assessed the uncertainty in the reanalysis temperature data relative to the radiosonde measurements.

In Chapter 3, we developed and implemented a cloud classification scheme based on logic-based rules derived from established studies of the clouds. We determined the occurrences of optically thin midlevel clouds in the context of all tropospheric clouds that have been detected by CALIPSO over four years. Our logic-based rules use cloud top temperatures and altitudes to identify high- (H), mid- (M) and low- (L) level clouds. Additionally, we used the ability of CALIOP lidar signals to penetrate the clouds to separate optically thin and thick clouds. These logic-based rules resulted in seven types of clouds (L1, M1, M2,

M3, H1, H2 and H3), where optically thin midlevel ice clouds are referred to as M1 clouds. We tested the classification sensitivity to temperature thresholds by varying the temperature thresholds by the uncertainty in the reanalysis data, and found that the classification was not sensitive to these changes. We examined the occurrence of the M1 clouds during day and night, and found that at the single profile scale (5 km) there were differences in the cloud occurrences, while at the two-profile scale (10 km) there was no change in cloud occurrence. Given our interest in Arctic clouds, where day-night differences could yield seasonal variations, we then analyzed the CALIPSO data set at 10 km resolution.

Having categorized the clouds, we then investigated the global distribution and seasonal variations of these seven cloud types, and day-night differences in cloud occurrences have been investigated. The global distribution of cloud types are found to be consistent with the dominant climate regimes produced by the large-scale atmospheric circulation. Low level L1 clouds occur more commonly than all other clouds. Over the tropics in the regions dominated by mean upward motions and deep convection there are higher amounts of optically thin H1 clouds and the highest amounts of optically thick H3 clouds. Over the sub-tropical regions, dominated by mean downward motions with convection confined to the boundary layer, L1 clouds dominate over oceans while over land (i.e., deserts) there are low amounts of high and midlevel clouds and a complete lack of L1 clouds. Over midlatitudes, where large-scale cyclonic systems dominate the general circulation, there are higher amounts of optically thin H1 clouds and optically thick H3 and M3 clouds. In polar regions there are higher amounts of optically thin M1 and H1 clouds than in any other region.

Having identified thin midlevel M1 clouds we present the following key findings:

1. The global mean occurrence of M1 clouds is 4.5% and represents 7.3% of all tropospheric clouds detected by CALIPSO.

2. M1 clouds occur most commonly in the polar regions and during Arctic midwinter. M1 clouds occur 19% of the time.

3. In polar regions M1 clouds occur most commonly (both hemispheres) in the DJF months. However, there is no hemispheric symmetry in M1 cloud occurrences indicating that these clouds are formed through a variety of local processes.

4. Small day-night differences in M1 cloud occurrences are observed regionally.

5. M1 clouds can extend to large scales of 500 km, though they primarily occur at smaller spatial scales with median scale of 25 km.

6. M1 clouds are commonly found over Greenland and Tibet, particularly during the JJA months suggesting orographic formation.

In Chapter 4, we identified five distinct M1 clouds and investigated their radiative effects through model simulations. These case studies of were selected as large (>500 km) distinct M1 clouds that were representative of the environment and consistent with the scale of the reanalysis data and model assumptions. We assume these clouds are thin altostratus clouds. We validated the radiative model based on published studies and then applied the model to our case studies.

From our study of these five case studies, we present the following key findings:

1. During nighttime, M1 clouds have a warming effect at the surface. For the five case studies presented here the warming effect varies between 23 and 48 W/m^2.

2. During daytime, M1 clouds have a net cooling effect due to reflection of shortwave radiation. For this study during winter days (solar zenith angle < 70^o) the cooling effect varies between 3 and 10 W/m^2.

3. The optical depth of M1 clouds is less than 1.0 for 80% of these clouds. For these M1 clouds the radiative forcing is insensitive to the cloud phase.

5.2 Conclusions

We have identified optically thin midlevel ice clouds as a class (M1) of tropospheric clouds that have been previously underreported. Globally, M1 clouds represent 7.3% of tropospheric clouds and occur 4.5% of the time. These clouds are primarily found in the polar regions, equally commonly in the Arctic and Antarctic. M1 clouds occur most commonly in the Arctic winter and Antarctic summer. In the Arctic individual clouds can extend over 500 km horizontally, though the median horizontal scale of the clouds is 25 km.

We show that M1 clouds make significant contributions to the wintertime Arctic radiative budget. Based on our analysis of five large clouds we show that individual clouds have a

cloud radiative forcing of 23 – 48 W/m^2, and have a net warming effect. Occurring 19% of the time, we conclude that these clouds contribute 4.4 – 9.3 W/m^2 to the midwinter Arctic radiative budget. This is a significant contribution to the wintertime forcing of 40 W/m^2. In the global average the Arctic region represents 4.1% of the Earth's surface and the winter season represents 25% of the year. Thus we estimate that over the whole year and whole Earth these Arctic clouds contribute a forcing of 45 – 93 mW/m^2. Given uncertainties of ~1 W/m^2 in the IPCC global radiation budget, these clouds represent ~5 – 10% of the overall uncertainty in the radiation budget of the whole Earth system.

Our study highlights the importance of active satellite-based remote sensing in globally detecting and characterizing optically thin clouds. Our estimates of occurrence and fraction of clouds represents a lower bound, as M1 clouds can be obscured by optically thicker H3 and M3 clouds. The volume of measurements provided by the satellite allowed us to identify a small but consistent set of large clouds with which we could conduct a contemporary radiative analysis.

5.3 Future work

The role of the Arctic in the global climate system is a major topic of current research, as scientists attempt to understand the implications of changes in the Arctic for both the Arctic and the entire Earth system (see *Bhatt et al.* (2014) and references therein). The Arctic itself is expected to become warmer and more humid. The relationship between sea-ice and clouds is critical in understanding the changes in the Arctic. Changes in sea-ice cover are expected to result in changes in the cloud cover (*Liu et al.*, 2012). Both wintertime and summertime clouds can influence the Arctic sea-ice. Studies have shown a positive feedback as increased summertime cloudiness over an ice-free ocean enhances the downwelling longwave radiation and contributes to further surface warming (*Knudsen et al.*, 2015). Studies also show how wintertime cloudiness impacts the summer sea-ice by controlling how sea-ice grows during the winter (*Liu and Key*, 2014).

Given the importance of clouds in the Arctic climate system, we present polar stereographic maps of M1 cloud occurrence in all seasons in Figure 5.1. We present the following questions for further work.

1. Why is there a pronounced seasonal asymmetry in the cloud occurrences in the Arctic and Antarctic, where M1 clouds are most common in the Arctic during winter and

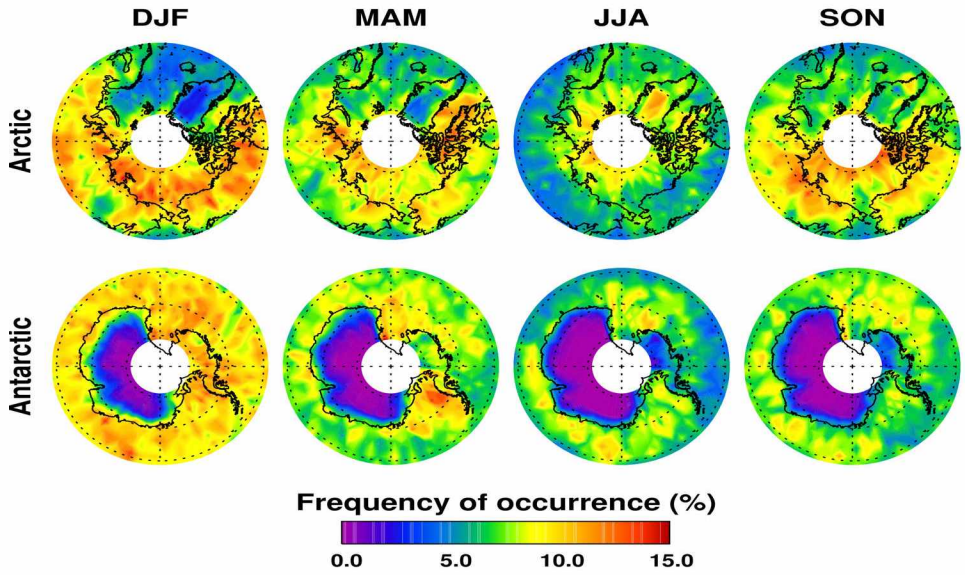

Figure 5.1: Seasonal variation in frequency of occurrence of M1 clouds over the polar regions.

in the Antarctic during summer?

2. Why are these clouds least common over Greenland in winter and most common in summer, unlike the rest of the Arctic?

3. Can mesoscale modeling explain the horizontal scales of these clouds and why their geographic and seasonal occurrences do not appear to change with scale?

4. How will the geographic and seasonal pattern of these clouds change as the Arctic becomes warmer and more humid?

References

Anderson, G., S. Clough, F. Kneizys, J. Chetwynd, and E. Shettle (1986), AFGL atmospheric constituent profiles (0-120 km), *Air Force Geophys. Lab*, Tech Rep, AFGL-TR-86-0110.

Andre, E. (2009), The Impact of ice crystals on radiative forcing and remote sensing of Arctic boundary-layer mixed-phase clouds, PhD Thesis, Johannes Gutenberg-Universitat Mainz, Germany.

Ansmann, A., M. Tesche, P. Seifert, D. Althausen, R. Engelmann, J. Fruntke, U. Wandinger, I. Mattis, and D. Muller (2009), Evolution of the ice phase in tropical altocumulus: SAMUM lidar observations over Cape Verde, *Journal of Geophysical Research-Atmospheres*, *114*, 1–20.

Atkinson, D. E., K. Sassen, M. Hayashi, C. F. Cahill, G. Shaw, D. Harrigan, and H. Fuelberg (2013), Aerosol properties over interior Alaska from lidar, DRUM Impactor sampler, and OPC-sonde measurements and their meteorological context during ARCTAS-A, April 2008, *Atmospheric Chemistry and Physics*, *13*(3), 1293–1310.

Baum, B. A., A. J. Heymsfield, P. Yang, and S. T. Bedka (2005a), Bulk scattering properties for the remote sensing of ice clouds. Part I: Microphysical data and models, *Journal of Applied Meteorology*, *44*(12), 1885–1895.

Baum, B. A., P. Yang, A. J. Heymsfield, S. Platnick, M. D. King, Y. X. Hu, and S. T. Bedka (2005b), Bulk scattering properties for the remote sensing of ice clouds. Part II: Narrowband models, *Journal of Applied Meteorology*, *44*(12), 1896–1911.

Belward, A., and T. Loveland (1996), The IGBP newsletter, *27*(http://www-surf.larc.nasa.gov/surf/pages/ftppage.html).

Bergeron, T. (1935), On the physics of clouds and precipitation, *Proces Verbaux de l'Association de Météorologie, IUGG*, 156–178.

Bhatt, U. S., D. A. Walker, J. E. Walsh, E. C. Carmack, K. E. Frey, W. N. Meier, S. E. Moore, F. J. W. Parmentier, E. Post, V. E. Romanovsky, and W. R. Simpson (2014), Implications of Arctic sea-ice decline for the earth system, *Annual Review of Environment and Resources, Vol 39*, *39*, 57 – 89.

Bony, S., B. Stevens, D. M. W. Frierson, C. Jakob, M. Kageyama, R. Pincus, T. G. Shepherd, S. C. Sherwood, A. P. Siebesma, A. H. Sobel, M. Watanabe, and M. J. Webb (2015), Clouds, circulation and climate sensitivity, *Nature Geoscience*, *8*(4), 261–268.

Chandrasekhar, S. (1950), *Radiative transfer*, Oxford University Press.

Collis, R. T. H., and P. B. Russell (1976), Lidar measurement of particles and gases by elastic backscattering and differential absorption, in *Laser Monitoring of the Atmosphere*, edited by E. D. Hinkley, Oxford University Press.

Comstock, J. M., T. P. Ackerman, and G. G. Mace (2002), Ground-based lidar and radar remote sensing of tropical cirrus clouds at Nauru Island: Cloud statistics and radiative impacts, *Journal of Geophysical Research-Atmospheres*, *107*(D23), AAC 16–1–AAC 16–14.

Cox, S. (1971), Cirrus clouds and the climate, *Journal of Atmospheric Sciences*, *28*, 1513–1515.

Curry, J. A., and E. E. Ebert (1992), Annual cycle of radiation fluxes over the Arctic-ocean - sensitivity to cloud optical properties, *Journal of Climate*, *5*(11), 1267–1280.

Curry, J. A., F. G. Meyer, L. F. Radke, C. A. Brock, and E. E. Ebert (1990), Occurrence and characteristics of lower tropospheric ice crystals in the Arctic, *International Journal of Climatology*, *10*(7), 749–764.

Dong, X. Q., B. K. Xi, K. Crosby, C. N. Long, R. S. Stone, and M. D. Shupe (2010), A 10 year climatology of Arctic cloud fraction and radiative forcing at Barrow, Alaska, *Journal of Geophysical Research-Atmospheres*, *115*, 1–14.

Duan, A. M., and G. X. Wu (2005), Role of the Tibetan Plateau thermal forcing in the summer climate patterns over subtropical Asia, *Climate Dynamics*, *24*(7-8), 793–807.

Eastman, R., and S. G. Warren (2010), Interannual variations of Arctic cloud types in relation to sea ice, *Journal of Climate*, *23*(15), 4216–4232.

Ebert, E. E., and J. A. Curry (1993), An intermediate one-dimensional thermodynamic sea-ice model for investigating ice-atmosphere interactions, *Journal of Geophysical Research-Oceans*, *98*(C6), 10,085–10,109.

Fernald, F., B. Herman, and J. A. Reagan (1972), Determination of aerosol height ditribution by lidar, *Journal of Applied Meteorology*, *11*, 482–489.

Field, P. R. (1999), Aircraft observations of ice crystal evolution in an altostratus cloud, *Journal of the Atmospheric Sciences*, *56*(12), 1925–1941.

Findeisen, W. (1938), Kolloid-meteorologische vorgänge bei neiderschlags-bildung, *Meteor. Z*, *55*, 121–133.

Fleishauer, R. P., V. E. Larson, and T. H. Vonder Haar (2002), Observed microphysical structure of midlevel, mixed-phase clouds, *Journal of the Atmospheric Sciences*, *59*(11), 1779–1804.

Folkins, I., S. J. Oltmans, and A. M. Thompson (2000), Tropical convective outflow and near surface equivalent potential temperatures, *Geophysical Research Letters*, *27*(16), 2549–2552.

Fu, Q., P. Yang, and W. B. Sun (1998), An accurate parameterization of the infrared radiative properties of cirrus clouds for climate models, *Journal of Climate*, *11*(9), 2223–2237.

Fu, Q. A. (1996), An accurate parameterization of the solar radiative properties of cirrus clouds for climate models, *Journal of Climate*, *9*(9), 2058–2082.

Garrett, T. J., and C. F. Zhao (2006), Increased arctic cloud longwave emissivity associated with pollution from mid-latitudes, *Nature*, *440*(7085), 787–789.

Gedzelman, S. D. (1988), In praise of altocumulus, *Weatherwise*, *41*, 143 – 149.

Grise, K. M., and L. M. Polvani (2014), Southern hemisphere cloud-dynamics biases in CMIP5 models and their implications for climate projections, *Journal of Climate*, *27*(15), 6074–6092.

Gueymard, C. A. (2004), The sun's total and spectral irradiance for solar energy applications and solar radiation models, *Solar Energy*, *76*(4), 423–453.

Hallett, J., and S. Mossop (1974), Production of secondary ice particles during the riming process, *Nature*, *249*, 26–28.

Hartmann, D. L., K. J. Kowalewsky, and M. L. Michelsen (1991), Diurnal-variations of outgoing longwave radiation and albedo from Erbe scanner data, *Journal of Climate*, *4*(6), 598–617.

Hartmann, D. L., M. E. Ockertbell, and M. L. Michelsen (1992), The effect of cloud type on earths energy-balance - Global analysis, *Journal of Climate*, *5*(11), 1281–1304.

Heymsfield, A. J., L. M. Miloshevich, A. Slingo, K. Sassen, and D. O. C. Starr (1991), An observational and theoretical-study of highly supercooled altocumulus, *Journal of the Atmospheric Sciences*, *48*(7), 923–945.

Hobbs, P. V., and A. L. Rangno (1998), Microstructures of low and middle-level clouds over the Beaufort Sea, *Quarterly Journal of the Royal Meteorological Society*, *124*(550), 2035–2071.

Hogan, R. J., P. N. Francis, H. Flentje, A. J. Illingworth, M. Quante, and J. Pelon (2003), Characteristics of mixed-phase clouds. I: Lidar, radar and aircraft observations from CLARE'98, *Quarterly Journal of the Royal Meteorological Society*, *129*(592), 2089–2116.

Hu, Y. X., and K. Stamnes (1993), An accurate parameterization of the radiative properties of water clouds suitable for use in climate models, *Journal of Climate*, *6*(4), 728–742.

Hu, Y. X., D. Winker, M. Vaughan, B. Lin, A. Omar, C. Trepte, D. Flittner, P. Yang, S. L. Nasiri, B. Baum, W. B. Sun, Z. Y. Liu, Z. Wang, S. Young, K. Stamnes, J. P. Huang, R. Kuehn, and R. Holz (2009), CALIPSO/CALIOP cloud phase discrimination algorithm, *Journal of Atmospheric and Oceanic Technology*, *26*(11), 2293–2309.

Illingworth, A. J., R. J. Hogan, E. J. O'Connor, D. Bouniol, M. E. Brooks, J. Delanoe, D. P. Donovan, J. D. Eastment, N. Gaussiat, J. W. F. Goddard, M. Haeffelin, H. K. Baltink, O. A. Krasnov, J. Pelon, J. M. Piriou, A. Protat, H. W. J. Russchenberg, A. Seifert, A. M. Tompkins, G. J. van Zadelhoff, F. Vinit, U. Willen, D. R. Wilson, and C. L. Wrench (2007), Cloudnet - continuous evaluation of cloud profiles in seven operational models using ground-based observations, *Bulletin of the American Meteorological Society*, *88*(6), 883–898.

Intrieri, J. M., C. W. Fairall, M. D. Shupe, P. O. G. Persson, E. L. Andreas, P. S. Guest, and R. E. Moritz (2002), An annual cycle of Arctic surface cloud forcing at SHEBA, *Journal of Geophysical Research-Oceans*, *107*(C10-8039), 1–14.

Kahn, B. H., M. T. Chahine, G. L. Stephens, G. G. Mace, R. T. Marchand, Z. Wang, C. D. Barnet, A. Eldering, R. E. Holz, R. E. Kuehn, and D. G. Vane (2008), Cloud type comparisons of AIRS, CloudSat, and CALIPSO cloud height and amount, *Atmospheric Chemistry and Physics*, *8*(5), 1231–1248.

Kay, J. E., T. L'Ecuyer, A. Gettelman, G. Stephens, and C. O'Dell (2008), The contribution of cloud and radiation anomalies to the 2007 Arctic sea ice extent minimum, *Geophysical Research Letters*, *35*(8), L08,503 1–5.

Kayetha, V. K. (2014), Ice clouds over Fairbanks, Alaska, MS Thesis, University of Alaska Fairbanks.

Key, J. R., P. Yang, B. A. Baum, and S. L. Nasiri (2002), Parameterization of shortwave ice cloud optical properties for various particle habits, *Journal of Geophysical Research-Atmospheres*, *107*(D13), AAC 7–1 – AAC 7–10.

Klett, J. D. (1981), Stable analytical inversion solution for processing lidar returns, *Applied Optics*, *20*(2), 211–220.

Knudsen, E. M., Y. J. Orsolini, T. Furevik, and K. I. Hodges (2015), Observed anomalous atmospheric patterns in summers of unusual Arctic sea-ice melt, *Journal of Geophysical Research-Atmospheres*, *120*(7), 2595–2611.

Kylling, A., K. Stamnes, and S. C. Tsay (1995), A reliable and efficient 2-stream algorithm for spherical radiative-transfer - Documentation of accuracy in realistic layered media, *Journal of Atmospheric Chemistry*, *21*(2), 115–150.

Lampert, A., A. Ehrlich, A. Dornbrack, O. Jourdan, J. F. Gayet, G. Mioche, V. Shcherbakov, C. Ritter, and M. Wendisch (2009), Microphysical and radiative characterization of a subvisible midlevel Arctic ice cloud by airborne observations - a case study, *Atmospheric Chemistry and Physics*, *9*(8), 2647–2661.

L'Ecuyer, T. S., N. B. Wood, T. Haladay, G. L. Stephens, and P. W. Stackhouse (2008), Impact of clouds on atmospheric heating based on the R04 CloudSat fluxes and heating rates data set, *Journal of Geophysical Research-Atmospheres*, *113*, D00A15 1–15.

Liou, K. N., and R. Scotland (1971), Multiple backscattering and depolarization from water clouds for a pulsed lidar system, *Journal of Atmospheric Sciences*, *28*, 772–784.

Liu, Y. H., and J. R. Key (2014), Less winter cloud aids summer 2013 Arctic sea-ice return from 2012 minimum, *Environmental Research Letters*, *9*(4), 1–9.

Liu, Y. H., J. R. Key, Z. Y. Liu, X. J. Wang, and S. J. Vavrus (2012), A cloudier Arctic expected with diminishing sea ice, *Geophysical Research Letters*, *39*, L05,705 1–5.

Liu, Z. Y., M. Vaughan, D. Winker, C. Kittaka, B. Getzewich, R. Kuehn, A. Omar, K. Powell, C. Trepte, and C. Hostetler (2009), The CALIPSO lidar cloud and aerosol discrimination: version 2 algorithm and initial assessment of performance, *Journal of Atmospheric and Oceanic Technology*, *26*(7), 1198–1213.

Lubin, D., and A. M. Vogelmann (2006), A climatologically significant aerosol longwave indirect effect in the Arctic, *Nature*, *439*(7075), 453–456.

Lucchesi, R. (2012), File specification for MERRA products, *GMAO Office Note No.1, Version 2.3*, 82.

Luo, Y. L., K. M. Xu, H. Morrison, G. M. McFarquhar, Z. Wang, and G. Zhang (2008), Multi-layer arctic mixed-phase clouds simulated by a cloud-resolving model: Comparison with ARM observations and sensitivity experiments, *Journal of Geophysical Research-Atmospheres*, *113*(D12), D12,208 1–21.

Marchand, R., G. G. Mace, T. Ackerman, and G. Stephens (2008), Hydrometeor detection using Cloudsat - An earth-orbiting 94-GHz cloud radar, *Journal of Atmospheric and Oceanic Technology*, *25*(4), 519–533.

Mayer, B., and A. Kylling (2005), Technical note: The libRadtran software package for radiative transfer calculations - description and examples of use, *Atmospheric Chemistry and Physics*, *5*, 1855–1877.

Measures, M. R. (1992), *Laser remote sensing - fundamentals and applications*, Krieger Publishing Company, Florida.

Minnis, P., D. F. Young, K. Sassen, J. M. Alvarez, and C. J. Grund (1990), The 27-28 October 1986 FIRE IFO cirrus case-study - cirrus Parameter relationships derived from satellite and lidar data, *Monthly Weather Review*, *118*(11), 2402–2425.

Mitchell, D. L. (2002), Effective diameter in radiation transfer: General definition, applications, and limitations, *Journal of the Atmospheric Sciences*, *59*(15), 2330–2346.

Miyamoto, Y., Y. Kajikawa, R. Yoshida, T. Yamaura, H. Yashiro, and H. Tomita (2013), Deep moist atmospheric convection in a subkilometer global simulation, *Geophysical Research Letters*, *40*(18), 4922–4926.

Morris, T., and Braham (1968), The occurrence of ice particles in Minnesota cumuli, in *Proceedings of Weather Modification*, p. 306, American Meterological Society.

Okamoto, H., K. Sato, and Y. Hagihara (2010), Global analysis of ice microphysics from CloudSat and CALIPSO: Incorporation of specular reflection in lidar signals, *Journal of Geophysical Research-Atmospheres*, *115*, D22,209 1–20.

Omar, A. H., J. G. Won, D. M. Winker, S. C. Yoon, O. Dubovik, and M. P. McCormick (2005), Development of global aerosol models using cluster analysis of Aerosol Robotic Network (AERONET) measurements, *Journal of Geophysical Research-Atmospheres*, *110*(D10), D10S14 1–14.

Omar, A. H., D. M. Winker, C. Kittaka, M. A. Vaughan, Z. Y. Liu, Y. X. Hu, C. R. Trepte, R. R. Rogers, R. A. Ferrare, K. P. Lee, R. E. Kuehn, and C. A. Hostetler (2009), The CALIPSO automated aerosol classification and lidar ratio selection algorithm, *Journal of Atmospheric and Oceanic Technology*, *26*(10), 1994–2014.

Pandey, V. K., and P. Kurtakoti (2014), Evaluation of GODAS using RAMA mooring observations from the Indian ocean, *Marine Geodesy*, *37*(1), 14–31.

Petty, G. (2006), *A First Course in Atmospheric Radiation*, Sundog Publishing.

Platt, C. M. R., D. W. Reynolds, and N. L. Abshire (1980), Satellite and lidar observations of the albedo, emittance and optical depth of cirrus compared to model-calculations, *Monthly Weather Review*, *108*(2), 195–204.

Powell, K. A., C. A. Hostetler, Z. Y. Liu, M. A. Vaughan, R. E. Kuehn, W. H. Hunt, K. P. Lee, C. R. Trepte, R. R. Rogers, S. A. Young, and D. M. Winker (2009), CALIPSO lidar calibration algorithms. Part I: nighttime 532-nm parallel channel and 532-nm perpendicular channel, *Journal of Atmospheric and Oceanic Technology*, *26*(10), 2015–2033.

Powell, K. A., M. A. Vaughan, R. R. Rogers, R. E. Kuehn, W. H. Hunt, K. P. Lee, and T. D. Murray (2010), The CALIOP 532-nm channel daytime calibration: version 3 algorithms, in *Proceedings of the 25th International Laser Radar Conference*, pp. 1367–1310.

Pruppacher, H., and J. Klett (1997), *Microphysics of clouds and precipitation*, second ed., 954 pp., Springer, New york.

Ramanathan, V., R. D. Cess, E. F. Harrison, P. Minnis, B. R. Barkstrom, E. Ahmad, and D. Hartmann (1989), Cloud-radiative forcing and climate - results from the earth radiation budget experiment, *Science*, *243*(4887), 57–63.

Randall, D. A. (2015), *An introduction to the global circulation of the atmosphere*, Princeton University Press.

Ricchiazzi, P., S. R. Yang, C. Gautier, and D. Sowle (1998), SBDART: A research and teaching software tool for plane-parallell radiative transfer in the earth's atmosphere, *Bulletin of the American Meteorological Society*, *79*(10), 2101–2114.

Rienecker, M. M., M. J. Suarez, R. Todling, J. Bacmeister, L. Takacs, H. C. Liu, W. Gu, M. Sienkienwicz, R. D. Koster, R. Gelaro, I. Stajner, and J. E. Nielsen (2008), The GOES-5 data assimilation system-documentation of versions 5.0.1, 5.1.0 and 5.2.0, *NASA/TM-2008-104606*, NASA Tech Rep, Series on Global Modelling and Data Assimilation.

Riihimaki, L. D., S. A. McFarlane, and J. M. Comstock (2012), Climatology and formation of tropical midlevel clouds at the Darwin ARM Site, *Journal of Climate*, *25*(19), 6835–6850.

Rosenfeld, D., and W. L. Woodley (2000), Deep convective clouds with sustained supercooled liquid water down to -37.5 degrees C, *Nature*, *405*(6785), 440–442.

Rossow, W. B., and R. A. Schiffer (1999), Advances in understanding clouds from ISCCP, *Bulletin of the American Meteorological Society*, *80*(11), 2261–2287.

Sassen, K. (1987), Ice-cloud content from radar reflectivity, *Journal of Climate and Applied Meteorology*, *26*(8), 1050–1053.

Sassen, K. (1991), The Polarization lidar technique for cloud research - a review and current assessment, *Bulletin of the American Meteorological Society*, *72*(12), 1848–1866.

Sassen, K. (2002), Cirrus clouds: a modern perspective, in *Cirrus*, edited by D. K. Lynch, K. Sassen, D. O. Starr, and G. Stephens, Oxford University Press.

Sassen, K. (2005), Dusty ice clouds over Alaska, *Nature*, *434*(7032), 456–456.

Sassen, K., and J. R. Campbell (2001), A midlatitude cirrus cloud climatology from the facility for atmospheric remote sensing. Part I: Macrophysical and synoptic properties, *Journal of the Atmospheric Sciences*, *58*(5), 481–496.

Sassen, K., and B. S. Cho (1992), Subvisual thin cirrus lidar data set for satellite verification and climatological research, *Journal of Applied Meteorology*, *31*(11), 1275–1285.

Sassen, K., and G. C. Dodd (1988), Homogeneous nucleation rate for highly supercooled cirrus cloud droplets, *Journal of the Atmospheric Sciences*, *45*(8), 1357–1369.

Sassen, K., and V. I. Khvorostyanov (2008), Cloud effects from boreal forest fire smoke: evidence for ice nucleation from polarization lidar data and cloud model simulations, *Environmental Research Letters*, *3*(2), 1–12.

Sassen, K., and Z. Wang (2008), Classifying clouds around the globe with the CloudSat radar: 1-year of results, *Geophysical Research Letters*, *35*(4), 1–5.

Sassen, K., and Z. Wang (2012), The clouds of the middle troposphere: composition, radiative impact, and global distribution, *Surveys in Geophysics*, *33*(3-4), 677–691.

Sassen, K., P. J. DeMott, J. M. Prospero, and M. R. Poellot (2003), Saharan dust storms and indirect aerosol effects on clouds: CRYSTAL-FACE results, *Geophysical Research Letters*, *30*(12), 35 1–4.

Sassen, K., Z. Wang, and D. Liu (2009), Global distribution of cirrus clouds from CloudSat/Cloud-Aerosol Lidar and Infrared Pathfinder Satellite Observations (CALIPSO) measurements, *Journal of Geophysical Research-Atmospheres*, *113*(D20), 1–12.

Scotland, R., K. Sassen, and R. Stone (1971), Observations by lidar of linear depolarization ratios for hydrometeors, *Journal of Applied Meteorology*, *10*, 1011–1017.

Seifert, P., A. Ansmann, I. Mattis, U. Wandinger, M. Tesche, R. Engelmann, D. Muller, C. Perez, and K. Haustein (2010), Saharan dust and heterogeneous ice formation: Eleven years of cloud observations at a central European EARLINET site, *Journal of Geophysical Research-Atmospheres*, *115*, 1–13.

Shaw, G. E. (1995), The Arctic haze phenomenon, *Bulletin of the American Meteorological Society*, *76*(12), 2403–2413.

She, C. Y. (2001), Spectral structure of laser light scattering revisited: bandwidths of nonresonant scattering lidars, *Applied Optics*, *40*(27), 4875–4884.

Shettle, E. (1989), Models of aerosols, clouds and precipitation for atmospheric propagation studies, in *AGARD Conference Proceedings No. 454, Atmopsheric propagation in the UV, Visible, IR and MM-region and Related System Aspects*, pp. 1–359.

Shupe, M. D., and J. M. Intrieri (2004), Cloud radiative forcing of the Arctic surface: The influence of cloud properties, surface albedo, and solar zenith angle, *Journal of Climate*, *17*(3), 616–628.

Shupe, M. D., J. S. Daniel, G. de Boer, E. W. Eloranta, P. Kollias, C. N. Long, E. P. Luke, D. D. Turner, and J. Verlinde (2008), A focus on mixed-phase clouds: The status of ground-based observational methods, *Bulletin of the American Meteorological Society*, *89*(10), 1549–1562.

Shupe, M. D., V. P. Walden, E. Eloranta, T. Uttal, J. R. Campbell, S. M. Starkweather, and M. Shiobara (2011), Clouds at Arctic atmospheric observatories. Part I: Occurrence and macrophysical properties, *Journal of Applied Meteorology and Climatology*, *50*(3), 626–644.

Silfvast, T., W (2004), *Laser fundamentals*, 670 pp., Cambridge University Press.

Slingo, A. (1989), A GCM parameterization for the shortwave radiative properties of water clouds, *Journal of the Atmospheric Sciences*, *46*(10), 1419–1427.

Smith, A. J., V. E. Larson, J. G. Niu, J. A. Kankiewicz, and L. D. Carey (2009), Processes that generate and deplete liquid water and snow in thin midlevel mixed-phase clouds, *Journal of Geophysical Research-Atmospheres*, *114*, 1–18.

Solomon, S., D. Qin, M. Manning, Z. Chen, M. Marquis, K. B. Averyt, M. Tignor, and H. L. Miller (2007), *Contribution of working group I to the fourth assessment report of the Intergovernmental Panel on Climate Change*, Cambridge University Press.

Stamnes, K., S. C. Tsay, W. Wiscombe, and K. Jayaweera (1988), Numerically stable algorithm for discrete-ordinate-method radiative-transfer in multiple-scattering and emitting layered media, *Applied Optics*, *27*(12), 2502–2509.

Stephens, G. L. (1978), Radiation profiles in extended water clouds. II: Parameterization schemes, *Journal of the Atmospheric Sciences*, *35*(11), 2123–2132.

Stephens, G. L., D. G. Vane, S. Tanelli, E. Im, S. Durden, M. Rokey, D. Reinke, P. Partain, G. G. Mace, R. Austin, T. L'Ecuyer, J. Haynes, M. Lebsock, K. Suzuki, D. Waliser, D. Wu, J. Kay, A. Gettelman, Z. Wang, and R. Marchand (2008), CloudSat mission: performance and early science after the first year of operation, *Journal of Geophysical Research-Atmospheres*, *113*(D23), D00A18 1–18.

Stone, R. (1957), A compendium on cirrus and cirrus forecasting, *Aws tr 105-130*, Air Force Weather Service Technical Report.

Sun, Z., and K. P. Shine (1995), Parameterization of ice-cloud radiative properties and its application to the potential climatic importance of mixed-phase clouds, *Journal of Climate*, *8*(7), 1874–1888.

Trenberth, K. E., J. T. Fasullo, and J. Kiehl (2009), Earth's global energy budget, *Bulletin of the American Meteorological Society*, *90*(3), 311–323.

Turner, D. D. (2005), Arctic mixed-phase cloud properties from AERI lidar observations: Algorithm and results from SHEBA, *Journal of Applied Meteorology*, *44*(4), 427–444.

Twomey, S. (1977), The influence of pollution on the shortwave albedo of clouds, *Journal of the Atmospheric Sciences*, *34*(7), 1149–1152.

Vaughan, M. A., D. M. Winker, and K. A. Powell (2005), CALIOP algorithm theoretical basic document: Part 2 - Feature detction and layer properties algorithms, *PC-SCI-202.02*, NASA Langely Research Center, Hampton, Virginia.

Vaughan, M. A., K. A. Powell, R. E. Kuehn, S. A. Young, D. M. Winker, C. A. Hostetler, W. H. Hunt, Z. Y. Liu, M. J. McGill, and B. J. Getzewich (2009), Fully automated detection of cloud and aerosol layers in the CALIPSO lidar measurements, *Journal of Atmospheric and Oceanic Technology*, *26*(10), 2034–2050.

Verlinde, J., J. Y. Harrington, G. M. McFarquhar, V. T. Yannuzzi, A. Avramov, S. Greenberg, N. Johnson, G. Zhang, M. R. Poellot, J. H. Mather, D. D. Turner, E. W. Eloranta, B. D. Zak, A. J. Prenni, J. S. Daniel, G. L. Kok, D. C. Tobin, R. Holz, K. Sassen, D. Spangenberg, P. Minnis, T. P. Tooman, M. D. Ivey, S. J. Richardson, C. P. Bahrmann, M. Shupe, P. J. DeMott, A. J. Heymsfield, and R. Schofield (2007), The Mixed-Phase Arctic Cloud Experiment, *Bulletin of the American Meteorological Society*, *88*(2), 205–221.

Wang, Z. (2011), Level 2 combined radar and lidar cloud scenario classification product process description and interface control document, *JPL Document, Version 1.0*(http://www.cloudsat.cira.colostate.edu/dataICDlist.php).

Warren, S. G., C. J. Hahn, J. London, R. M. Chervin, and R. Jeene (1986), Global distribution of total cloud cover and cloud type amounts over the land, *NACR Tech Note, 29*.

Warren, S. G., C. J. Hahn, J. London, R. M. Chervin, and R. Jeene (1988), Global distribution of total cloud cover and cloud type amounts over the ocean, *NACR Tech. Note, 41*.

Wegener, A. (1911), *Thermodynamik der atmosphäre*, 331 pp., Leipzig.

Wendler, G., and P. Nicpcon (1975), Low-level temperature inversions in Fairbanks, Central Alaska, *Monthly weather review, 103*, 34–44.

Winker, D. M., M. A. Vaughan, A. Omar, Y. X. Hu, K. A. Powell, Z. Y. Liu, W. H. Hunt, and S. A. Young (2009), Overview of the CALIPSO mission and CALIOP data processing algorithms, *Journal of Atmospheric and Oceanic Technology*, *26*(11), 2310–2323.

WMO (1987), International Cloud Atlas I and II, *World Meteorological Organization, Geneva.*

WMO (1988), Manual of codes, Vol. I, *WMO Publ Vol 306, World Meteorological Organization, Geneva.*

Wyser, K., C. G. Jones, P. Du, E. Girard, U. Willen, J. Cassano, J. H. Christensen, J. A. Curry, K. Dethloff, J. E. Haugen, D. Jacob, M. Koltzow, R. Laprise, A. Lynch, S. Pfeifer, A. Rinke, M. Serreze, M. J. Shaw, M. Tjernstrom, and M. Zagar (2008), An evaluation of Arctic cloud and radiation processes during the SHEBA year: simulation results from eight Arctic regional climate models, *Climate Dynamics*, *30*(2-3), 203–223.

Yang, P., K. N. Liou, K. Wyser, and D. Mitchell (2000), Parameterization of the scattering and absorption properties of individual ice crystals, *Journal of Geophysical Research-Atmospheres*, *105*(D4), 4699–4718.

Yasunaga, K., K. Yoneyama, H. Kubota, H. Okamoto, A. Shimizu, H. Kumagai, M. Katsumata, N. Sugimoto, and I. Matsui (2006), Melting layer cloud observed during R/V Mirai cruise MR01-K05, *Journal of the Atmospheric Sciences*, *63*(11), 3020–3032.

Zhang, D., Z. Wang, and D. Liu (2010), A global view of midlevel liquid-layer topped stratiform cloud distribution and phase partition from CALIPSO and CloudSat measurements, *Journal of Geophysical Research-Atmospheres*, *115*(D00H13), 1–10.

Zhang, M. H., W. Y. Lin, S. A. Klein, J. T. Bacmeister, S. Bony, R. T. Cederwall, A. D. Del Genio, J. J. Hack, N. G. Loeb, U. Lohmann, P. Minnis, I. Musat, R. Pincus, P. Stier, M. J. Suarez, M. J. Webb, J. B. Wu, S. C. Xie, M. S. Yao, and J. H. Zhang (2005), Comparing clouds and their seasonal variations in 10 atmospheric general circulation models with satellite measurements, *Journal of Geophysical Research-Atmospheres*, *110*(D15), D15S02 1–18.

Zhao, C. F., and T. J. Garrett (2015), Effects of arctic haze on surface cloud radiative forcing, *Geophysical Research Letters*, *42*(2), 557–564.

Zhao, G. Y., and L. Di Girolamo (2007), Statistics on the macrophysical properties of trade wind cumuli over the tropical western Atlantic, *Journal of Geophysical Research-Atmospheres*, *112*(D10), D10,204, 1–10.

Appendix A
Radiative transfer in clouds

A.1 Basic quantities

The power of electromagnetic (EM) radiation at a certain position and time is quantified by the radiant energy flux Φ (in units W). There are two normalized quantities that describe the radiant energy with respect to its measurement and are central to most problems in atmospheric science: irradiance and radiance (*Petty*, 2006). The radiant energy flux density or *irradiance F* (in units of W m^{-2}) is a measure of radiant energy flux incident on a plane surface with unit area dA and orientation $\vec{n}$.

$$F = \frac{d\Phi}{dA} \tag{A.1}$$

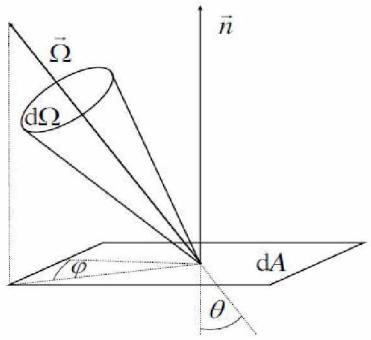

Figure A.1: Plane geometry used to define radiative quantities.

The orientation of the reference plane can be random but for describing radiative transfer in the atmosphere it is considered to be horizontal (Figure 1). In such case, the irradiance is weighted with the cosine of the angle of incidence θ (zenith angle) on the horizontal surface with $\theta = 0^o$ referring to the perpendicular incidence. Now, the *radiance* (in units of W m^{-2} sr^{-1}) can be defined as the radiant energy flux Φ transferred through a unit plane area dA within the solid angle $d\Omega$ along the direction of propagation of the radiation $\vec{\Omega}$.

$$I(\vec{\Omega}) = \frac{d^2\Phi}{cos\theta \cdot dA \cdot d\Omega} \tag{A.2}$$

where, solid angle $d\Omega = sin\theta \cdot d\theta \cdot d\varphi$ (in units of *sr*), and ϕ is the azimuthal angle.

From the equations 1.1 and 1.2, F can be solved as:

$$F = \int_{4\pi}\int_{sr} I(\vec{\Omega}) \cdot cos\theta \cdot d\Omega = \int_0^{2\pi}\int_0^{\pi} I(\theta,\varphi) \cdot cos\theta \cdot sin\theta \cdot d\theta \cdot d\varphi \tag{A.3}$$

Considering the lower and upper hemisphere separately that are divided by a horizontal surface, the irradiance can be expressed in terms of an upwelling ($\uparrow$) and downwelling ($\downarrow$) irradiance components:

$$F^{\downarrow} = + \int_0^{2\pi}\int_0^{\frac{\pi}{2}} I(\theta,\varphi) \cdot cos\theta \cdot sin\theta \cdot d\theta \cdot d\varphi \tag{A.4}$$

$$F^{\uparrow} = - \int_0^{2\pi}\int_{\frac{\pi}{2}}^{\pi} I(\theta,\varphi) \cdot cos\theta \cdot sin\theta \cdot d\theta \cdot d\varphi \tag{A.5}$$

Here the downwelling irradiance $F^{\downarrow}$ propagating through the atmosphere consists of a direct ($F^{\downarrow}_{dir}$) and an indirect component ($F^{\downarrow}_{diff}$):

$$F^{\downarrow} = F^{\downarrow}_{dir} + F^{\downarrow}_{diff} \tag{A.6}$$

$F^{\downarrow}_{dir}$ represents the solar radiation that has not encountered scattering processes in the atmosphere yet. $F^{\downarrow}_{diff}$ refers to the part of the radiation that has been scattered/absorbed/emitted by atmospheric molecules and particles or was reflected from the surface back into the atmosphere. The upwelling irradiance has only a diffuse component ($F^{\uparrow} = F^{\uparrow}_{diff}$).

Since, irradiance (F) represents the radiant flux Φ propagating through a plane unit surface from all possible directions of a hemisphere and radiance (I) represents flux Φ at a certain direction, irradiance measurements are used to assess the radiative energy budget/transfer calculations. The radiative forcing of clouds ΔF at a certain altitude z is defined as the difference of the net irradiances in cloudy and clear sky conditions.

$$\Delta F(z) = \left[F^{\downarrow}(z) - F^{\uparrow}(z)\right]_{cloudy} - \left[F^{\downarrow}(z) - F^{\uparrow}(z)\right]_{clear} \tag{A.7}$$

The positive (negative) values of ΔF are interpreted as follows: the clouds have a warming (cooling) effect at the surface or on the atmosphere below the altitude z. In practice radiative transfer calculations are done separately for the solar (ΔF_{sol}) and thermal infrared

spectral ranges ΔF_{IR}. Thus the net radiative forcing at an altitude z, due to clouds can be written as:

$$\Delta F_{net}(z) = \Delta F_{sol}(z) + \Delta F_{IR}(z) \tag{A.8}$$

A.2 Optical and microphysical properties of cloud particles

EM radiation propagating through the atmosphere can be absorbed/scattered/emitted by gas molecules, cloud and aerosol particles. The interactions between EM radiation and individual particles in the atmosphere can be described by three single-scattering properties: the extinction cross section C_{ext}, the single-scattering albedo $\tilde{\omega}$, and the scattering phase function $\mathcal{P}$. These properties depend not only on the cross-section area, surface and volume, and refractive index but also on the shape and orientation of individual particles. While the cloud particles in water clouds are spherical droplets, the particles in ice clouds are a variety of non-spherical shaped crystals.

A.2.1 Single scattering properties

The extinction cross section C_{ext} (m^2) is a measure of how much of the radiation that is incident on a particle is extinguished, either due to scattering or absorption. It is defined as the sum of scattering cross section C_{sca} (m^2) and absorption cross section C_{abs} (m^2):

$$C_{ext} = C_{sca} + C_{abs} \tag{A.9}$$

Single-scattering albedo ($\tilde{\omega}$) is a dimensionless quantity defined as the ratio of scattering to extinction cross-sections:

$$\tilde{\omega} = \frac{C_{sca}}{C_{ext}} \tag{A.10}$$

The values of $\tilde{\omega}$ ranges from 0 for completely absorbing to 1 for completely scattering particles, respectively. The other dimensionless quantity is the scattering phase function $\mathcal{P}(\vartheta, \varphi)$ and it describes the probability that the radiation (photons) incident on an cloud particle is scattered in a particular direction that is different from the direction of incidence by a scattering angle ϑ. Here, φ denotes the azimuth angle. For the case where the particle has no absorption (i.e., $\tilde{\omega} = 1$), the normalization condition which ensures the radiant energy is conserved can be written as:

$$\int_{4\pi}\int_{sr} \mathcal{P}(\vartheta,\varphi)\cdot d\Omega = \int_0^{2\pi}\int_0^{\pi} \mathcal{P}(\vartheta,\varphi)\cdot sin\vartheta\cdot d\vartheta\cdot d\varphi = 4\pi\cdot sr \tag{A.11}$$

For randomly oriented particles, the azimuthal dependence vanishes, so that the scattering phase function is only a function of scattering angle and can be expressed as $\mathcal{P}(cos\vartheta)$. It is used in the definition of the asymmetry parameter g, which is expressed as the mean cosine of the scattering angle:

$$\begin{aligned} g = \langle cos\vartheta\rangle &= \frac{1}{4\pi sr}\int_{4\pi}\int_{sr} \mathcal{P}(\vartheta)\cdot cos\vartheta\cdot d\Omega \\ &= \frac{1}{2}\int_{-1}^{+1} cos\vartheta\cdot\mathcal{P}(cos\vartheta)\cdot dcos\vartheta \end{aligned} \tag{A.12}$$

The asymmetry parameter is a measure of the anisotropy of the scattering phase function and ranges between -1 (total backward scattering) and +1 (total forward scattering). The value of g = 0 describes equal scattering in the forward and backward hemisphere.

The optical properties of a cloud volume are obtained by integration of the single-scattering optical properties weighted by the number size distribution of the scattering cloud particles $\frac{dN}{dD}(D)$. The (spectral) volumetric extinction coefficient b_{ext} (in units of m^{-1}) is calculated by:

$$b_{ext} = \int C_{ext}(\tilde{D})\cdot\frac{dN}{dD}(\tilde{D})d\tilde{D} \tag{A.13}$$

A.2.2 Microphysical properties

The effective radius $R_{eff}(\mu m)$ is an area-weighted mean radius characterizing a particle size distribution in radiative transfer calculations. It can be understood as the representative distance a photon travels through a particle without any internal reflections or refraction. It thereby is the relevant dimension for the interaction of a single particle with EM radiation (*Mitchell*, 2002). Depending on the cloud radiative parameterization scheme, different definitions of R_{eff} exist in the literature. Here we define effective radius as (*Yang et al.*, 2000; *Key et al.*, 2002):

$$R_{eff} = \frac{3}{4}\cdot\frac{\int V(\tilde{D})\cdot\frac{dN}{dD}\cdot(\tilde{D})\cdot d\tilde{D}}{\int A(\tilde{D})\cdot\frac{dN}{dD}\cdot(\tilde{D})\cdot d\tilde{D}} \tag{A.14}$$

with D (μm) being the maximum dimension of an ice crystal, $\frac{dN}{dD}(D)$ being the number of

particles with maximum dimension D, V and A being the volume and projected area of the particles, respectively.

The cloud water path (CWP, gm^{-2}) is defined as the integral of cloud water content (CWC, gm^{-3}) over its base to top altitudes. For pure ice or water clouds CWP is ice water path (IWP) or liquid water path (LWP), while for mixed-phase clouds it is sum of IWP and LWP that is expressed as:

$$IWP = \int_{z_{base}}^{z_{top}} IWC(\tilde{z})d\tilde{z} \tag{A.15}$$

$$LWP = \int_{z_{base}}^{z_{top}} LWC(\tilde{z})d\tilde{z} \tag{A.16}$$

The cloud optical thickness (τ) is defined as the integral of the volumetric extinction coefficient of a cloud from its base to top altitudes.

$$\tau(z) = \int_{z_{base}}^{z_{top}} b_{ext}(\tilde{z})d\tilde{z} \tag{A.17}$$

Thus, the optical depth of ice or water cloud τ can be estimated from the microphysical cloud properties effective using the approximation:

$$\tau = \frac{3 \cdot IWP}{2 \cdot \rho_{ice} \cdot R_{eff}} \tag{A.18}$$

$$\tau = \frac{3 \cdot LWP}{2 \cdot \rho_{water} \cdot R_{eff}} \tag{A.19}$$

where, ρ_{ice} is the density of ice (0.916 g cm^3), and ρ_{water} is the density of water (1 g cm^3).

A.3 Radiative transfer equation

With all the necessary radiative quantities, optical properties, and microphysical cloud properties defined, the attenuation of direct solar radiance I_{dir} in the (cloudy) atmosphere along τ as the vertical coordinate can be described by the Law of Beer, Lambert, and Bouguer:

$$I_{dir}(\tau, \mu_0, \varphi_0) = \frac{S_0}{4\pi sr} \cdot exp\left[-\frac{\tau}{\mu_0}\right] \tag{A.20}$$

where, S_0 is the solar constant, $\mu_0 = cos\theta_0$, and φ_0 is the solar zenith angle.

Interpreting equation 1.20 shows that I_{dir} decreases exponentially along τ. Thus, I_{dir} is strongly attenuated in the presence of clouds, allowing a description of the solar radiative transfer in clouds by the diffuse radiance I_{diff} only. The one-dimensional (1D) radiative transfer equation (RTE) assuming a plane parallel and a horizontally homogeneous atmosphere is (*Chandrasekhar*, 1950):

$$\mu \frac{dI_{diff}(\tau, \mu, \varphi)}{d\tau} = I_{diff} - (J_{dir} + J_{diff} + J_{emi}) \tag{A.21}$$

where J_{dir} and J_{diff} represents the amount of radiation that is scattered into the viewing direction, either from the direct solar beam (J_{dir}, single-scattering term) or from diffuse radiation (J_{diff}, multiple-scattering term). In the solar spectral range (which will subsequently be considered, wavelength range $\lambda = 0.2 - 4\ \mu m$), thermal emission can be neglected: $J_{emi} = 0$. The viewing direction (or direction of propagation of I_{diff}) is characterized by $\mu = cos\theta$, the cosine of the zenith angle θ, and the azimuth angle φ. J_{dir} and J_{diff} depend on $\tilde{\Omega}$ and $\mathcal{P}$ and are defined as:

$$J_{dir} = \frac{\tilde{\omega}(\tau)}{4\pi sr} \cdot S_0 \cdot exp\left[-\frac{\tau}{\mu_0} \right] \cdot \mathcal{P}(\tau, [-\mu_0, \varphi_0] \longrightarrow [\mu, \varphi]) \tag{A.22}$$

$$J_{diff} = \frac{\tilde{\omega}(\tau)}{4\pi sr} \int_0^{2\pi} \int_{-1}^{1} I_{diff}(\tau, \mu', \varphi') \cdot \mathcal{P}(\tau, [\mu', \varphi'] \longrightarrow [\mu, \varphi]) \cdot d\mu' \cdot d\varphi' \tag{A.23}$$